TUM School of Computation, Information and Technology
Technische Universität München

Multi-Radio Access Technology Coexistence and Resource Allocation Approaches for Aircraft Related Communication

Jörg Alejandro von Mankowski, M.Sc.

Vollständiger Abdruck der von der TUM School of Computation, Information and Technology der Technischen Universität München zur Erlangung des akademischen Grades eines

Doktors der Ingenieurwissenschaften (Dr.-Ing.)

genehmigten Dissertation.

Vorsitz:
Prof. Dr.-Ing. Wolfgang Utschick

Prüfer der Dissertation:
1. Prof. Dr.-Ing. Wolfgang Kellerer
2. Prof. Dr.-Ing. Armin Dekorsy

Die Dissertation wurde am 02.04.2024 bei der Technischen Universität München eingereicht und durch die TUM School of Computation, Information and Technology am 03.09.2024 angenommen.

TUM School of Computation, Information and Technology
Technical University of Munich

Multi-Radio Access Technology Coexistence and Resource Allocation Approaches for Aircraft Related Communication

Jörg Alejandro von Mankowski, M.Sc.

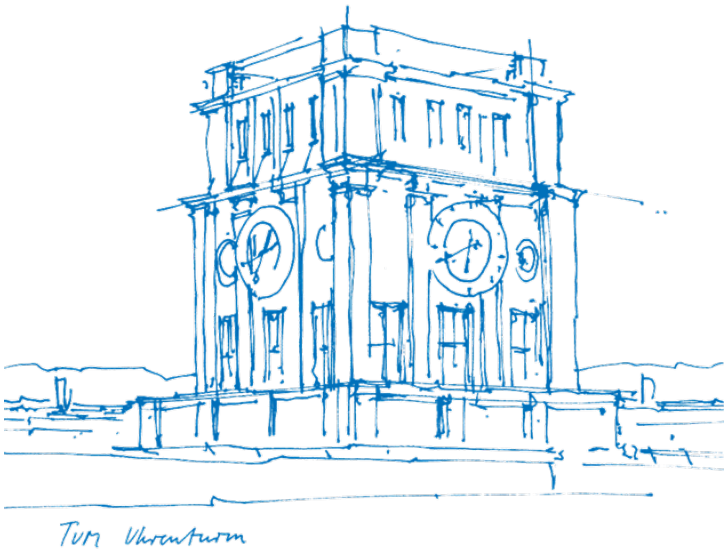

Multi-Radio Access Technology Coexistence and Resource Allocation Approaches for Aircraft Related Communication

Jörg Alejandro von Mankowski, M.Sc.

MediaTUM

Kurzfassung

Mit der fortschreitenden Digitalisierung der Gesellschaft weitet sich der Bedarf an höheren Datenraten und ununterbrochener Konnektivität auch auf den Bereich der Luftfahrt aus, insbesondere bezüglich Flugzeugkabinen. Passagierflugzeuge werden zunehmend zu digitalen Ökosystemen, die robuste und effiziente Kommunikationstechnologien erfordern, um die vielfältigen Anforderungen an Bord zu erfüllen. Die Motivation für diese Arbeit ergibt sich aus den Herausforderungen, die die Radio Frequency (RF)-Kommunikation in der Kabine mit sich bringt. Dies umfasst die Einschränkungen bestehender Kanalmodelle, die Einführung neuer Technologien und Dienstleistungen sowie den Bedarf an höchst zuverlässigen Kommunikationssystemen.

Zur Bewältigung dieser Herausforderungen präsentieren wir zunächst eine umfassende Analyse der Kommunikationskanäle innerhalb einer Flugzeugkabine. Zur Modellierung dieser physikalischen Schicht konzentrieren wir uns auf die Herleitung und Generierung von Path Loss (PL)-, Tapped Delay Line (TDL)- und Clustered Delay Line (CDL)-Modellen mithilfe von Ray-Tracing-Simulationen. Im Gegensatz zu bisherigen Studien basieren unsere Modelle auf einem erweiterten Repertoire an Zufallsverteilungen, beziehen mehr Prädiktoren ein und betrachten verschiedene Empfänger- und Senderszenarien, was die Präzision der Modelle erhöht. Für unsere Simulationen verwenden wir ein detailliertes 3D-Modell einer Boeing 737-300-Kabine, welches öffentlich zugänglich gemacht wurde und damit ein Basiswerkzeug für weitere Forschung zur drahtlosen Kanalmodellierung bietet.

Um die Link-Ebene der Kommunikation innerhalb der Flugzeugkabine zu verbessern, erforschen wir die Verwendung von beamforming (BF)-Technologien im Kontext von Wireless Fidelity (WiFi) 6 und 5G. Insbesondere die Multi-Radio Access Point (RAP)- und Multi-Radio Access Technology (Multi-RAT) Situation stellen hier eine besondere Herausforderung dar. Wir begegnen dieser mit einer zentralisierten Strategie, die die Sendeleistung, Senderichtung und den Abstrahlwinkel jedes RAPs optimiert, sodass Interferenzen minimiert werden und jeder Nutzer einen fairen Durchsatz erfährt. Hierfür verwenden wir eine Software für mathematische Optimierung, Meta-Heuristiken und Deep Reinforcement Learning (DRL). In diesem Kontext zeigen wir auch die Vorteile von BF bei der Reduzierung von Interferenzen und der Unterstützung einer höheren Anzahl von Geräten.

Um die kommunikationsbasierten Dienstleistungen für Passagiere weiter zu verbessern, neue Einnahmequellen für Fluggesellschaften zu schaffen und RF-Kommunikationsdienste zukunftssicher zu machen, integrieren wir die Flugzeugkabinen der gesamten Flotte einer Fluggesellschaft in ein globales Multi-Layer Network (MLN) und setzen Multi-Access Edge Computing (MEC)-Server auf ausgewählten Flugzeugen der Fluggesellschaft ein. Dieses Netzwerk besteht aus einer terrestrischen Ebene mit Gateways, einer aeronautischen Ebene mit kommerziellen Flugzeugen und einer Satelliten-Ebene mit einer spezifischen Satellitenkonstellation. Wir zeigen, dass solche Netzwerke eine dynamische Optimierung des Routings von Diensten und deren Platzierung erfordern. Dies erreichen wir, indem wir zwei Optimierungsprobleme aufstellen: eine mit dem Ziel, die Latenz zu minimieren, und eine, um den Energieverbrauch für die bereitgestellten Dienste im Netzwerk zu minimieren. Für eine praktische Implementierung passen wir diese Formulierungen weiter an und schaffen damit Lösungszeiten, die weit unter dem durch die Bewegung der Knoten im Netzwerks auferlegten Grenzen liegen. Weiter zeigen wir, dass unser MLN es uns nicht nur ermöglicht, Dienste wie VoIP oder Gaming für die Flugzeugkabine bereitzustellen, sondern auch Rechenressourcen für die Satelliten-Ebene bereitzustellen.

Die gezeigten Forschungsergebnisse bilden die Grundlage für zukünftige Kommunikationssysteme für Flugzeugkabinen. Diese sind darauf ausgelegt, die Anforderungen moderner RF-basierter Netzwerke zu erfüllen, deren Effizienz zu steigern und Möglichkeiten eröffnen die die Qualität von Diensten an Bord verbessern können.

Abstract

As the digitalization of society advances, the need for higher data rates and continuous connectivity extends into the realm of aviation, particularly within aircraft cabins. Modern aircraft are increasingly becoming digital ecosystems, necessitating robust and efficient communication technologies to meet the diverse needs onboard. This work is motivated by the challenges faced in in-cabin Radio Frequency (RF)-communication, including the limitations of existing channel models, the introduction of new technologies and services, and the need for highly reliable communication systems.

In order to overcome these challenges we first present a comprehensive analysis of the physical layer within the aircraft cabin, focusing on the derivation of Path Loss, Tapped Delay Line, and Clustered Delay Line models from ray-tracing data. Unlike existing studies, this work provides models for various cabin scenarios, incorporating a broader range of random distributions and multiple predictors to enhance model accuracy. A detailed 3D model of a Boeing 737-300 cabin is introduced, offering a foundational tool for accurate wireless channel modeling accessible for further research and simulations.

Improving the communication inside the aircraft cabin, we explore the application of beamforming (BF) technologies in the context of Wireless Fidelity (WiFi) 6 and 5G, addressing the challenges posed by the cabin's Multi-Radio Access Point (RAP) and Multi-Radio Access Technology (Multi-RAT) environment. A centralized strategy is proposed to optimize transmission power, link direction, and beam angle for each RAP to minimize interference and ensure fair throughput. The work presents various or different solution methods including meta-heuristics and Deep Reinforcement Learning (DRL) demonstrating the benefits of BF in reducing interference and supporting a higher number of devices.

To further enhance passenger services, create new revenue opportunities for airlines, and future-proof RF-communication-based services, we connect the aircraft cabins of an airline's entire fleet into a global Multi-Layer Network (MLN) and deploy Multi-Access Edge Computing (MEC) servers on selected commercial aircraft. We demonstrate that such a network consisting of an terrestrial layer with gateways, aerial layer with commercial aircraft and satellite layer with a specific satellite constellation requires a dynamic optimization of service routing and placement. We achieve this by providing two different optimization formulations, one with the goal to minimize latency and one to minimize energy consumption for the provided services in the network. To enable a practical implementation, we further adapt these formulations, resulting in solving times much smaller than the limit imposed by dynamicity of the network. We further show that our MLN not only allows us to provide services as VoIP or Gaming to the aircraft cabin but also provides computational resources to the satellite layer.

These advancements lay the foundation for future aircraft cabin communication systems, designed to fulfill the requirements of contemporary wireless networks. They also create opportunities to improve the quality of in-flight services and operational efficiency.

Acknowledgement

Embarking on this academic journey has been one of the most challenging yet rewarding experiences of my life. It has been a period of intense learning, growth, and personal development, none of which would have been possible without the support and encouragement of several key individuals. I take immense pleasure in expressing my gratitude to them.

Firstly, I extend my deepest appreciation to Prof. Wolfgang Kellerer. Your guidance and expertise have been pivotal in shaping both my research and my character. Your unwavering support and belief in my abilities have been sources of inspiration and motivation. Thank you for being more than a professor—a mentor, whose lessons extend far beyond the classroom.

I am profoundly grateful to Hansini Vijayaraghavan, not just a colleague but a best friend who has been by my side through every high and low of this journey. Your willingness to invest countless hours discussing our research, offering insights, and providing emotional support has been nothing short of extraordinary. Beyond the mental nourishment for my research, you have sustained me with an endless supply of tea, accompanied by pistachios, chocolates and indian snacks, making even the longest days more enjoyable. Your friendship is a treasure, and I am beyond thankful for everything.

To my husband, Yannik Hilla, it is all your fault. If you would not have believed in me, make me sit down with you to write my first application for a PhD position I would probably be still sitting in a cellar conducting boring tests. Your endless patience, encouragement, and love have been my stronghold. Through every mood, every challenge, and every moment of doubt, you were there, pushing me to fight harder and reminding me of my potential. Your unwavering support played a crucial role in my decision to pursue this path and continue on it. I could not have embarked on or completed this journey without you by my side.

I extend my deepest gratitude to Munich Aerospace for awarding me a scholarship and for their unwavering support through the graduate school journey. Their generosity and guidance have been invaluable, significantly contributing to my academic and professional development.

This thesis is not just a reflection of my work but a testament to the strength of the relationships that have supported me through it. Thank you all for being my pillars, my sources of inspiration, and for contributing in countless ways to my growth and success.

Jörg v. Mankowski, Munich, March 31, 2024

Contents

Abbreviations

3GPP	Third Generation Partnership Project	28
A-MEC	Aerial Multi-Access Edge Computing	63
AA-MEC	Aerial-Aided Multi-Access Edge Computing	87
AIC	Akaike information criterion	87
AP	Access Point	39
BF	beamforming	87
BER	Bit Error Rate	7
CDL	Clustered Delay Line	87
DA2G	Direct Air-to-Ground	69
DBSCAN	Density-Based Spatial Clustering of Applications with Noise	23
DL	down-link	42
DRL	Deep Reinforcement Learning	88
ETSI	European Telecommunications Standards Institute	25
GA	genetic algorithm	43
GEO	Geostationary Earth Orbit	14
GLM	Generalized Linear Model	81
IFECS	In-Flight Entertainment and Connectivity Service	63
IoT	Internet of Things	65
IRS	Intelligent Reflecting Surface	66
LEO	Low Earth Orbiting	64
LoS	Line-of-Sight	69
MAE	Mean Absolute Error	30
MAPE	Mean Absolute Percentage Error	28
MCD	Multi-path Component Distance	23
MEC	Multi-Access Edge Computing	88
MEO	Medium Earth Orbit	14
MINLP	Mixed Integer Nonlinear Program	88
MIMO	Multiple Input Multiple Output	67
MLN	Multi-Layer Network	87
MPC	Multi-path Component	28
MToA	Mean Time of Arrival	28
Multi-RAT	Multi-Radio Access Technology	87
MU-MIMO	Multi User MIMO	88
NLoS	Non-Line-of-Sight	22

OFDMA	Orthogonal Frequency-Division Multiple Access	43
PED	personal electronic device	31
PDP	Power Delay Profile	22
PL	Path Loss	87
PPO	Proximal Policy Optimization	52
QoS	Quality of Service	63
RAP	Radio Access Point	87
RCL	Radio Client	41
RF	Radio Frequency	19
RL	Reinforcement Learning	65
RMSE	Root Mean Squared Error	28
RTP	Radio Transmission Point	44
RV	Random Variable	21
SINR	Signal to Interference and Noise Ratio	42
SISO	Single Input Single Output	19
SNR	Signal-to-Noise Ratio	7
SOCKS	Satellites Offloading Computational Tasks	63
SSA	Sparrow Search Algorithm	51
std	standard deviation	50
SV	Saleh-Valenzuela	22
UAV	Unmanned Aerial Vehicle	65
UE	user equipment	14
UL	up-link	42
TDL	Tapped Delay Line	87
VoIP	Voice over Internet Protocol	69
WiFi	Wireless Fidelity	87
WLAN	Wireless Local Area Network	41

Chapter 1

Introduction

The rapid digitalization of society, coupled with an unyielding demand for higher data rates and uninterrupted connectivity, has seamlessly permeated into the domain of transportation including the aviation sector [Hei+22; Aira; Sch+21]. Today's modern aircraft have transformed into dynamic digital ecosystems, equipped with an array of communication technologies designed to cater to the varied needs onboard. This transformation has set new expectations among passengers for a flawless digital experience, mirroring their connected lifestyles on the ground, even as they soar through the skies.

Airlines, in response, are not just focused on elevating the passenger experience; they are also keen on optimizing operational efficiencies and bolstering safety through the deployment of real-time monitoring [Unz+20] and control systems while reducing capital and operational costs [Sch17; CC18; MC+23]. However, the quest for such digital excellence within the aircraft cabin encounters several challenges. Foremost among these is optimizing in-cabin Radio Frequency (RF) communication networks to suit the unique environment of the aircraft, ensuring both the comfort and safety of passengers and crew alike.

As of today, cabin networks experience high re-transmission rates [Gür+16], rely on decades old channel models [Dia+04; HVB05; MC08; FKP08; Mor+09], that fail to reflect the evolved cabin materials and layout, and do not take into account the drastic shift in cabin design, passenger behavior, and the advent of new Wireless Fidelity (WiFi) and mobile standards. Specifically, the Single Input Single Output (SISO) based communication as specified in WiFi 1 and 2 is being replaced by a Multiple Input Multiple Output (MIMO) and beamforming (BF) based communication as outlined in WiFi 5 and 6. Moreover the incorporation of 5G-NR-U, which will replace the 2G cellular service, will operate on the same frequency increasing the chance of interference. We, therefore, need a robust framework for wireless communication networks, consisting of updated channel models and network solutions which allow Multi-Radio Access Technology (Multi-RAT) and Radio Access Point (RAP) while mitigating the interference within the network.

Passengers, now more than ever, expect to seamlessly use their personal devices for entertainment and access to the internet during flights, demanding high-quality service at minimal cost. They anticipate a selection of the latest movies, access to the internet, their favorite music and video streaming services, the ability to stay continuously connected with friends through messaging or voice calls, online gaming and more, all contributing to an unparalleled in-flight experience. This shift underscores the need for systems which support the growing demand for data and connectivity while also offering Quality of Service (QoS) and low latency communication. In other words, the goal is to support the maximum number of user devices with a certain QoS with the minimal number of RAPs needed, resulting in an increase in efficiency and reduction in cost because of reduced cabling, weight, and maintenance.

To offer such a wide array of services, the aircraft cabin must be connected not just to the internet, but also to computational and storage resources where, e.g., streaming providers can cache and process data. In this context, a Multi-Layer Network (MLN) equipped with Multi-Access Edge Computing (MEC) servers presents an ideal solution, seamlessly weaving together terrestrial, aerial, and satellite layers to create a robust communication network. This is achieved due to the multiple

links between the nodes providing a redundancy, ensuring consistent service availability despite potential failures in any network layer. Moreover, this setup guarantees uninterrupted connectivity even at high altitudes or in remote locations, while intelligently managing resources to improve passenger experience and operational efficacy.

Yet, the orchestration of resources within an MLN is not without its challenges. The heterogeneous characteristics and mobility of nodes within the network necessitate a dynamic and sophisticated approach to route and place services, one that can adapt to the evolving landscape of communication technologies and passenger demands.

This thesis thoroughly investigates these points, aiming to unveil novel strategies and models that can elevate the state of aircraft and aircraft cabin communication to new heights, thereby ensuring that the skies serve not only as a mode of travel but also as a venue for exceptional digital connectivity, opening up new avenues for airlines to generate revenue.

1.1 Consolidated Research Questions and Major Contributions

Given the evolving passenger demands, advancing technological requirements, and operational necessities outlined previously, a series of research challenges come to the forefront. To systematically address these complexities, we categorize the challenges into three distinct but interconnected layers: the physical layer, link layer, and application layer. This layered approach not only aligns with the structured nature of communication systems but also enables a focused examination of challenges and solutions at each level of network architecture.

1.1.1 Physical Layer

Exploring the intricacies of the physical layer within aircraft cabins necessitates a critical examination of the existing channel models for aircraft cabins. Previous works, primarily based on measurement campaigns were conducted in mostly empty cabins [Dia+04; Mor+09] or through ray-tracing simulations [HVB05], at times include passengers [FKP08; Top+22]. These studies predominantly offer Path Loss (PL) and Tapped Delay Line (TDL) models, with a noticeable gap in comprehensive Clustered Delay Line (CDL) model comparisons. Specifically CDL-models are required for predicting the effect of channels on the signal transmitted with BF. To our knowledge, no holistic work has been presented that encompasses PL, TDL, and CDL models for the same cabin setting. Furthermore, these models often rely on specific distributions to simulate random channel components or set a specific path loss value at 1 meter [Mor+09], overlooking the intricacies of multipath components and disregarding many random distributions that would fit the underlying data better. Additionally, they often explore only a single frequency, neglecting the examination of multiple frequencies essential for achieving the desired network capacity [Cav+18]. Furthermore, the majority of these studies limit their investigation to a singular configuration of transmitter and receiver placements, primarily positioning the transmitter at the cabin's front and the receiver at head height [Dia+04; Mor+09]. This approach yields channel models that may not accurately reflect the actual use within an aircraft cabin, where RAPs are typically installed beneath the ceiling cladding and the receivers range from seat screens to personal passenger devices. Considering these gaps and limitations, we delineate the following **research questions**:

1. How can a comprehensive 3D model of a Boeing 737-300 cabin enhance the accuracy of wireless channel modeling?
2. What methodologies can be employed to derive PL, TDL, and CDL models that accurately represent in-cabin communication channels?
3. How do PL, TDL, and CDL models derived through ray tracing improve networks in terms of accuracy and applicability to real-world aircraft cabin environments?

4. In what ways do different cabin scenarios (along the aisle, seat screens with and without passengers, and passenger devices with passengers) affect the channel models?

5. How does the inclusion of human presence and consideration of propagation direction (aft, cockpit) in CDL models contribute to a more realistic representation of aircraft cabin communication systems?

This thesis significantly **contributes** to the field of in-cabin wireless communication for aviation on the physical layer by:

Introducing a detailed 3D model of a Boeing 737-300 cabin, which is publicly available [Man+23a], serving as a foundational tool for accurate wireless channel modeling. In addition, we present comprehensive PL, TDL, and CDL models for 2.45 GHz and 5.16 GHz that reflect realistic cabin scenarios, including variations with and without passengers, along the aisle, seat screens, and passenger devices. These models are meticulously designed to mirror the actual conditions and usage within aircraft cabins, thereby enhancing the fidelity of simulations and analyses. Moreover, we implement a statistical modeling process that employs model selection based on the Akaike information criterion (AIC), incorporating a diverse range of random distribution options and predictors. This process significantly refines the model fitting, offering more precise and applicable descriptions of the communication channels within the cabin environment. The models provide predictions based on seat rows and seat number rather than just the distance along the aisle, providing a more intuitive and directly applicable framework for experimental setups and future in-cabin communication system designs. These adjustments to the modeling approach makes the research findings immediately useful to practitioners and researchers focusing on enhancing in-cabin communications through improved wireless communication systems.

1.1.2 Link Layer

In the era of WiFi 6 and 5G, technologies like MIMO and BF have become pivotal in enhancing network efficiency and capacity. However, the aircraft cabin presents a unique challenge due to the presence of multiple RAPs operating on similar frequencies, leading to potential interference. Given the limited spectrum available, which is a critical resource constraint for airlines aiming to minimize operational costs, there's a pressing need to support a high density of devices including seat screens, passenger devices, and sensors. This necessitates an exploration of resource allocation strategies such as beam alignment and power management to mitigate interference and ensure equitable throughput across the network. While technologies like cooperative BF and Multi User MIMO (MU-MIMO) offer potential solutions [YT20], their reliance on precise and timely channel estimates poses significant practical challenges. These include, the development of algorithms capable of quickly processing signal feedback and share it among multiple RAP, resulting in a large system overhead consuming valuable bandwidth and computational resources; which also raises issues of scalability and integration with existing onboard systems. Thus, this study is guided by following **research questions**:

1. How can BF and transmission power be optimized in a multi-RAP aircraft cabin environment to minimize interference and maximize throughput fairly?

2. How would a new antenna design with four sub-antennas, optimize beamwidth to balance user coverage and interference reduction?

3. How does optimizing beam patterns in combination with power affect: network sum rate, fairness, and energy efficiency?

4. How can we promote coexistence in a Multi-RAT network deploying BF?

5. How do different heuristics compare in optimizing the network, and what advantages does a Deep Reinforcement Learning (DRL) based solution offer for practical implementation?

This thesis significantly **contributes** to the field of in-cabin wireless communication systems on the link layer by: proposing an innovative antenna design optimized for in-cabin use, featuring four sub-antennas to achieve an ideal beam-width. This design effectively supports multiple users while minimizing interference, showcasing a targeted advancement for dense in-cabin communication scenarios with multi-RAP deployment. We introduce a central controller designed to dynamically allocate wireless communication resources such as transmission power, link direction, and beam angle for each RAP within the aircraft cabin. This central controller is pivotal in minimizing interference and ensuring fair throughput distribution across the network, marking a crucial step towards efficient Multi-RAT in-cabin wireless network management. For this, we develop a comprehensive mathematical model of the in-cabin wireless communication system. Through strategic simplifications, the application of different heuristics and a DRL solution to optimally allocate the different resources we are able to minimize the number of unserved Radio Client (RCL) and increase the throughput compared to existing schedulers such as Roundrobin. Lastly, our findings suggest that merely increasing the number of RAPs does not straightforwardly translate to enhanced network performance, thereby challenging conventional approaches to network expansion within the cabin.

1.1.3 Application Layer

The evolution of in-flight services is pushing the boundaries of what's possible within the confines of an aircraft cabin. Passengers now expect access to a range of services during their flight, including streaming, email, and more, mirroring their on-ground digital experience. To meet these demands without the logistical and resource-intensive burden of carrying all necessary data onboard, the deployment of MEC servers within MLNs presents a strategic solution. These servers not only facilitate the handling of requests that exceed the aircraft's internal capacities, such as web browsing and VoIP but also open avenues for airlines to generate new revenue streams by offering computational resources to satellite providers.

This integration into a MLN, comprising satellite, aerial, and terrestrial layers, represents a shift towards more dynamic and resource-efficient network management. Unlike previous research that primarily focuses on offloading to Unmanned Aerial Vehicles (UAVs) [Che+17; Pac+21; Wei+23], which operate on a small area, our approach focuses on globally operating airlines, supporting service requests and endpoints in the aerial layer itself, thereby enhancing the network's functionality and reach. **Research questions** that guide this study include:

1. Can integrating MEC servers into the MLNs improve in-cabin and satellite communication systems in terms of coverage, latency, and capacity?

2. Do we benefit from dynamically optimizing the placement of MEC servers in an aerially aided network for computational offloading from satellites, compared to a static network configurations?

3. How does the deployment of aerial MEC servers alongside terrestrial gateway MEC affect flow latency, network bandwidth occupation, and the overall reliability of cabin communication systems?

This thesis significantly **contributes** to the field of aircraft wireless communication systems on the application layer by: showcasing how a MLNs benefits from the introduction of aerial MEC servers alongside traditional terrestrial gateways. We acknowledge the mobility of network nodes and propose dynamic optimization strategies for routing data streams and selecting optimal service endpoints based on latency and energy considerations. For this we provide two distinct optimization formulations: one to reduce latency and one to reduce energy consumption. This approach not only highlights potential energy savings but also ensures compliance with service latency constraints. We not only support the seamless delivery of in-cabin services, such as internet access, but also open avenues for new revenue streams by offering computational resources to satellite providers. We

demonstrate that the optimization formulation is feasible to be conducted at a central controller, managed by the airlines. By showcasing substantial improvements in flow latency and energy efficiency, this work lays a foundation for future innovations in aircraft communication systems, paving the way for the next generation of aviation technology advancements.

1.2 Outline

This thesis lays the foundation for the next generation of aircraft cabin communication through the lens of cutting-edge technologies and network optimization. An overview of the structure of the thesis is given in Figure 1.1. The ensuing chapters are structured as follows.

Chapter 2, sets the stage by laying out the key concepts to understanding the subsequent analyses. It introduces ray tracing as a pivotal computational method for modeling electromagnetic wave propagation in the complex environment of an aircraft cabin. The discussion then transitions to the intricacies of MU-MIMO and BF, highlighting their significance in increasing link capacity and mitigating interference. Furthermore, this chapter explores the architecture and utility of MLN, emphasizing their role in bridging terrestrial, aerial, and satellite communication layers, focusing on one satellite constellation and presents the mathematical formulation to model the access between all nodes in the MLN.

In Chapter 3: Characterization of the 2.45 GHz and 5.16 GHz Channels in Aircraft Cabins, we derive and analyze channel models, obtained through ray tracing, specific to the aircraft cabin environment. Employing PL, TDL, and CDL models, the chapter meticulously examines signal propagation under various cabin conditions and changing transmitters and receiver positions. This analysis not only sheds light on the communication challenges within the cabin but also sets a precedent for optimizing in-cabin communication strategies.

Chapter 4: Resource Allocation in Beamformed Multi-Technology Networks, presents a novel approach to optimizing the beam angles of multiple RAPs, jointly with the transmission power and client scheduling. By integrating multiple technologies within a multi-RAP network, this chapter addresses the challenge of increasing throughput for each RAP and reducing interference between the RAP's networks. Through detailed deployment studies, the effectiveness of beam angle optimization in enhancing the quality of in-cabin communication is demonstrated.

Chapter 5: Service Placement and Routing in Aerial-Aided Multi-Access Edge Computing Networks, explores the dynamicity in MLNs, focusing on the optimization of traffic routing and service placement amidst the constant movement of network nodes. The chapter contrasts two optimization objectives - minimizing latency and energy consumption - thereby unraveling the complexities and trade-offs inherent in routing service requests to predefined MEC servers within an MLN.

We present our Summary and Conclusion in Chapter 6. It recapitulates the significant advancements made in optimizing aircraft cabin communication and outlines the challenges that were encountered and overcome. The chapter finishes by presenting opens avenues for future research, pointing towards emerging technologies and methodologies that promise to further refine and enhance aircraft connectivity.

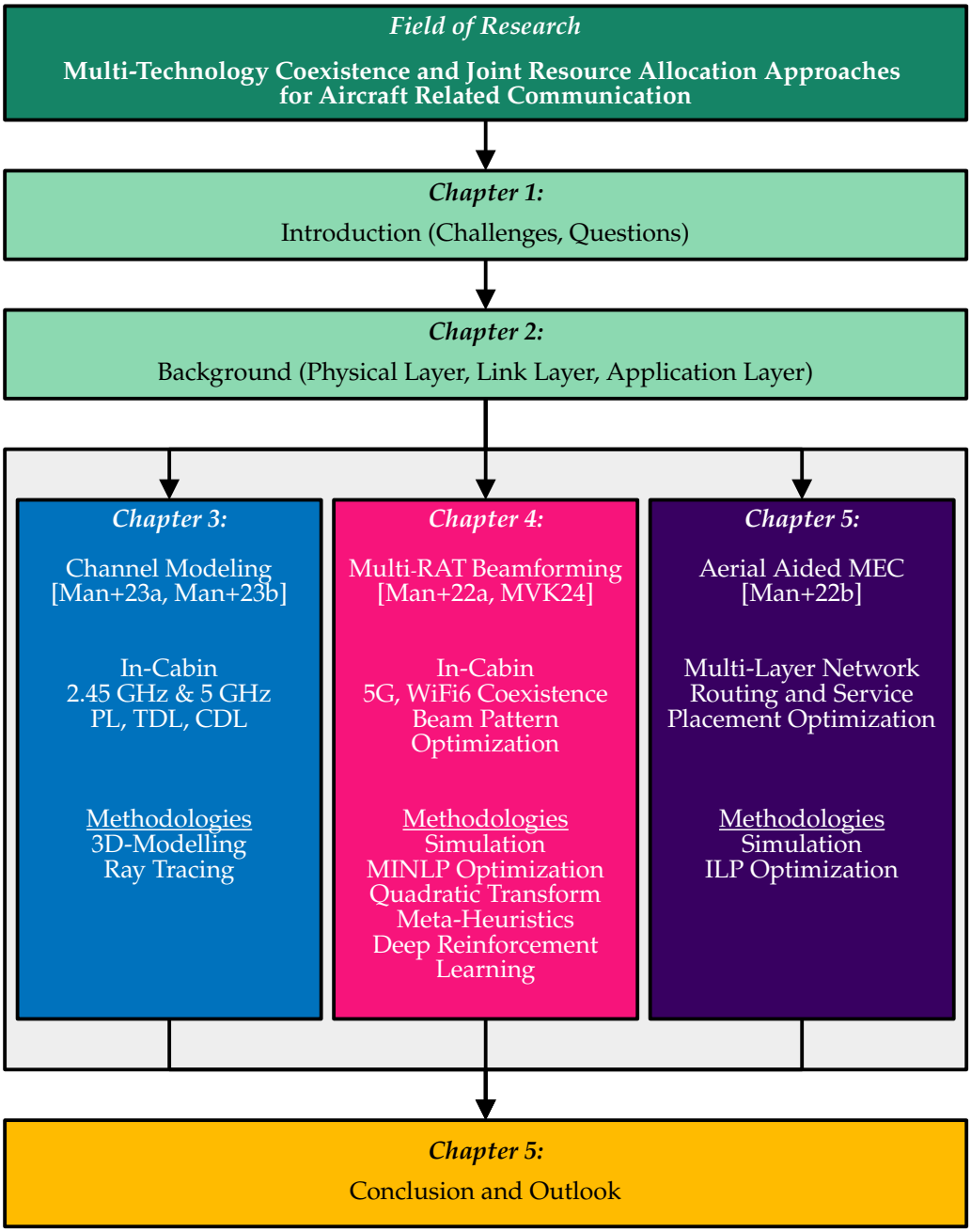

Figure 1.1 Thesis outline, including research fields, methodologies, and main references of each chapter.

Chapter 2

Background and Related Work

In this chapter, we establish the underlying concepts for understanding the subsequent chapters. We delve into physical methods to derive various channel models, we compare the concepts of beamforming (BF) and Multi User MIMO (MU-MIMO) within an aircraft cabin to enhance passenger experience, highlighting the advantages of BF, and outline the fundamental assumptions necessary for a successful deployment of different aircraft related applications within a Multi-Layer Network (MLN).

2.1 Physical Layer: Channel Models

Exploring the physical layer of in-cabin wireless communications, involves navigating the constraints of the available frequency spectrum. It is crucial to select frequencies that are globally accessible, avoiding those limited by local regulations, as aircraft and airlines operate internationally. The regulatory body is governed by strict safety and certification standards, especially since multiple frequencies are essential for aviation communications and the aircraft itself [ICA22]. For instance, the 5 GHz band is partly occupied by aircraft weather radar, and the TCAS, the Traffic Collision Avoidance System, operates at 1 GHz - all systems that cannot be compromised. Additionally, airlines have an economic incentive to use free/open frequencies to avoid the operational costs and licensing fees required across different countries.

Lastly, cabin comfort is a major priority in the aviation industry [Airb], significantly shaped by services designed to cater to passenger requirements. Among these, the entertainment system stands out as a major contributor to wireless traffic within the cabin. For this case the spectrum is further narrowed down, by the operating frequencies of the technologies used by the passengers and technologies used to deliver large data to screens as Wireless Fidelity (WiFi). Consequently, this leads to the identification of the 2.45 GHz and 5 GHz bands as the most viable frequencies for in-depth investigation. They strike a balance between global availability, regulatory compliance, and the need to support high-density wireless applications within the aircraft cabin, setting the stage for our exploration of channel models.

2.1.1 Channel Models

Channel models, with their ability to predict the performance of communication links, play a major role in network design. Ranging from single-user communication to complex networks, these mathematical representations of the physical layer facilitate critical estimates for various communication channel metrics. These include, e.g., interference, Signal-to-Noise Ratio (SNR), Bit Error Rate (BER), channel capacity, etc. Established models like Path Loss (PL), Tapped Delay Line (TDL), or Clustered Delay Line (CDL) are employed, each tailored to their specific environment [ETS20]. The focus of this thesis, however, is to adapt these models for the unique environment of aircraft cabins.

Channel models derived from measurement campaigns are often the gold standard; yet, depending on the situation, other options such as ray tracing or finite element method (FEM) provide viable

solutions. We, therefore, first present the concepts behind ray tracing, followed by a discussion on which option we employ in this work.

2.1.2 Ray tracing

Ray tracing within the Radio Frequency (RF) domain is a sophisticated computational approach that accurately models the propagation behavior of electromagnetic waves [Bal12]. More specifically, it abstracts electromagnetic waves as vectors in a three-dimensional space, tracing the path of each vector and evaluating how the characteristics of each wave changes when it interacts with the surface of an object. Through the incorporation of physics-based principles, as geometric optics and extending them by wave theory, it is able to consider events like reflection, refraction, diffraction, and scattering of the wave. This enables us then to accurately model signal behavior, including path loss, coverage, and multipath effects, which are essential for the description of various channel models.

To simulate ray tracing effectively, following points need to be considered. The first point involves obtaining a detailed model of the environment that is investigated. This includes physical structures (windows, doors, walls, objects, etc.) along with their electromagnetic characteristics such as permittivity and conductivity. The careful selection of the structures' parameters is essential to make sure that the propagation model is accurate. A transmitter model sends out electromagnetic waves, each wave consists of a set of rays spreading out in all directions. These rays serve as a geometrical representation and estimate of the continuous wavefront. Each individual ray is then traced along its path within the environment. Each time a ray comes across an object or moves through a material, it is transformed by either a *reflection*, *refraction*, *diffraction* or *scatter* as visualized in Figure 2.1. In *reflection*, a part of the energy from the ray hitting a surface is bounced back according to the Law of Reflection, which says that the angle at which the ray hits the surface is equal to the angle at which it reflects. How much is reflected depends on the properties of the material and the angle at which the ray strikes the surface. When a ray crosses the border between materials with different refractive indices, its path and speed change because it is moving through a different medium. The amount of *refraction* is controlled by Snell's Law, depending on the refractive indices of the materials and the entry angle of the ray. When the waves hit edges or openings, they experience *diffraction*, which means they bend and spread out around the obstacle. The Huygens-Fresnel principle is commonly used to explain this behavior. The rays can also *scatter* in case they hit surfaces that have irregularities or sizes similar to the wavelength of the ray. Scattering is usually explained using statistical or physical theories, like the Rayleigh, Mie, or geometric scattering models. To simulate ray propagation, a range of algorithmic approaches is available, each offering different strengths and optimization capabilities. At the receiver, the combined effect of all arriving rays is aggregated. In general, all rays, each with different amplitudes, phases, and times of arrival, create the total received signal. However, depending on the property, the equations on how to sum the various ray properties differ. From this data we are able to construct coverage maps, channel impulse responses, and other important measurements.

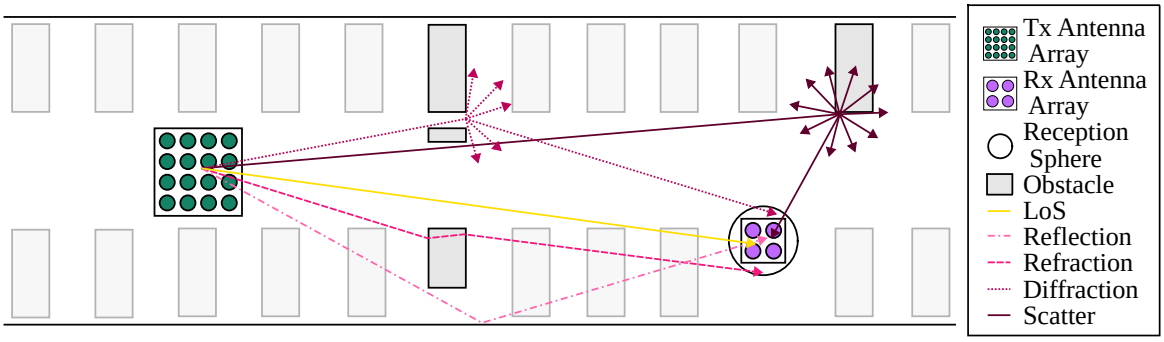

Figure 2.1 Different types of ray interactions during Ray Tracing, where obstacles in a different height plane that do not participate in the ray path are greyed out

2.1.2.1 Ray Tracing Concepts

To allow a better understanding of ray tracing, following theoretical based concepts are introduced:

Physical Optics, is a technique used for approximating the propagation of high frequency waves to estimate the fields scattered due to incoming electromagnetic waves. It is typically used for surfaces that are large and smooth. In specific cases it is combined with the Shooting and Bouncing Rays algorithm to take the scattering of signals into account.

Geometrical Theory of Diffraction, expands upon the ray-optics technique by including diffraction effects and therefore considering edges as secondary wave sources. For this, it applies geometric approximations and diffraction coefficients derived from the Maxwell's equations. It is particularly suited for high-frequency signal propagation and complex environments with multiple obstacles.

Uniform Theory of Diffraction, is built on the Geometrical Theory of Diffraction. It introduces enhanced diffraction coefficients that remain finite in transition regions, resulting in a more uniform and precise handling of diffraction effects. This results in more accurate representation of environments including a high number of edges and transitions.

Different underlying concepts on how to trace rays exist: **Ray Tube Tracing**, is an algorithm that groups rays into tubes, where each ray within a tube shares similar characteristics, including phase and direction of propagation. This reduces the computational complexity as fewer rays are needed to represent the wavefront. As the tube interacts with surfaces, its cross-section may change shape and size to accommodate the new direction of the reflected or refracted rays. However, the deformed tube remains a contiguous entity. This method is effective for simulating the spread of waves that have relatively large wavelengths.

Shooting and Bouncing Rays, is a ray tracing method which provides detailed information about the trajectory and interactions. In contrast to the previous algorithm, each ray is considered as a single line or path. To model the supported interactions - reflection, refraction, transmission, and diffraction - it relies on the previously described concepts with the corresponding property coefficients. The high details limited by the amount of simulated rays makes it very suitable for RF signal propagation analysis. In this work the X3D algorithm from Wireless InSite is used, which is based on the Shooting and Bouncing Rays algorithm [Rem20].

2.1.2.2 Antenna models

Each type of antenna brings a unique characteristic that significantly influences the simulation outcome [Tar+21]. Among the variety of antennas - such as horn, dipole (full and half), isotropic, parabolic reflectors, etc. - each possesses distinct gain properties, waveform behaviors, transmission line losses, receiver thresholds, and often specific polarizations. These characteristics are fundamental in determining how the rays' properties are modified, particularly concerning the angles of departure and arrival.

The influence of antenna choice on channel models can be illustrated through a thought experiment comparing an isotropic antenna with a parabolic reflector. The isotropic antenna, theoretically radiating equally in all directions, contrasts sharply with the parabolic reflector, which focuses energy in specific directions while being shielded from signals of its rear. This leads to a significant alteration in channel characteristics - such as the measured path loss, the number of multipath components, and the presence or absence of signal clusters — by preventing the interaction of waves that do not align with its focal direction.

Moreover, the operational context of these antennas, whether they function independently or as elements within an antenna array, further impacts simulation results. When utilized within an array, the properties of the rays are initially computed based on the array's centroid. Subsequently, these calculations are adjusted to account for the specific deviations from the center, thereby refining the simulation's accuracy by considering the spatial configuration of the antenna elements.

2.1.3 Ray Tracing vs Measurements

Although real environment-based experiments are preferred to derive channel models, under specific circumstances, simulation-based models can offer a viable alternative.

In the particular case of aircraft cabins, a unique set of technical, logistical, regulatory, and other restrictions arise [Dia+02]. To start with, the aircraft cabin is filled with numerous obstacles and reflective surfaces, which can significantly impact the channel and result in a intricate environment. Therefore, highly precise measurement equipment is needed, capable of handling large volumes of measurement data efficiently. Logistical challenges further complicate the process, given the significant amount of equipment that must be transported, installed, and powered. Parallel operation of receivers is a must, as time is strongly limited due to access. On the organizational front, finding an airline which would grant access to an aircraft poses substantial hurdles. The aircrafts are in constant operation, leaving little to no downtime for exclusive access. A measurement of this magnitude would require a week-long timeframe for exclusive use. Additionally, we would need to identify and coordinate a group of individuals to act as passengers for the aircraft. Regulatory concerns also play a significant role. Gaining access to aircraft is also a security issue. Researchers must navigate restricted airport areas and measurements must not interfere with the airport's and aircraft's normal functioning or the passenger's safety. This is especially the case for the 5 GHz band which is also used for radar systems in aviation. Consequently, these types of measurements cannot be performed while the aircraft is operational. All in all, the measurement equipment, the logistics and the organizational challenges would result in a very expensive and time-consuming undertaking. Therefore, for the particular nature of aircraft cabins the use of ray-tracing simulations is an appropriate method to gather data to characterize the channel.

Additionally, a ray-tracing simulation can reveal more details about the channel, e.g., on which objects the wave is reflected before arriving at the receiver, or the amount of signal loss due to destructive interference. This information could be used to better position the antennas of the different devices, or to use materials with different electrical properties.

2.2 Link Layer

Exploring the link layer shifts the focus from modelling the cabin channel to leveraging the diverse spatial properties to enable reliable, high-throughput communication.

A single-aisle A319 aircraft accommodates approximately 130 passengers, whereas the double-deck, double-aisle A380 can transport about 550 passengers. Within these compact environments, technologies such as WiFi and 5G compete for the scarce unlicensed spectrum. To cater to all the requested services, from streaming to crew communications, we require a reliable high throughput network solution.

In addressing this challenge, BF and Multiple Input Multiple Output (MIMO) emerged, leveraging the spatial domain. While MIMO increases the throughput by using the spatial diversity of the communication channel, BF reduces the interference by optimizing the power allocation in space, resulting in a reliable high throughput.

2.2.1 Multi User MIMO (MU-MIMO)

Multi User MIMO (MU-MIMO) extends the principle MIMO to multiple users [Ges+07]. Unlike traditional single-antenna systems, MIMO employs spatial multiplexing, where multiple data streams are transmitted simultaneously over the same channel but through different antennas. By exploiting the spatial diversity of the multiple antenna configurations, these streams are effectively separated and reconstructed, despite potential interference. In MU-MIMO, signals are carefully adjusted using channel properties to ensure that only the intended signal reaches each receiver, while the undesired signals are effectively cancelled out. This method significantly increases the communication capacity,

allowing for higher throughput without the need for additional bandwidth or increased transmit power.

In our MU-MIMO network, we increase the number of supported devices, by allocating one Radio Access Point (RAP) antenna to one Radio Client (RCL) as visualized in 2.2. However, while the signals within one RAP-network are cancelled out, they still cause interference on links spanned by other RAPs.

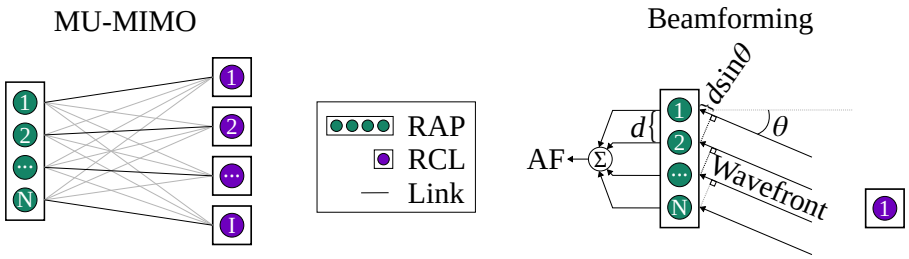

Figure 2.2 Signal link comparison for MU-MIMO and BF

2.2.2 Beamforming (BF)

In traditional communication systems, omni-directional antennas are commonly used, transmitting or receiving signals uniformly in all directions. However, these systems can be less effective in situations where the desired signal is weak or when there are multiple interfering signals. The core concept of BF lies in manipulating signal components through constructive and destructive interference, by fine-tuning the phase and amplitude of signals at individual antenna elements. The resulting radiation pattern directs the energy in the desired direction. BF is implemented through digital, analog, and hybrid techniques. Digital BF involves creating signals for each antenna element digitally to shape the array's beam, while analog BF modifies a single digital signal with analog circuits for each antenna element. Hybrid BF, as discussed in [Ahm+18], combines these methods to optimize installation space and power consumption. In our case, this decision is abstracted by the mathematical description which applies to all three techniques.

Given far field communication with an equally spaced linear antenna array, as displayed in Figure 2.2, consisting of N isotropic sub antennas, we can denote the antenna array factor AF, as the sum of the received signals at each sub-antenna:

$$\mathrm{AF} = \sum_{n=1}^{N} e^{j(n-1)\frac{2\pi}{\lambda} d \sin\theta} \tag{2.1}$$

with assuming a sub-antenna spacing of $d = \lambda/2$. Multiplying (2.1) by $e^{j\pi \sin\theta}$ gives:

$$\mathrm{AF} \cdot e^{j\pi \sin\theta} = e^{j\pi \sin\theta} + e^{j2\pi \sin\theta} + \cdots + e^{jN\pi \sin\theta} \tag{2.2}$$

Subtracting (2.2) from (2.1) and using the Taylor series definition results in:

$$\mathrm{AF} = e^{j\frac{1}{2}(N-1)\pi \sin\theta} \frac{\sin\left(\frac{1}{2}N\pi \sin\theta\right)}{\sin\left(\frac{1}{2}\pi \sin\theta\right)} \tag{2.3}$$

Since we use 4 sub-antennas and we are only interested in the magnitude of the gain we write:

$$\mathrm{AF} = \left| \frac{\sin\left(2\pi \sin\theta\right)}{\sin\left(\frac{1}{2}\pi \sin\theta\right)} \right| \tag{2.4}$$

When this antenna is deployed with BF, we are able to steer the beam according to the beam angle θ_a, we, therefore, need to replace the $\sin\theta$ with $\sin\theta - \sin\theta_a$. To derive the expected gain, we further correct the gain by a cosine rolloff introduced due to the angle of incidence on the antenna array:

$$g(\theta_a, \theta) = \left| \frac{\sin\left(2\pi(\sin\theta - \sin\theta_a)\right)}{\sin\left(\frac{1}{2}\pi(\sin\theta - \sin\theta_a)\right)} \cos\theta \right| \tag{2.5}$$

2.2.3 MU-MIMO and BF in an A340-300 cabin

In the aircraft cabin setting, maintaining connectivity for all RCLs is imperative to guarantee the Quality of Service (QoS) for various passenger-provided services. This connectivity directly impacts the reliability and performance of in-flight entertainment, real-time communication, and personalized service offerings, thereby enhancing the overall passenger experience.

Given the option of deploying MU-MIMO and BF based technologies, we compare their performance in the setting of an A340-300 - a double aisle aircraft - and a General scenario, to investigate if results are generalizable. More specifically, we compare the percentage of unserved RCL in case we serve the RCLs randomly (Random Scheduler) or ordered by seat and row (Roundrobin Scheduler). Further, as the number of RAPs in a scenario may influence the outcomes, we deploy between 2 to 8 in Aircraft and 4 for General.

Based on the link descriptions for MIMO in Section 2.2.1, the BF gain in Section 2.2.2 and the system model in Section 4.3, we calculated the expected Signal to Interference and Noise Ratio (SINR) and counted the number of RCLs that, according to Table 4.1, exhibited a spectral efficiency of 0. For BF, the beam angles were determined based on the positions of a singular RCL chosen by the scheduler. The results for 1000 iterations are depicted in Figure 2.3, where N in Aircraft-N denotes the number of RAP deployed.

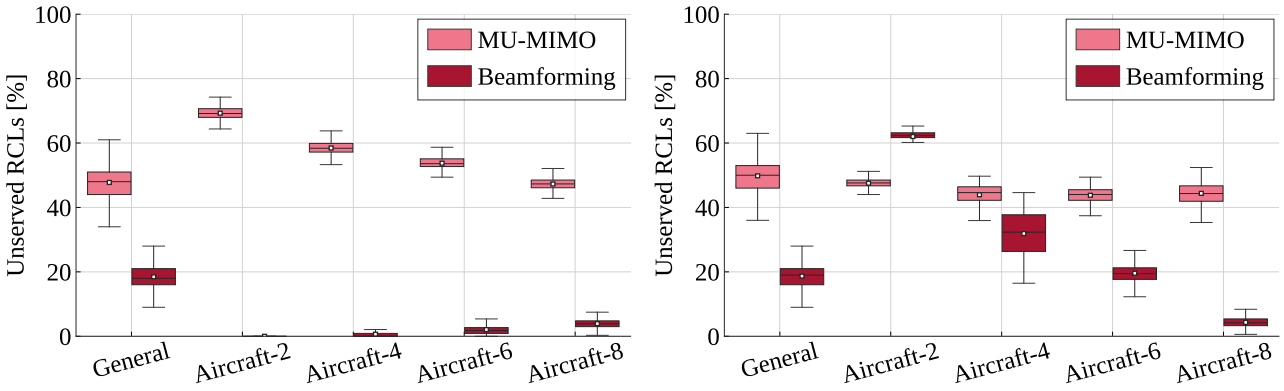

(a) Random **(b)** Roundrobin

Figure 2.3 Percentage of unserved RCLs for different schedulers

As illustrated in Figure 2.3, our examination reveals that MU-MIMO serves an inferior number of RCLs compared to BF for most scenarios. Only in the specific case of employing Roundrobin in Aircraft-2, an aircraft with two RAPs, MU-MIMO is able to serve more RCLs. However this is due to the two beams serving only RCLs that are located in the same region of the aircraft cabin during the simulation duration. A case that does not occur for the Random scheduler. In Random MU-MIMO exhibits a decrease with increasing RAP count, as more links become available with every additional RAP. This is also the case for BF, however the percentage of unserved RCLs increases as these beams start to overlap and increase interference in the network. In Roundrobin, MU-MIMO, exhibits a constant percentage of unserved RCLs, which seems to be the limit for this technology. However, for BF the number of unserved RCLs decreases with increasing RAP count. This is due to the increasing number of links balancing out the interference caused by the beams pointing in the same direction.

All in all, we observe that BF outperforms MU-MIMO, while the different effects make it apparent that we need to optimize the scheduler deciding when which link becomes active. Moreover, BF orchestrates the transmission energy predominantly towards the intended user while averting potential interference sources. Due to its inherent beam gain, BF doesn't necessitate rapid adaptation to fluctuating channel conditions, thereby reducing reliance on channel state information compared to MU-MIMO. In addition, BF's ability to serve multiple users via one beam renders it particularly apt for the high density user distributions found in aircraft cabins. Consequently, we have chosen to focus our investigation on the application of BF technology within the aircraft cabin.

2.3 Application Layer

Exploring the application layer in aerospace networks shifts the focus from the confines of the cabin to the broader context of external communication, positioning the aircraft itself as an integral node within a larger network. This ensures certain in-cabin communication services (e.g., VoIP), but also gives the opportunity to enhance the passenger experience by opening new possibilities for In-Flight Entertainment and Connectivity Service (IFECS). Furthermore, redefining aircraft as network nodes themselves enables their transformation from mere sources of service requests into active service providers within the network.

This necessitates a comprehensive understanding of the entire network architecture and the services provided within it. Accordingly, we begin by delineating use cases relevant to such a network. Subsequently, we present a detailed overview of how aircraft integrate into the MLN framework, which also includes satellites and gateways. Lastly, we elaborate on the essential physical principles that guarantee connectivity between nodes, despite their high mobility and fluctuating altitudes. This involves considering factors such as the nodes' physical positions, channel characteristics, link capacities, and transmission power.

2.3.1 Service Use Case in Aerospace Networks

In networks involving aircraft and satellites, our focus is primarily on specific services within the IFECS use case and the provision of processing resources for computational tasks that arise in the network.

2.3.1.1 In-Flight Entertainment and Connectivity Service (IFECS)

As of today, most airlines offer IFECS during flights to varying degrees, with services ranging from access to newspapers to the latest movie selections. However, most of the entertainment content relies on limited storage on servers within the aircraft, resulting in a limited selection which is further constrained to content pre-agreed upon in contracts between the airline and industry-specific content providers. Expanding these services to offer a broader selection or to enable passengers to use their own streaming services would greatly enhance the in-flight experience [Fut]. This approach not only caters to diverse passenger preferences but also aligns with the growing trend of personalization in entertainment consumption. Allowing passengers to access their preferred streaming platforms ensures that they can enjoy a more familiar and tailored entertainment experience, potentially leading to higher customer satisfaction.

Moreover, introducing a new form of entertainment in the aircraft, such as gaming, could significantly enrich the in-flight experience. Gaming, especially online and multiplayer formats, is increasingly popular and could be a significant draw for passengers. However, gaming, especially online games, require low-latency network connections [WRA19].

Offering robust web services during flights enhances the passenger experience by enabling them to browse the internet, check emails, and stay connected on social media. This connectivity is especially beneficial for business travelers who can continue working, attend virtual meetings, and access cloud

services, thereby maximizing their productive hours while in transit. Additionally, passengers can access real-time flight information, weather updates, and destination guides, or even make post-flight arrangements such as booking taxis and hotels.

Voice over Internet Protocol (VoIP) services onboard facilitate voice communication over the internet, allowing passengers to stay in touch with family, friends, or business associates during their flight. This service is not only more cost-effective [CMP19] compared to traditional satellite phone calls but also ensures high-quality, uninterrupted voice calls, thanks to advances in technology.

2.3.1.2 Provision of processing resources

In an increasingly connected world, where unmanned aerial vehicles link to satellites [Wei+23] and IoT devices with limited computational capacity offload computational tasks [Cui+20], the constraint of computational capability becomes apparent. Multi-Access Edge Computing (MEC) servers within the network address this challenge by offering processing resources in the network. Specially MEC servers located at satellite gateways, equipped with advanced processing capabilities, are more adept and efficient at handling complex computational tasks than the relatively limited onboard systems of satellites. However, tethering MEC servers to gateways limits their mobility, thereby constraining their potential locations and applications. This limitation is particularly pronounced in scenarios like sparsely populated or remote areas, and in specialized applications such as military operations, emergency relief, and disaster response. In our work, we extend the deployment of MEC servers beyond traditional satellite gateways to aircraft. We further abstract the origin of the computational tasks by assuming that these tasks originate directly from the satellite. The strategic placement of MEC servers throughout the network brings processing power closer to the source but also significantly minimizes latency, thereby optimizing network performance and enabling more efficient communication between satellites relayed computational tasks.

2.3.2 Multi-Layer Network (MLN)

In a network composed of satellites, gateways, and aircraft, each node type exhibits distinct characteristics, enabling them to fulfill specific roles within the communication ecosystem. The unique attributes and operational domains of these nodes collectively form the layers of an MLN, where each layer's unique properties contribute to a robust, interconnected system and each layer may compensate weaknesses of the other [Wan+21]. In our case, we structure the network into three distinct layers.

Within the terrestrial layer, one typically encounters nodes like base stations, satellite gateways, Direct Air-to-Ground (DA2G) gateways, and user equipment (UE) [Var+19]. In our specific framework, this layer consists of satellite gateways enhanced with DA2G capabilities, along with integrated MEC servers. These nodes serve as service endpoints for both of our use cases.

The aerial layer is capable of hosting various entities such as aircraft, low and high-altitude platforms (LAP, HAP), and Unmanned Aerial Vehicles (UAVs) [Qin+21]. Nodes in this layer are characterized by significant mobility variation, often serving as bridges or relays, and frequently originating service requests. For our specific model, the aerial layer is comprised solely of Lufthansa passenger aircraft, some of which are designated to accommodate MEC servers, referred to in this context as Aerial Multi-Access Edge Computing (A-MEC) servers.

The satellite layer encompasses a range of satellites including Low Earth Orbiting (LEO), Medium Earth Orbit (MEO), and Geostationary Earth Orbit (GEO). These satellites offer extensive coverage from space, often operating as relay stations to bridge communication gaps from lower layers. Communication between satellites typically covers long distances, which can lead to higher latency, yet the links used for this communication are known for their high bandwidth capacity, facilitating substantial data transmission rates. In our specific setup, the satellite layer consists of Iridium Next satellites [Iri]. These nodes primarily function as communication relays and, depending on the use case, may also act as sources of service requests.

The overlapping coverage of nodes in each layer typically allows increasing the total available data rate, the user experienced data rate, and the device density. Further, it introduces a redundancy resulting in a fail-safe and more reliable network. This is especially important during natural disasters, war, and other events which are able to interrupt information routes. While global air traffic spans a vast network, a volcanic eruption can disrupt large areas, excluding them from air travel. In such cases, communication can be rerouted from aircraft-to-aircraft to go via satellites. Moreover, MLNs allow the usage of different layers for different applications [GZ21]. The satellite layer, for instance, minimizes handovers for nodes traversing globally, offering consistent connectivity. On the other hand, the aerial layer excels in providing low-latency communication, ideal for time-sensitive operations within localized regions. However, the high mobility of nodes in both the aerial and satellite layers leads to a dynamic network topology, increasing the network's overall flexibility but also increasing the complexity for routing traffic. A comparison between the layer properties is provided in Table 2.1, with nodes used in this work denoted in *italic*.

Table 2.1 Overview of advantages and disadvantages for different layers in an MLN [Man+22a]

Layer	Nodes	Advantages	Disadvantages
Satellite	GEO satellite, MEO satellite, *LEO satellite*	Large coverage, Resilient infrastructure independent	LoS channel only, Large propagation delay, Large cost
Aerial	HAP, LAP, UAV, *Aircraft*	Wide coverage, Flexible deployment, Medium cost	Intermittent links, High mobility, Reduced capacity
Terrestrial	Basestation, UE, *(DA2G)-Gateway*	High throughput, Low cost	Limited coverage, Vulnerable infrastructure

2.3.3 Satellite Constellation Networks

Building on the MLN, it is worth noting that the satellite layer in such networks often extends beyond individual satellites, encompassing entire satellite constellations for more comprehensive coverage and functionality. A satellite constellation is a group of satellites orbiting a planet, working together towards a shared objective, e.g., providing mobile communication services. Examples of operational constellations are Iridium, Intelsat, Kuiper, OneWeb, and StarLink. These constellations are characterized by satellites that may have varying trajectories and altitudes, and they exhibit considerable mobility.

The mobility, alongside the specific design of each satellite constellation, significantly impacts the QoS. This impact is measurable in terms of communication latency, handover frequency, and throughput. Additionally, other critical factors influenced by the constellation's design include manufacturing costs, orbital periods, the total number of satellites within the constellation, and the complexity involved in routing.

Our focus is on LEO satellites, operating within an altitude range of 160 to 2,000 km. These satellites are preferred due to their lower communication latency and higher relative ground speed, which contribute to greater network flexibility. This preference aligns with the ongoing trend of deploying LEO satellite constellations [Sae+21], a development driven by recent technological advancements and the growing need for latency-sensitive applications. Furthermore, the abundance of satellites in these constellations facilitates multiple traffic flows, enhancing routing flexibility and making them particularly suitable for backbone network use. However, the inherent flexibility of these constellations also introduces frequent changes in network topology, leading to increased routing

complexity. The specific network that forms the basis of our results is the Iridium-Next satellite constellation network [Iri], which comprises 80 satellites orbiting at an altitude of 781 km.

Nonetheless, satellites within the satellite layer necessitate a connection to ground-based gateways for control traffic, typically maintaining a link with one gateway at a time, as noted by [Che+21a]. Therefore, enabling seamless access to these terrestrial endpoints is fundamental for non-terrestrial networks. Once established, these gateways can serve as MEC nodes, providing the computational services outlined in our use cases.

Another aspect to consider is that satellites within the satellite layer need to maintain a connection to at least one gateway to manage control traffic; typically, each satellite is connected to single gateway at any given time [Che+21a]. Thus, it is crucial to enable non-terrestrial networks, to access these endpoints. To further utilize these nodes, we position an MEC server at each gateway to serve services as described in our use cases.

For the Iridium-Next Satellite network, the distribution of gateways is not uniform globally. Instead, they are predominantly located in regions with high usage, such as North America and Europe. Table 2.2 provides a detailed overview of the gateway locations for the Iridium-Next network.

Table 2.2 Gateways of the Iridium-Next network [Inc16]

Gateway Location	Country	Latitude [deg]	Longitude [deg]
Fairbanks	USA	64.82	-147.72
Tempe	USA	33.28	-111.90
Svalbard	Norway	78.23	15.390
Punta Arenas	Chile	-52.94	-70.87

2.3.4 Access in MLN

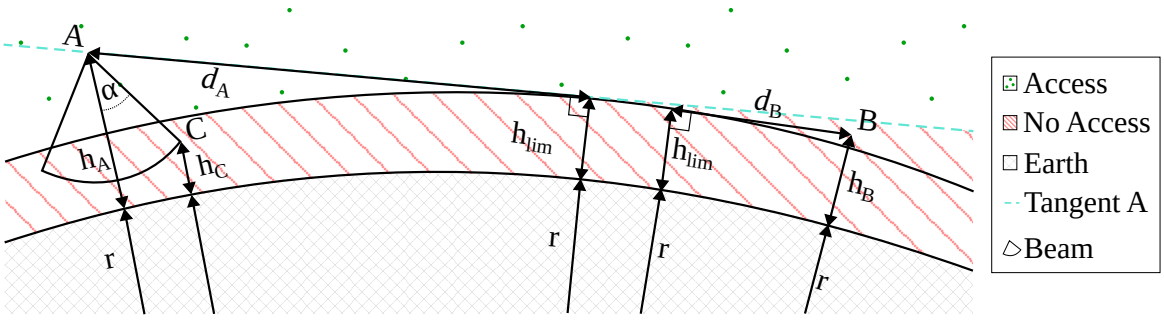

Figure 2.4 Geometrical relationships for two nodes to determine access.

Due to Earth's curvature and the varying PL properties of different atmospheric layers, it is necessary to determine the feasibility of a link between two nodes in an MLN. To assess whether two nodes A and B, that fly at an altitude h_A and h_B, can communicate, we first calculate the maximum transmission distance for each node denoted as d_A and d_B before a signal reaches the 'No Access' zone. This zone is defined by the Earth's radius r and additional factors accounted in h_{lim}, such as assumed building height obstructing transmission or atmospheric conditions leading to increased PL. Specifically, for a required Line-of-Sight (LoS) connection, the maximum transmission distance of node A can be determined by using the right-angled triangle where d_A is the adjacent side, $r + h_{\text{lim}}$ is the opposite side, and $r + h_A$ is the hypotenuse, as illustrated in Figure 2.4. Therefore, d_A and d_B can be written as

$$d_A = \sqrt{(h_A + r)^2 - (h_{\text{lim}} + r)^2}, \quad d_B = \sqrt{(h_B + r)^2 - (h_{\text{lim}} + r)^2}, \tag{2.6}$$

Additionally, based on the antenna technology employed, the transmitting node must be within the transceiver's beam. To check if node C, at altitude h_c, is in the beam of A we require to calculate the angle α

$$\alpha = \cos^{-1} \frac{(r + h_A)^2 + (\|\mathbf{AC}\|_2)^2 - (r + h_C)^2}{2(r + h_A)\|\mathbf{AC}\|_2} \tag{2.7}$$

and confirm that it is smaller than half of the beam opening angle β. Therefore, we can summarize the requirements for establishing an active link between two nodes as follows:

$$h_A \geq h_{\text{lim}}, \quad h_B \geq h_{\text{lim}} \tag{2.8}$$

$$\|\mathbf{AB}\|_2 \leq (d_A + d_B) \tag{2.9}$$

and in case a beam is deployed also

$$\alpha \leq \frac{\beta}{2} \tag{2.10}$$

The links between different node types are distinguished by their transmission characteristics. Inter-satellite links operate at a frequency $f_c = 30$ GHz and consequently experience high path loss below the stratosphere. This necessitates setting $h_{\text{lim}} = 80000$ m for these links. For all other link types, we assume $h_{\text{lim}} = 100$ m, accounting for potential obstructions caused by buildings. Additionally, we postulate that only satellites employ beams with an opening angle of 128° for communication with aircraft and gateways, while other links utilize omni-directional communication.

2.3.5 Channel Models, Link Capacities and Transmit Powers

In our MLN, the links between different nodes exhibit unique properties, influenced by factors such as distance, carrier frequency, and the type of antenna technology utilized. In our model, we assume that communication between various network nodes occurs through LoS links, aligning with common assumptions in related research [Pan+21a; Pan+21b]. While these studies often adopt a Rayleigh block fading channel model, our approach ensures a more complex approach: we increase the transmit power with increasing distance to maintain a constant channel capacity until the transmit power reaches a node specific maximum, from there on the capacity of the channel decreases with increasing distance.

The channel effect h is, therefore, based on the distance (d)-dependent PL with a path loss exponent of 2, an antenna gain factor g_a and atmospheric absorption losses l_a, alongside the carrier frequency f_c of the transmit signal and the speed of light c. The corresponding equation is:

$$h = \frac{10^{(g_a - l_a)/10}}{(4d\pi f_c/c)^2} \tag{2.11}$$

We further model the noise by

$$\xi = \text{BW}kT \tag{2.12}$$

with the T being the system temperature, BW the bandwidth of the signal, and k the Boltzmann constant. We assume the temperature for the satellites to be 10 K, while for other nodes, 218 K. Subsequently, we calculate the required power for maintaining the desired link capacity C. This calculation takes into account the number of MIMO n_{MIMO} antennas, the channel bandwidth BW, the previously described noise and channel effect

$$P = \max\left(\frac{\xi\, n_{\text{MIMO}}\, 2^{C/n_{\text{MIMO}}/\text{BW}-1}}{h}, P_{\text{max}}\right) \tag{2.13}$$

Lastly, we calculate the actual link capacity C by:

$$C = \max\left(n_{\text{MIMO}}\text{BW}\log_2\left(1 + \frac{P}{n_{\text{MIMO}}}\frac{h}{\xi}\right), C_{\text{max}}\right) \tag{2.14}$$

This model is applied on all links in the system. The resulting link properties of the MLN are used in Chapter 5, where its detailed attributes are outlined in Section 5.3.1 and Table 5.1.

2.4 Summary

This chapter begins by stating the constraints and requirements on the physical network layer within aircraft cabins, focusing on the requirements for channel models dictated by regulations and passenger device use. We then transitioned to presenting ray tracing as an option to derive channel models, detailing its fundamental interaction effects and summarizing underlying theoretical concepts. The physical layer section concludes by reasoning why ray tracing is the preferable method in our scenario over measurement campaigns, establishing a solid foundation for Chapter 3: Characterization of the 2.45 GHz and 5.16 GHz Channels in Aircraft Cabins, where we formulate channel models tailored to the aircraft cabin environment.

We continued by moving our focus to the link layer, where we explored the potential of MU-MIMO and BF technologies to meet the diverse service requirements of an aircraft cabin. We elaborated how we modeled MU-MIMO links and BF gains, and evaluated the performance of both technologies in terms of the number of RCLs served. This underscored the advantages of BF in this dense scenario, establishing it as the foundational technology for our research on resource allocation within a Multi-Radio Access Technology (Multi-RAT) network in Chapter 4: Resource Allocation in Beamformed Multi-Technology Networks.

Finally, we provided a comprehensive overview of the methodologies and technologies underpinning our research in Chapter 5: Service Placement and Routing in Aerial-Aided Multi-Access Edge Computing Networks. This entailed defining the services and service requirements found in aircraft cabins, establishing an appropriate MLN structure, and detailing the calculations for determining node access in a dynamic, global network. Furthermore, we presented the channel, transmission power and link capacity model, which will be used in our research to calculate the link capacities of the network in an MLN.

Chapter 3

Characterization of the 2.45 GHz and 5.16 GHz Channels in Aircraft Cabins

3.1 Introduction

The drive to improve and expand the Radio Frequency (RF) channel models for commercial aircraft stems from a multitude of factors. A significant uptick in demand for In-Flight Entertainment and Connectivity Services, the proliferation of passenger devices and sensors, and the vision of a connected cabin [God+22] all contribute to this need. Moreover, the advent of beamforming and Multiple Input Multiple Output (MIMO) within cabin spaces, coupled with the use of new materials in aircraft construction, adds a layer of complexity. Thus, accurate, up-to-date channel models for these scenarios have become increasingly imperative.

Despite the availability of numerous existing models, they often exhibit limitations. Many neglect factors such as passenger presence or focus exclusively on Path Loss (PL) and Tapped Delay Line (TDL), with Clustered Delay Line (CDL) frequently disregarded [Mor+09; Dia+04; Wen+19]. Moreover, these studies typically concentrate on specific components, like the PL induced by seats, or signal strength reception outside the cabin. They may also cater to frequencies (such as 28 GHz [Top+22] or 60 GHz [FKP08]) that are not typically utilized within aircraft cabins.

In contrast to these limitations, our work encompasses multiple scenarios and prioritizes the globally accessible 2.45 GHz and 5.16 GHz frequencies. To the best of our knowledge, no previously published research has offered a detailed 3D model usable in ray-tracing simulations. Such a model would permit the replication or extension of simulations from past studies. We have made our proposed model publicly accessible [Man+23a], enabling fellow researchers to evaluate and expand upon it for new applications, such as incorporating antennas in armrests.

We will present in the following sections an integrated model, proficient in facilitating Single Input Single Output (SISO) comparisons of PL, TDL, and MIMO (CDL) components. Not only does our model enable comparisons of receivers distributed along the aisle, seat screens, and passenger devices, but it also addresses problematic transmitter deployments. This is particularly valuable in scenarios where transmitters have been positioned at the start of the aisle, in lavatories, or at specific seats.

Channel models derived from measurement campaigns are often the gold standard in various environments. However, as discussed in Section 2.1.3, for the particular nature of aircraft cabins the use of ray-tracing simulations is an appropriate method to gather data to characterize the channel.

All in all, ray-tracing allows us an efficient use of resources and provides valuable insights into the expected performance of the system. Additionally, our ray-tracing simulations can also help to identify any potential issues or limitations that may not be apparent during a measurement campaign, specifically constructive and destructive interference components.

3.1.1 Key Contributions

In this chapter, we present innovative channel models tailored to the challenges within aircraft cabins, catering to both SISO and MIMO transmissions, building on the groundwork established in [Man+23b]. The main contributions are as follows:

1. We provide an open and comprehensive 3D model of a commercial aircraft. The model includes structural details and corresponding material properties, which allows for an enhanced accuracy when capturing the wireless communication environment

2. We present 2.4 GHz and 5.16 GHz channel models for the provided aircraft model. Here we focus on three different scenarios: the cabin aisle (Aisle), the seat-mounted screens (Screens), and the passenger-held devices (Seats). We argue for the necessity of incorporating human presence into channel modeling and offer a more realistic depiction of the onboard communication environment.

3. We present new PL models for all previously mentioned scenarios and show the advantage of switching predictors from a meter-based distance to seats and rows. In addition, we demonstrate that small-scale effects can be modeled more effectively using various random distributions.

4. We present new TDL models that considering two predictors and demonstrate the benefit of modeling the gain in [dB] as opposed to the commonly used linear model.

5. We present new CDL models, showing how the cluster parameters alter with distance.

6. We demonstrate the necessity of modeling the channels dependent on the propagation direction (transmitter towards aft; transmitter towards cockpit)

7. We propose a generalized methodology to derive channel models based on multiple predictors. This methodology allows a better understanding of the channels and can be also applied to data from measurements. The resulting models can then be used to optimize the performance of different wireless technologies on board.

This work continues with Section 3.2, where we will identify the limitations inherent in the existing approaches and outline how our work seeks to advance these methodologies. The following Section 3.3 contains the used 3D model, extends on ray-tracing and explains the channel, statistics, and fitting techniques used. In Section 3.4, we present, evaluate, and discuss the mathematical descriptions that constitute the channel models. We conclude with a discussion on the implications and limitations of our results, along with unexplored avenues for potential future research, in Section 3.5.

3.2 Related Work

The state of the art relevant to our proposal encompasses: PL, TDL, and CDL based channel models. Wireless networks in aircraft cabins involve multiple technologies, each displaying unique signal characteristics. The appropriateness of a particular channel model depends on the specific technology being utilized. For instance, a PL model may be adequate for Bluetooth, while for Wireless Fidelity (WiFi), particularly when including beamforming, a more detailed CDL model that outlines the effects based on the angle of departure and arrival would offer a more nuanced depiction. Thus, a comprehensive description of this specific environment promotes a superior understanding of the channel effects within such a multi-technology network. However, no existing work presents a unified channel description incorporating SISO and MIMO characterizations with PL, TDL, and CDL models.

3.2.1 Path Loss (PL)

Path loss prediction models for radio signals in various environments have been extensively studied. The survey [PSG12], is one example that summarizes this. However, in our work, we explore models explicitly tailored to the unique conditions of aircraft cabins. In addition, works presented investigated PL solely on the Euclidean distance between a transmitter and a receiver position, where as we show that it is crucial to consider the two-dimensional distance to the receiver as it significantly influences the path loss.

In the study [Mor+09], measurements were conducted inside a Boeing 737-400 aircraft at 1.8, 2.1, and 2.45 GHz. These measurements were used to derive PL models for receivers placed both in the aisle and at the seats. Yet, the model presented is applicable only for the specific transmitter positions described in the study. As a result, any alteration in the transmitter's location would compromise the validity of these models. To address this constraint, our study explores the effects of changing the transmitter position. Additionally, we incorporate the impact of passenger presence on the PL. However, we use the model presented in [Mor+09] as a baseline to compare our proposed PL model.

Owing to the lack of public availability of measurement data from aircraft cabins, we utilize ray-tracing to generate the necessary data to characterize the channel. This approach has already been used in other studies as well. For instance, [Top+22] employs ray-tracing to model the path loss at 28 GHz within an aircraft cabin to derive their PL model based on a log-distance function supplemented by a zero-mean Gaussian Random Variable. Likewise, the authors in [Sch+20] implement a comparable ray-tracing method within an Airbus A321 at 2.45 GHz.

The authors investigate in [Jac+09], PL based models based on measurements conducted within a mock-up of a wide-bodied aircraft cabin at 5.5 GHz. For this, they expand the log-distance component by incorporating linear terms which vary with frequency, and a normally distributed Random Variable (RV) with a standard deviation which varies quadratically with frequency. Further, they also evaluated the impact of different transmitter locations, specifically the upper front section of the cabin and various receiver locations such as the headrest, armrest, and aisle. In alignment with this approach, our study also contemplates the location of receivers at seats, where passenger handheld devices are most likely to be found. The models were based on measurements conducted within a mock-up of a wide-bodied aircraft cabin at 5.5 GHz.

In [Dia+04], the authors characterize the path loss for an Airbus A319, Airbus A330-200, and a Boeing 777-200. For this, they probed the channel at various operating frequencies (GSM-900, GSM-1800, Terrestrial UMTS, Bluetooth and IEEE 802.11b) with variable transmitter positions and receivers throughout the aircrafts, e.g., near the ears where passengers would be seated. However, the linear regression models introduced in the aforementioned studies do not adequately capture the distance-dependent effect on path loss. Given the tunnel-like structure of an aircraft cabin, which gives rise to constructive and destructive interference, the loss is expected to fluctuate in a non-linear fashion with distance.

The study in [HVB05] also incorporates losses modeled with floor separations and partitions dependent on the Euclidean distance, supplementing the log-distance-based loss. However, by treating the X (over the seat row) and Y (along the aisle) distances as separate variables rather than just relying on the Euclidean distance, we can take full advantage of the unique structural characteristics of the aircraft, thus yielding more authentic models.

The research reported in [Wen+19] integrates the relative X, Y coordinates of the receiver and the operating frequency into the PL model. However, their methodology relies on supervised machine learning techniques, which can potentially be problematic when faced with insufficient data samples. In this work, we employ regression techniques to derive analytical formulas for PL. This approach offers the benefit of analytically explaining the influences of various environmental factors on PL. Moreover, such analytical models grant insights into the effects of diverse input features when changes occur in the environment.

3.2.2 Tapped Delay Line (TDL)

TDL models, describing the impulse response of a radio channel, have been investigated in literature [AWL08]. Part of the TDL models surveyed, propose a function for tap amplitude that monotonically decreases with tap number; however, the rationale for the selection of the number of taps is typically not made clear. Conversely, other models present the number of taps as an RV, with parameters based on the Euclidean distance between the transmitter and receiver. Acknowledging that the unique architectural design of an aircraft cabin considerably impacts the channel's impulse response, we specifically investigate models constructed for such environments.

Felbecker, Keusgen, and Peter in [FKP08] offer initial insights into this area, as they visually demonstrate the magnitude of various multipath components and the distribution of their delays in a wide-bodied aircraft at 60 GHz using ray-tracing. However, their research does not delve into in-depth analysis or provides a reusable channel model, an aspect that we improve upon.

The study [Jem+08] applies the established Saleh-Valenzuela (SV) model [SV87] to represent the impulse response within an Airbus A319 aircraft. They use a quadratic function to demonstrate the power decay across multipath component clusters, and a linear function for decay modeling within each cluster. This adaptation of the SV model contributes to our understanding of the impulse response in aircraft cabins. Regrettably, the absence of the model parameters from the authors' description presents a challenge when it comes to re-purposing their model for aircraft cabin channel depiction.

In [CCM09], the authors investigate the Ultra Wide Band channel of a Boeing 737-200. They suggest different parameterized Power Delay Profile (PDP)-models for receivers positioned along the aisle and for Non-Line-of-Sight (NLoS) scenarios. The suggested models consist of an exponential function with its parameters being dependent on the Euclidean distance and a zero-mean Gaussian RV with a constant variance between the transmitter and the receiver. This description denotes the decay of linear power including the delay. Yet, even with the provision of a statistical model for the PDP, the authors did not utilize this information to derive a TDL model.

The work [Cha+19] extrapolates a TDL model from the PDP for 60 GHz millimeter-wave signals within a bus. Though not an aircraft environment, it merits inclusion here due to the thorough statistical modeling approach employed to characterize the channel in an indoor vehicular setting that structurally bears resemblance to an aircraft cabin. While the study regards the number of taps as a constant, we model it as a RV in our investigation. Furthermore, their assumption of a constant delay difference between the taps does not align with our observations, particularly for higher tap indices. As a result, we account for a RV in our description to accommodate this variation.

Following a similar approach, the research conducted in [Dia+04] provides channel models for an Airbus A319 and A330-200 including statistical components. For this, they divided the aircraft cabin into sections and modelled, for example, the number of multipath components with the help of a Nakagami distribution, with its parameters dependent on the sections. We delve deeper by characterizing the parameters, factoring in the distances between the transmitter and the receiver as opposed to limiting the analysis to cabin sections. Although the authors formulate the linear gain as an exponentially decreasing function complemented by a variable that changes based on the aircraft and antenna, we employ a more nuanced methodology in our evaluation.

Enhancing the state of the art, this work introduces statistical representations for the number of multipath components, the tap delays and the gains. Additionally, we incorporate two-dimensional distances between the transmitter and receiver, where applicable, offering an improvement in the model's accuracy over traditional methods.

3.2.3 Clustered Delay Line (CDL)

Channel propagation attributes in a MIMO system can be captured using a cluster-based model. The study [BHV07] applies this approach to evaluate the capacity at distinct seating positions within an aircraft cabin. This is done by identifying four clusters in the Boeing-777 ray-tracing data, based

on similar arrival and departure angles, as well as arrival times. However, the work stops short of providing an exhaustive clustered channel model or details about cluster properties. To the best of our knowledge, there are no other studies that delve into a clustered channel model specific to aircraft cabins. Therefore, we look to relevant studies beyond this specific application.

The authors in [Wu+16], establish a clustered channel model by applying ray-tracing to a street canyon environment at 28 GHz. For this, they grouped the rays based on their arrival times and angles, utilizing the Euclidean distance as a clustering metric. The clusters are then described including the delay spread and angular spread. All parameters of the clusters are then described with the help of probability distribution functions. However, the description of the channel is irrespective of the distance between the transmitter and the receiver.

Adopting a different approach, [Che+21b] presents a clustered channel model for indoor environments at Terahertz frequencies. This model employs the Density-Based Spatial Clustering of Applications with Noise (DBSCAN) algorithm to classify multipath components, utilizing the Multipath Component Distance (MCD) as the distance metric. In contrast to the aforementioned studies, our research takes a step further by examining the properties of multipath component clusters in the channel with respect to the distance between transmitters and receivers. This aspect becomes particularly significant in the context of an aircraft environment, where the structure of the cabin exerts a notable influence on the behavior of each cluster dependent on the exact position.

3.3 Methods

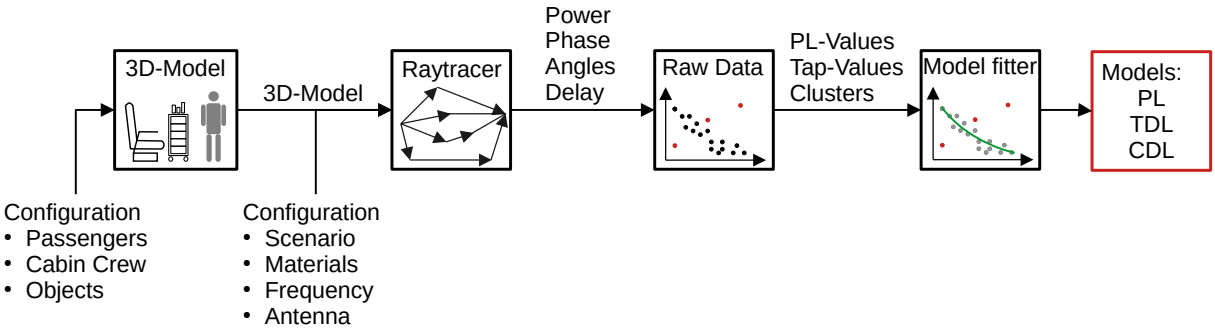

Figure 3.1 Flow diagram of the simulation chain

To derive the different channel models, we have developed a comprehensive processing chain, as illustrated in Figure 3.1. The first step involved creating a detailed model of the aircraft cabin based on the dimensions of a Boeing 737-400. This model takes into account various elements such as passengers, cabin crew, and trolleys, allowing us to accurately simulate the channel characteristics during flight operation. The cabin model was then fed into the ray-tracing software, where material properties and different types of antennas were incorporated based on the specific channel model being considered. At this step, we also specified the center frequency for the probing signal. The ray-tracing software then generated raw data, including received power, signal phase shift, angles of departure and arrival, and other relevant parameters for each ray. This raw data was subsequently processed to calculate channel-specific information, such as the gain and phase shift values for each tap and receiver position in the case of tapped delay line modeling. In the final step, the processed data was analyzed to identify the best-fitting models that accurately captured the observed channel characteristics over different predictors. Each step of the processing chain is described in greater detail in the subsequent sections, to provide a comprehensive understanding of our approach.

3.3.1 3D Modeling

The aircraft cabin model used in this study is based on the dimensions of a Boeing 737-400. The cabin itself has a width of 3.54 m, a length of 21.73 m, and a height of 2.26 m at the center of the aisle. Within the cabin, there are 26 rows of six seats each, with each row spaced at 0.81 m. The detailed 3D model of the cabin can be obtained from the provided link [Man+23a]. To analyze the wireless communication in the cabin, we consider three distinct scenarios. Figure 3.2 provides a visual representation of the different receiver positions corresponding to these scenarios. For reference, the transmitter positions are listed in Table 3.1, with the origin located at the start of the aisle.

Figure 3.2 Transmitter and receiver positions in the cabin. Red: Tx0, Cyan: Receiver Aisle, Blue: Receiver Screens, Green: Receiver Seats

Table 3.1 Transmitter positions

	x [m]	y [m]	z [m]
Tx0	0	0	1.8
Tx2	0	10.6	2.25
Tx4	0	5.375	2.25
Tx4.1	0	5.275	2.25
Tx4.2	0.1	5.375	2.25
Tx5	0	16.125	2.25

In the Aisle scenario, we employ a group of 9 transmitters placed at the vertices and center of a cube with a side length of 6 cm, positioned at Tx0. Along the width of the aisle, we position 45 receivers, spaced at intervals of 1 meter along the length of the aisle. This scenario is commonly used in literature, allowing for comparisons with existing results. However, considering that the majority of wireless communication within a cabin is related to In-Flight Entertainment and Connectivity Services (IFECSs), the Screens scenario is of particular interest. In this scenario, the transmitters are located below the cabin ceiling, which is a typical installation position in commercial aircraft. Specifically, we position transmitters at positions Tx2, Tx4, Tx4.1, Tx4.2, and Tx5, depending on the specific analysis. To then simulate the usage of the IFECS, we position a group of 6 receivers in front of each seat screen. In the Seats scenario, we focus on handheld-device usage by utilizing transmitters Tx4 and Tx5. To imitate this usage, we position a group of 27 receivers in front of the passengers. By considering these different scenarios, we can thoroughly investigate the wireless communication performance in various areas of the aircraft cabin, providing valuable insights into the channel characteristics and potential challenges in different usage scenarios.

3.3.2 Ray-Tracing

To accurately simulate the physical propagation of a sinusoidal waveform with a bandwidth of 20 MHz at a frequency of 2.45 GHz, we utilize the software Wireless InSite [Rem20]. This software employs a ray-tracing technique, which involves tracing the path of individual rays as they interact with various objects and surfaces in the environment. In our ray-tracing model, we employ a shooting and bouncing algorithm. The rays are initially shot from the transmitter, and they bounce off surfaces, undergo reflections, and diffract around obstacles. The ray spacing in our model is set to 0.25 degrees, ensuring sufficient resolution for capturing the propagation effects. Research by Athanasiadou and Nix in [AN00] suggests that a ray-tracing model with five reflections and a single diffraction event can

Table 3.2 Objects and material properties

Material	Objects	2.4 GHz			5 GHz		
		Permittivity		Conductivity	Permittivity		Conductivity
		Real	Imaginary		Real	Imaginary	
CRP [Lag+98]	Doors, Container, Haul	5.9000	1.5000	0.2012	4.9900	4.8000	0.5167
GRP [Sok+05]	Cladding, Ceiling	4.6358	0.0498	0.0067	4.5517	0.0611	0.017
Nomex [GRO]	Floor	1.0900	0.0220	0.0030	1.0900	0.0220	0.0063
PCB [Sei19]	Screens, Electronics	11.3700	0.0085	0.0011	11.320	0.0170	0.0049
PEEK [Raj+09]	Seats, Toilets	24.0000	0.0122	0.0016	24.000	0.0122	0.0035
Plexiglass [Gor+20]	Windows	2.6100	0.0040	0.0005	2.6100	0.0040	0.001
Polyimide [WY+19]	Screens	3.2950	0.0626	0.0083	3.2700	0.0768	0.0220
Leather [AAS17]	Seats	1.7900	0.0752	0.0101	1.7740	0.0710	0.0204
Polyurethane [Mey15]	Seats	1.0627	0.0018	0.0002	1.0492	0.0018	0.0005
Polycotton [Ada+15]	Humans	3.2300	0.1906	0.0256	3.2300	0.1292	0.0371
Skin [Kom12]	Humans	44.0000	-	35.114	-	3.7170	
Muscle [Kom12]	Humans	53.5730	-	1.8105	48.9910	-	5.2010
Bone [Kom12]	Humans	4.8000	-	0.2100	9.6750	-	1.1540

produce accurate results. We consider a maximum of 6 reflections and up to 2 transmissions for each ray. Additionally, we include up to 1 diffraction event in the model. Therefore, our model adheres to this recommendation to strike a balance between accuracy and computational efficiency.

The frequency dependent material properties of the different objects used in our 3D model can be found in Table 3.2. All objects assumed to be made of metal are modeled as perfect electric conductors.

The PL and TDL models are based on isotropic SISO antennas at both the transmitter and receiver, which allow for an omni-directional coverage pattern as they radiate and receive signals equally in all directions. Whereas for CDL models we employ a 4 by 4 MIMO antenna array for the transmitters and a 2 by 2 MIMO antenna array for the receivers with both having a half wavelength sub-antenna spacing. The sub-antennas are spaced apart by half a wavelength. Further, the sub-antennas used for the transmitters mounted at the ceiling and the screen receivers are directional, meaning they have a specific radiation pattern focused in a particular direction. In contrast, receivers positioned on the seats contain isotropic sub-antennas. All of the antennas in our models are vertically polarized, meaning that the electric field vector of the transmitted and received signals is oriented in the vertical direction. This polarization choice is commonly used in wireless communication systems and is suitable for the aircraft cabin environment. By incorporating different types of antennas with their specific characteristics, our models can accurately represent the antenna behavior and its impact on the wireless channel within the aircraft cabin. Nonetheless, when comparing the models presented in various works, it is important to exercise caution due to different works using different antenna types, e.g., leaky-line [Dia+04], patch and discone antenna [Mor+09], half dipoles [FKP08], etc. The different radiation and gain patterns influence substantially the expected path loss and angles of arrival of the probing signal. Apart from that, we set the transmission power to 20 dBm according to European Telecommunications Standards Institute (ETSI) standards for 2.45 GHz [ETS19] and to 23 dBm for 5.16 GHz [ETS17]. Rays exhibiting a power value below the noise floor (7×10^{-14} W) are disregarded.

3.3.3 Methods and Model Fitting

Using the data obtained from the ray-tracing simulation, we first calculate the different channel parameters for each receiver position. For this we use a specific function which transforms different properties (e.g., time of arrival, received power, etc.) from each ray into the required model parameters. Secondly, we try to find a suitable description for these parameters based on different predictors. In the following subsections, we will delve into more detail on the methodology and techniques used to derive these channel models, providing a comprehensive understanding of the process.

3.3.3.1 Path Loss (PL)

To derive a PL model, we calculate the path loss at each receiver position for each transmitter $\mathrm{PL}_{\mathrm{Rx}}^{\mathrm{Tx}}$ as described in Equation 3.1. In the following we will omit the transmitter-receiver nomenclature.

$$PL = -10\log_{10}\left|\left(\sum_{i=1}^{I}\sqrt{g_i}\cdot e^{j\phi_i}\right)^2\right| \text{[dB]} \tag{3.1}$$

where g_i and ϕ_i are the gain and phase shift of ray i. In the next step of our analysis, we fit various models using different predictors (distance, row number, seat number) to capture the trend of the path loss across the aircraft cabin. These models incorporate linear, logarithmic, exponential, or periodic terms, either individually or in combination. Next, we select the best-fitting model based on the lowest Akaike information criterion (AIC) value, a criterion commonly used in model selection. This process is applied to all the channel models considered in our study. Moving on, we focus on modeling the residuals of the selected model to account for the impact of small deviations in receiver positions. For this, we fit various probability distributions (such as Normal, Lognormal, Exponential, Gamma, Rayleigh, Rician, Nakagami, Weibull, Logistic, Extreme Value, Generalized Extreme Value, exGaussian) on the residuals and kreep the best-fitting distribution based on the AIC. Finally, we present the PL model as a combination of a predictor-dependent function and a Random Variable. This procedure enables us to derive accurate and versatile PL models for the different scenarios for further in-depth analysis.

3.3.3.2 Tapped Delay Line (TDL)

For our TDL models, we distinguish between Line-of-Sight (LoS) and NLoS components. When LoS is present, the tap delay τ for the LoS tap is set to 0, while the gain is calculated according to Equation 3.2.

$$\alpha = -(PL_0 + 20\log_{10}(d)) \tag{3.2}$$

where PL_0 is the free space path loss at 1 m for the transmit frequency, and d is the Euclidean distance between transmitter and receiver. For the NLoS components, we divide the rays into bins of $\tau = 8.33$ ns. The amplitude α_m and phase ϕ_m of bin m are calculated by summing the complex-valued NLoS rays, weighted by an envelope function as described in [MCF21]. The calculations are presented in Equation 3.3 and Equation 3.4, where $g_{m,i}$ represents the gain of ray i in bin m, $w_{m,i}$ represents the corresponding weight, and $|\cdot|$ and $arg(\cdot)$ denote the magnitude and phase, respectively.

$$\alpha_m = \left|\sum_i \sqrt{g_{m,i}}\cdot w_{m,i}\cdot e^{j\phi_{m,i}}\right| \tag{3.3}$$

$$\phi_m = arg\left(\sum_i \sqrt{g_{m,i}}\cdot w_{m,i}\cdot e^{j\phi_{m,i}}\right) \tag{3.4}$$

Bins without rays are then removed from the set of taps. The remaining taps are then assigned consecutive indices, starting from $n = 1$ and the total number of taps is denoted as N. Due to the

resulting varying nature of N we decided to directly fit this parameter as a random variable whose parameters depend on the scenario specific predictors. To decide which random distribution best fits our underlying data, we assigned 3 points for the best fitting distribution according to AIC, 2 points for the second best and 1 point for the third best, for each predictor. The distribution with most points is then kept to describe the behavior of N.

Due to the previously described removal of empty bins, the tap delay, τ_n, increases proportionally with the tap index, n, until the first originally discarded bin. At that point, the tap delay no longer follows a linear function but includes a RV component. This transition from a linear function to a linear function plus an RV is described by a border function, which is fitted using the same nature of equations as in the PL models.

$$\tau_n = \begin{cases} (n-1) \cdot 8.33 \times 10^{-9} & \text{if } n < \text{border} \\ (n-1) \cdot 8.33 \times 10^{-9} + \text{RV} & \text{elsewhere} \end{cases} \tag{3.5}$$

In this context, the group of random distributions we fit is extended by the same distributions accounting for a zero-inflation. These zero-inflated RVs, denoted by ZI-Distribution, are able to better fit data which includes a high amount of zeros. This is necessary because in some cases, depending on the predictor, no bins are discarded which would yield zero for the residuals.

The gain α_n is modeled as a function that considers the tap index n along with predictors such as distance, row number, and seat number. The residuals of the best-fitting model are treated as a RV, capturing the small deviations in the receiver position's impact on the channel. Based on the observed data we model the phase shift ϕ_n uniformly distributed between $[0, 2\pi]$. By combining these components according to Equation 3.6, we derive the channel model.

$$\text{TDL}^{\text{NLoS}} = \sum_{n=1}^{N} \alpha_n \cdot e^{j\phi_n} \delta(\tau - \tau_n). \tag{3.6}$$

3.3.3.3 Clustered Delay Line (CDL)

The CDL models are based on MIMO simulations. Due to the multiple sub-antennas used in MIMO, we need to address the gain overestimation of the received signal. For this, we divide the gain values by the number of antennas. Additionally, we discard rays that have a gain value 22 dB below the strongest ray at each predictor value. This adjustment ensures that the gain values are appropriately scaled and removes weak signals that do not significantly contribute to the overall channel characteristics. Moving on, we focus on clustering the rays based on their arrival and departure angles. We utilize the DBSCAN algorithm [Est+96], a density-based clustering method, for this task. To measure the distance between angles, we use a modified version of the MCD as the distance metric [Czi+05]. By transforming the angles from the Spherical coordinate system (AoA, AoD) to the Cartesian coordinate system ($\overrightarrow{\text{AoA}}$, $\overrightarrow{\text{AoD}}$), we can calculate the MCD using the Euclidean distance formula as described in Equation 3.7. This approach allows us to group together rays that exhibit similar arrival and departure angles.

$$\text{MCD}_{i,j} = \sqrt{\left\| \overrightarrow{\text{AoA}_i} - \overrightarrow{\text{AoA}_j} \right\|_2 + \left\| \overrightarrow{\text{AoD}_i} - \overrightarrow{\text{AoD}_j} \right\|_2}. \tag{3.7}$$

It is important to note that in our clustering process, we deliberately exclude the time of arrival as a clustering parameter. This decision is motivated by the fact that the time of arrival is dependent on the position of the receiver, which would introduce inconsistencies in the clustering results across different predictor values. For the clustering itself, we set a minimum requirement of 50 rays per cluster. The neighborhood search radius is determined as a fraction dependent on the Scenario (specifically, Aisle: $\frac{1}{7}$; Screens: $\frac{1}{8}$; Seats: $\frac{1}{7.5}$) of the mean of the MCDs, ensuring that nearby rays are considered in the clustering process. A different fraction for each scenario is required, as every scenario exhibits a different span in angles, contains different antennas and is influenced by the cabin

structure differently. Any rays that cannot be successfully clustered are discarded, as they do not contribute to the formation of clusters. This ensures that we focus only on the relevant clusters that exhibit meaningful channel characteristics. The number of Multi-path Components (MPCs) within each cluster is determined through a sub-clustering process based on the time of arrivals. To achieve this, we align and scale the time of arrival values using the formula Equation 3.8:

$$t_i' = \frac{t_i - \min(t_i)}{\max(t_i) - \min(t_i)} \quad \forall i \in I_c, \tag{3.8}$$

where t_i represents the time of arrival for ray i within the set of all rays I_c belonging to cluster c. In the MPCs sub-clustering process, the neighborhood search radius is set to $\frac{1}{20}$ of the mean distance between the time of arrivals within the cluster. No rays are discarded during this sub-clustering process. The clusters that are identified are then described based on the parameters suggested by Third Generation Partnership Project (3GPP) [ETS20], which are calculated following the methodology outlined in [Rem20]. These parameters include the number of MPCs, the gain, the Mean Time of Arrival (MToA), the delay spread, and the mean ($\overline{x}$) and standard deviations ($\sigma(x)$) of the four angles. The channel model at a receiver is then described by the following equation Equation 3.9:

$$\text{CDL} = \sum_{c=1}^{C} \sum_{n=1}^{N} \alpha_{c,n} \cdot \delta(\theta^D - \theta^D_{c,n}) \cdot \delta(\phi^D - \phi^D_{c,n}) \cdot \delta(\theta^A - \theta^A_{c,n}) \cdot \delta(\phi^A - \phi^A_{c,n}) \cdot \delta(\tau - \tau_{c,n}), \tag{3.9}$$

where n denotes the specific MPC, and θ^D, ϕ^D, θ^A, ϕ^A, and τ represent the elevation and azimuth angles of departure and arrival, as well as the time of arrival, respectively, within cluster c. The gain is denoted by $\alpha_{c,n}$. In addition to providing the unified 3GPP model for the entire aircraft aisle, we also calculate the cluster parameters for each receiver position and model their variations throughout the aircraft cabin. For this we use the same baseline equations as in the PL and keep the best fitting model in accordance with AIC. It is important to note that these equations are limited to specific distances, as not all clusters span across the entire length of the aisle. To quantify the improvement of our model prediction of the behavior of the cluster parameters, we calculate the difference between the Root Mean Squared Error (RMSE) of the 3GPP model and our proposed models for each cluster and its parameters. Here, a positive value indicates that our proposed model predicts the cluster parameter better than the 3GPP model.

3.3.3.4 Error calculation

To assess the accuracy of our proposed models, we split the ray-tracing data into a training set and a test set, using a ratio of 0.5. We then evaluate the performance of the model equations by calculating the RMSE and the Mean Absolute Percentage Error (MAPE) for both the training and test sets. Furthermore, we analyze the error associated with the RVs used in our models. To do this, we calculate the cumulative absolute differences, as described in Equation 3.10, between the probability density function of the RVs obtained from the training set and those obtained optimizing on the test set.

$$\text{err}_{\text{R.V.}} = \int_{-\infty}^{\infty} \left| f_{\text{testing}}(x) - f_{\text{train}}(x) \right| dx \tag{3.10}$$

3.4 Evaluation and Analysis

For all our evaluations, we ensured that for every unique predictor value, the same amount of rays was present. While evaluating Seats and Screens receiver positions we additionally investigated the influence of the transmit direction, from the transmitter towards the *cockpit* or towards the *aft*.

3.4.1 Path Loss (PL)

First, we evaluated the path loss data throughout the cabin. For this, we fit different models as described in Section 3.3.3 and present them, including error metrics, in Table 3.3.

3.4.1.1 2.45 GHz PL Models

Table 3.3 Proposed PL models including error metrics

Scenario	Path Loss [dB]	RV	$\text{err}_{\text{R.V.}}$	RMSE [dB]		MAPE [%]	
				Train	Test	Train	Test
Aisle Baseline	$40.7 + 10.1 \log_{10}(d)$	GEV (0.06, 3.69, -2.35)	0.0123	5.13	5.00	7.53	7.64
Aisle	$41.3 + 9.24 \log_{10}(d)$ $-1.69 \sin(0.491d + 1.49)$	exG (-4.53, 2.12, 0.22)	0.0123	5.00	4.85	7.28	7.37
Screens *Aft*	$69.4 + 12.5 \log_{10}(r)$ $-20 \sin(-0.115r - 12.3) + 0.518 \lvert s \rvert$	Normal (0.00, 7.06)	0.0415	7.06	7.67	6.15	6.47
Screens *Cockpit*	$53.2 + 1.85r + 2.86 \sin(0.284r + 10.9)$ $+10 \sin(0.635 \lvert s \rvert + 0.0716)$	GEV (-0.10, 6.10, -2.95)	0.0385	6.96	6.86	6.86	6.68
Screens Human *Aft*	$39.3 + 4.28r + 20 \sin(0.145r + 7.16)$ $+0.619 \lvert s \rvert$	Normal (0.00, 6.77)	0.0650	6.77	7.18	5.86	6.16
Screens Human *Cockpit*	$67 + 7.31 \log_{10}(\lvert s \rvert) + 7.71 \log_{10}(r)$ $-20 \sin(-0.101r + 7.13)$	exG (-5.22, 4.94, 0.19)	0.0385	7.25	6.96	7.09	6.82
Seats Human *Aft*	$53.8 + 17.6 \log_{10}(r)$ $+20 \sin(0.123r + 5.5) + 3.17 \lvert s \rvert$	exG (-4.62, 5.09, 0.22)	0.0649	6.85	6.88	6.70	6.76
Seats Human *Cockpit*	$34.1 + 1.89r$ $+20 \sin(0.0983r + 6.36) + 2.78 \lvert s \rvert$	GEV (-0.13, 6.45, -2.94)	0.0011	7.11	7.06	7.64	7.69
Screens Human *Aft* 5.16 GHz	$56.3 + 3.63r + 20 \sin(0.162r + 6.74)$ $+0.68 \log_{10}(\lvert s \rvert)$	Normal (0.00, 6.52)	0.0051	6.52	6.45	5.15	5.11
Screens Human *Cockpit* 5.16 GHz	$61.6 + 1.28r - 20 \sin(0.0931r + 3.13)$ $+0.627 \lvert s \rvert$	exG (-4.82, 5.17, 0.21)	0.0257	7.07	7.41	6.05	6.12
Seats Human *Aft* 5.16 GHz	$35.8 + 3.63r + 20 \sin(0.131r + 13.1)$ $+10 \sin(0.706 \lvert s \rvert - 0.485)$	Logistic (-0.19, 3.82)	0.0224	6.85	7.16	6.00	6.39
Seats Human *Cockpit* 5.16 GHz	$48.4 + 1.71r - 20 \sin(0.116r + 2.91)$ $+2.64 \lvert s \rvert$	exG (-4.87, 5.30, 0.21)	0.0164	7.15	6.95	6.78	6.60

In Aisle, we start with the log-distance model as a baseline - a commonly found model in the literature. We encounter a free space path loss of 40.7 dB (as seen in Table 3.3), which is similar to the 40.2 dB reported in [Mor+09]. However, the path loss exponent differs by 1.29. We attribute this to the different antennas (discone versus half-wave dipoles). Our half-wave dipole allows the signal wave to be reflected at the cockpit and the side walls of the cabin resulting in a path loss factor much lower than 2. While the standard deviation of the small-scale effect reported by [Mor+09] is 3.26 dB we report 5.00 dB. This is due to us not averaging the samples for every meter, thus retaining the actual variance of the data.

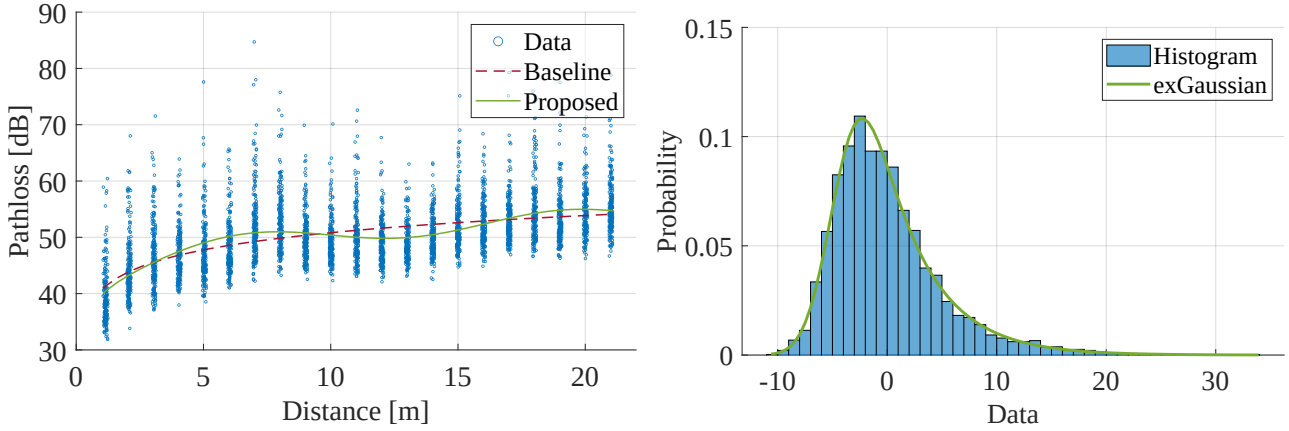

(a) Different models fitting the path loss in the Aisle

(b) Small-scale effect in the Aisle modeled with an RV

Figure 3.3 PL for the Aisle

The comparison between the fit of our proposed model and the baseline model on the data set is visualized in Figure 3.3a. We observe a periodicity over the aisle which is attributed to the destructive and constructive interference, modeled by extending the baseline with a sinusoidal term. The lower AIC (25697 vs. 25911) confirms that a model including the sinusoidal term fits the underlying data better. The residuals, as depicted in Figure 3.3b, do not follow a Normal, Rician, or Rayleigh distribution (as commonly found in literature) but fit best to an exGaussian (exG) distribution. We, therefore, propose the following model: $41.3+9.24\log_{10}(d)-1.69\sin(0.491d+1.49)+\text{exG}(-4.53, 2.12, 0.22)$ [dB], with d being the distance between transmitter and receiver and an $\text{err}_{\text{R.V.}}$ of 0.0123. Although the RMSE and MAPE errors for the baseline and proposed equation are of the same magnitude, the proposed equation can help to identify how the cabin structure affects the signal propagation and channel estimation.

For Screens, we first investigate the effect of micro-deviations of the transmitter positions. For this, we move the transmitter by 10 cm along the length (Tx4.1) and width (Tx4.2) of the aisle. After determining the best fitting model, we compare the Mean Absolute Error (MAE) and a maximum error between the model predictions. Moving the transmitter along the length causes an MAE of 0.58 dB and a maximum error of 1.46 dB. Whereas, a movement along the width results in a MAE of 0.56 dB and maximum error of 0.99 dB. Both values are inside the small-scale model, described by the RV. Hence the proposed models are not sensitive to small deviations in positions and are generalizable.

For Tx4 in *aft* direction, we are able to model the channel with the following equation: $80+1.99d_y-6.08\sin(0.36d_y+1.64)$, with d_y being the distance between the transmitter and receiver along the length of the cabin and an AIC of 4274. The model that achieves the best fit does not incorporate a logarithmic component, due to the constructive and destructive interference, this highlights the importance of finding the optimal fitting model for every scenario. However, we also expect an influence on the PL based on the distance to the walls of the cabin. Therefore, we fitted the data to a 2D equation which resulted in the equation: $75.4+2.25d_y-8.31\sin(-0.28d_y+0.65)+1.66\sin(5.65\,|d_x|-4.46)$, with d_x being the distance along the width of the cabin and an AIC of 4261. This model allows us to explain up to 3 dB of deviation along the cabin as shown in Figure 3.4. The d_x-sine term can be explained by the increased distance the wave has to propagate. For aisle-seat-screens, most rays were reflected by the ceiling and the floor before hitting a receiver, whereas for window-seat-screens the rays were additionally reflected at the lower part of the overhead compartment. Consequently, we propose 2D models from here on and confirm that all 2D models in this work exhibited better AIC values.

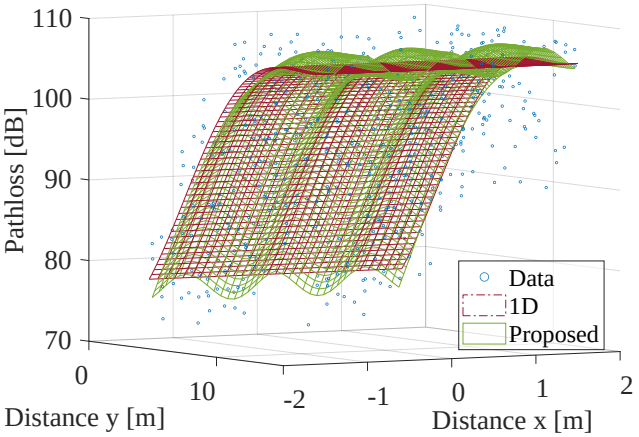

Figure 3.4 PL for Screens with a one- and two-dimensional prediction

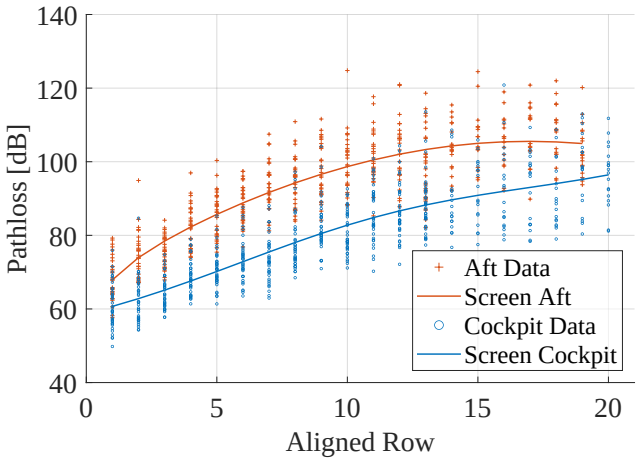

Figure 3.5 PL for Screens in *aft* and *cockpit* direction

Moving forward, our models are based on the seat s and row r numbers, considering that seat or row spacing can differ depending on the airline. Furthermore, most applications focus on the specific seat rather than the distance. Additionally, we combine the results from the Tx2, Tx4, and Tx5 to study the impact of the propagation direction, specifically towards the *cockpit* and *aft*. For this analysis, we align the results according to the relative distance between the receiver and transmitter positions. This approach allows to become independent of the precise transmitter position. The discrepancy in the number of rows between the *aft* and *cockpit* directions stems from the specific placement of the transmitters, leading to a difference of one row. The resulting models can be found in Table 3.3. The Screens *aft* model predicts a logarithmic effect while the *cockpit* model predicts a linear effect along the length of the cabin, in addition to a periodic term. The mean components of these two models, across all seats, are depicted in Figure 3.5. The apparent linear trend in the *cockpit* model arises due to receivers in close proximity to the transmitter experiencing destructive interference, which transitions to constructive interference with increasing distance, and eventually returns to destructive for the furthest rows. This dynamic causes a deviation from a typical logarithmic model. Higher PL values for the *aft* can be attributed to the absence of a LoS component, as the rays must reflect off the seats prior to reaching the screens.

To emulate a typical flight scenario, we populated the cabin with human models and positioned two trolleys at distances of 5.75 m and 14.8 m in the aisle, respectively. The models derived from this setup are denoted as Screens Human *Aft* and *Cockpit* in Table 3.3. For *aft*, the PL with human presence across the initial 12 rows is lesser compared to the scenario without humans. However, the trend reverses beyond this point. For *cockpit*, a similar trend is observed, with the turning point at row 16. This phenomenon is attributed to the humans serving as additional interaction points for the rays, resulting in a distinct pattern compared to the scenario without human presence. Furthermore, unique trends can also be observed along the seats. In *aft*, the linear slopes differ, whereas in the *cockpit*, the seats exhibit either a periodic or logarithmic contribution.

To accommodate the growing usage of personal electronic devices (PEDs) within the cabin, we strategically placed receivers on every passenger seat. The models developed from this arrangement are detailed in Table 3.3, labeled as Seats Human *Aft* and *Cockpit*. For *aft*, the PL exhibits a blend of a logarithmic and periodic term along the cabin's length, whereas for *cockpit*, we discern a combination of a linear and periodic term along the length of the cabin. Both models exhibit a linear term across the cabin's width. Upon comparing the Seats and Screens scenarios, a consistent pattern is seen, showing a higher PL for *aft* relative to *cockpit*. Yet, the PL for Screens surpasses that of Seat. This can be attributed to the Screens receiver positions being more obstructed from incoming rays.

3.4.1.2 5.16 GHz PL Models

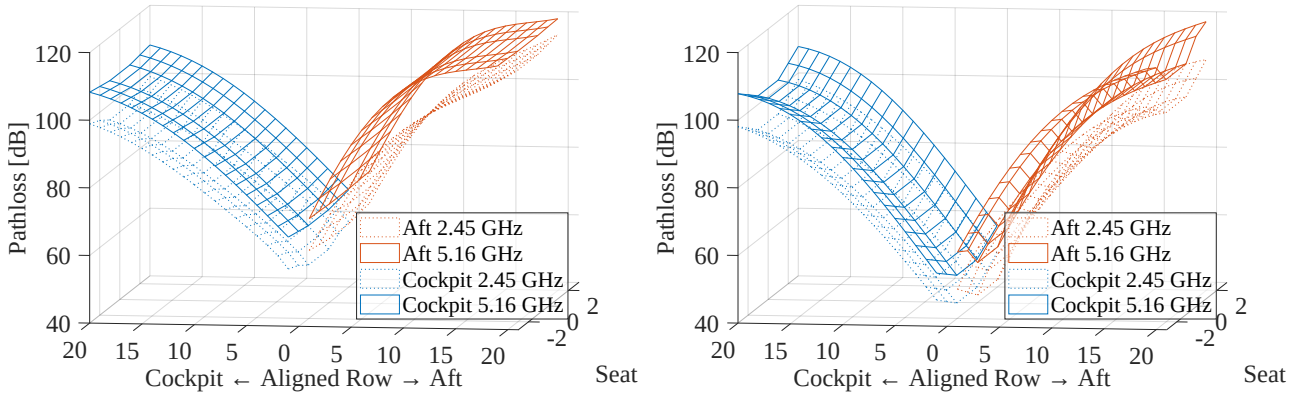

(a) Screens Scenario **(b)** Seats Scenario

Figure 3.6 Comparison of 2.45 GHz and 5.16 GHz Scenarios

As shown in Figure 3.6, the PL is smaller for 2.45 GHz compared to 5.16 GHz. This is due to the different material properties and higher dissipation of the 5.16 GHz waves. However, for the Screens scenario, in Figure 3.6a, we are able to observe that the differences in PL first increase and then decreases with increasing row number. However, for *aft*, the decrease difference is bigger compared to *cockpit*. We attribute this to the different constructive interference patterns for each frequency. In the Seats scenario, as visualized in Figure 3.6b, we observe an analogous trend to the Screens scenario along the aisle. However, a more pronounced escalation in PL across the seats is depicted. This is attributed to the aisle seats being more exposed to incoming rays, while seats near the window are considerably more shielded, hence limiting the access of rays. Comparing absolute values between Seats and Screens, we observe a smaller difference in PL between the frequencies for Seats. This is due to the screens being more shielded, missing LoS components and therefore resulting in more losses in 5.16 GHz.

3.4.2 Tapped Delay Line (TDL)

Although PL models are instrumental for estimating coverage and signal strength, this section delves into TDL models. These models offer more nuanced insights into how environmental interactions influence signal properties in the time domain, specifically considering the multipath effects emerging from the cabin's spatial diversity.

3.4.2.1 2.45 GHz TDL Models

We start with modeling parameters for the Aisle. The number of multipath components, N, (equivalent to the channel's taps), is modeled as an RV with varying parameters along the aisle. This RV follows a normal distribution, with the models for these parameters being detailed in Table 3.4. Although a $\text{err}_{\text{R.V.}} = 16\%$ appears quite large, its actual influence on prediction quality is merely a fraction of it, since the number of multipath components predicted are integer values. This is evidenced by the prediction errors for parameters' models, which remain within a single multipath component ($\text{MAE}_{\mu} = 0.94, \text{MAE}_{\sigma} = 0.16$). As distance increases, both the mean and spread of N decreases. This is attributed to the diminishing power of the received rays, which increasingly drop below the detection threshold.

Table 3.4 Proposed Multipath Component (N) TDL Models including error metrics

Scenario	Distribution	Model	$\text{err}_{\text{R.V.}}$
Aisle	Normal	$\mu = 34.4 - 0.206d$, $\sigma = 2.97 - 0.0626d$	0.1594
Screens Human *Aft*	Inverse Gaussian	$\mu = 7.97 - 0.295r$, $\lambda = 292e^{-0.152r}$	0.0981
Screens Human *Cockpit*	Inverse Gaussian	$\mu = 8.4 - 0.269r$, $\lambda = 361e^{-0.151r}$	0.0695
Seats Human *Aft*	Inverse Gaussian	$\mu = 8.49 - 0.255r$, $\lambda = 436e^{-0.195r}$	0.0925
Seats Human *Cockpit*	Inverse Gaussian	$\mu = 9.22e^{-0.0348r}$, $\lambda = 804e^{-0.216r}$	0.0901
Screens Human *Aft* 5.16 GHz	Inverse Gaussian	$\mu = 7.02 - 0.311r$, $\lambda = 278e^{-0.19r}$	0.1428
Screens Human *Cockpit* 5.16 GHz	Inverse Gaussian	$\mu = 7.49 - 0.262r$, $\lambda = 254e^{-0.158r}$	0.0982
Seats Human *Aft* 5.16 GHz	exGaussian	$\mu = 7.82e^{-0.0883r}$, $\sigma = 1.07 - 0.172\log(r)$, $\lambda = 1.02$	0.1295
Seats Human *Cockpit* 5.16 GHz	Inverse Gaussian	$\mu = 8.72e^{-0.0487r}$, $\lambda = 452e^{-0.199r}$	0.0963

The optimal fit for the border function, integral to the description of τ as per Equation 3.5, is highlighted in Table 3.5 and illustrated in Figure 3.7a. When tap number exceed this border, the arrival time is supplemented by the zero-inflated exponential RV as specified in Table 3.5.

Table 3.5 Proposed τ TDL Models including error metrics

Scenario	Border Function	RV	$\text{err}_{\text{R.V.}}$
Aisle	$28.8 - 0.495d$	ZI-Exp (0.45, 4.89)	0.0022
Screens Human *Aft*	$9.41 - 0.279r + 0.616\sin(0.5r + 3.35) - 0.316\lvert s\rvert$	Exp (0.699)	0.0882
Screens Human *Cockpit*	$9.05 - 0.268r + 0.61\sin(0.853r - 1.38) - 0.1\lvert s\rvert$	Exp (0.560)	0.0204
Seats Human *Aft*	$3.57 + 6.2e^{-0.105r} - 0.329\lvert s\rvert$	Exp (0.679)	0.0429
Seats Human *Cockpit*	$6.13 + 0.883\log(r) - 4.44\sin(0.148r + 93.3) - 0.237\lvert s\rvert$	Exp (0.546)	0.0113
Screens Human *Aft* 5.16 GHz	$8.56 - 0.316r + 0.912\sin(0.525r + 2.97) - 0.263\lvert s\rvert$	Exp (0.586)	0.1640
Screens Human *Cockpit* 5.16 GHz	$9.12 + 1.69\log(r) - 10\sin(0.0713r + 12.6) - 0.35\lvert s\rvert$	Exp (0.559)	0.0018
Seats Human *Aft* 5.16 GHz	$8.52 - 0.208r - 0.788\sin(-0.322r + 12.1) - 0.566\lvert s\rvert$	Exp (0.726)	0.0229
Seats Human *Cockpit* 5.16 GHz	$5.27 + 0.507\log(r) - 2.44\sin(-0.196r - 58.1) - 0.225\lvert s\rvert$	Exp (0.406)	0.0262

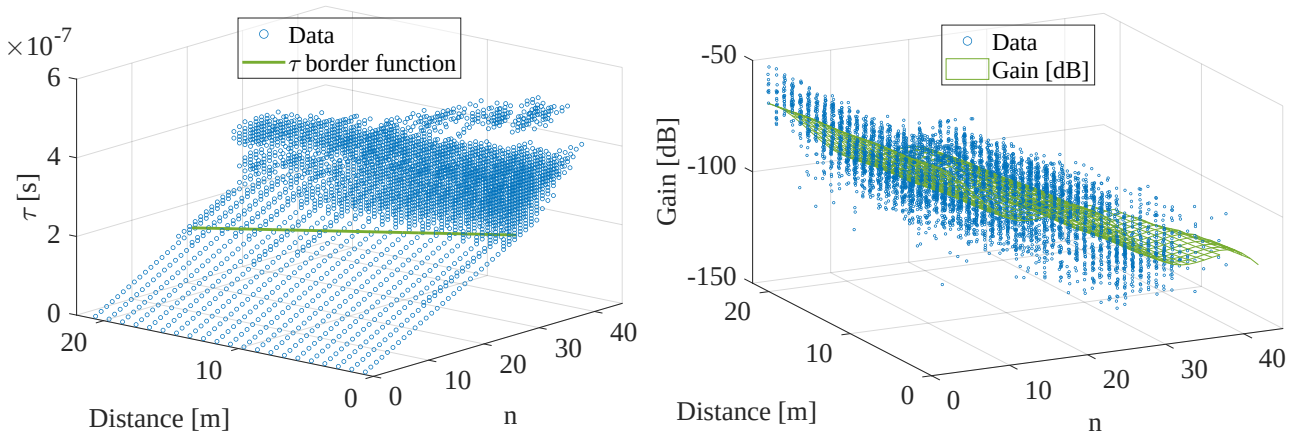

(a) Border function for τ

(b) Gain Model in dB

Figure 3.7 Aisle Scenario Proposed Models

To effectively model the gain of the taps, we improve upon the State of the Art as in [Dia+04], incorporating a sine term to achieve the optimal fit given by: $\alpha = 0.00902e^{-0.476n}(e^{-0.382d} + 0.283\sin(0.0858d + 0.64))$. This results in a substantial RMSE of 38.2 dB, a consequence of α spanning across multiple decades. In light of this, we propose a modification: modeling the data in dB, which is likely to

represent smaller values more efficiently. This approach also reduces the RMSE by approximately 28 dB. The same issue is mirrored in the RV, where the $\text{err}_{\text{R.V.}} = 0.0069$ is reduced to 0.0018. The gain model can be found in Table 3.6 and is visually represented in Figure 3.7b. Of note, the periodicity found in the PL model of the Aisle is also observable here in the distance term d and additionally across the multipath components n.

Table 3.6 Proposed Gain TDL models including error metrics

Scenario	Gain [dB]	RV	$\text{err}_{\text{R.V.}}$	RMSE [dB]		MAPE [%]	
				Train	Test	Train	Test
Aisle	$-63.2 - 1.46n - 7.04\sin(0.31n + 4.32)$ $-0.47d - 0.29\sin(0.76d - 1.69)$	Normal(0.00, 9.95)	0.0018	9.95	9.98	8.74	8.79
Screens Human *Aft*	$-61.9 - 4.16n + 5.38\sin(0.615n + 0.277)$ $-2.08r + 15\sin(-0.11r + 5.92) - 1.82\lvert s\rvert$	Logistic(0.396, 5.64)	0.0127	10.6	10.1	7.34	7.26
Screens Human *Cockpit*	$-54.8 - 6.63n + 5.98\sin(0.879n - 0.0215)$ $-2.08r + 0.941\sin(0.778r - 0.982) - 2.09\lvert s\rvert$	Logistic(0.423, 5.31)	0.0196	9.79	9.62	7.36	7.15
Seats Human *Aft*	$-50 - 5.56n + 6\sin(0.617n + 0.569)$ $-2.31r + 6.66\sin(0.153r + 3.02) - 4.11\lvert s\rvert$	Logistic(0.247, 5.54)	0.0068	10.1	10.1	7.70	7.85
Seats Human *Cockpit*	$-61 - 12\log(n) + 15\sin(0.405n + 1.16)$ $-2.15r + 1.59\sin(0.737r - 1.06) - 3.86\lvert s\rvert$	Logistic(0.174, 6.03)	0.0015	10.8	10.8	8.88	8.86
Screens Human *Aft* 5.16 GHz	$-87.6 - 3.58\log(n) + 15\sin(0.406n + 1.21)$ $-2.21r + 15\sin(-0.131r + 5.99) - 1.27\lvert s\rvert$	Logistic(0.423, 5.23)	0.0204	9.88	9.65	6.41	6.41
Screens Human *Cockpit* 5.16 GHz	$-66.5 - 6.25n + 5.55\sin(0.97n - 0.161)$ $-2.09r - 1.71\lvert s\rvert$	Logistic(0.454, 5.02)	0.0461	9.38	9.36	6.50	6.45
Seats Human *Aft* 5.16 GHz	$-62.5 - 5.24n + 6.24\sin(0.611n + 0.707)$ $-2.42r + 4.53\sin(0.232r + 2.22) - 4.45\lvert s\rvert$	Logistic(0.220, 5.34)	0.0060	9.79	9.83	6.96	7.04
Seats Human *Cockpit* 5.16 GHz	$-78.8 - 4.93n + 9.08\sin(0.564n + 1.02)$ $-0.361r + 15\sin(0.178r + 1.53) - 3.69\lvert s\rvert$	Logistic(0.204, 5.68)	0.0077	10.2	10.1	7.72	7.63

Henceforth, we will concentrate on scenarios that incorporate humans. In Screens the number of multipath components N is modelled best with an Inverse Gaussian RV. For *aft* we encounter an $\text{err}_{\text{R.V.}} = 9.81\%$ and for *cockpit* an $\text{err}_{\text{R.V.}} = 6.95\%$. For both directions the average of N decreases with distance. This is due to the increasing amount of rays with power below the noise floor. Whereas the standard deviation (std) for *cockpit* decreases minimally by 0.28, the std of the *aft* increases till row 7 and then falls covering a range of 0.43 std. However, both have a small effect on the resulting N.

To find the best model for the border function of τ for Screens we again move to the predictors row r and seat s. This results in a linear trend along the seats for *aft* and *cockpit*. For both directions, the tap delays begin to diverge from the linear prediction earlier as the measurement distance from the transmitter increases. This is attributed to the impact of the cabin structure on the ray arrival time. As one moves further from the transmitter, gaps in arrival times begin to surface earlier. Additionally, the residuals of the tap delays are best modelled by an exponential RV, $\text{err}_{\text{R.V.}} = 8.82\%$ for *aft* and 2.04% for *cockpit*. Importantly, there is no need for a zero-inflated distribution compared to the Aisle model, as the majority of the tap delays that fall beyond the border function exhibit a deviation from the linear prediction as described in Section 3.3.3.2.

Furthermore, as the tap number increases, we observe a corresponding decrease in gain, as outlined in the respective function in Table 3.6. Generally, the *cockpit* exhibits a higher tap gain than the *aft*, which aligns with the findings from the PL analysis. However, for higher tap numbers this is not always the case. This is not reflected in the PL model, as the smaller gain values of higher taps barely contribute to the PL models.

Similar to the Screens scenario, the multipath components N of the Seats scenario are also modelled with an Inverse Gaussian RVresulting in an $\text{err}_{\text{R.V.}} = 9.25\%$ for *aft* and 9.01% for *cockpit*. Moreover, the mean of the total multipath components decreases with row number, while the std increases with row number. This occurs because, as row numbers increase, seats situated at the edges become

more difficult for the rays to reach. As a result, a wider spread in arrival times causes an increased dispersion in arrival times and therefore multipath components.

In *cockpit* the border function exhibits a periodic decrease with increasing row distance, whereas for *aft* the decrease is strictly monotonic. The residuals are modelled with an exponentially distributed RV, which results in an $\text{err}_{\text{R.V.}} = 1.13\%$ and $\text{err}_{\text{R.V.}} = 4.29\%$, respectively. This leads to a very similar trend in both propagation directions for the arrival times of the multipath components. However, this similarity does not extend to the tap gain. While the gain decreases with row distance for *aft* and *cockpit*, the gain trend over tap numbers is similar until tap 9 where it starts to increase for *cockpit*, while it continues to fall for *aft*. This variation in trend is attributed to different materials' impact on the amplitude of the ray depending on the propagation direction. For *cockpit* the rays are reflected on the screens and seats whereas for *aft* the rays are reflected on the humans.

3.4.2.2 5.16 GHz TDL Models

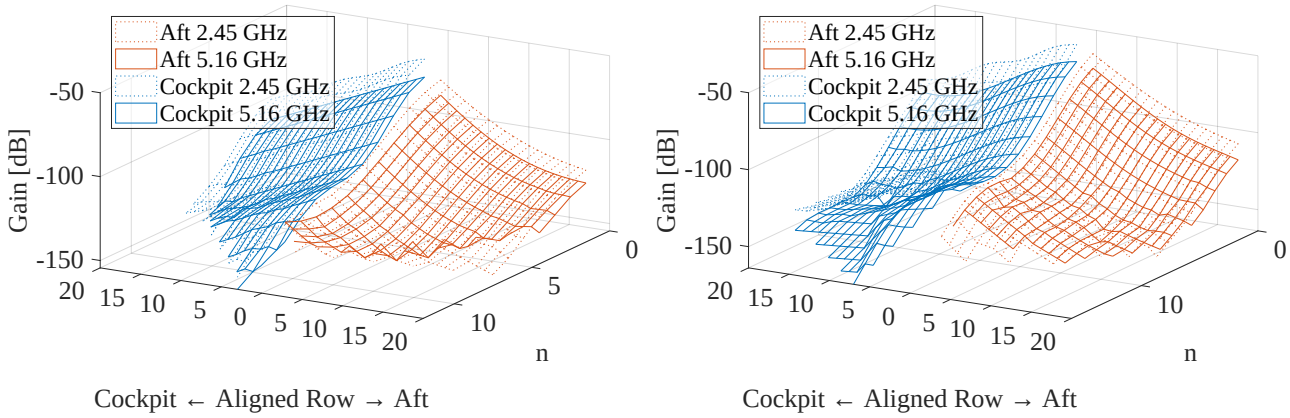

(a) Screens Scenario

(b) Seats Scenario

Figure 3.8 Comparison of 2.45 GHz and 5.16 GHz Scenarios

Extending the channel models to 5.16 GHz, the multipath component N of Screens decrease with increasing distance and are below the 2.45 GHz values. We attribute this to the higher dissipation of the 5.16 GHz signal. The difference in N is constantly around 1 tap. The border functions of τ decreases periodically and are below the 2.45 GHz results. This further shows how the frequency dependent material properties impact the tapped delay line model. As can be visualized in Figure 3.8a, similar to 2.45 GHz, the gain decreases with increasing distance and multipath component n. However, for the last few taps of *aft*, the gain increases again. On average, the 5.16 GHz signal is 6.65 dB lower for *aft* and 7.09 dB for *cockpit*.

For Seats, *aft* and *cockpit* multipath components n decrease with increasing distance. For 5.16 GHz, *aft* and *cockpit* exhibit up to 1 multipath component less than the 2.45 GHz model. However, comparing the multipath components between Seats and Screens, Seats exhibit more multipath components. This is due to the accessibility of the receiver positions from multiple directions, resulting in a higher spread in arrival times. The border function for *aft* and *cockpit* decrease periodically over distance. As expected, the gain decreases with increasing distance and multipath component n as seen in Figure 3.8b. Comparing the behavior for frequencies, the gain is larger for 2.45 GHz. However, while the difference in *aft* remains nearly constant at 5.92 dB, the difference for *cockpit* increases drastically after tap 11. This is due to the gain increase in the 2.45 GHz model.

3.4.3 Clustered Delay Line (CDL)

While TDL models consider the time delay and amplitude of multipath components, CDL models take it a step further by additionally accounting for the clustered nature of multipath reflections,

thus capturing spatial characteristics of the signal propagation environment. This results in a more realistic and accurate portrayal of the actual propagation environment. We propose to extend the CDL model of [ETS20] by making the cluster properties dependent on the receiver position. For this we incorporate the same predictors as for the PL and TDL models. The resulting CDL descriptions of the 3GPP and predictor-based models can be found in Section A.1 and Section A.2, respectively.

3.4.3.1 CDL Models 2.45GHz

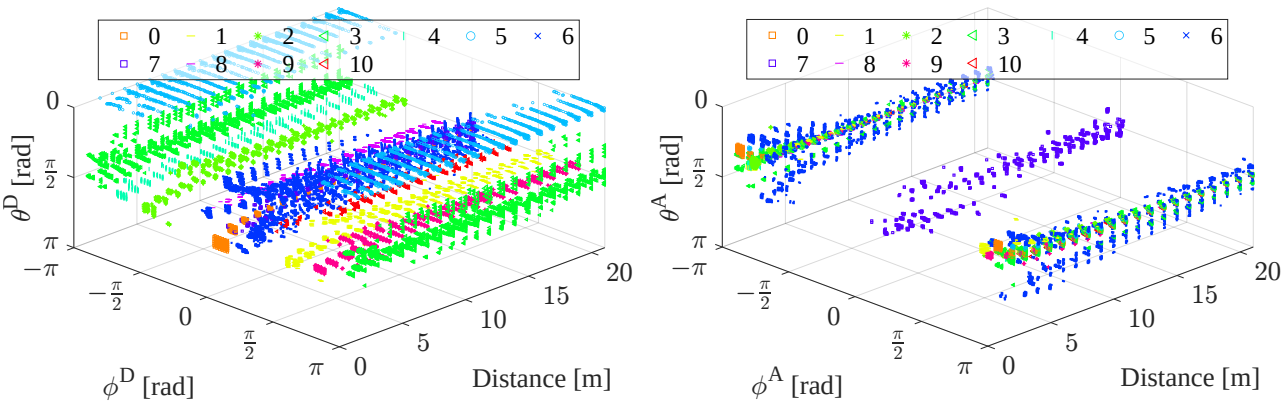

(a) Departure **(b)** Arrival

Figure 3.9 Clusters for the Aisle

The clustered rays for each distance value of the Aisle scenario are depicted in Figure 3.9. In this context, $\phi = 0$ corresponds to the direction pointing towards the aft, while $\phi = \pm\pi$ signifies the cockpit's direction. Similarly, $\theta = 0$ represents the direction pointing upwards towards the ceiling, and $\theta = \pi$ indicates the direction downwards towards the floor. In total, 7.5% of the rays could not be clustered. The figures reveal a decreasing trend in the angular spread with increasing distance. In the initial few meters, reflections primarily originate from the front of the seats and cockpit, reaching the receiver. However, as we progress further down the cabin, fewer rays are reflected by the seats and cabin walls, thereby reducing the angular spread. Depending on the specific cluster, different cabin components interact with the signal. For instance, cluster 5 exhibits significant interaction with the ceiling and floor, in stark contrast to cluster 3, which is predominantly reflected by the cockpit. Therefore, we decided to model these individual trends with different equations.

Table 3.7 Models for the properties of Cluster 7

Property	Model
Gain [dB]	$-46.8 - 12.9\sin(0.109d)$
MToA	$(0.92 + 1.15\log(d))10^{-8}$
Delay Spread	1.01×10^{-8}
$\overline{\phi^A}$ [rad]	$0.12 - 0.0068d$
$\sigma(\phi^A)$ [rad]	0.068
$\overline{\theta^A}$ [rad]	$1.52 + 0.687e^{-0.257d}$
$\sigma(\theta^A)$ [rad]	$0.114 - 0.045\sin(0.948d - 0.847)$
$\overline{\phi^D}$ [rad]	$0.058 - 0.047\log_{10}(d)$
$\sigma(\phi^D)$ [rad]	$0.022 - 0.010\sin(0.268d + 3.88)$
$\overline{\theta^D}$ [rad]	$1.6 + 0.607e^{-0.404d}$
$\sigma(\theta^D)$ [rad]	$0.046 - 0.015\sin(0.965d - 0.654)$
MPC	$\lfloor 1.68 + 1.6\log_{10}(d) \rfloor$

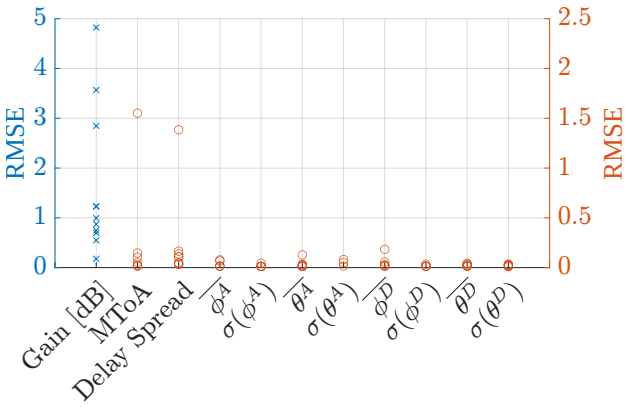

Figure 3.10 RMSE for Aisle clusters and properties

As exemplified in Table 3.7 for Cluster 7, the gain decreases until it reaches 14 m, beyond which it increases. This pattern is a consequence of the cabin reflections, which induce a constructive interference pattern yielding a sinusoidal form, with the gain surpassing that of a conventional PL model with a PL exponent of 2. The MToA showcases a logarithmic increase with distance. The increase in time of arrival can be attributed to the extended duration required for the rays to reach their respective receivers. The mean elevation angle θ demonstrates an initial decrease for departure and arrival and eventually convergences towards the end of the cabin. This phenomenon is primarily attributed to the vertical disparity between the transmitter and the receiver, giving rise to steeper angles at minimal distances and a subsequent convergence over increased distance. The similarity in trends for both angles is explained by the rays bouncing off the floor and seats before reaching the receiver. The azimuth angles for both departure and arrival hover around zero, with minor spreads as the cluster encompasses rays directly pointing towards the receiver. The quantity of MPCs increases with distance due to the widening spread of the rays' arrival times. However, this is not mirrored in the delay spread, because of the power-weighted distribution of the rays as explained in [Rem20].

To assess the accuracy of the proposed CDL parameter models we use the RMSE. The RMSE is based on the residuals between the values predicted by the model, derived from the training set, and the actual values from the test set. It should be noted that, the error values presented for both delay spread and MToA are based on the z-standardized data. As depicted in Figure 3.10, the errors in gain are of the same magnitude as those observed in the PL and TDL models. However, the errors for delay spread and MToA of cluster 7 and the error for the ϕ^D of cluster 5 stand out due to the considerable range of values associated with each predictor.

To assess the benefit of our models compared to the 3GPP models we calculate RMSE between the 3GPP models and the predicted value for each receiver position. As shown in Table 3.8, the biggest improvements are obtained for the LoS component. This is logical as its properties would be expected to be most dependent on the predictors. In general, we observe that mean angle improvements are larger than angle spread improvements. This is due to the mean components varying with distance more than the spreads, as a result of the angle-based clustering. More specifically, we see larger improvements for mean elevation angles compared to azimuth angles, as they are more dependent on distance. Overall, improvements are highly dependent on the cluster, as the interactions with the cabin differ significantly with over the different clusters.

Table 3.8 RMSE improvement between 3GPP and predictor-based Cluster description for the Aisle

Type	Cluster	Gain [dB]	MToA	Delay Spread	$\overline{\phi^A}$ [rad]	$\sigma(\phi^A)$ [rad]	$\overline{\theta^A}$ [rad]	$\sigma(\theta^A)$ [rad]	$\overline{\phi^D}$ [rad]	$\sigma(\phi^D)$ [rad]	$\overline{\theta^D}$ [rad]	$\sigma(\theta^D)$ [rad]	MPC
LoS	0	9.49	0.001	0.002	0.000	0.012	0.092	0.011	0.000	0.012	0.092	0.011	0.595
NLoS	1	6.02	0.001	0.040	0.071	0.012	0.058	0.006	0.016	0.004	0.059	0.006	0.056
NLoS	2	6.04	0.001	0.015	0.074	0.002	0.058	0.005	0.017	0.005	0.061	0.005	0.580
NLoS	3	3.24	0.001	0.009	0.001	0.011	0.024	0.011	0.001	0.002	0.004	0.006	0.481
NLoS	4	6.29	0.002	0.013	0.056	0.001	0.050	0.003	0.008	0.000	0.050	0.002	0.193
NLoS	5	2.01	0.004	0.000	0.000	0.001	0.082	0.003	0.001	0.001	0.000	0.001	0.508
NLoS	6	4.79	0.002	0.089	0.001	0.073	0.090	0.023	0.001	0.096	0.033	0.066	1.023
NLoS	7	1.31	0.088	0.000	0.011	0.000	0.037	0.007	0.004	0.002	0.032	0.003	0.126
NLoS	8	2.31	0.043	0.035	0.005	0.001	0.009	0.001	0.014	0.004	0.005	0.001	0.302
NLoS	9	4.70	0.089	0.126	0.060	0.001	0.050	0.004	0.001	0.004	0.049	0.008	0.188
NLoS	10	2.05	0.048	0.035	0.023	0.001	0.013	0.000	0.012	0.004	0.006	0.000	0.341

For Screens and Seats, which are visualized in Figure 3.11, we utilized Tx4 and Tx5. Similar to the Aisle, the angular spread of the clusters decreases with increasing row number. In contrast to the Aisle, most clusters do not span over all rows, due to higher power loss. In general, departure clusters are relatively compact, pointing slightly below the transmitter in θ^D and down the aisle in azimuth. Depending on the specific cluster, the first interactions are on the aft of the aircraft, on the humans or the edges of the seats. For the first rows, overhead compartments also come into play as interaction

points. Interestingly, the cabin's walls and windows are not the initial interaction points, as those rays cannot reach the receiver. The arrival angles of the clusters, on the other hand, are more dispersed. Many clusters contain rays reaching the receiver from a higher elevation. Clusters with ϕ^A near zero and $\theta^A \approx \frac{\pi}{2}$ contain rays with humans as their last interaction point, while an θ^A near zero indicates the lower part of the overhead compartments as the last interaction point.

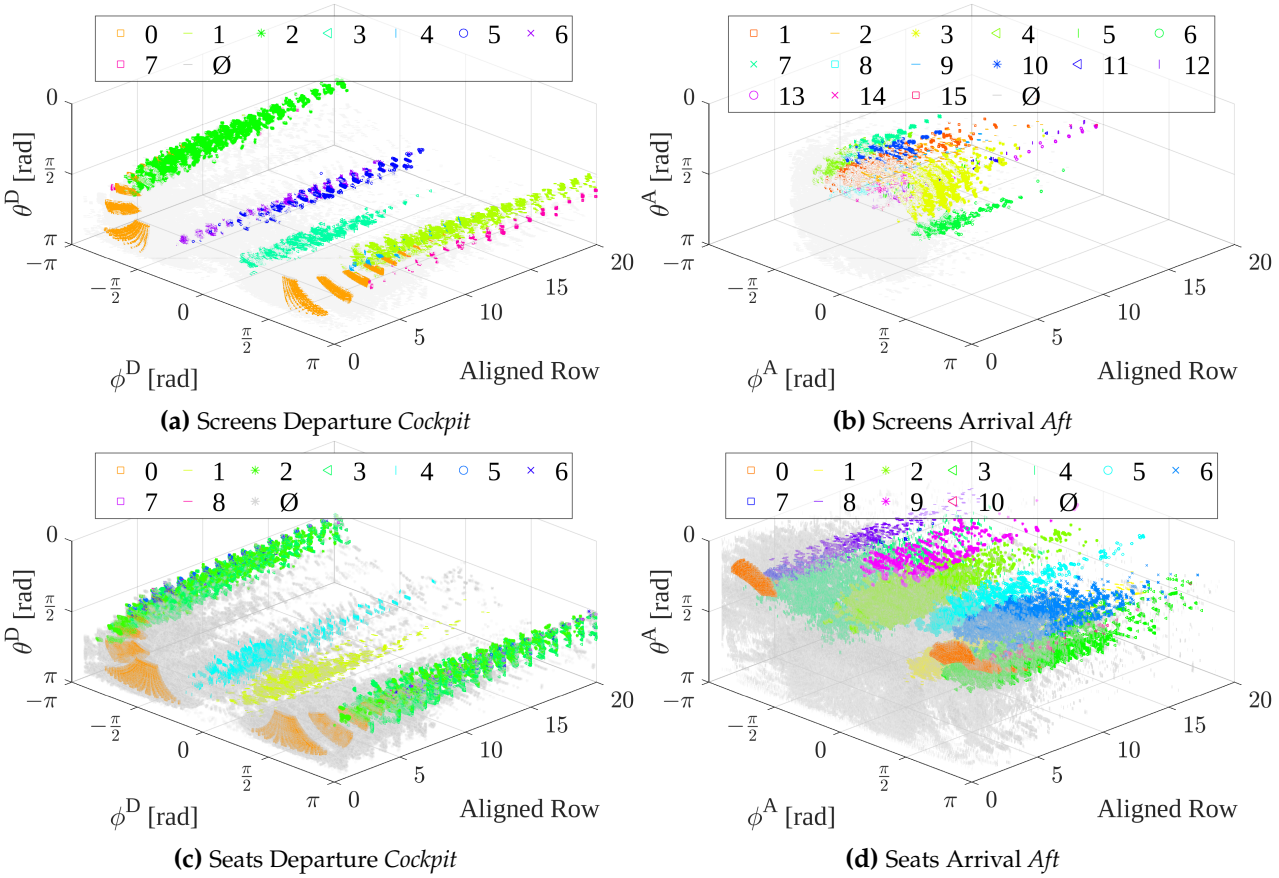

(a) Screens Departure *Cockpit*

(b) Screens Arrival *Aft*

(c) Seats Departure *Cockpit*

(d) Seats Arrival *Aft*

Figure 3.11 Screens and Seats Clusters 2.45 GHz including rays that could not be clustered (Ø)

For the *Cockpit*, we observe a LoS for the initial rows. This LoS component gradually disappears due to obstructions caused by humans and seats. The departure angles of the NLoS indicate that clusters with $\phi^D \approx \pm\frac{\pi}{4}$ move down the aisle, interact with humans and the toilet walls at the cabin's end before being reflected and reaching the receivers. Clusters with an $\phi^D \approx \pm\pi$ and an $\theta^D \approx \frac{\pi}{2}$ first interact with the overhead compartments, while clusters with a lower elevation angle strike humans or seats first. Comparing Screens and Seats, the *Aft* in Screens does not exhibit a LoS cluster due to the seat obstructions. The arrival angles confirm the explanation from PL and TDL, that the screen receiver positions are able to be reached only from the front side of the screen, whereas the seat receivers can be reached from every direction.

The Figure 3.11 also depicts the rays which could not be clustered. For Screens specifically this was 83.2% of the rays for *aft* and 72.3% for *cockpit*, whereas for Seats this was 73.2% of the rays for *aft* and 72.1% for *cockpit*. This would indicate that the channels do not behave in a clustered manner. However, with increasing distance between the transmitter and receiver, the ratio between the unclustered rays and the total rays reduces, and the clustered behavior of the channel becomes more pronounced.

Assessing the accuracy of the proposed CDL parameter models, gain errors are similar to the errors of the PL and TDL models. Only the $\overline{\phi^D}$ error of the LoS cluster sticks out. This is due to the LoS properties being highly dependent on the test and train set allocation of the data and the dependency

on the predictors. However, we are still able to improve its RMSE by 0.2507 rad compared to the 3GPP model for Screens and for Seats by 0.4865 rad for *aft* and 0.3955 rad for *cockpit*.

3.4.3.2 CDL Models 5.16 GHz

The clustering of rays in 5.16 GHz for both scenarios exhibits similarity to the 2.45 GHz case. However, not all clusters were preserved in the Seats scenario and an additional cluster was even found for its *aft*. As expected, the higher dissipation of 5.16 GHz rays results in less rays with increasing row numbers compared to 2.45 GHz. This manifests in a clustered behavior predominately in the middle section, and in clusters not extending over the same rows. This is especially pronounced in Screens for *aft*. The number of unclustered rays extends to more rows compared to the 2.45 GHz scenario and is considerably greater in the initial rows for 5.16 GHz. Errors associated with the clustering echo those found in the 2.45 GHz case, with the largest error consistently corresponded to the Line-of-Sight (LoS) component.

3.4.4 Application

The utilization of the various presented models in this section is straightforward. For example, to calculate the PL for *aft*, for the screen at a window seat ($s = \pm 3$) which is 5 rows ($r = 5$) from the access point, use the Screens *aft* equation from Table 3.3 and add a realization of the RV from the distribution mentioned.

3.5 Summary and Conclusion

In this chapter, we have described the process of deriving PL, TDL, and CDL models from ray-tracing data. Our large scale PL models exhibit the same error range as existing models in literature [Mor+09]. However, we have improved the accuracy of small-scale effects by considering a wider range of random distributions and multiple predictors, rather than restricting ourselves to specific distributions and a single predictor. Our TDL models exhibit a similar number of multipath components as in [Dia+04]. Nevertheless, we have been able to reduce the error in gain estimation by transforming the gain logarithmically and simplifying the model equations. We have presented the first detailed CDL model specifically designed for aircraft cabins, building upon the initial work in [BHV07]. Our model incorporates the influence of humans and considers different propagation directions (*aft* and *cockpit*) to provide a more realistic representation of the channel. We have also identified unexpected trends in the models, highlighting the interactions between the cabin structure and the signal.

All these channel models have practical implications for the deployment of Access Points (APs) in aircraft cabins. They can help ensure that receivers do not fall below the desired Signal to Interference and Noise Ratio (SINR) threshold and assist in determining the number of APs needed to achieve full coverage by evaluating the maximum range of rows each AP can cover. The impact of propagation direction on channel gain, as observed in all the models, underscores the importance of considering directionality when deploying APs in aircraft. Additionally, by understanding the effects of human presence on the channels, combined with the angle description provided by the CDL models, IFECSs can be designed to provide reliable and high-throughput wireless communication services to passengers and crew members by minimizing destructive interference. On another note, the CDL models could also be utilized for receiver or passenger localization inside the cabin. These statistical channel models can serve as a valuable tool to validate and confirm channel models obtained through machine learning techniques. Furthermore, we have developed an open and detailed aircraft cabin model that includes material properties, allowing other researchers to build upon and expand our work.

In future work, it is possible to evaluate the impact of different materials on the channel models and investigate how factors such as frequency, seat spacing, and seat configurations influence the channel characteristics. As hardware capabilities continue to advance, surpassing current limitations, more

detailed and accurate ray-tracing simulations can be conducted, further enhancing the robustness of our approach. Additionally, we propose exploring optimal probability distributions for various cluster properties and fitting models to these parameters, instead of assuming Gaussian distributions in the CDL model. This approach has the potential to yield more accurate and insightful results in the analysis of the propagation environment.

Overall, our contributions in this chapter lay the foundation for a comprehensive understanding of the wireless channel in modern aircraft cabins, enabling better design and optimization of wireless communication systems in such environments.

Chapter 4

Resource Allocation in Beamformed Multi-Technology Networks

In this chapter, we investigate the deployment of beamforming (BF) in an aircraft to improve the passenger experience, help to connect wireless sensors and actuators, and lay the foundation for an efficient connected cabin. The content of this chapter is based on a published conference contribution [Man+22b] and journal publication [MVK24].

4.1 Introduction

In an aircraft a dual imperative exists: ensuring the safe operation of all systems inside the aircraft and satisfying the needs of the passengers. Specifically, aircraft cabins foster the demand for wireless communication services for personal devices, for in-flight entertainment systems, and for sensors and wireless control systems, which govern aspects such as lighting and service requests. All this with the goal to improve the operational efficiency and passenger convenience.

This wireless traffic demand will continue to increase as airlines want to offer more in-flight entertainment options as high resolution video streaming and gaming. The network requirements will become more stringent and robustness will play a major role to support the addition of more and new type of sensors and actuators, as needed and described for example in [God+22]. Also, as aircrafts switch from wired to wireless solutions to reduce weight and operate more efficiently, we can expect more and different kinds of data traffic.

These human and machine-type communications in the aircraft cabin require tailored solutions, resulting in a network composed of multiple technologies. Moreover, due to the longevity of technology in the aviation sector, the support of different technologies becomes crucial, as it cannot be foreseen which technologies will prevail in machine-to-machine communication or be used by passengers in the future. The seamless operation of these diverse systems is critical to ensure passenger satisfaction, safety, operational integrity, and efficiency.

All these sources of wireless transmissions result in the aircraft cabin containing not only multiple users, but being a dense user and Radio Access Point (RAP) environment. Depending on the aircraft size, 1 to 12 RAPs are deployed to support a varying number of connected Radio Clients (RCLs). This mandates, therefore, the deployment of multiple RAPs and a robust connectivity provision to reduce interference. Further, due to aircrafts flying worldwide, it is important to operate the networks on a globally available frequency. In addition, the low economic margins of airlines, demand a low-cost operating solution. Therefore, only a limited spectrum is available, specifically the unlicensed 2.45 GHz or 5.16 GHz band.

To cater to all these requirements and challenges, we focus on two wireless technologies, cellular communication and Wireless Local Area Network (WLAN). The imminent advent of next-generation network technologies, featuring capabilities such as centimeter-level localization, opens new options for enhancing the Quality of Service (QoS) and user experience within the aircraft cabin. In this area, two forms of transmissions have emerged, Multiple Input Multiple Output (MIMO) and BF,

each bearing its distinctive merits. While MIMO techniques, promise a substantial throughput augmentation by leveraging the spatial domain and deploying multiple data streams, they may not be inherently optimized for maximizing connectivity in high-density environments due to interference. Conversely, BF systems focus the transmission energy predominantly towards the intended RCLs while reducing the chance to become a potential interference source. A detailed comparison of these concepts is delineated in Section 2.2.3.

Nevertheless, these networks' achievable rate and robustness depends on the Signal to Interference and Noise Ratio (SINR), which in BF is based on the beam angle, the transmission power and link direction (up-link (UL) or down-link (DL)) of the RAPs and the transmission properties of the RCLs. Therefore, we suggest in this work, a specific antenna constellation for BF, and provide a mathematical description of the network based on the aforementioned properties of an RAP. This allows us to devise a robust resource allocation framework, which we investigate by deriving an optimization problem, that is solved with different strategies to efficiently orchestrate the RAPs.

4.1.1 Key Contributions

In this chapter, we present a Multi-Radio Access Technology (Multi-RAT) network, as it would be deployed in aircraft cabins, including 5G and Wireless Fidelity (WiFi) transmission options for all users, building on the groundwork established in [Man+22b] and [MVK24].

The main contributions are as follows:

1. Development of a Resource Allocation Framework: This work outlines the creation of a novel framework tailored for a Multi-RAT network, aiming at optimizing network sum throughput and ensuring equitable data rate distribution among RCLs over multiple time slots. This is achieved through the strategic allocation of beam angles, transmission powers for RAPs, and defining UL or DL transmission slots for all devices within a specified time frame.

2. Diverse Solution Techniques: The work showcases a diverse array of solution strategies to address the resource allocation problem. This includes the exploration of meta-heuristics and reinforcement learning techniques, alongside the integration of a Mixed Integer Nonlinear Program (MINLP) solver to optimally solve a simplified implementation of the problem, acting as a benchmark to demonstrate the effectiveness of the proposed techniques.

3. Thorough Evaluation of the Framework: An extensive evaluation of the proposed resource allocation solutions for an aircraft scenario and a scenario proving generalizability, is presented. A rigorous assessment provides valuable insights into the performance and adaptability of the framework in varying RAP deployment scenarios, and highlights the advantages of the proposed approaches against common scheduling approaches or a random allocation.

4.1.2 Organization

The subsequent sections of this chapter are organized as follows: Section 4.2 provides an overview of the state-of-the-art methodologies in systems deploying beamforming, in which we present the drawbacks inherent to existing strategies and how this work overcomes them. We then continue with a description of the different components of the network found in an aircraft cabin in Section 4.3. Building on this descriptions, we mathematically describe the network by providing an objective function, for which we then present three different solution methods in Section 4.4. These solutions are then assessed in Section 4.5, which also includes an envisioned practical implementation. The chapter finishes with a summary of our work, future research fields and practical implications in Section 4.6.

4.2 Related Work

Multiple publications have investigated different facets of beam allocation in networks. This section summarizes the insights and limitations identified in literature.

In [Wan+22], an adaptive beam alignment scheme for mmWave transmission for High-Speed Railways is presented. The goal of the work is to optimize the received power via Reinforcement Learning (RL) techniques to dynamically modulate the Mobile Relay's beam direction in alignment with the train's position. While this work's focus shares the transport scenario domain with our work, our goal is to optimize networks for UL and DL, over time, deployed within transportation vehicles.

The authors of [CXJ19] assume a unified antenna source for a Multi-RAT network to search for an optimal allocation of multiple RCLs within a cluster over Orthogonal Frequency-Division Multiple Access (OFDMA), thereby simplifying interference concerns. Contrarily, our approach does not require the sharing of information required for a unified antenna source, as we optimize the beam allocation based on the RCL positions, handling interference from both RCLs and RAPs while optimizing resource allocation.

The study [CF20] analyses the benefits of clustering RCLs for spectrum sharing. However, they potentially allow for unfair rate distributions as the beam allocation over time neglects the cluster density, an aspect we take into account in our optimization problem and network description.

The fairness aspect with varying cluster densities is addressed in [KWL14]. However, the work does not optimize UL and DL, whereas our work jointly optimizes for UL and DL transmissions to improve overall system capacity and efficiency.

The study [ASS19] proposes employing a narrow beam to increase the SINR and mitigate interference by designating different frequencies to spatially overlapping beams. We, on the other hand, transmit on the complete available channel bandwidth while employing wider beams. Therefore, we solve the complex problem of reducing the overlap of beams in a confined space, which results in higher spectral efficiency.

The same idea is investigated in [FSC18], where the authors also mitigate overlapping beam interference via frequency assignment. However, they disregard edge-of-sector interference, which is addressed in our work, as we reduce the inter-cell interference throughout the network, resulting in more precise resource allocation.

The objective in [SF20] is a mobility-aware subband and beam allocation for mmWave systems to maximize system throughput, ensuring an adaptive resource allocation in dynamic environments. For this, the authors formulate a mixed-integer combinatorial optimization problem. The problem is solved in two steps: first, they allocate the subband by applying a meta-heuristic (genetic algorithm (GA)) - second, they minimize the beam overlap by orthogonalization of beam width and direction. In comparison, our methodology strives to optimize the beam allocation of multiple RAPs to mitigate interference across networks while upholding link fairness.

The goal of [Ahn+22] is to maximize the time-averaged utility of RCLs given a time-averaged transmit power. The proposed solution selects the best beam out of a predefined beam set, schedules the RCLs accordingly, and finds the optimal power values in a MIMO based mmWave network. This is achieved by splitting the problem into three subproblems: the pattern selection, the RCL scheduling, and power allocation. After simplifying the mathematical description, these problems are iteratively solved. In contrast to their network utilizing mmWave with narrow beams, our system serves multiple RCLs concurrently with wider beams at lower frequencies. Moreover, while their work selects beam position from a predefined set, our approach is based on one equation describing the system to discern the optimal beam position, resulting in reduced interference in dense radio environments with multiple technologies.

The study presented in [Wu+21] applies machine learning to guide the optimal beam selection for a singular RAP, based on RCL location data. Nonetheless, this approach overlooks considerations related to multiple RCLs, multiple RAPs, and interference management — aspects we examine in our work.

The publication [RNK22] tackles the blind beam alignment challenge in multi-base-station and multi-user mmWave communications systems by using a centralized Deep Reinforcement Learning (DRL) approach. This machine learning-based solution optimizes the base station selection for an RCL and the optimal beam position predicated on the SINR. However, this work does not include Multi-RAT nor includes a fairness component to maximize the network sum rate.

The authors of [Gao+20] adopt Deep Q-Networks to jointly optimize a mmWave-based beam for the transmitter and receiver by finding the best common beamwidth and the best transmission power of the RAP to maximize the instantaneous sum rate based on information on the channel. In contrast, we fix our beam width to ensure that all RCLs are fairly served.

In [Ben+23], a novel contribution to mmWave vehicular communication is made through a learning-based approach for beam alignment, predicting the azimuth Angle of Departure from the base station to maximize signal strength. Our focus, however, is directed towards determining the best azimuth angle alongside transmission power and slot allocation.

All in all, compared to previous work, we integrate the optimization of beam angles, link directions, and power allocations for 5G and WiFi technologies across multiple RAPs within the aircraft cabin. Unlike other studies, our strategy leverages a unique antenna design and does not rely on precise channel estimates, which are a prerequisite for similar optimizations and require the immediate transmission of the channel information to a central controller. This holistic approach allows us to address the varied connectivity needs in the cabin more effectively.

4.3 System Model

In this section, we describe the system model, the underlying concepts of our network, the user devices, and the type of antennas we use to allocate different beams. In addition, we present the scenarios in which we consider to deploy our antenna and for which we later will optimize the network.

4.3.1 Wireless Devices

A Radio Transmission Point (RTP) can be an RAP or an RCL. Further, RTPs are either 5G-NR-U or Wi-Fi 6 devices. Each RCL is associated to one RAP in the network. The link between the RCL and its RAP is denoted by i, which belongs to the set of all links $\mathcal{I}$, with I denoting the total number of links. As the links in the network and the number of RCLs are the same, we use i interchangeably for RCLs and links. The association of each RCL is held in $\boldsymbol{\alpha} = [1, \ldots, \alpha_I]$. Moreover, an RAP index is denoted by a, and the total number of RAPs as A. All RCLs transmit omni-directionally, whereas, all RAPs employ BF. The beam is generated with the help of the antenna described in Section 4.3.3. For our simulations we assume a 20 MHz wide channel, resulting in a maximum achievable rate of 148.1 Mb/s for 5G and 166.6 Mb/s for WiFi per RAP, as shown with the mapping of SINR to spectral efficiencies [WLF20] [Urb19], in Table 4.1.

Table 4.1 5G and WiFi SINR mapped to Spectral Efficiency

min SINR [dB]	-∞	-6.9	-3.3	0.3	3.9	6	7.9	9.8	11.7	13.6	15.8	17.7	19.6	21.4	23.3	25.2
5G [bits/s/Hz]	0	0.152	0.377	0.877	1.477	1.914	2.406	2.731	3.322	3.902	4.523	5.115	5.555	6.227	6.914	7.406
min SINR [dB]	-∞	3	6	8	11	15	21	26	28	31	33					
WiFi [bits/s/Hz]	0	0.5	1.0	1.5	2.0	3.0	5.0	6.0	6.67	7.5	8.33					

In all our scenarios, we limit the transmission power between the minimum configurable transmission power for WiFi of 0.1 mW and the maximum allowed indoor transmission power in Europe of 100 mW.

4.3.2 Scenarios

To evaluate the efficacy and applicability of our beamforming approach, we investigate a General scenario and varying Aircraft scenarios. The General scenario is used as baseline for comparison and to show the generalizability of our proposed methodology, whereas the Aircraft scenarios serve as a demonstration of a practical implementation. All our channel models are based on the distance d between two RTPs (n, n'), calculated based on the positions $(\boldsymbol{x}_n, \boldsymbol{x}_{n'})$,

$$d_{n,n'} = \|\boldsymbol{x}_n - \boldsymbol{x}_{n'}\|_2.$$

In the General scenario, RCLs are randomly positioned across an area measuring 100 m by 200 m, while the RAPs are strategically placed at coordinates specified in Table 4.2. We model the channel, based on the work of [Alh+19], with the help of

$$\mathrm{PL}_{\mathrm{Channel}}(d) = \mathrm{PL}_0 + 20\log_{10}(d) + \mathrm{Lognormal}(\mu = 0, \sigma = 4.1)\ [\mathrm{dB}] \tag{4.1}$$

with $\mathrm{PL}_0 = 20\log_{10} 4\pi f_c/c$ being the frequency (f_c) dependent component and c the speed of light.

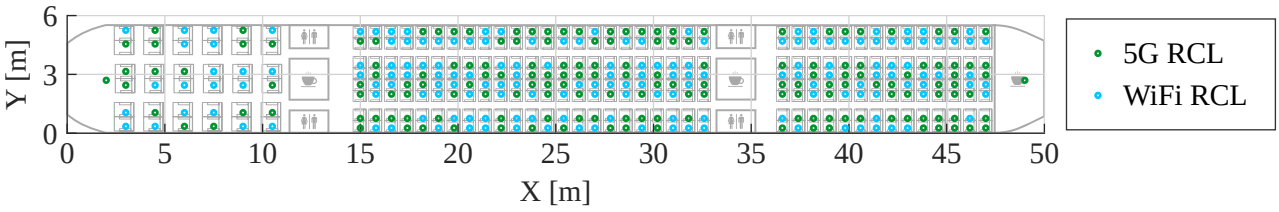

Figure 4.1 Passenger seating of the Aircraft scenario showing one distribution of RCL technologies

The Aircraft scenario is based on an airplane of type Airbus A340-300. The layout of the RCLs is illustrated in Figure 4.1. We distinguish the Aircraft scenarios by the number of RAPs deployed, and this number is annotated in the name: e.g., Aircraft-2 for 2 RAPs. The exact positions of the RAP are tabulated in Table 4.2. Compared to the General scenario, in this scenario the technology of each RCL is varied throughout the simulation runs, while the position of the RTPs remain fixed. The channel is based on the results in [MC08], and modeled by

$$\mathrm{PL}_{\mathrm{Channel}}(d) = \mathrm{PL}_0 + 26.5\log_{10}(d) + 10\log_{10}\mathrm{Rician}(\nu = 0.465, \sigma = 0.150)\ [\mathrm{dB}]. \tag{4.2}$$

Table 4.2 RAP coordinates (x,y) for the different scenarios in meters

Scenario	RAP-1	RAP-2	RAP-3	RAP-4	RAP-5	RAP-6	RAP-7	RAP-8
General	(50.0, 25.0)	(150.0, 75.0)	(50.0, 75.0)	(150.0, 25.0)	-	-	-	-
Aircraft-2	(24.0, 1.9)	(24.0, 3.7)	-	-	-	-	-	-
Aircraft-4	(12.0, 1.9)	(34.0, 3.7)	(12.0, 3.7)	(34.0, 1.9)	-	-	-	-
Aircraft-6	(1.0, 1.9)	(24.0, 3.7)	(49.0, 1.9)	(1.0, 3.7)	(24.0, 1.9)	(49.0, 3.7)	-	-
Aircraft-8	(1.0, 1.9)	(19.0, 3.7)	(29.0, 1.9)	(49.0, 3.7)	(1.0, 3.7)	(19.0, 1.9)	(29.0, 3.7)	(49.0, 1.9)

Further, we posit that all RTPs in the network operate in the 2.4 GHz band, with $f_c = 2.45$ GHz and use a signal bandwidth BW = 20 MHz. We take into account that the coherence time of all channels is 40 ms [TV05], given the low mobility scenario with a user speed of less than 0.36 m/s.

4.3.3 Antenna Array

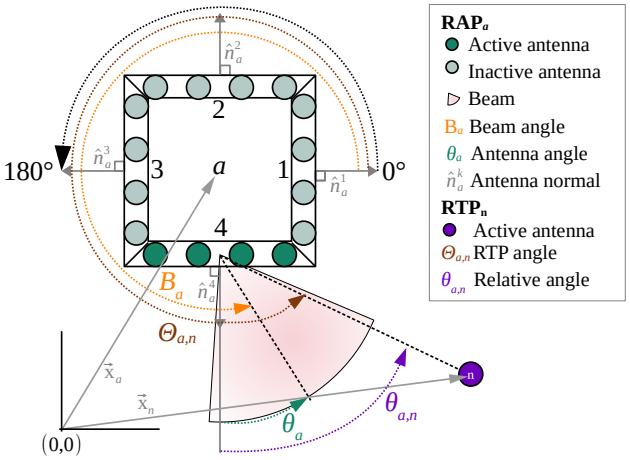

Figure 4.2 RAP Antenna Array designed for small installation spaces, e.g., an aircraft

The deployment of multi-antenna arrays necessitates a substantial installation space, a requirement often unmet in transportation scenarios, specifically in an aircraft. Given this constraint, we investigate a small antenna array. Therefore, we assume that each RAP is furnished with four antenna arrays, with each individual array composed of four sub-antenna elements. Contrary to employing Multi User MIMO (MU-MIMO) or BF on a dedicated antenna array to connect a subset of RCLs, the entire sub-antenna array is utilized to connect multiple RCLs via OFDMA. This approach results in a broader beam, compared to conventional BF, resulting in a beam width of approximately 47° at an antenna spacing of $\frac{\lambda}{2}$. The antenna arrays are positioned at 90° to each other. The antenna is depicted in Figure 4.2.

While much research focuses on optimizing signals at each antenna in an array, our approach diverges by abstracting the entire array to concentrate on the beam angle. Based on the description of the gain in BF from Section 2.2.2, the global RTP coordinates and variables need to be transformed relative to the local antenna array, in order to calculate the gain between an RAP and an RTP. The (local) antenna angle θ_a of an antenna array depends on the (global) beam angle of the RAP, b_a. θ_a is the deviation to the closest normal vector of an antenna array, as given in

$$\theta_a = b_a - \arg(\hat{n}_a^k) \tag{4.3}$$

with $\hat{n}_a^k$ being the antenna normal and $k = \left\lceil \frac{B_a}{2\pi} - \frac{\pi}{4 \cdot 2\pi} \right\rfloor$ selects the index of the closest antenna. The (local) relative angle $\theta_{a,n}$ is based on the deviation between the (global) RTP angle $\Theta_{a,n}$ and the same antenna normal, as given by

$$\theta_{a,n} = \Theta_{a,n} - \arg(\hat{n}_a^k) \tag{4.4}$$

with $\Theta_{a,n}$ being the angle between the RAP and the RTP as given by

$$\Theta_{a,n} = \arg(\boldsymbol{x}_a - \boldsymbol{x}_n)\,. \tag{4.5}$$

We define, that RTPs positioned behind an active RAP antenna array receive a gain of 0, else the gain between an RAP a and an RTP n is determined with the following set of equations:

$$g_{a,n} = \begin{cases} g(\theta_a, \theta_{a,n}) g(\theta_n, \theta_{n,a}) & \text{if } n \text{ is an RAP} \\ g(\theta_a, \theta_{a,n}) & \text{if } n \text{ is an RCL} \end{cases} \tag{4.6}$$

The gain $g()$, is based on the derivation described in Section 2.2.2, and given by

$$g(\theta_a, \theta_{a,n}) = \left| \frac{\sin\left(2\pi \left[\sin(\theta_{a,n}) - \sin(\theta_a)\right]\right)}{\sin\left(0.5\pi \left[\sin(\theta_{a,n}) - \sin(\theta_a)\right]\right)} \cos(\theta_{a,n}) \right| \tag{4.7}$$

Finally, the gain between an RCL and an RAP is calculated with $g_{n,a} = g_{a,n}$ and the gain between two RCLs is 1.

4.3.4 Link and Coverage

In all scenarios, the service of all RCLs associated to an RAP cannot be covered by the beam, due to the inherent beam width. This results in the need for beam steering. Consequently, we direct the beam towards different positions for a duration of 1 ms each, aiming to optimize coverage. The choice of a 1 ms duration is based on the common denominator for 5G — excluding 5G-URLLC — and for WiFi, which accommodates a transmission span of 1 ms across all modulation schemes. The maximum duration that an RCL can be without coverage, before being disconnected, is 400 ms in the case of 5G-NR-U (specifically for timer T300 [3GP18]), and less than 1 s for WiFi 6. Further, a 5G-NR-U RTP is only allowed to occupy the channel for up to 8 ms [3GP18], requiring a repositioning of the beam at intervals smaller than 8 ms.

All RTPs can operate in UL and DL. However, the transmit direction of the RAP defines the link direction of all its associated RCLs. We operate under the assumption that all RTPs use the same channel frequency as described in Section 4.3.2. Consequently, a link is subject to interference from every RAP operating in DL and RCLs in UL, with the sole exception of the other RCLs connected to the same RAP.

4.4 Problem Formulation and Solutions

Table 4.3 List of Notation

Notation	Description
N, n	Number of RTPs, RTP index
$\mathcal{I}, I, i$	Set of links, Number of RCLs, RCL/link indices
A, a	Number of RAPs, RAP indices
$\boldsymbol{\alpha}, \alpha_i$	Association vector and element
$\mathcal{J}_i$	Set of interfering links on link i
T, t	Total time slots, individual time slot
$\boldsymbol{L}, L_{a,t}$	Link Matrix, element for all RAPs and slots
$\boldsymbol{B}, B_{a,t}$	Beam Matrix, element for all RAPs and slots
$\boldsymbol{P}, P_{n,t}$	Power Matrix, element for all RTPs and slots
$\boldsymbol{b}, b_a$	Beam vector, beam angle of RAP a for one slot
$\boldsymbol{l}, l_a$	Link vector, link direction of RAP a for one slot
$\boldsymbol{p}, p_a$	Power vector, transmit power of RAP a for one slot
ψ	Ratio of DL to total transmission
$r_i^{\mathrm{UL}}, r_i^{\mathrm{DL}}$	UL, DL rate of link i
$r_i^{\mathrm{HUL}}, r_i^{\mathrm{HDL}}$	UL, DL penalty factors of link i
η_i	SINR of link i
$d_{n,n'}$	Distance between RTP n and n'
$h_{n,n'}$	Channel gain between RTP n and n'
$g_{n,n'}$	Gain between RTP n and n'
m_i, n_i	Helper variables to select active receiver and transmitter in a link
p_{n_i}, p_{n_j}	Transmit power of transmitter and interferer
$q_i^{\mathrm{UL}}, q_i^{\mathrm{DL}}$	Binary indicator if link i has been served
x_n, y_n	Coordinates of an RTP
o_r, o_q	Scaling factors for rate and unserved users
$R, R^{\mathrm{UL}}, R^{\mathrm{DL}}$	Network Sum Rate, Network Sum Rate in UL and DL
$F, F^{\mathrm{UL}}, F^{\mathrm{DL}}$	Fairness, Fairness for UL and DL
E	Percentage of Energy that can be saved when optimizing for power
$S, S^{\mathrm{UL}}, S^{\mathrm{DL}}$	Part of network sum rate transmitted over sidelobes, in UL and DL

In this section, we derive the problem formulation aimed at maximizing the throughput across all RCLs, whilst incorporating user fairness, for both DL and UL, and reduce the service waiting time experienced by RCLs. Table 4.3 summarizes the notation used throughout this section.

4.4.1 Optimization Problem Formulation

To delineate the network and derive a utility function for optimization, we first introduce some preliminary definitions. Let $\boldsymbol{l} = [l_1, ..., l_A]$ be the vector of binary variables that indicates the link direction with $l = 0$ representing UL and $l = 1$ DL of an RAP, $\boldsymbol{b} = [b_1, ..., b_A]$ holding the beam angle of an RAP and $\boldsymbol{p} = [p_1, ..., p_N]$ the transmission power of an RTP. Let the channel gain between two RTPs, n and n', be calculated by

$$h_{n,n'} = \mathrm{PL}_{\mathrm{Channel}}(d_{n,n'}) \,. \tag{4.8}$$

Let m_i and n_j be auxiliary variables to select the active receiver and transmitter, respectively, in a link i defined as:

$$m_i = \alpha_i(1 - l_{\alpha_i}) + i l_{\alpha_i} \tag{4.9}$$

$$n_i = \alpha_i l_{\alpha_i} + i(1 - l_{\alpha_i}). \tag{4.10}$$

Let $\mathcal{J}_i = \{i' \in \mathcal{I} \mid \alpha_{i'} \neq \alpha_i\}$ be a set of all links except the links associated to the same RAP α_i. Following these definitions, we calculate the SINR of a link i with

$$\eta_i = \frac{g_{i,\alpha_i} h_{i,\alpha_i} p_{n_i}}{\sum\limits_{j \in \mathcal{J}_i} g_{m_i,n_j} h_{m_i,n_j} p_{n_j}} \,. \tag{4.11}$$

In the next step, we convert the SINR η_i to rate r_i based on the spectral efficiency to rate mapping in Table 4.1 and correct for the number of RCLs associated to the same RAP denoted as k_i, as described in

$$r_i^{\mathrm{xL}} = f(\eta_i)\frac{\mathrm{BW}}{k_i} \,. \tag{4.12}$$

At this point we need to differentiate between the rate in UL and DL and therefore, extend the symbols with a superscript, r_i^{DL} and r_i^{UL}. To weight the DL differently from the UL we introduce a weight factor ψ in

$$\sum_{i=1}^{I} \psi r_i^{\mathrm{DL}} + (1 - \psi) r_i^{\mathrm{UL}} \,, \tag{4.13}$$

which we fix at 0.8, the average ratio of typical asymmetric DL to total traffic in the considered scenarios [YH01].

Finally, we extend (4.13), by introducing time t and a penalty factor for DL (r_i^{HDL}) and UL (r_i^{HUL}). The time component helps to assert coverage by finding the optimal beam angle, transmission power and link patterns. Based on the channel coherence time, the maximum time an RCL can be left unserved before disconnection, and the common denominator for the channel access time for both technologies, we set the time slot duration to $t = 1$ ms and the total number of time slots to $T = 40$. This adaptation requires the optimization variables to be extended by another dimension for time. So the vectors $\boldsymbol{l}^t$, $\boldsymbol{b}^t$ and $\boldsymbol{p}^t$ become matrices $\boldsymbol{L} = [\boldsymbol{l}^1, ..., \boldsymbol{l}^T]$, $\boldsymbol{B} = [\boldsymbol{b}^1, ..., \boldsymbol{b}^T]$ and $\boldsymbol{P} = [\boldsymbol{p}^1, ..., \boldsymbol{p}^T]$. The time component and the penalty factors, allows us to optimize the data rate while adopting a proportional fair metric as described by [And04] resulting in the utility function

$$\mathrm{UF}(t) = \sum_{i=1}^{I} \psi \frac{r_i^{\mathrm{DL}}(t)}{r_i^{\mathrm{HDL}}(t)} + (1 - \psi)\frac{r_i^{\mathrm{UL}}(t)}{r_i^{\mathrm{HUL}}(t)} \tag{4.14}$$

with the penalty factors based on the achieved rate of the previous time steps as described by

$$r_i^{\mathrm{HxL}}(t) = \begin{cases} 1 & \text{if } t = 1 \\ \frac{r_i^{\mathrm{HxL}}(t-1)t}{t+1} + \frac{r_i^{\mathrm{xL}}(t-1)}{t+1} & \text{if } t > 1 \end{cases} \,. \tag{4.15}$$

The value of r_i^{HxL} increases each time the link has been served. The penalty ensures that links that have already been served are penalized so that solutions benefiting different RCLs can be found. This ensures higher coverage of RCLs, a fairer rate distribution among the RCLs, disregarding channel effects, for both link directions.

Hence, the optimization problem is formulated as:

$$\max_{\mathbf{B},\mathbf{P},\mathbf{L}} \mathrm{UF}(t) \tag{4.16}$$

$$L_{a,t} \in \{0,1\} \qquad B_{a,t} \in [0, 2\pi] \qquad P_{n,t} \in [0, 20]$$

with $L_{a,t} = 1$ representing DL, $L_{a,t} = 0$ the UL, $B_{a,t}$ the beam angle and $P_{n,t}$ the transmission power of RTP in dBm. We note, that the power values obtained by the solution methods are converted to linear terms inside the optimization formulation.

4.4.2 Baseline Approaches

We investigate four basic strategies to allocate the beams and links, creating a baseline for comparison.

The *Random* allocation strategy selects an RCL arbitrarily to direct the beam towards. Subsequently, it determines, with a probability of ψ, whether to operate in DL or $(1-\psi)$ in UL, with the goal to keep the intended balance between the UL and DL rate of the network.

The *Systematic* strategy, on the other hand, also incorporates fairness by taking into account the history of the achieved rate through penalty factors r_i^{HUL} and r_i^{HDL}. In case $\psi > 0.5$, we correct the penalty factors for DL as $r_i^{\mathrm{HDL}'} = (\psi r_i^{\mathrm{HDL}})/(1-\psi)$, else we apply the correction on the UL penalty. In the next step, we steer the RAP's beam to the RCL exhibiting the smallest penalty factor among the RCLs associated to that RAP using $\arg\min_i r_i^{\mathrm{HxL}'} \mid i \in \mathcal{I}_i$ with $\mathcal{I}_i = \{i' \in \mathcal{I} \mid \alpha_i = \alpha_{i'}\}$. The RCL is then served in DL if $r^{\mathrm{HDL}'} < r^{\mathrm{HUL}'}$, else in UL. This tactic ensures preserving the DL-UL balance and that the least served RCL will be served over the 40 time slots.

The *10%* strategy, mitigates the risk that is faced by *Systematic* where a beam is perpetually fixated on one RCL. It prioritizes the rate maximization of the lowest 10% of RCLs. If $\sum_{i\in I'} r_i^{\mathrm{HUL}'} < \sum_{i\in I'} r_i^{\mathrm{HDL}'}$, the beam is oriented randomly to an RCL from the set of RCLs that satisfy the condition $r_i^{UL'} < 0.1 \max_i r_i^{UL'} \mid i \in I'$. The RCL is then served in UL. The process is analogous for DL.

The *Roundrobin* strategy iterates through all RCL of an RAP. In case $\psi > 0.5$, it starts by serving all links in DL, then transitions to UL, and reverts back to DL until the DL weight is attained.

4.4.3 Analytical Approach / MINLP Solver

Our previously derived utility function, (4.14), exhibits multiple non-linearities, e.g., the SINR to rate conversion, splitting the bandwidth among the RCLs in the beam, and the SINR itself. In addition, it includes discrete variables such as the link. We, therefore, cannot directly solve this MINLP problem in this state without simplifying it. So, we introduce the following simplifications and adaptations to render the problem solvable using Gurobi [Gur23], an optimization software.

We substitute r_i^{UL} and r_i^{DL} by the corresponding SINR η_i. However, we keep the penalty terms r_i^{HDL} and r_i^{HUL} in rate, as these are anyway constants. Moreover, to differentiate the link direction we add l_{α_i} resulting in

$$\mathrm{UF}^{\mathrm{Gurobi}}(t) = \sum_{i=1}^{I} \psi l_{\alpha_i} \frac{\eta_i}{r_i^{\mathrm{HDL}}(t)} + (1-\psi)(1-l_{\alpha_i}) \frac{\eta_i}{r_i^{HUL}(t)}. \tag{4.17}$$

Drawing from our prior observations [Man+22b], wherein the transmission power had only a small influence on the achievable rate, we fix the transmission power to 20 mW when the RCL transmits

(UL: 0) and to 100 mW when the RAP transmits (DL: 1), replacing the power terms (p_{n_i}, p_{n_j}) of η in (4.11) by

$$p_i = 20(1 - l_{\alpha_i}) + 100 l_{\alpha_i} \text{ mW}$$
$$p_j = 20(1 - l_{\alpha_j}) + 100 l_{\alpha_j} \text{ mW}$$

At this point, the gain g is dependent on the link $\boldsymbol{l} = [l_1, \ldots, l_A]$ and beam $\boldsymbol{b} = [b_1, \ldots, b_A]$ of the RAPs. To disentangle these variables, we fix the link and time slot t and optimize just for the beam. This converts our problem formulation into 2^A independent optimization problems one for each possible link vector, of which each problem comprises a summation of fractions. This allows us to employ the quadratic transform technique as proposed in [SY18], where it says that a problem characterized by the structure

$$\max_{x} \sum_{i=1}^{I} \frac{V_i(\boldsymbol{x})}{W_i(\boldsymbol{x})} \tag{4.18}$$

can be transformed to

$$\max_{\boldsymbol{x},\boldsymbol{y}} \sum_{i=1}^{I} \left(2 y_i \sqrt{V_i(\boldsymbol{x})} - y_i^2 W_i(\boldsymbol{x}) \right) \qquad | \; y_i \in \mathbb{R} \tag{4.19}$$

and that the optimal value of y, while x is treated as a constant, is

$$y_i^\star = \frac{\sqrt{V_i(\boldsymbol{x})}}{W_i(\boldsymbol{x})} \qquad \forall i = 1, \ldots, I. \tag{4.20}$$

Substituting y with $y^\star$ in (4.19) facilitates solving for x. This process is iteratively carried out until the value of x reaches convergence. Nonetheless, this method is viable only when V_i and W_i are convex functions, if not, the optimality of the solution cannot be ensured.

Mapped to our problem, the terms of the quadratic transform are $y_i = \eta_i$, $V_i = g_{i,\alpha_i} h_{i,\alpha_i} p_{n_i}$, and $W_i = \sum_{j \in \mathcal{J}_i} g_{m_i,n_j} h_{m_i,n_j} p_{n_j}$. This leads to

$$\max_{\boldsymbol{b}} \sum_{i=1}^{I} \psi l_{\alpha_i} \frac{\eta_i}{r_i^{\text{HDL}}} + (1 - \psi)(1 - l_{\alpha_i}) \frac{\eta_i}{r_i^{HUL}} \tag{4.21}$$

$$b_a \in [0, 2\pi]$$

while keeping $\boldsymbol{l}$ and $\boldsymbol{p}$ constant. Further, we approximate the non-convex beam gain $g_{n,n'}$ between two RTPs n and n' of (4.6) by a piece-wise linear version of the function. The linearization is based on (i) turning points; (ii) points which are at half the gain of the two turning points; and (iii) points of discontinuity in the original beam gain function. The introduced inaccuracies are quantified with a mean error of 0.02, standard deviation (std) of 0.086, and a median error of 0.0 in gain. After optimizing all combinations of links, we select the solution with the highest objective value. This is repeated for all $T = 40$ time slots. Notably, due to the non-convex nature and the dependency of convergence on the starting points in the search space, we introduce various criteria to either halt or re-optimize the problem. A detailed description of our approach is provided in Algorithm 1 [MVK24].

Algorithm 1 Optimization Approach for each time slot

```
results = [], qt_ctr = 0; reset_ctr = 0; ϵ = 0.001; t^max = 300 s
for each l in 2^A link combinations do
    b ← rand()                                              # Fix the starting beams
    obj_val ← 0
    # Apply quadratic transform
    while qt_ctr < 10 do                                    # Repeat up to 10 times
        Update each y_i^⋆ as in (4.20) and substitute in (4.19)
        Obtain new beam b^⋆ and objective value obj_val^⋆ by solving (4.21) transformed using (4.19)
        if b == b^⋆ or (obj_val^⋆ - obj_val) < ϵ then
        # Found optimal solution
            break
        else if reset_ctr == 3 then
        # No solution found even after restarting 3 times
            obj_val^⋆ ← −∞                                  # Impede solution selection
            break
        else if solve_time ≥ t^max and reset_ctr < 3 then
        # Time limit reached - restart and try again
            b ← rand()
            reset_ctr ← reset_ctr + 1
        else if infeasible and reset_ctr < 3 then
        # Problem is infeasible
            if qt_ctr > 0 then                              # Keep last feasible solution
                break
            else                                            # New starting beams
                b ← rand()
                reset_ctr ← reset_ctr + 1
            end if
        end if
        b ← b^⋆
        obj_val ← obj_val^⋆
    end while
    results.append(obj_val^⋆, b, l)
end for
    # Find highest objective value, keep corresponding beam and link
j ← arg max results[:][0]
b ← results[j][1]
l ← results[j][2]
```

4.4.4 Meta-Heuristics

A common strategy to find solutions to MINLP is to employ meta-heuristic solvers. Therefore, to derive a solution for our problem and to provide a comparison to our analytical solution, we employ GA [Gol89] and Sparrow Search Algorithm (SSA) [XS20].

The GA is inspired by the process of natural selection, wherein the most suitable candidate solutions from each generation are selected to reproduce and generate candidates for the subsequent generation.

The SSA draws inspiration from the behaviors of sparrows in search for food, combining individual local searches with collective global searches to traverse the solution space. The two searches enable SSA to explore (probing the expansive solution space) and exploit (fine-tuning within a promising region). This exhibits enhanced adaptability to various types of optimization problems. Specifically, the stochastic explore and exploit behavior serves as a way to avoid being stuck in local optima.

We analyze the limits of GA and SSA with and without transmission power optimization. However, to simplify the problem, we limit ourselves to the transmit power of the RAP, although the original optimization problem includes the transmit power of RCLs. We set the transmit power of the RCL $P_{i,t}$ to 13 dBm and the RAP $P_{a,t}$, when not optimized, to 20 dBm, else $P_{a,t} \in [0, 20]$ dBm.

4.4.5 Deep Reinforcement Learning

Besides the aforementioned methods, we also employ a DRL algorithm, specifically Proximal Policy Optimization (PPO) [Sch+17] from the Stable-Baselines3 library [Raf+21] version 2.0.0.

In PPO, an agent engages with an environment with the goal to execute actions that maximize a certain cumulative reward. This is done by learning on the training data set of scenarios. The challenge lies in maintaining a balance between exploration (the search for new actions) and exploitation (opting for known actions that lead to high rewards). PPO performs very well at managing high-dimensional input spaces, as those encountered in our scenarios; and is especially suited for control problems [Sch+17], in our instance, the beam alignment task. The neural networks inside PPO are employed to either predict the value of a set of actions or directly the optimal policy. In contrast to other algorithms, PPO stabilizes learning by imposing penalties on substantial policy alterations during updates, thereby ensuring a steady progression of improvement. For our problem, we define the states, actions, and reward as follows.

State space: $\mathcal{S} = \{t, 1, \ldots, A, \alpha_1, \ldots, \alpha_I, q_1^{\mathrm{UL}}, \ldots, q_I^{\mathrm{UL}}, q_1^{\mathrm{DL}}, \ldots, q_I^{\mathrm{DL}}, x_1, \ldots, x_{I+A}, y_1, \ldots, y_{I+A}\}$
The states s contain the time slot $t \in \{1, \ldots, 40\}$, the RCL association $\alpha_i \in \{1, \ldots, A\}$ and the association of each RAP to itself $a \in \{1, \ldots, A\}$, two binary variables that indicate whether an RCL has been served over the last $t-1$ slots — one for UL $q_i^{\mathrm{UL}} \in \{0, 1\}$ and one for DL $q_i^{\mathrm{DL}} \in \{0, 1\}$, and the RTP's coordinates x_n and y_n with n indicating the RTP. We normalize all states so that their values lie in the range $[0, 1]$.

Action space: $\mathcal{A} = \{l_1, \ldots, l_A, b_1, \ldots, b_A\} \qquad \mathcal{A}^{\mathrm{Power}} = \mathcal{A} \cup \{p_1, \ldots, p_A\}$
We differentiate between two action sets, one excluding the optimization of transmit power $\mathcal{A}$ and one including the transmit power for each RAP $\mathcal{A}^{\mathrm{Power}}$. The actions encompass a binary decision variable for the link direction of each RAP $l_a \in \{0, 1\}$, a discrete decision variable differentiating 720 distinct beam positions for every RAP $b_a \in [0, 720)$ and a discrete variable for 21 different power values $p_a \in [0, 20]$ representing 0 to 20 dBm.

Reward function: We define the reward based on the achieved UL and DL weighted sum-rate, penalized by subtracting the number of unserved RCLs in UL and DL. Specifically as in

$$\frac{\sum_{i=1}^{I} \psi r_i^{\mathrm{DL}} + (1-\psi) r_i^{\mathrm{UL}}}{o_{\mathrm{r}}} - \frac{\sum_{i=1}^{I} q_i^{\mathrm{DL}} + q_i^{\mathrm{UL}}}{o_q}. \tag{4.22}$$

where o_r, a factor dependent on the number of RAPs, scales the rate from 0 to 100 and $o_q = I\frac{2}{300}$ is a factor that scales unserved users. We require these scaling factors to improve the learning of the PPO algorithm.

4.4.6 Quality Metrics

Further, to compare the different proposed solutions, we define following quality metrics: The Network Sum Rate consists of the sum over the average rate of each RCL over the 40 ms. Further, we distinguish between the Network Sum Rate UL for the UL component and the Network Sum Rate DL for the DL component, with all described by

$$R^x = \sum_{i=1}^{I} \sum_{t=1}^{T} \frac{r_i^x(t)}{T}. \tag{4.23}$$

with r_i^x being either the total link rate, the link rate during the UL or the link rate during the DL. Moreover, we give the Jain fairness index [JCH+84] based on

$$F^x = \frac{\left(\frac{1}{IT} \sum_{i=1}^{I} \sum_{t=1}^{T} r_i^x(t)\right)^2}{\frac{1}{I} \sum_{i=1}^{I} \left(\frac{1}{T} \sum_{t=1}^{T} r_i^x(t)\right)^2} \tag{4.24}$$

with r_i^x being either the total link rate, the link rate for UL or the link rate for DL.

Further, we analyze the energy consumption of each RAP in the network and calculate the percentage of energy that can be saved if we optimize the transmit power compared to the usage of a fixed power value, as described in

$$E = \left(1 - \frac{\sum_{a=1}^{A}\sum_{t=1}^{T} P_{a,t} L_{a,t}}{\sum_{a=1}^{A}\sum_{t=1}^{T} P'_a L'_{a,t}}\right) 100\ \% \tag{4.25}$$

where $L'_{a,t}$ is the link direction and P'_a the constant transmission power when the network is not optimized for transmission power.

Lastly, we calculate the amount of data that is transmitted via the sidelobes of the beam. For this, we check if the RCL is inside or outside the main lobe of the beam. Therefore, the sidelobe usage is calculated as the ratio between the amount of data that is transmitted outside the main beam to the total data transmitted, as given by

$$S^x = \frac{1}{R^x T} \sum_{t=1}^{T} \sum_{i=1}^{I} r_i^x(t) \qquad \text{where } |\theta_{\alpha_i,i} - \theta_{\alpha_i}| > \frac{\text{bw}}{2} \tag{4.26}$$

with R^x being the network sum rate in either UL, DL or both directions, $r_i^x(t)$ the current link rate of RCL i for time step t in UL, DL or both directions and bw being the beamwidth.

4.4.7 Statistical Tests

In our analysis, we employ statistical t-tests to rigorously compare the outcomes of our quality metrics across different experimental conditions. The t-test [Stu08] is a statistical method used to determine if there is a significant difference between the means of two groups. It calculates a t-value, which helps to assess whether any observed differences in means are likely to occur due to chance. The significance of this difference is quantified using a p-value, which indicates the probability of observing the current results, or more extreme, under the null hypothesis that there is no true difference between the group means. A p-value below a predetermined threshold, here 0.05, suggests that the difference between the means is statistically significant, indicating that the observed effect is likely not due to random variation. In this work, unless otherwise specified, each set of results contains data from 1000 simulation iterations. In case we execute multiple t-tests on the same data-set we correct with the Bonferroni Method [Dun61]. The outcomes of these tests are annotated in our figures with the following notation:

$$\begin{aligned} \text{ns} &: p > .05 \\ * &: .01 < p <= .05 \\ ** &: .001 < p <= .01 \\ *** &: .0001 < p <= .001 \\ **** &: p <= .0001 \end{aligned}$$

4.5 Results

We first present performance results from different baseline schedulers and compare them with our analytical solution in a small scenario with 2 RAPs in an aircraft. We then present the performance of the GA and SSA meta-heuristics, including the performance impact of optimizing the transmit power. In continuation, we delve into the results of our PPO realization and give a comparison of solve

times. Finally, we analyze energy costs, spectral efficiency and sidelobe usage inside the network. The simulation parameters for the presented methods are tabulated in Table 4.4.

Table 4.4 Simulation Parameters

Parameter	Value
DL weight ψ	0.8
Number of Scenarios in the Test set	1000
Gurobi MIP Gap	5×10^{-4}
Stop criterion for qt algorithm ϵ	0.001
Run limit for Gurobi	300 s
Population size of GA/SSA	150
Maximum iterations for GA/SSA	150
Number of training epochs for PPO	100
PPO discount factor γ	0.99
Learning rate of PPO	0.0001
PPO neural network sizes	$\pi^{\text{PPO}} = [384, 384]$ $vf^{\text{PPO}} = [384, 384]$

4.5.1 Analytical Approach / MINLP Solver

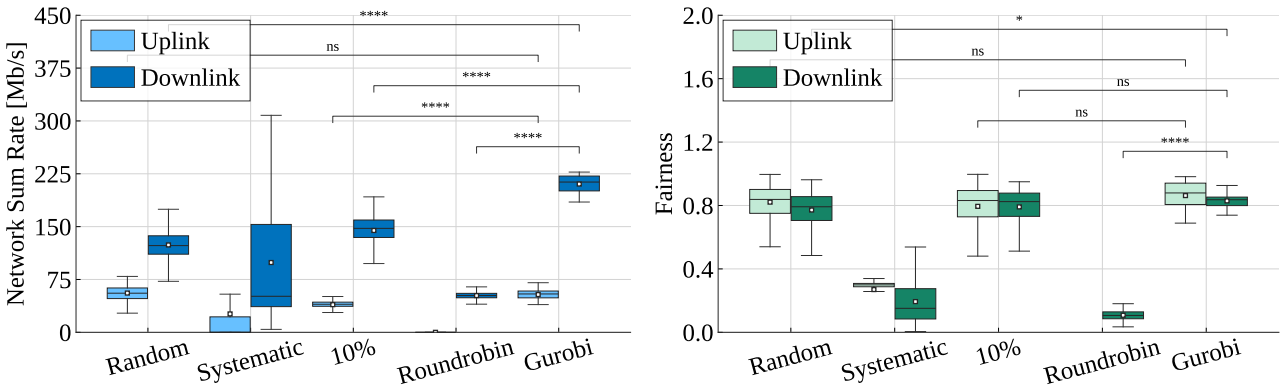

(a) Network Sum Rate

(b) Fairness

Figure 4.3 Comparison of the performance of the baseline schedulers and proposed analytical solution approach with Gurobi, evaluated in the Aircraft-2 scenario, showing the overall superiority of our proposed Gurobi-based solution.

In evaluating the efficacy of various beam allocation algorithms, we aim to not only highlight the performance disparities, as demonstrated in Figure 4.3a, but also to compare these algorithms using statistical analysis. Notably, all beam allocation algorithms, showcase better results for the DL network sum rate compared to the UL. This is a result of ψ. Further, the Systematic beam allocation algorithm displays the widest sum rate range. This is a result of its objective to continually serve the link with the lowest rate, which leads to serving more links either in DL or UL. Consequently, in a specific run, this creates either high DL and low UL values or vice versa. As a result, the distribution of residuals exhibits two maxima, violating the prerequisites of normal distribution of the data required to conduct a t-test. Coupled with the fact that it has a high number of unserved RCLs (mean: 159, std: 55.4), we exclude the Systematic algorithm from further comparisons. We also do not conduct any t-test for UL Roundrobin, as no RCL was served in UL due the number of RCLs per RAP being much larger than the available time slots, which results in UL: 0 Mb/s and a non-existent fairness. To statistically assess the differences between the mean values of the remaining algorithms' quality

metrics, we employ t-tests. This approach allows us to ascertain whether observed differences in performance are statistically significant (indicated by *) or by chance (indicated by ns), providing a robust basis to determine the best performing algorithm.

Further, as depicted in Figure 4.3b, Random, 10% and Gurobi show high fairness values, whereas Systematic and Roundrobin exhibit the lowest. For Systematic, this is due to the huge variance in rate values and for Roundrobin, as described in Section 2.2.3, this is due to the beam being stuck on an area of the aircraft resulting in the lowest network sum rate values and lowest fairness.

Overall, our proposed analytical solution solved with Gurobi, demonstrates a significant improvement in terms of network sum rate and a UL-DL relation which is closer to the set value of ψ. However, the average solving time of ca. 15 h for a single run, along with its inability to scale to scenarios with additional RAPs, makes a practical implementation infeasible.

4.5.2 Meta-heuristics

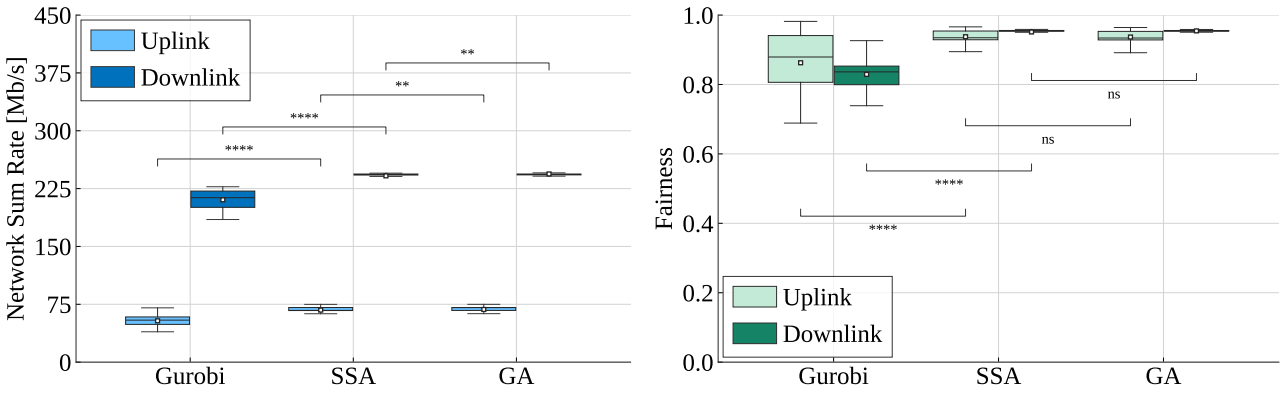

(a) Network Sum Rate **(b)** Fairness

Figure 4.4 Comparing the proposed analytical approach with the Meta-heuristics SSA and GA for the Aircraft-2 scenario.

In an effort to reduce simulation time and explore scenarios with more than two RAPs, we examined the performance of SSA and GA. The results for network sum rate in Aircraft-2 are depicted in Figure 4.4a and demonstrate a notable improvement with SSA compared to Gurobi of +14 Mb/s in UL and +32 Mb/s in DL. Comparing the two meta-heuristics, GA is able to perform statistically significantly better than SSA, but the improvement is practically negligible with +0.81 Mb/s in UL and +2.48 Mb/s in DL.

Diving into fairness, visualized in Figure 4.4b, we observe that the meta-heuristics are able to significantly outperform the Gurobi-based solution. However, in contrast to the network sum rate, no significant differences are observed among the meta-heuristics for fairness. We attribute the increase in fairness to the missing rate correction component, Equation 4.12, in the Gurobi-based solution. While the UL-DL difference in fairness for Gurobi is explained by the RCL UL rates varying less compared to DL, the difference in the meta-heuristics is due to less slots being allocated to UL not allowing the rates of each individual RCL to balance out.

Due to the slightly better results of GA in network sum rate we extend our investigation to its performance in a general and in an aircraft scenario with varying RAP count.

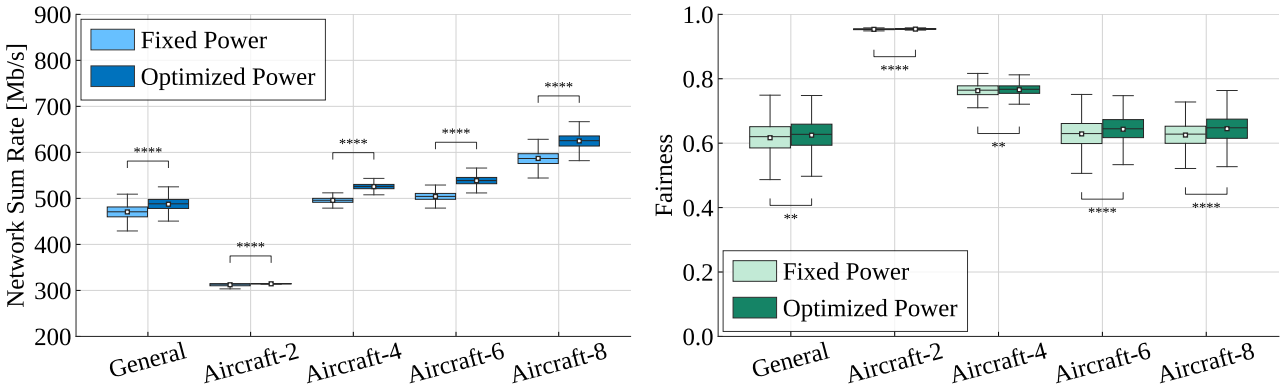

(a) Network Sum Rate **(b)** Fairness

Figure 4.5 Performance indicators of GA for different scenarios without and with optimizing the transmission power of RAPs

We hypothesize, first, that a variable RAP transmit power can enhance the sum rate within the network. The underlying rationale is that a reduction in transmit power is likely to lead to decreased interference. Indeed, we are able to confirm this, as depicted in Figure 4.5a, sum rate exhibits a significant uptick in network sum rate across all scenarios. Secondly, we hypothesize, that this effect may be more pronounced in scenarios with a larger count of RAPs. This is confirmed by the increasing difference for 2 RAPs: 2.01 Mb/s, 4 RAPs: 29.9 Mb/s, 6 RAPs: 34.4 Mb/s, and 8 RAPs: 37.9 Mb/s. However, the increase shows signs of saturation, which we attribute to the increased probability of interfering RTPs. While for two RAPs only 50% of the RTPs act as interferers, this increases to 87.5% for 8 RAPs. In addition, the RAPs' placement plays a major role. The lowest increase can be observed from Aircraft-4 to Aircraft-6. This is due to the additional RAPs' positions at the beginning and the end of the cabin. These RAPs often point their beams outwards to reduce the interference with the RAP in the center, resulting in a lower utilization of these additional RAPs.

For fairness, we hypothesize that: fairness will increase when optimizing for power. Although the reduced transmit power leads to a lower received signal strength it also reduces interference. This specifically increases the rate of RCLs, previously exhibiting a low SINR due to interference, reducing the variance in rate among all RCLs. Indeed, the fairness increases when optimized for power as depicted in Figure 4.5b. We would expect that the fairness would increase with the number of RAPs. However, the fairness decreases with the number of RAPs deployed. Similar to the saturation effect for the sum rate, the increasing number of interfering RTPs results in a larger variance in link rates, resulting in lower fairness values. However, the fairness shows a plateau for 6 and 8 RAPs around 0.6, which indicates that there is a lower limit for the fairness.

4.5.3 Deep Reinforcement Learning

Although using GA and SSA results in good network performance, we would like to improve the solving time, to enable a practical implementation. Therefore, we trained a DRL-based model with PPO to solve the problem.

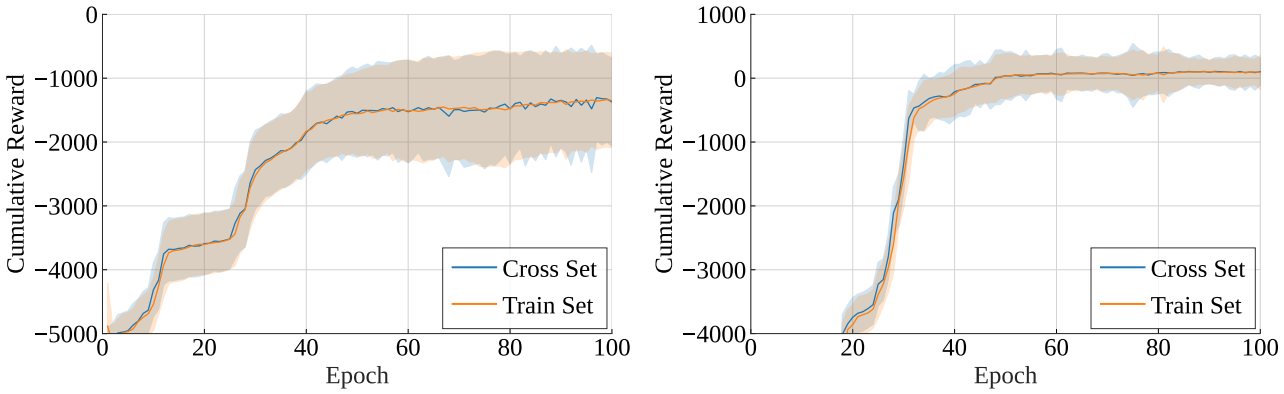

(a) General **(b)** Aircraft-8

Figure 4.6 The Cumulative Reward of the training and cross-validation data sets in the General and Aircraft-8 scenario for PPO over training epochs with the solid lines depicting the mean and the band depicting one standard deviation.

The trajectory of training performance, visualized for both scenarios as the cumulative reward in Figure 4.6, increases over the epochs and eventually reaches a plateau post the 50-epoch mark. This indicates that our proposed objective function is not only effective in aircraft scenarios but is also generalizable. Further, the trajectories underscore the efficacy of the PPO algorithm in progressively refining its policy over time, whereas the onset of the plateau signals a phase where the agent has largely assimilated a near-optimal policy tailored to the specific environment. The performance trajectory of the cross-validation set, which closely mirrors that of the training set, speaks for the model's consistency across both data sets. Interestingly, we do not see a deviation of the cross set from the train set, indicating that we have not over-trained our algorithm. We, therefore, decide to use the models from the last trained epoch for all scenarios.

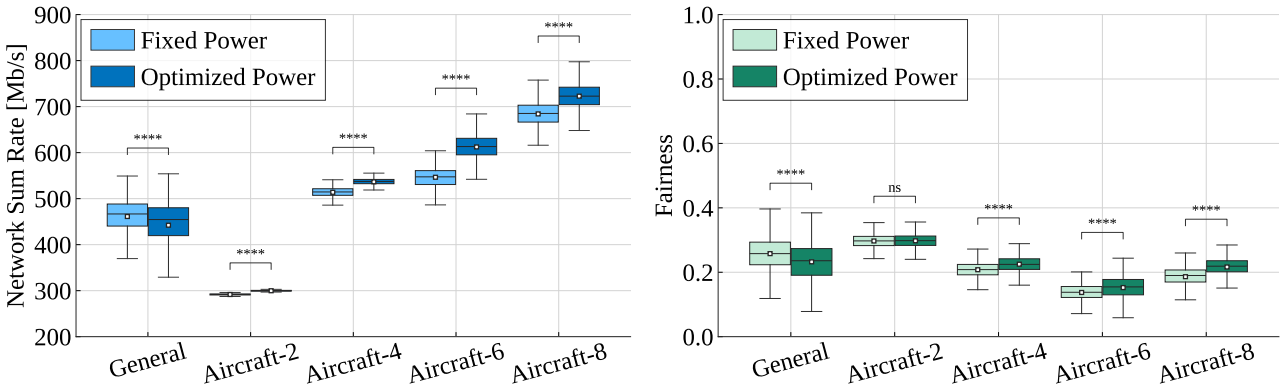

(a) Network Sum Rate **(b)** Fairness

Figure 4.7 Performance indicators of PPO for different scenarios without and with optimizing the transmission power of RAPs

Consistent with the outcomes from the meta-heuristic analysis, we note a significant increase in the network sum rate when we optimize for RAP transmit power, as illustrated in Figure 4.7a, with the exception of the General scenario. We attribute this exception to the larger distances between the RTPs, for which we anyway require higher transmission powers, resulting in a complex scenario for the DRL algorithm, which tries to optimize the power resulting in lower received power values, reducing the SINR and therefore a lower rate. Further, like GA, the small sum rate difference between Aircraft-4 and Aircraft-6 can be attributed to the same RAPs. However, this time their beams point mostly inward to the cabin, increasing the interference and limiting the RAP rates.

Continuing with the aspect of fairness, we observe again the similar trends as depicted in Figure 4.7b. While an optimized power benefits the fairness for most Aircraft scenarios, we cannot generalize this to other scenarios. The decline in fairness over the increasing number of RAPs with the dip for Aircraft-6 is attributable to the positioning of the 6 RAPs. Here, the RAPs in the center of the cabin serve the highest number of RCLs resulting in a large variance in rates provided between the RAPs and therefore the lowest fairness.

In general, we are able to see the same trends, when comparing Figure 4.4 and Figure 4.7, for an increasing number of RAPs the network sum rate increases for GA and PPO. However, comparing PPO and GA for the same number of deployed RAPs, PPO demonstrates a higher network sum rate compared to GA. This is due to a higher rate for specific RCL, which results in a larger variance in rate among all RCLs and in consequence lower fairness values for PPO compared to GA. We attribute this behavior to the fact that the meta-heuristics find, for each slot and scenario, the best solution, whereas the PPO generalizes the information that it acquired during the training with other network configurations.

4.5.4 First Served Slot, Spectral Efficiency, Energy Saving and Sidelobe Usage

We further compare the performance of GA and PPO for the first slot in which an RCL was served within the 40 slots, the spectral efficiency of the RAPs, the energy saving potential, and the sidelobe usage.

For specific applications, a low reaction time of the network is important. We, therefore, visualize in Figure 4.8a the distribution of the first served slot for the RCLs. A value of 0 indicates that the RCL was unserved, and 1 to 40 the time slot in which they were served. We observe that GA takes fewer slots to completely serve all RCLs. However, PPO has a higher probability to serve more RCLs in the first few slots. This can be explained by the fact that PPO considers future rewards, allowing it to serve an RCL at a later time slot to maximize the reward at the current time slot. GA, on the other hand, always optimizes the current time slot, and will, therefore, serve all RCLs in an earlier stage.

Based on the results of the network sum rate we expect the spectral efficiency to decline with increasing numbers of RAPs deployed, which we confirm by the visualization in Figure 4.8b. This further reveals a large spread in spectral efficiency over the RAPs compared to the network sum rate. The figure also shows that deploying additional RAPs results in a complete change of spectral efficiency throughout the RAPs. While the large range of efficiency for GA in Aircraft-6 and Aircraft-8 are due to the RAPs positioned at the beginning and end of the cabin, this is not the case for PPO. For PPO, this is due to the RAPs at the edge pointing their beam inwards, and therefore causing a different interference pattern. This is then partially compensated by optimizing the transmit power and resulted in higher rates.

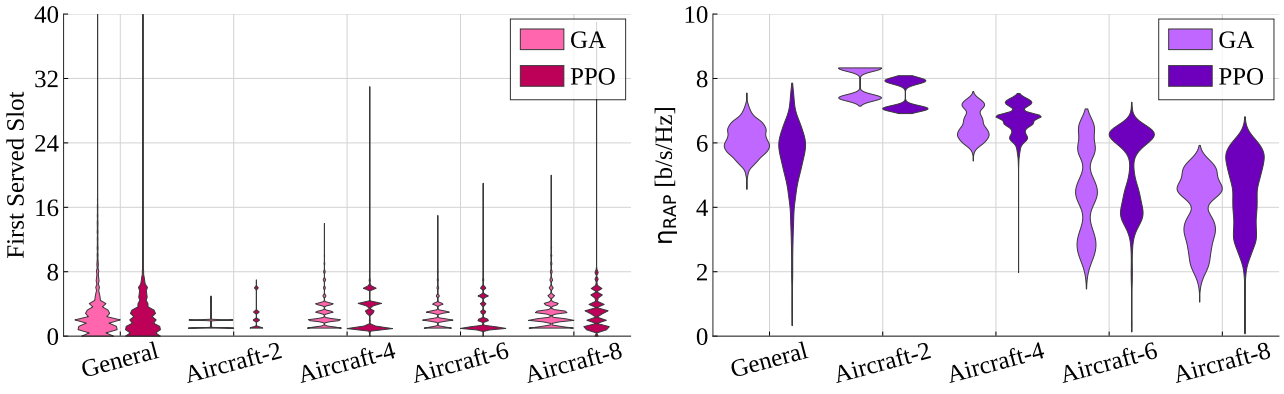

(a) First Served Slot of RCLs

(b) Spectral Efficiency of RAPs

Figure 4.8 First Served Slot for RCLs and Spectral efficiency for each RAP when optimizing transmit power

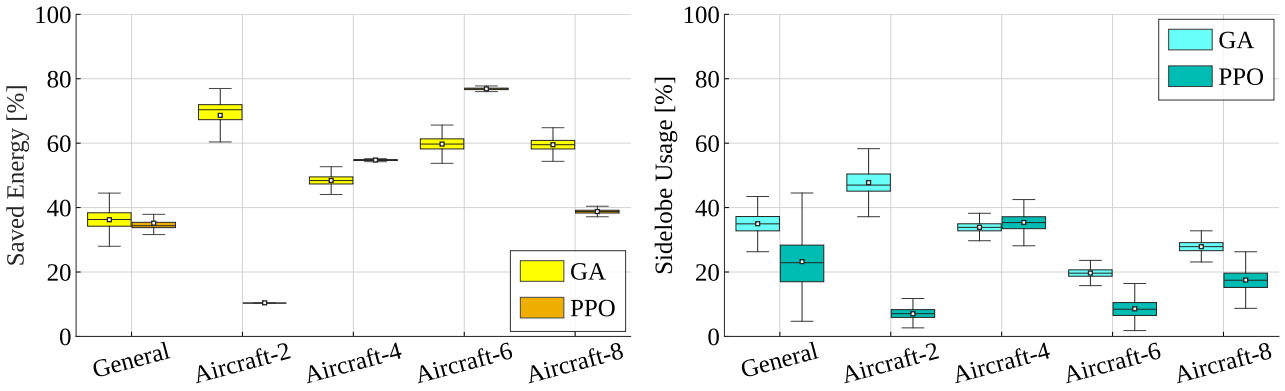

(a) Energy Saved

(b) Sidelobe Usage

Figure 4.9 Saved Energy and Sidelobe Usage for GA and PPO when transmission power for RAPs is optimized

Diving into the energy consumption, while optimizing power, GA is able to save ca. 60% of energy through all Aircraft scenarios as depicted in Figure 4.9a. But, we observe a different trend for PPO, where the range goes from 10% with Aircraft-2 to up to 80% in Aircraft-6. However, as this is the typical configuration of RAPs for these aircrafts this is not problematic. PPO, by introducing the option of adapting the transmit power, moves the beam less in all scenarios and compensates the resulting higher interference by reducing the transmit power. However, in Aircraft-2 this is not necessary as the beams barely overlap and it exhibits the lowest number of interferers. This, in combination with a reward function excluding a power minimization term, results in Aircraft-2 displaying the lowest energy saving. Nevertheless, these are good results given that the objective lacked any energy saving specific terms. A detailed analysis of the data also reveals that the transmission power in GA varied more compared to PPO. Again, we attribute this to the fact that GA optimizes the actual scenario under test whereas PPO transfers previously acquired knowledge through the training process.

Interestingly, between 10% to 50% of the data is transmitted via the sidelobes of the beam, as depicted in Figure 4.9b. This is undesirable in other beam optimization techniques, as it is viewed as a cause of interference. Nevertheless, in this work we are able to benefit from it.

4.5.5 Solve time

A comprehensive summary of the solving times across all solution methodologies is presented in Table 4.5.

Table 4.5 Duration of different solution techniques to solve the optimization problem for $T = 40$ slots given in seconds

	Gurobi		GA		SSA		PPO	
	Mean	STD	Mean	STD	Mean	STD	Mean	STD
General	-	-	232	16.4	198	16.6	0.089	0.009
Aircraft-2	55933	6200	461	41.7	493	52.7	0.056	0.001
Aircraft-4	-	-	619	78.6	630	104.0	0.089	0.002
Aircraft-6	-	-	625	46.3	762	76.2	0.124	0.011
Aircraft-8	-	-	1296	67.5	1346	113.0	0.157	0.003

The data shows Gurobi's limited performance in scalability and solve time. However, as shown in previous research [MVK24], in small transportation scenarios, Gurobi renders solutions that allow a better performance than the presented baseline algorithms. On the other hand, GA and SSA, solve all scenarios and exhibit fast solving times. But, these increase with the scenario complexity,

showing a stronger increase with every additional RAP. While the solving times of both meta-heuristics for up to 4 RAPs are relatively similar, they start to diverge for more RAPs, showing a slight superiority of GA over SSA. Whereas, this is not the case for PPO, which exhibits the lowest mean and std accentuating its superior efficiency, scalability, and consistency in solving times across varying scenario complexities.

4.5.6 Deployment Vision

In the previous section, we showed the benefit of optimizing the beam pattern to improve the network sum rate, fairness among RCLs, and serve them. However, this solution requires an orchestrator which assigns beam angles, link direction and transmission powers to the different RAPs in the network. For this, we propose a central controller which coordinates these RAP properties. The central controller receives the positions and channel conditions of the RCLs from the RAPs they are connected to. This data is used to build a digital twin of the environment, which is used to train the PPO algorithm. The training is required to ensure fairness and to maximize sum rate in real-world applications. After the training phase, the controller is integrated into the network. Here it constantly receives the RCL positions and assigns the most efficient beam, link and power configuration to the RAPs. The required bandwidth to operate the controller is estimated based on the assumption that we require a resolution of 32 bits per RCL position, $32 \cdot I$ b/s, in the direction to the controller. In the direction towards the RAPs, we send $\log_2(20)$ bits for power, $\log_2(720)$ bits for the beam angle and 1 bit for the link direction per RAP, which accumulates to ca. $10 \cdot A$ kb/s.

4.6 Summary and Conclusion

In this chapter, we have described a comprehensive framework to solve the problem of optimizing a beamformed Multi-RAT multi-RAP network. First, we described the antenna we use for BF, we defined how RCLs and RAPs communicate and gave a mathematical formulation for the network. We then reduced the complexity of the MINLP by replacing parts of the formulation (e.g., bandwidth sharing, SINR rate mapping), provided a linear approximation of the gain between two RTPs, and solved the problem with our proposed algorithm integrating the quadratic transform. We demonstrated the superiority of this solution by showing an increase of 143% in network sum rate and an elevation in fairness from 0.83 to 0.87, surpassing the performance of the leading scheduler in these aspects, while also discussing its limitations in solve time and scalability. We overcame these limitations by applying two meta-heuristics (SSA and GA), which reduced the solving time by a factor of ca. 120, and demonstrated that we are able to further improve on network sum rate by up to 6.8% and fairness by up to 3.2% when also optimizing transmit power. Given the marginally superior performance of GA compared to SSA, GA became our new baseline for subsequent comparisons. To expedite solving times significantly, we utilized PPO, a DRL algorithm, successfully reducing solving times from minutes to milliseconds and increasing the network sum rate at the cost of fairness. We further showed GA and PPO's are able to reduce energy consumption in the network by ca. 77% and 71% respectively, that the spectral efficiency reduces with increasing RAP count and that including sidelobes of a beam as a form of transmitting data benefit contribute to the network capacity. Finally, we conclude that PPO is the best option for an implementation in a central controller to orchestrate the RAPs, improving the network sum rate, adhering to fairness and saving energy while minimizing the number of unserved RCLs.

This framework can be used as a base to investigate the performance of a Multi-RAT network for different Aircrafts, by simply substituting the channel model to the one of interest. Further, the gain description of the antenna can be replaced by other radiation patterns. This allows, to test the efficacy of different antenna arrays. Moreover, one can obtain an insight on how much traffic could be transmitted over the sidelobes, and use this information to optimize for the interference suppression

of the sidelobes. Moreover, this framework can be used as a base for a digital twin, and allows the comparison of various DRL algorithms.

In a future work, we could aim to increase the fairness in our machine learning algorithm by tweaking the reward function. We would also include a penalty for energy to further reduce the energy cost. We further would like to compare different antenna technologies, as these could help reduce interference and increase our quality metrics. A deeper investigation into the implications, benefits, and challenges associated with sidelobe utilization for data transmission could be highly beneficial.

Overall, our contributions in this chapter lay the foundation for a comprehensive understanding of the expected potential of beamforming in modern aircraft cabins, enabling a better design and optimization of wireless networks in such environments.

Chapter 5

Service Placement and Routing in Aerial-Aided Multi-Access Edge Computing Networks

Following the optimization of aircraft cabin communication at the link levels, our attention shifts towards integrating the aircraft cabin with a global network, thereby facilitating the introduction of novel services. This chapter presents the development of an Aerial-Aided Multi-Access Edge Computing (AA-MEC) architecture aimed at significantly improving the passenger experience by upgrading In-Flight Entertainment and Connectivity Service (IFECS). Moreover, it provides airlines with an innovative revenue opportunity by offering computational resources to satellites. The content of this chapter is based on the journal publication [Man+22a].

5.1 Introduction

Multi-Layer Network (MLN) have been proposed to increase the capacity, the user experienced data rate, and energy efficiency, and supports a higher node density while decreasing the latency [Liu+18]. MLN that combine terrestrial, aerial and satellite layers achieve this by harnessing the benefits and compensating for the deficits of each of these network layers. This opens up new possibilities, such as using aircraft as potential Multi-Access Edge Computing (MEC) nodes, in addition to the ones deployed at the satellite gateways, creating an AA-MEC network. This approach spreads processing and storage capabilities across the network, enhancing both ubiquitous and edge computing.

Gateway MEC servers for satellite constellations have fixed positions and cover just specific regions. These limitations could be overcome by strategically placing Aerial Multi-Access Edge Computing (A-MEC) servers at the cost of adding dynamicity to the network. By examining different MEC deployment algorithms, we can analyze the key factors influencing the network quality metrics and understand how the dynamic positioning of MEC servers impacts network efficiency.

This AA-MEC network facilitates applications such as IFECS - by offering storage for video streaming services, access to mirrored websites or even game servers - and Satellites Offloading Computational Tasks (SOCKS) - by bringing computing resources nearer to satellites allowing them to offload computational tasks, e.g., for AI. However, these services exhibit a maximum delay in which they have to be served. Therefore, it is necessary to optimally route these services throughout the network to the best MEC destinations. In this context, we distinguish two goals, minimizing latency and minimizing energy consumption, while a reduced latency benefits, e.g., the ping in online gaming or fills streaming buffers faster, minimizing the energy required reduces the cost of operating the network and is more sustainable.

An MLN faces challenges due to the mobility of nodes like satellites and aircrafts, leading to a constantly evolving network topology. This dynamic nature complicates routing, task placement, and maintaining Quality of Service (QoS), especially latency. Static routing and MEC destination selections become ineffective in such an environment. Therefore, a dynamic approach is essential for optimizing routing and placement to maintain network performance. This requires to find an

optimization frequency for the network to balance route stability with the dynamic movement of the nodes.

5.1.1 Key contributions

In this chapter, we present an MLN, as it could be operated by a major airline and satellite operator with the goal to minimize service latency and energy consumption. For this a subset of the operated aircrafts serve as computing entities for other components in the satellite and aerial layer. This work is based on the journal publication [Man+22a].

The main contributions are as follows:

1. Development of an Optimization Framework: The work introduces an AA-MEC architecture, featuring a tri-layered structure: a satellite layer composed of Low Earth Orbiting (LEO) satellites, an aerial layer including commercial aircraft from an airline, and a terrestrial layer comprising gateways. Both gateways and aircraft are capable of hosting MEC servers. All nodes are able to communicate with each other based on inter node specific channel models, allowing inter-layer communication and creating a comprehensive three-dimensional network.

2. Multiple Objective Formulations: A formulation is provided to minimize the summed latency for all services in the network. The formulation complexity is reduced, allowing a faster solving time of the problem without compromising solution quality. In addition, a formulation to minimize energy consumption in the network is provided. All formulations consider the dynamicity of the nodes in the different layers of the network resulting in an optimal route and destination throughout the simulated operation of the network.

3. Use cases: Two primary use cases are presented: IFECS, focusing on applying the objectives for passenger-centric services requiring an airborne internet connection, and SOCKS, which centers on offloading computational tasks from satellites.

4. Thorough Evaluation of the Framework: An extensive evaluation of the proposed AA-MEC is given. The work compares the performance gain to State of the Art solutions [Var+19], with MEC servers solely found at gateways. Further, the influence of all objectives on different network quality metrics are investigated. Finally, the work provides recommendations on when to apply each objective and outlines the desired characteristics of aircraft equipped with MEC servers.

5.1.2 Organization

The remainder of this chapter is structured as follows. We continue with an in-depth review of the relevant literature in Section 5.2. The system's architecture is detailed in Section 5.3, while Section 5.4 outlines the formulation of the optimization problems. Key results of the study are showcased in Section 5.5, and a discussion on the implications of the AA-MEC is provided in Section 5.6.

5.2 Related work

The state of the art relevant to our proposed solution draws from three primary domains: Services for Aircraft, Computational Task Offloading in Aerial enabled Networks, and MLNs Architectures.

5.2.1 Services for Aircrafts

The consideration of aircraft as sources of service requests in MLNs is a relatively underexplored area in the literature, which often focuses on ground users [Che+17; Pac+21]. The rising demand for airborne internet, however, underscores the importance of addressing the unique challenges

associated with aircraft as sources of service requests. These challenges are primarily due to the high velocities of aircraft, leading to swift alterations in both network topology and channel conditions.

In the study [Med+10], an innovative approach to an aerial mesh network is presented, wherein the network is tailored to support airborne internet services. In this model, content requested by aircraft is initially transmitted from a satellite gateway located on the ground to the nearest aircraft. Subsequently, this content is relayed to other aircraft via a multi-hop network in the sky. Such a method of optimized routing significantly diminishes latency because aircraft function as efficient relays for transferring content from ground stations.

In a different approach, [Che+21c] investigates a scenario where content is cached both on the ground and aboard aircraft, coupled with the creation of inter-aircraft communication links. To navigate the intricacies of this more complex routing, they employ a Reinforcement Learning (RL) algorithm aimed at enhancing the network's energy efficiency. However, their methodology does not take into account the latency demands crucial for QoS, a significant oversight considering the potential need for latency-sensitive applications by aircraft passengers. Additionally, the dynamic nature of aerial links, which could lead to frequent disconnections and escalating latency, is not factored into their model. Our research fills this gap by dynamically optimizing MEC destinations for service deployment, while also ensuring adherence to latency constraints.

Building on these concepts, [Var+19] explores the provision of airborne internet within the framework of a European Space-Air-Ground-Integrated Network, placing a particular emphasis on latency considerations. In their setup, services are stationed in ground-based data centers. Their comparative analysis of different optimization algorithms, focusing on aspects such as routing, service placement, and migration, is instrumental in our evaluation of our model's efficacy. By drawing on their insights, we aim to advance the understanding of service delivery optimization in MLNs, especially in scenarios involving high-speed aircraft. In contrast, our strategy involves deploying MEC servers directly on aircraft, optimizing for latency and energy reduction rather than abstract cost metrics. In addition, our model details access mechanisms with greater precision, incorporating real satellite trajectories and all flights of a globally operating airline instead of just a regional focus.

5.2.2 Computational Task Offloading

The rise of processing-intensive applications, particularly in AI/ML domains, Tasks offloaded from IoT devices to satellites, accentuates the significance of computational offloading. To address this, various studies have explored offloading schemes in MEC. Surveys like [Pha+20] offer a comprehensive overview of MEC in 5G and beyond networks. Our focus, however, is on summarizing works that directly relate to implementing MEC in aerial networks or MLNs, as these are more tailored to our proposed concept.

In [Wan+18], MEC nodes are deployed within satellite and terrestrial networks. This setup examines how satellite MEC servers assist ground servers by processing tasks once terrestrial capacities are exceeded. The authors propose an algorithm to optimize energy usage and reduce latency by assigning computational tasks at minimal cost. Similarly, [ZZT19] suggests an architecture where MEC services are delivered via satellite links, adaptable to various scenarios and server locations. Nonetheless, these studies do not account for the complexities introduced by high-speed aerial MEC nodes, which could further reduce latency by dynamically assigning the task to a MEC server near a task source. Our research addresses this gap, offering MEC services with minimal latency and without considering satellite based MEC deployment due to its inherent latency and computational limitations.

[Che+19] introduces aerial MEC nodes in a network comprising a LEO constellation, Unmanned Aerial Vehicles (UAVs), and Internet of Things (IoT) devices. Here, UAVs serve as flying MEC servers, and a task scheduling mechanism for this architecture is developed using reinforcement learning. However, this study overlooks the interactions between terrestrial gateways and aircraft and limits aerial nodes to computational roles, excluding them as destinations for content requests, a scenario we incorporate in our approach.

The authors in [Yu+21] propose an MLN MEC network, integrating content sharing across satellite, aircraft, and terrestrial layers with servers. While they introduce a deep imitation learning-driven algorithm for offloading and caching, their model lacks task requests originating from non-terrestrial layers, an aspect gaining importance with the increasing offer of internet services on aircraft in aerial environments.

Distinct from the aforementioned studies, our work not only extends MEC capabilities to aircraft, thus positioning computational resources and content services in closer proximity to airborne request origins but also accommodates network dynamicity. We achieve this by implementing a re-configurable optimization strategy for selecting offloading task destinations.

5.2.3 Architecture

The conception of an optimal MLN architecture is vital for supporting latency-critical applications and a comprehensive network that accommodates aerial use cases. Inmarsat ORCHESTRA [Sat] proposes a dynamic, multi-layered network architecture, integrating satellite and terrestrial layers to support 5G. Their aim is to achieve global network coverage for mobile nodes, enabling novel applications such as Smart Ships and Urban Air Mobility connectivity. However, this concept primarily focuses on connectivity, overlooking the potential of network elements as computational entities and omitting an aerial layer in its architecture. Additionally, even within their two-layer network, there is room for optimization, particularly in terms of latency.

The authors in [Che+21a] focus on optimizing terrestrial gateway placements for SpaceX's Starlink constellation. They consider latency, node load, and load balancing among gateways, applying a genetic algorithm to determine optimal placements. Yet, such optimization is constrained by political and economic factors influencing gateway locations. Networks with fixed gateway positions and an additional aerial layer containing MEC servers, like ours, present a more complex optimization challenge and more realistic deployment solutions.

The aerial layer in an MLN could comprise dynamic aircraft or UAVs. While substantial research, such as [Pan+21a], has explored using UAVs for communication and optimizing these networks for various objectives (e.g., security), our focus diverges. We consider nodes in the aerial layer as potential MEC destinations or sources of content requests, optimizing an aerial MEC-enabled network to minimize latency. Unlike [Pan+21a] and [Pan+21b], which focus on UAV trajectory optimization, our architecture involves commercial aircraft with predetermined paths, not subject to our optimization. These studies also employ Intelligent Reflecting Surface (IRS) for communication optimization, whereas our work aims to minimize latency in an AA-MEC network without incorporating IRS.

In [Qin+21], an aerial layer with short-range UAVs, along with a terrestrial layer of users and base stations, is introduced. Users can offload computational tasks to MEC servers on base stations or aerial servers. However, the growing use of AI/ML applications on satellites, resulting in computationally intensive tasks, necessitates considering a satellite layer in MLNs. The authors optimize for energy consumption and task placement but do not guarantee maximum latency for offloaded tasks. They also exclude tasks originating within the aerial layer, which could be served by other aerial nodes, thus missing the opportunity to address a highly dynamic network topology.

Our MLN includes an aerial and a satellite layer as sources for content and task requests, reflecting the increasing demand for web services and complex applications in aerial environments. The problems that arise through the high dynamicity of the network, are solved by our re-configurable optimizations, which optimize not only for latency but also for energy consumption, providing QoS assurances by guaranteeing maximum delays for data packets and prepare the network for the 6G goal of energy efficiency.

5.3 System Model and Use Cases

To analyze the benefits of MEC server deployments on aircrafts we design an AA-MEC topology as depicted in Figure 5.1.

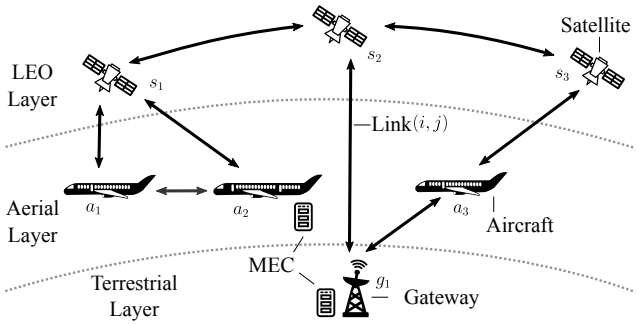

Figure 5.1 Designed Multi-Layer Network Architecture

In this topology, the satellites facilitate communication with both terrestrial gateways and aircraft in the aerial layer. The satellites also act as sources of computational tasks. Whereas the aircraft in the aerial layer are either sources of service requests or carry MEC servers with computing capability to process satellite offloaded tasks or specific service requests. All nodes in these two layers are able to route traffic to all node types. Terrestrial nodes, maintain communication channels with both satellite and aerial layer nodes and always contain a MEC server. A detailed description on how the access between two nodes in the network is established, based on the physical position and the angle between the nodes, is explained in Section 2.3.4. In total, our network encompasses 80 Iridium Next satellites, 328 aircraft, and 4 Iridium terrestrial gateways. The flight data of the satellites was obtained with [Kel]. Whereas the flight data for the aircraft was obtained by monitoring the Lufthansa fleet for the 21st of November 2023.

In the following, we describe the channel model used for the links, go into more detail of the use cases and describe the different types of MEC server deployment among the aircraft.

5.3.1 Channel Model

Details of the channel model are elaborated in Section 2.3.5. Properties of the channel specific to each link type are outlined in Table 5.1. Each link type exhibits a targeted link capacity and a maximum supported transmission power. These properties are designed such that most of the links in the network have values close to these targets. The frequencies are selected based to ensure minimal dampening in the transmission medium. The bandwidth, antenna gain and loss, as the number of Multiple Input Multiple Output (MIMO) antennas are configured to result in the targeted capacities. The specific values are based on [DCC19; Kal+19; Num+22; BS15; ETS12].

Table 5.1 Link properties in an Aerial Aided Network

Link	Capacity [Mb/s]	Power [W]	Frequency [GHz]	Bandwidth [MHz]	Antenna [dBi]	Loss [dB]	MIMO Antennas
Gateway ↔ Satellite	1300	400	28.5	155	60	0	1
Gateway ↔ Aircraft	300	20	2.0	20	31.8	0	2
Satellite ↔ Satellite	5000	400	30.0	250	60	0	2
Aircraft ↔ Aircraft	300	10	14.0	100	40	0	4
Satellite ↔ Aircraft	550	10	2.0	125	37.7	2	4

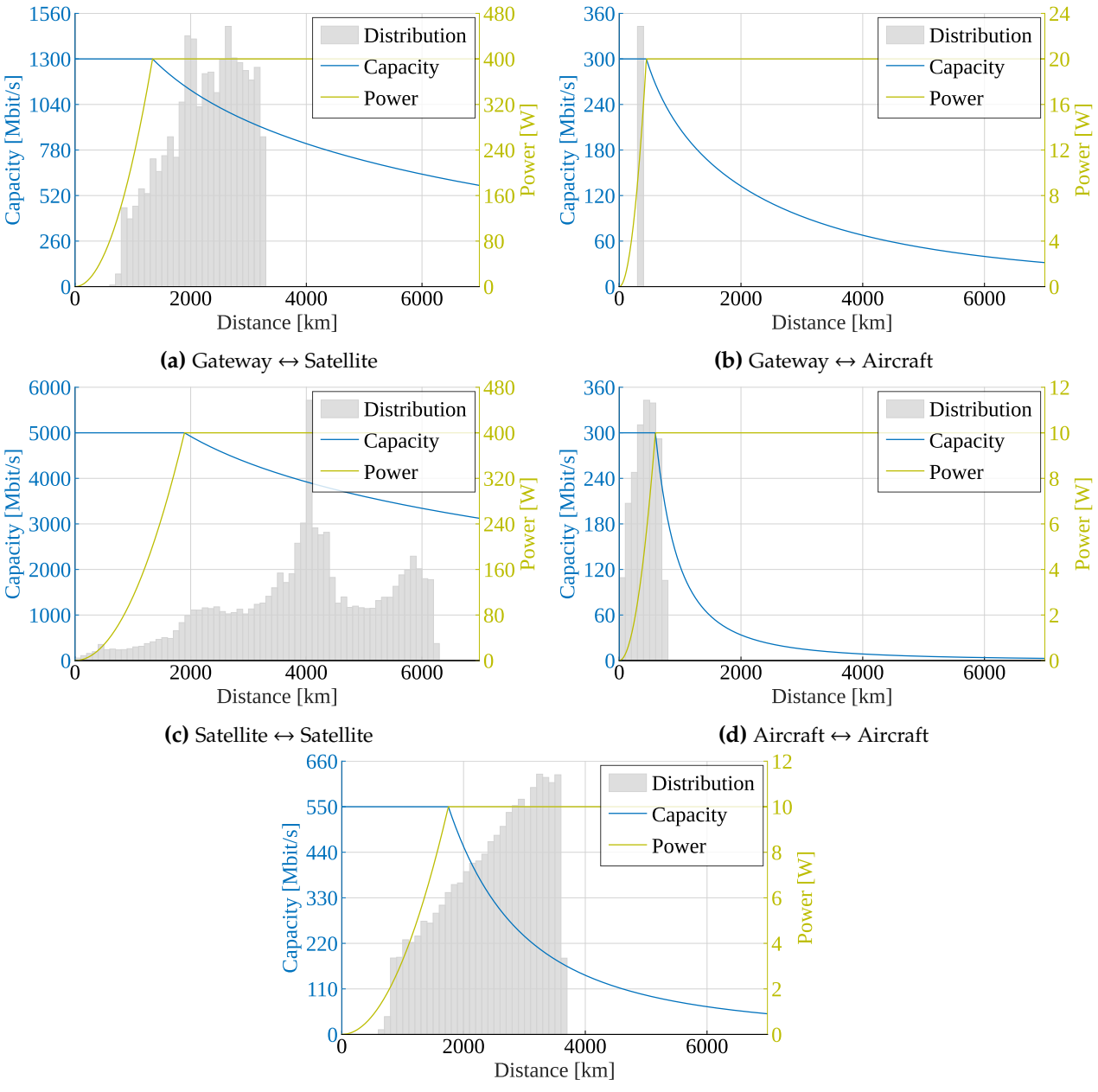

(a) Gateway ↔ Satellite

(b) Gateway ↔ Aircraft

(c) Satellite ↔ Satellite

(d) Aircraft ↔ Aircraft

(e) Satellite ↔ Aircraft

Figure 5.2 Distribution of distances, and the capacity and transmission power depending on distance for each link type found in the simulation.

To provide a clear understanding of the interactions between the link distances, channel capacities, and required transmit power for each type of link in our simulations we present Figure 5.2. Each

link type exhibits a unique range of distances and distribution of these. Specifically, inter-aircraft links are the shortest within the network, as indicated by the gray histogram in Figure 5.2d, with the exception of the aircraft-gateway links. This is due to only one flight route passing near enough to a gateway. The abrupt cutoff of the histogram for larger distances in gateway-satellite and satellite-aircraft links is due to the loss of Line-of-Sight (LoS) as described in Section 2.3.4. The figure further shows a trade-off between the achievable capacity and the required transmit power. This allows to either select links with a lower power to save energy while using the full capacity of the link, or to reduce the capacity and transmit over longer distances at maximum transmit power. The system is strategically designed such that the maximum transmission power and channel capacity align with the most common link distances, which we can visually confirm for aircraft links. However, in case of satellite links an alignment would not bring a benefit, as it would introduce additional interference to other nodes due to the larger communication range. The highest power consumption occurs in inter-satellite links, which also boast the highest capacity. While inter-aircraft capacity is limited, it is notably energy-efficient due to regulatory limitations in transmission power.

5.3.2 Use Cases

A key requirement in a MEC network is to minimize the user-perceived latency. This study aims to find the effects of the proposed multi-layer architecture on the user-perceived latency for the use cases of airborne internet and computational offloading.

Table 5.2 Services provided through airborne internet [ETS16; STV15; GB18]

Use Case	Service Type k	Bandwidth C^k_{BW} [kb/s]	Delay Req. τ^k [ms]	Utilization Ratio γ^k [%]	Packet Size P^k [Byte]	Computational Req. O^k [Instruction]
IFECS	*Games*	50	60	4	24	-
	VoIP	64	100	15	829	-
	Web	100	500	14	933	-
	Streaming	1500	300	67	1378	-
SOCKS	*Tasks*	1600	5000	-	1378	2.5e9

5.3.2.1 Airborne Internet

Airborne internet connectivity allows critical information, such as weather, flight altitudes and landing conditions to be exchanged. Besides, it enables passengers to receive web services such as messaging services, web-surfing, gaming, Voice over Internet Protocol (VoIP), video and music streaming, etc. The main obstacle to airborne connectivity is the lack of communication infrastructure, especially while flying over regions such as deserts, the poles and large bodies of water. In such cases, the connectivity is traditionally provided by satellites, which results in high latency. This is also the case if a LEO constellation is used. Aerial MEC nodes and Direct Air-to-Ground (DA2G) can alleviate this problem, especially in time-sensitive services. An overview of the service requirements can be found in Table 5.2. However, not all passengers engage with services from the IFECS that necessitate an internet connection, as airlines provide alternatives such as proprietary reading materials or a selection of films. It is estimated that approximately α=20% of passengers will utilize internet-requiring services [Var+19]. Consequently, we compute the traffic generated by each service by multiplying the number of passengers $n^{\text{Passenger}}$ on the specific aircraft by the given bandwidth C^k_{BW} and the utilization ratio γ^k to obtain the generated traffic $D_{v^k_n}$.

$$D_{v^k_n} = n^{\text{Passenger}} \alpha \gamma^k C^k_{\text{BW}} \tag{5.1}$$

Subsequently, we refer to this use case as In-Flight Entertainment and Connectivity Service (IFECS).

5.3.2.2 Computational Offloading

When computational tasks, arising in satellites, exceed the local processing capability, they can be offloaded to a MEC server. This comes at the cost of an additional propagation and transmission latency. However, deploying MEC in aircrafts and satellite gateways brings the computing resources closer to the satellite nodes, resulting in reduced propagation and transmission time. As a result, deploying AA-MEC could bring considerable gains to satellite networks. Nevertheless, the MEC capabilities between aircraft and gateways differ in computational efficiency as denoted in Table 5.3, with C_m denoting the number of instructions the processor is able to execute in series per second and E_m representing the energy required per instruction derived from the Thermal Design Power (TDP) of the processor.

Table 5.3 Specifications of MEC ARM processors

Processor Type	Deployment	Cores n_m^{Cores}	Computational Capacity C_m [Instruction/s]	Energy Cost E_m [W/Instruction]
Ampere Altra Max M128-30	Gateway	128	3.0e9	6.51e-10
Ampere Altra Max M128-26	Aircraft	128	2.6e9	5.71e-10

The computational *Tasks* that are offloaded are based on [Sth+21], specific properties are found in Table 5.2. We model the number of tasks n^{Task} of a satellite as a Poisson distributed random variable with an arrival rate λ. The total traffic generated by the service is based on the number of tasks that arise in the satellite multiplied by the bandwidth of a task, as described by:

$$D_{v_n^k} = n_{v_n}^{\text{Task}} C_{\text{BW}}^k \tag{5.2}$$

We designate this use case as Satellites Offloading Computational Tasks (SOCKS).

5.3.3 MEC-Algorithms

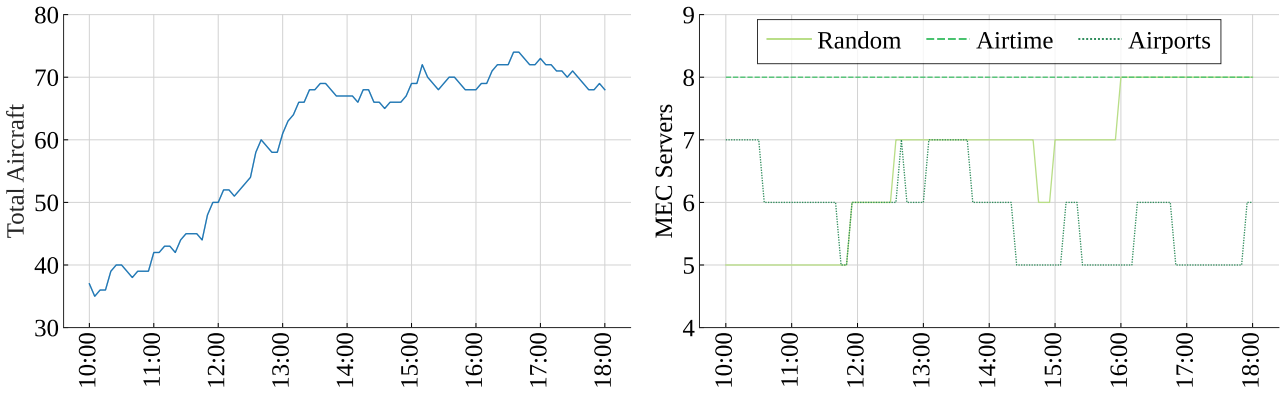

(a) Number of flying aircraft

(b) Active MEC servers

Figure 5.3 Comparative Analysis of Aircraft Activity and MEC Server Deployments

The goal of MEC selection algorithms is twofold, ensuring a high availability throughout the simulation and being deployed near the highest concentration of nodes. To target these goals, we differentiate three algorithms to deploy aerial MEC servers.

In Random, MEC servers are deployed randomly. This means for all active aircraft during the simulation time, n aircraft are selected and equipped with a MEC server. This algorithm, results in a large variance and seed dependent accessibility of MEC servers throughout the simulation.

In Airtime, the algorithm first computes the total airtime for each aircraft. It calculates airtime by determining the time difference between arrival and departure times for each flight in the data set. The flights are then aggregated by aircraft. The top n aircraft with the highest cumulative airtime, are then selected to work as MEC server. This method effectively ranks aircraft based on their total flying time during the simulation period, ensuring the highest number of accessible MEC servers throughout the simulation.

In Airports, we aim to identify the most frequently occurring aircraft registrations at each airport. It starts by merging the source and destination airports and calculates the occurrence of each airport. The algorithm sorts the airports in descending order by frequency. The aircraft with the highest appearance of the top airport in its flight-plan is then selected as a MEC server. The algorithm then iterates through the airports. For each airport it selects the aircraft, which most often contains the airport in its flight-plan as a MEC server. In case the aircraft is already selected as a MEC server, the next aircraft with the second most frequent occurrences is selected. This is repeated until n MEC servers are assigned. This algorithm emphasizes the identification of key aircraft for each airport based on their flight frequency.

As illustrated in Figure 5.3a, there is a noticeable increase in the number of nodes throughout the day. Consequently, it is anticipated that the various algorithms would allocate more MEC servers as the day progresses, as more flights become active and the chance increases that an aircraft carrying a MEC server is flying. However as shown in Figure 5.3b, only the Random algorithm follows this pattern. However, this metric does not address the secondary objective of minimizing the distance between the nodes offering services and those requesting them. Therefore, we continue to include Airtime and Airports in our analysis.

5.4 Problem Formulation and Solutions

Building on the previously described system model based on an AA-MEC network, we now direct our attention towards the mathematical formulation of route optimization and MEC destination selection within this framework. For this, we distinguish between two use cases IFECS, with the aim to provide *Games*, *VoIP*, *Web* and *Streaming* services to aircraft passengers and SOCKS allowing satellites to offload computational tasks to MEC server instances. In this context, we propose an optimization problem formulation to minimize latency and one to minimize energy consumption.

For all formulations, the following applies: we define our network topology with the help of a graph $\mathcal{F} = (\mathcal{N}, \mathcal{I})$, where $\mathcal{N}$ is the set of satellite, aircraft and gateway nodes of the network and $\mathcal{I}$ is the set of edges of the graph representing the available links between the nodes. The mobility of satellites and aircraft leads to variations in active nodes and the links between them. We model this behavior by taking multiple snapshots of the network over a defined simulation time interval. We assume that the network within a snapshot t is static [Pap+20]. We denote this snapshot by t, the set of snapshots by $\mathcal{T}$ and variables dependent on a snapshot by the superscript t. However, as we optimize each snapshot independently, we omit the superscript t for ease of readability and clarity. An overview over the common variables in all problem formulations is given in Table 5.4.

Table 5.4 Shared Variables among the various Optimization Problem Formulations

Variable	Description
$\mathcal{K}$	Set of service types
$\mathcal{T}, t$	Set of network snapshots with $t \in \mathcal{T}$
$\mathcal{S}^t, s$	Set of satellites at snapshot t with $s \in \mathcal{S}^t$
$\mathcal{A}^t, a$	Set of aircraft at snapshot t with $a \in \mathcal{A}^t$
$\mathcal{G}^t, g$	Set of gateways at snapshot t with $g \in \mathcal{G}^t$
$\mathcal{M}^t, m$	Set of MEC servers at a snapshot t with $m \in \mathcal{M}^t$
$\mathcal{N}^t_{\mathcal{S},\mathcal{A},\mathcal{G}}$	Set of all nodes in the network at snapshot t, $\mathcal{N}^t_{\mathcal{S},\mathcal{A},\mathcal{G}} = \mathcal{S}^t \cup \mathcal{A}^t \cup \mathcal{G}^t$
$\mathcal{N}^t, n$	Set of nodes in the network at snapshot t which create a service or task request with $n \in \mathcal{N}^t$
$\mathcal{V}^t, v^k_n$	Set of service requests at snapshot t with $\mathcal{V}^t = \{v^k_n \mid n \in \mathcal{N}^t, t \in \mathcal{T}, k \in \mathcal{K}\}$
$\mathcal{I}^t$	Set of links at a snapshot t with $I^t = \{(i,j) \mid i,j \in \mathcal{N}^t_{\mathcal{S},\mathcal{A},\mathcal{G}} i \neq j\}$
$B_{i,j}$	Capacity of a link at snapshot t with $(i,j) \in \mathcal{I}^t$ in Mb/s
$d_{i,j}$	Physical distance of a link at snapshot t with $(i,j) \in \mathcal{I}^t$ in m
$D_{v^k_n}$	Traffic for a service at snapshot t with $v^k_n \in \mathcal{V}^t$ in Mb/s
P^k	Size of a packet for a service type $k \in \mathcal{K}$ in bits
τ^k	Delay constraint for a packet of a service type $k \in \mathcal{K}$ in ms
$u_{v^k_n,i,j}$	Binary variable indicating if link $(i,j) \in \mathcal{I}^t$ is used for service v^k_n
$x_{v^k_n,m}$	Binary variable indicating if service v^k_n is served by MEC server m
$q_{s,g}$	Binary variable indicating if satellite s has a connection with gateway g

5.4.1 Latency Minimization Formulation

We begin with optimizing the network for latency for one snapshot t, understanding its critical role in network performance and the quality of experience in high-demand scenarios. For a detailed understanding of this process, additional notations employed in the latency optimization are outlined in Table 5.5.

Table 5.5 Latency-related Variables for the Optimization Problem

Variable	Description
$L^T_{v^k_n,i,j}$	Traffic latency for a service v^k_n on link $(i,j) \in \mathcal{I}^t$
$L^P_{k,i,j}$	Packet latency for a service v^k_n on link $(i,j) \in \mathcal{I}^t$
$L^C_{i,j}$	Propagation latency for a service on link $(i,j) \in \mathcal{I}^t$
$L^O_{v^k_n}$	Computational Latency for a service v^k_n
$z_{v^k_n}$	Auxiliary variable holding the largest link latency in a route of service v^k_n

5.4.1.1 IFECS

In the IFECS use case, we consider the services v^k_n provided to passengers within each aircraft $n \in N^t$ with $N^t = \mathcal{A} \setminus \mathcal{M}$. The services k considered are *Games*, *VoIP*, *Web* and *Streaming* and are held in the set $\mathcal{K}$. The latency $L^{T'}_{v^k_n,i,j}$ each of these services experiences on a link $(i,j) \in \mathcal{I}$, without the propagation delay, depends, therefore, on the traffic $D_{v^k_n}$ it generates in one second and the capacity $B_{i,j}$ of the link, specifically:

$$L^{T'}_{v^k_n,i,j} = \frac{D_{v^k_n}}{B_{i,j}}. \tag{5.3}$$

Whereas the latency of a single packet $L^{P'}$ of a service k is given by

$$L^{P'}_{k,i,j} = \frac{P^k}{B_{i,j}} \tag{5.4}$$

as we assume that for a specific service all packets are of the same size. We further define the propagation latency L^C for a transmission between two nodes as

$$L^C_{i,j} = \frac{d_{i,j}}{c} \tag{5.5}$$

with $d_{i,j}$ denoting the physical distance between the nodes i and j, and c the speed of light. The total latency for the traffic $L^T_{v^k_n,i,j}$ and packet $L^P_{k,i,j}$ can then be calculated by

$$L^T_{v^k_n,i,j} = L^{T'}_{v^k_n,i,j} + L^C_{i,j} \tag{5.6}$$

$$L^P_{k,i,j} = L^{P'}_{k,i,j} + L^C_{i,j}. \tag{5.7}$$

Our objective is to ensure QoS for IFECS. To this end, we aim to minimize the sum of service completion latencies within the network for each snapshot, while simultaneously adhering to a service-specific maximum delay constraint. Further, we calculate latency of a service v^k_n, by summing the packet latencies on each link with the largest traffic latency on the route resulting in following objective function:

$$\max_{(i,j)\in\mathcal{I}^t} L^{T'}_{v^k_n,i,j} u_{v^k_n,i,j} + \sum_{(i,j)\in\mathcal{I}^t} L^P_{k,i,j} u_{v^k_n,i,j} \tag{5.8}$$

To model the max term in this equation, we replace it with an auxiliary continuous variable $z_{v^k_n}$ which will hold the largest latency in the route with the following property:

$$z_{v^k_n} \geq L^{T'}_{v^k_n,i,j} u_{v^k_n,i,j} \quad \forall (i,j) \in \mathcal{I}^t, \forall v^k_n \in \mathcal{V}^t. \tag{5.9}$$

The optimization problem, therefore, centers around two key aspects. Firstly, it involves determining the optimal destination m for each service provided by every aircraft, represented by the optimization variable x. Secondly, the problem entails identifying the fastest path to this designated destination, encapsulated by the variable u. This dual-focused approach ensures efficient routing while maintaining the quality standards.

We present the optimization problem formulation as follows:

$$\min_{u_{v_n^k,i,j}, x_{v_n^k,m}} \sum_{v_n^k \in \mathcal{V}^t} \left(z_{v_n^k} + \sum_{(i,j)\in\mathcal{I}^t} L^P_{k,i,j} u_{v_n^k,i,j} \right) \tag{5.10}$$

$$\text{s.t.} \sum_{m\in\mathcal{M}^t} x_{v_n^k,m} = 1 \quad \forall v_n^k \in \mathcal{V}^t \tag{5.11}$$

$$\sum_{i\in\mathcal{N}^t_{\mathcal{S},\mathcal{A},\mathcal{G}}} u_{v_n^k,i,j} - \sum_{i\in\mathcal{N}^t_{\mathcal{S},\mathcal{A},\mathcal{G}}} u_{v_n^k,j,i} = \begin{cases} -1 & \text{if } j = src_{v_n^k,m} \\ x_{v_n^k,m} & \text{if } j \neq src_{v_n^k,m} \end{cases} \quad \forall j \in \mathcal{N}^t_{\mathcal{S},\mathcal{A},\mathcal{G}} \tag{5.12}$$

$$\sum_{(i,j)\in\mathcal{I}^t} L^P_{k,i,j} u_{v_n^k,i,j} \leq \tau^k \quad \forall v_n^k \in \mathcal{V}^t \tag{5.13}$$

$$\sum_{v_n^k\in\mathcal{V}^t} D^t_{v_n^k} u_{v_n^k,i,j} \leq B^t_{i,j} \quad \forall (i,j) \in \mathcal{I}^t \tag{5.14}$$

$$\sum_{s\in\mathcal{S}^t} q_{s,g} \leq 1 \quad \forall g \in \mathcal{G}^t \tag{5.15}$$

$$\sum_{v_n^k\in\mathcal{V}^t} u_{v_n^k,s,g} = q_{s,g} \sum_{v_n^k\in\mathcal{V}^t} x_{v_n^k,g} \quad \forall s \in \mathcal{S}^t, \forall g \in \mathcal{G}^t \tag{5.16}$$

$$x_{v_n^k,m} = 0 \quad \text{if } k = \textit{VoIP} \text{ and } m \in \mathcal{A} \tag{5.17}$$

$$z_{v_n^k} \geq u_{v_n^k,i,j} L^{T'}_{v_n^k,i,j} \quad \forall (i,j) \in \mathcal{I}^t, \forall v_n^k \in \mathcal{V}^t. \tag{5.18}$$

The objective function as formulated in (5.10) minimizes the latency for all services given the constraints (5.11) - (5.18). Within this set of equations, the binary variables: $u_{v_n^k}$ are set to 1 to indicate the usage of link (i, j) for a flow v_n^k of service k from aircraft $n \in N^t$ and 0 otherwise; $x_{v_n^k,m}$ are set to 1 to indicate the usage of MEC server m for service v_n^k and 0 if not; and $q_{s,g}$ are set to 1 to indicate the usage of gateway g for satellite s and 0 if not. Constraint (5.11) ensures the assignment of each service to a single MEC server. Constraint (5.12) represents the flow conservation constraint which balances the traffic inflow and outflow at any given node in the network, except for source $n \in N^t$ or destination nodes $m \in \mathcal{M}^t$. Constraint (5.13) ensures adherence to the upper limit of packet delay τ^k for each service. Constraint (5.14) holds up the bandwidth limitations on each link. Constraint (5.15) ensures that a maximum of one satellite can establish a connection with a gateway g. Constraint (5.16) ensures that the services that pass through a satellite are directed to its connected gateway. Lastly, Constraint (5.18) ensures that the variable z_n^k is larger than each link's latency in the route of the service.

5.4.1.2 SOCKS

We extend this formulation to the SOCKS use case, where satellites offload a specific number of computational tasks to the MEC servers in the network as described in Section 5.3.2.2. Due to the analogous nature of this problem to IFECS, we model the task offloading as single service k with varying properties over snapshots t. Therefore, we omit the service type variable k in the notation for this problem and $\mathcal{N}^t = \mathcal{S}^t$ since only satellites are sources of task offloading services. Further we modify the latency formulation to account for the required computational time to process *Tasks* service for each satellite. We define the computational latency as

$$L^O_{v_n,m} = \frac{O}{C_m} \tag{5.19}$$

with O being the instructions requirement of one task and C_m being the computational capacity of the MEC server m in instructions per second. As the computational tasks are processed in parallel

the latency introduced is independent of the number of tasks. This results in the following problem formulation:

$$\min_{u_{v_n,i,j},x_{v_n,m}} \sum_{v_n \in \mathcal{V}^t} \left(z_{v_n} + \sum_{m \in \mathcal{M}^t} L^O_{v_n,m} x_{v_n,m} + \sum_{(i,j) \in \mathcal{I}^t} L^P_{i,j} u_{v_n,i,j} \right) \tag{5.20}$$

The formulation adheres mostly to the same constraints as the previously described IFECS. Specifically, the following constraints remain applicable: (5.11), (5.12), (5.14), (5.15), (5.16) and (5.18). Constraint (5.13), regarding the delay bound is revised as follows:

$$\sum_{(i,j) \in \mathcal{I}^t} L^T_{v_n,i,j} u_{v_n,i,j} + \sum_{m \in \mathcal{M}^t} L^O_{v_n,m} x_{v_n,m} \leq \tau, \quad \forall\, v_n \in \mathcal{V}^t \tag{5.21}$$

In this constraint, the optimal approach would involve summing up the packet latencies and then adding the maximum traffic latency in the route of the service. However, to decrease the computation time, we sum over all traffic latencies in the route. Although this adjustment results in a stricter bound, it significantly reduces the solve time while still satisfying the actual constraint. Finally, we set a constraint on the calculation capacity, so that no MEC server processes more tasks than the number of cores available:

$$\sum_{v_n \in \mathcal{V}^t} n^{\text{Task}}_{v_n} x_{v_n,m} \leq n^{\text{Cores}}_m, \quad \forall\, m \in \mathcal{M}^t \tag{5.22}$$

5.4.1.3 Reducing the complexity of the optimization formulation

In pursuit of lower solve times, we reduce the complexity of the previously formulated optimization problems. This simplification aims to reduce computational complexity while retaining the core aspects of the problem. The following modifications and assumptions are, therefore, introduced: While the previously given latency description is based on the idea that the traffic latency of each service is based on summation of two terms, the first based on the time one packet of a service requires to traverse the network, depending on the link-speed of each link, and the second based on the time it takes for the complete traffic of the service on the slowest link in the route. To reduce the complexity, we replace the largest latency z in the formulation by the sum of the latencies L. This allows us to drop z as a variable and therefore the Constraint (5.18). In addition, we do not require the packet latency L^P in the objective function's sum term as it is smaller than the latency L of a service. The resulting problem formulation for IFECS is therefore:

$$\min_{u_{v^k_n,i,j},x_{v^k_n,m}} \sum_{v^k_n \in \mathcal{V}^t} \sum_{(i,j) \in \mathcal{I}^t} L^T_{v^k_n,i,j} u_{v^k_n,i,j} \tag{5.23}$$

subject to constraints (5.11), (5.12), (5.13), (5.14), (5.15) and (5.16).
For SOCKS this results in:

$$\min_{u_{v_n,i,j},x_{v_n,m}} \sum_{v_n \in \mathcal{V}^t} \left(\sum_{m \in \mathcal{M}^t} L^O_{v_n,m} x_{v_n,m} + \sum_{(i,j) \in \mathcal{I}^t} L^T_{v_n,i,j} u_{v_n,i,j} \right) \tag{5.24}$$

subject to constraints (5.11), (5.12), (5.14), (5.15), (5.16), (5.21) and (5.22).

5.4.2 Energy

Table 5.6 Energy-Specific Optimization Problem Notations

Variable	Description
$E_{v_n^k,i,j}$	Energy required for transmission of a service v_n^k on link $(i,j) \in \mathcal{I}^t$
$E^O_{v_n,m}$	Energy required to process the tasks offloaded by a satellite

In light of the growing emphasis on energy efficiency, our investigation explores methods to reduce the energy consumption within an AA-MEC network. We introduce an optimization formulation tailored to each use case to achieve this goal. An overview of the additional variables required is given in Table 5.6. The calculation of energy is based on the distance, type of nodes and the power of the transmitting node as detailed in Background Section 5.3.1. The energy expenditure for transmitting traffic generated by a service over a link is denoted as

$$E_{v_n^k,i,j} = L^{T'}_{v_n^k,i,j} P_i \tag{5.25}$$

with P_i being the transmission power of a node i.

5.4.2.1 IFECS

Applied to the use case of IFECS, this means to minimize the sum of the required energy to transmit the data over each link, resulting in following optimization formulation:

$$\min_{u_{v_n^k,i,j}, x_{v_n^k,m}} \sum_{v_n^k \in \mathcal{V}^t} \sum_{(i,j)\in\mathcal{I}^t} E_{v_n^k,i,j} u_{v_n^k,i,j} \tag{5.26}$$

subject to constraints (5.11), (5.12), (5.13), (5.14), (5.15) and (5.16).

5.4.2.2 SOCKS

In the SOCKS use case, we determine the energy required for processing all tasks offloaded by a satellite by multiplying the number of tasks by the number of instructions required to process it by the energy cost for one instruction, resulting in:

$$E_{v_n,i,j} = n^{Task}_{v_n} O E_m. \tag{5.27}$$

Expanding upon the optimization formulation established for IFECS, we integrate the newly defined energy equation for task-processing into our proposed optimization model for this use case as:

$$\min_{u_{v_n^k,i,j}, x_{v_n^k,m}} \sum_{v_n^k \in \mathcal{V}^t} \left(\sum_{m\in\mathcal{M}^t} E^O_{v_n,m} x_{v_n,m} + \sum_{(i,j)\in\mathcal{I}^t} E_{v_n,i,j} u_{v_n,i,j} \right) \tag{5.28}$$

subject to constraints (5.11), (5.12), (5.14), (5.15), (5.16), (5.21), and (5.22).

5.4.3 Quality Metrics

Despite the varied objectives of our optimization formulations, we establish a set of quality metrics that enable a comprehensive comparison between the original formulations and their simplified counterparts. Additionally, these metrics facilitate a multifaceted analysis of the network's performance, such as evaluating the impact of an increased number of MEC servers relative to a baseline scenario without any MEC servers on aircraft.

5.4.3.1 Optimization-specific Metrics

An important metric to gauge the complexity of the problem is the run time, which is indicative not only of the problem's computational demands but also of its feasibility for practical implementation. The run time encompasses the duration required for network graph generation, optimization model definition, and the optimization process (solve time).

Additionally, we quantify the deviation of our solution from the theoretical optimum, named optimality gap. This metric is defined as the relative difference between the utility of our solution and the optimal utility:

$$o^{\text{Gap}} = \frac{u^{\text{Solution}} - u^{\text{Upper}}}{u^{\text{Upper}}} \tag{5.29}$$

where u^{Solution} is the utility of our solution, and u^{Upper} represents the upper bound of the utility.

5.4.3.2 Service Metrics

The latency of a service for a single simulation snapshot t is defined as the time required to transmit the service's traffic from its source to the destination. This is calculated based on the packet latency and the slowest transmission time along the route for the service traffic:

$$L_{v_n^k}^{\text{Service},t} = \max_{(i,j)\in\mathcal{I}^t} L_{v_n^k,i,j}^{T'} u_{v_n^k,i,j} + \sum_{(i,j)\in\mathcal{I}^t} L_{k,i,j}^{P} u_{v_n^k,i,j} + \sum_{m\in\mathcal{M}^t} L_{v_n^k,m}^{O} x_{v_n^k,m} \tag{5.30}$$

where in case of IFECS $L_{v_n^k,m}^{O} = 0$.

To quantify the energy consumption of the network for each service, we define the required energy for a service in a given simulation snapshot t as

$$E_{v_n^k}^{\text{Service},t} = d^{\text{interval}} \left(\sum_{(i,j)\in\mathcal{I}^t} E_{v_n^k,i,j} u_{v_n^k,i,j} + \sum_{m\in\mathcal{M}^t} E_{v_n^k,m}^{O} x_{v_n^k,m} \right), \tag{5.31}$$

with $E_{v_n^k}^{O} = 0$ for IFECS. The term d^{Interval} adjusts for the simulation interval time, ensuring that the energy consumption is accurately projected for the duration that the snapshot represents. This adjustment is crucial as the network is optimized for 1 s of generated traffic.

5.4.3.3 Flight Aggregation

To analyze properties of the services for a flight in the IFECS use case, we aggregate latency and energy metrics, for each flight over the entire simulation duration. A flight is represented by f, and the set of all flights is denoted as $\mathcal{F}$. Let $\mathcal{T}^f$ denote the set of snapshots for belonging to an active flight f, and let v_f^k represent the corresponding service of type k. We then calculate the latency metric for a flight as follows:

$$L_{v_f^k}^{\text{Flight}} = \sum_{t\in\mathcal{T}^f} L_{v_f^k}^{\text{Service},t} \tag{5.32}$$

Similarly, the energy consumption is computed by:

$$E_{v_f^k}^{\text{Flight}} = \sum_{t\in\mathcal{T}^f} E_{v_f^k}^{\text{Service},t} \tag{5.33}$$

Within the context of SOCKS, these metrics represent the latency and energy per satellite.

5.4.3.4 MEC-specific Metrics

To provide an insight into the usage dynamics and advantages of AA-MEC, we introduce a metric which quantifies the proportion of MEC servers located on aircrafts utilized for each service, denoted as:

$$\alpha_k^{\text{A-MEC}} = \frac{\sum_{m' \in \mathcal{M} \setminus \mathcal{G}} \sum_{v_n^k \in \mathcal{V}} x_{v_n^k, m'}}{\sum_{m \in \mathcal{M}} \sum_{v_n^k \in \mathcal{V}} x_{v_n^k, m}} \qquad \forall k. \tag{5.34}$$

5.4.4 Statistical Tests

Building on the methodology outlined in Chapter 4, we employ two-sided student t-tests to ascertain the statistical significance of differences in mean values across group comparisons. To adjust for multiple comparisons, we apply the Bonferroni correction method. For an understanding of the p-value's interpretation, please see Section 4.4.7. Although tests performed on latency are conducted on linear values, they are presented in a logarithmic scale for visual clarity. The results of these tests are denoted in our figures using the following notation:

$$\begin{aligned} \text{ns} &: p > .05 \\ * &: .01 < p <= .05 \\ ** &: .001 < p <= .01 \\ *** &: .0001 < p <= .001 \\ **** &: p <= .0001 \end{aligned}$$

5.5 Performance Evaluation

The results were generated from simulations carried out on an AMD Ryzen 9 5950X 16-Core Processor, operating under Linux 6.6.2, programmed in Python 3.11 and employing Gurobi optimizer[Gur23] v10.0.3 for solving the optimization problem formulations. Following results are based on the data obtained by observing 143 Lufthansa flights between 10:00 and 18:00 on the 21st of November 2023.

The simulation time is quantized into 300 s intervals. We stop the optimization process if an optimality gap of 0.1% is reached within 300 s. If not, we allow an optimality gap of 0.5% and continue optimizing for another 300 s.

5.5.1 IFECS

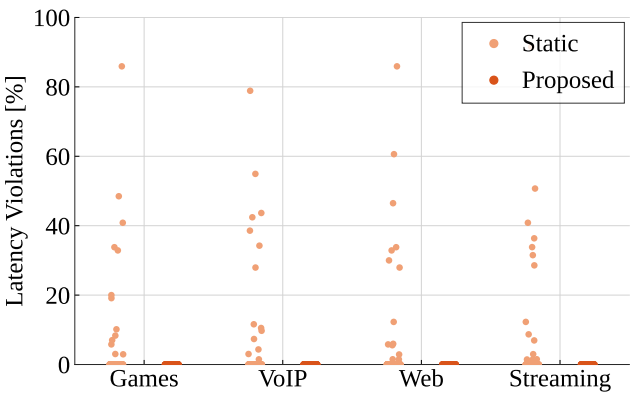

Figure 5.4 Constraint violations over the simulation time for static and our proposed dynamic destination optimization

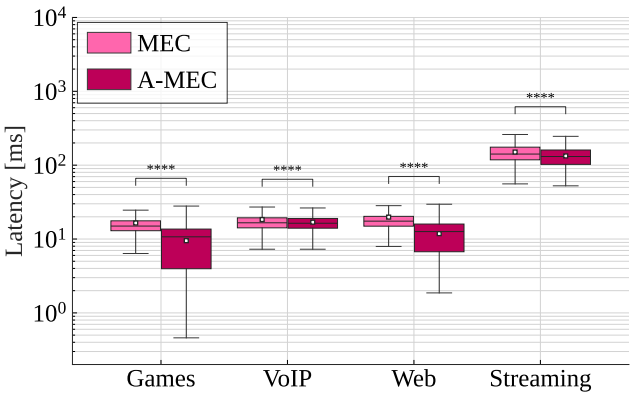

Figure 5.5 Latency comparison between MEC servers solely at gateways (MEC) and MEC servers at gateways and aircraft (A-MEC)

To illustrate the need for a dynamic service placement we implemented a baseline approach, which is based on the latency formulation, however, only selecting the optimal MEC server destination ($x_{v_n^k,m}$) for the first appearance of the service. This Static approach is contrasted in Figure 5.4 with the Latency Minimization Formulation (Proposed) for MEC servers placed solely at gateways. The figure shows the percentage of latency constraints (5.13) that were violated across IFECS for each simulation snapshot. It clearly demonstrates that a static MEC selection, even with route updates, fails to deliver the required QoS for any service. Conversely, a continuous update of the MEC selection ensures feasible routing, consistently meeting latency constraints.

To investigate the effect of additional MEC servers in the air, we deploy four aerial MEC servers (A-MEC) and compare the performance to a network with MEC servers solely positioned at the ground (MEC), as proposed in State of the Art [Var+19]. We observe in Figure 5.5 a reduction in service latency, not only for services that are directly offloaded to the nearest MEC server but also for *VoIP* which is always routed to a gateway - specifically: 42.4% for *Games*, 40.2% for *Web*, 11.4% for *Streaming* and 7.87% for *VoIP*. This is due to reduced traffic on the gateway-satellite link. Moreover, the deployment of additional MEC servers in the aerial layer reduces the optimality gap from 19% for MEC to 10% A-MEC. While merely 44% of snapshots achieve a solution with MEC servers solely at gateways, A-MEC ensures a solution in 100% of snapshots, indicating a substantial increase in system reliability. We denote that this is due to the increased limit of 900 s we imposed on the solve time (for the optimization process) only for these approaches.

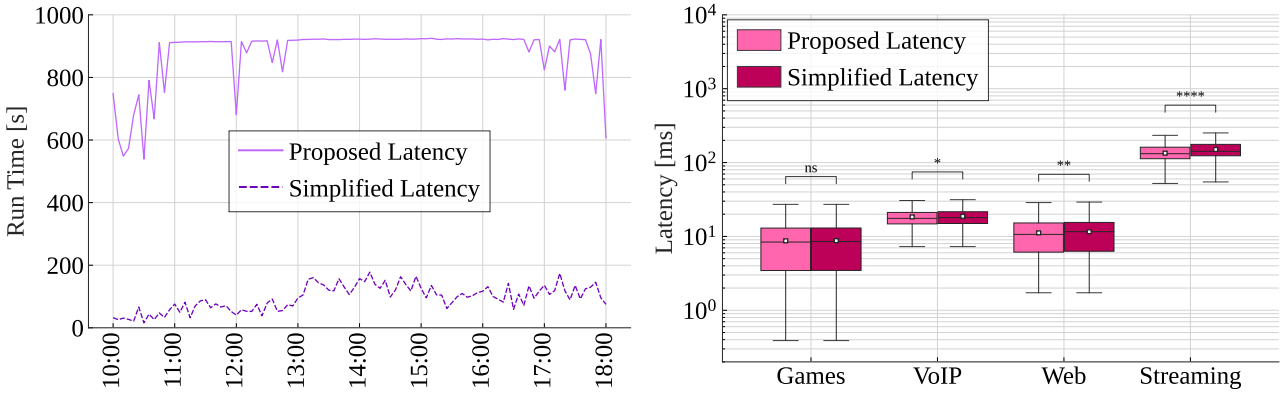

(a) Run Time for the simulation duration

(b) Latency in ms for IFECS services

Figure 5.6 Comparing the performance of our Proposed and Simplified latency objective formulation

The long run time for the Latency Minimization Formulation (Proposed) makes it unsuitable for a practical implementation, we, therefore, simplified the formulation as in Section 5.4.1.3 (Simplified) and compare the effects on run time in Figure 5.6a. The simplified formulation reduces the run time 89.1%. On the other side, Figure 5.6b illustrates the impact of the simplification on latency. It reveals that for *Games*, the latency change is not statistically significant. However, for *VoIP*, *Web*, and *Streaming*, there is a statistically significant increase in latency by approximately 0.3 ms, 0.4 ms, and 16 ms, respectively. Despite these increases, we assume that such changes do not adversely affect the passenger's quality of experience. Further, the optimality gap for our simplified approach is reduced to 0.05%, resulting in a solution closer to the best possible solution. This also allows us to make more definitive statements regarding the outcome, thereby increasing the reliability of the model's projections and decisions derived from it. We, therefore, continue from now on analyzing different properties of our MLN based on the simplified optimization formulation.

Figure 5.7 illustrates the impact of increasing the proportion of passengers using IFECS (denoted as α). As anticipated, there is a general trend of rising latency with higher α levels, although the increase is not statistically significant for *Games*, this is likely due to the minimal bandwidth required for this service and the relatively few passengers utilizing it on an aircraft. Concerning run time, a nonlinear escalation is apparent; the median run time suggests an increasing number of simulations reaching

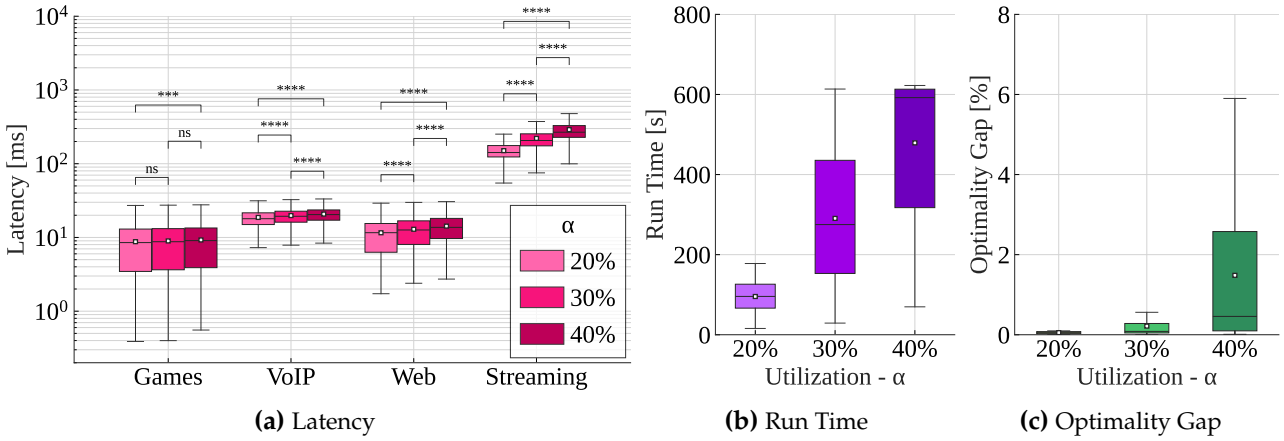

(a) Latency **(b)** Run Time **(c)** Optimality Gap

Figure 5.7 Comparison of different IFECS utilization ratios on simulation properties

the 600 s solve time limit, resulting in run time values above 600 s. This trend is corroborated by the optimality gap analysis, which shows an expanding gap at higher α percentages, especially at 40%, where many optimizations fail to meet the desired optimality threshold. Despite this, an average optimality gap of approximately 1.5% is still acceptable, as the latency figures remain well within the service limits, indicating that the system can accommodate an increase in passenger demand for individual services. It is also noteworthy to project that advancements in processing capabilities in computers will likely mitigate these challenges in the future.

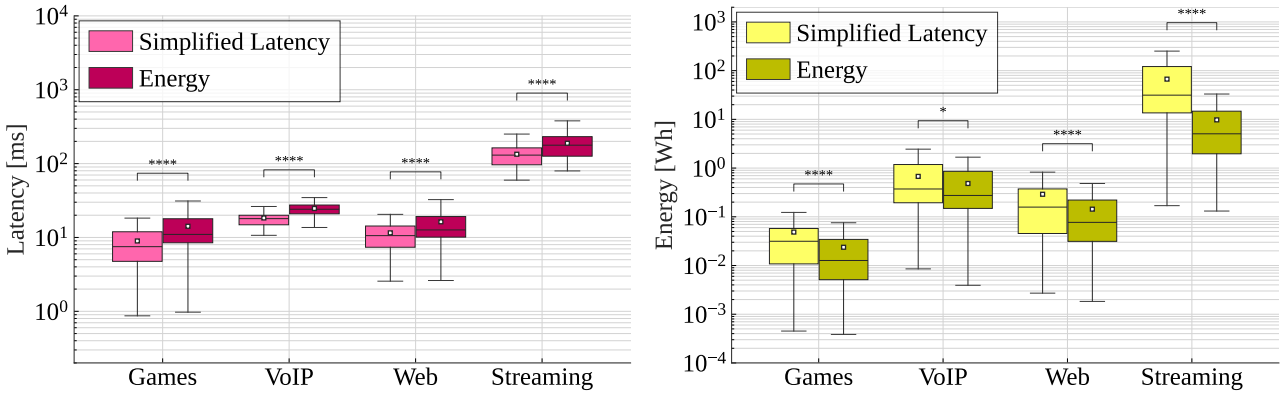

(a) Latency **(b)** Energy

Figure 5.8 Comparison between the Simplified Latency and Energy objective formulation on different properties for flights

With energy efficiency in networks becoming more and more important, we provided a formulation including an energy objective. Figure 5.8 compares the effects of both objectives on the latency and energy quality metric. As expected, optimizing for latency resulted in a significantly lower latency per flight for all services, whereas optimizing for energy resulted in a significantly lower energy. Specifically, for *Games*, the Energy formulation results in a latency that is 1.58 times higher than the Latency formulation, but it reduces energy consumption by a factor of 2.05. Similarly, with *Streaming*, the Energy formulation increases latency by a factor of 1.41 while decreasing energy usage by 6.86 times. In the case of *Web*, there is a 1.41 times increase in latency under the Energy formulation, accompanied by a 2.02 times decrease in energy usage. Lastly, for *VoIP*, the Energy formulation leads to a 1.34 times increase in latency but achieves a 1.4 times reduction in energy consumption. A deeper analysis revealed that in case of the energy objective more traffic was routed over aircraft-aircraft links which are more energy efficient compared to the satellite-satellite links which are typically selected

by the latency objective. This resulted in more service endpoints located at the aerial MEC servers, resulting also in the higher traffic on satellite-aircraft links for the energy objective.

Given that the assignment of MEC servers significantly affects quality metrics, we conduct a detailed analysis of its various properties in the following section.

5.5.2 MEC server selection effects

To investigate the impact of the Random MEC algorithm's seed on latency, we conduct Generalized Linear Model (GLM) regression analyses with seed as predictor (seed $\in [1, 10]$) and latency as dependent variable for each type of service. These analyses revealed that the absolute latency may differ for *Games* by [-2.15, 1.84], *VoIP* by [-0.36, 0.42], *Web* by [-2.13, 1.68], and *Streaming* by [-7.03, 2.59]. The respective intervals constitute the smallest and largest regression coefficient values of 95% confidence intervals. In this context, specific seeds influenced latency inconsistently, suggesting a seed-dependent effect on latency. However, this impact appeared random across different services, as various seeds had differing effects on latency for each service. All in all, this would not affect the passengers' experience due to the small absolute values of the effect on each service. This is exemplified in Figure 5.9, where the results are visualized for seeds one to four. Importantly, as the seed selects from the available aircraft at random, it would have been possible that an aircraft with a large downtime could have been selected. Therefore, this algorithm is not suitable due to its unpredictability in the results.

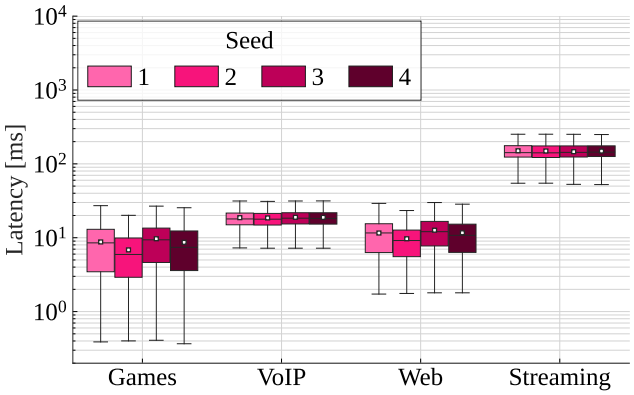

Figure 5.9 Effects of different seeds on Latency for the Random MEC selection algorithm

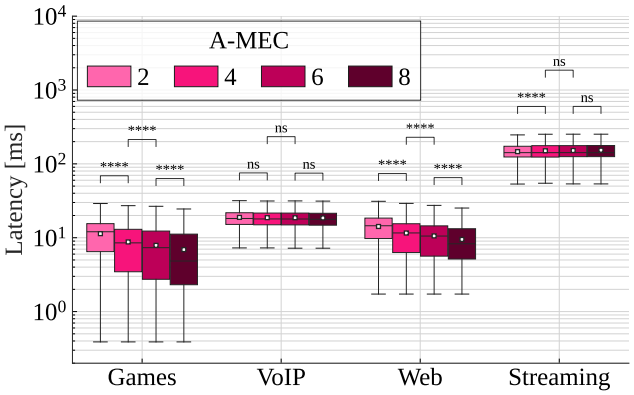

Figure 5.10 Effects of additional A-MEC servers on Latency for the Random MEC selection algorithm

Figure 5.10 depicts the impact of increasing the number of A-MEC servers in the network. *VoIP*, does not show any significant changes in latency, this can be attributed to the fact that *VoIP* is always routed to MEC servers at gateways, which would result in minimal routing changes. Whereas the latency of *Games* and *Web* significantly drops with each additional MEC server, as new destinations become available, which not only might be nearer but also reduce the load on the previous MEC servers links. However, in case of *Streaming* the picture is not consistent, the increase in latency from A-MEC two to four can be explained by a trade-off between services as we only optimize for the summed latency. This results in *Games* and *Web* experiencing a larger drop in latency compared to the other A-MEC values. The non-significant changes for four to eight are due to most traffic still being routed to MEC servers located at gateways and the large payload not being able to benefit for latency due to smaller capacity on aircraft links.

As the allocation of MEC servers significantly impacts network properties, we analyze the network when the Airtime and Airports MEC server selection algorithms are deployed. The Airtime algorithm focuses on maximizing the time a MEC server is available, thereby facilitating the study of how server availability affects the network. Conversely, the Airports algorithm aims to increase the presence of MEC servers around highly frequented airports, allowing us to examine the effect of physical

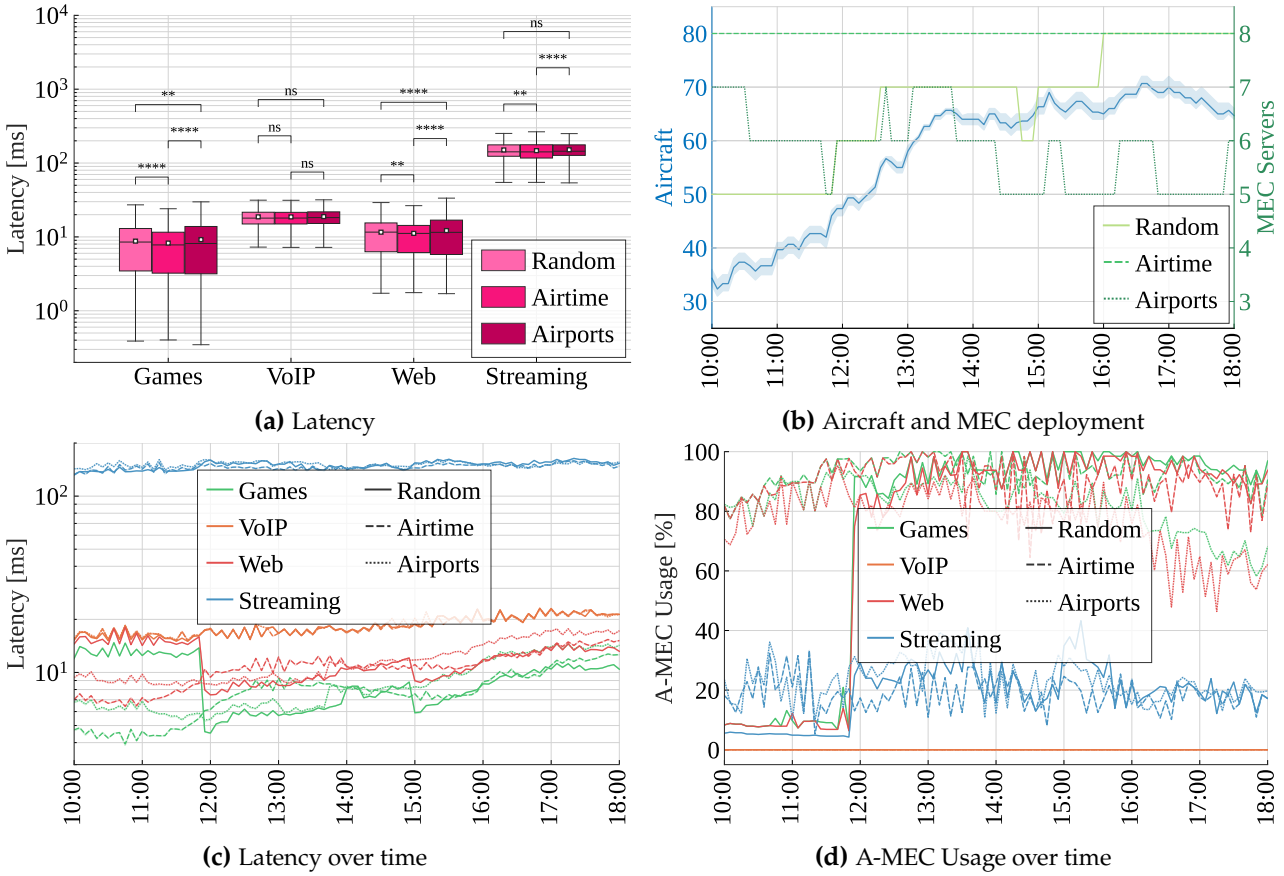

(a) Latency

(b) Aircraft and MEC deployment

(c) Latency over time

(d) A-MEC Usage over time

Figure 5.11 Comparison of effects different MEC Algorithms have on various network properties

proximity towards parts of the network exhibiting a high aircraft density. The different effects of the algorithms are visualized in Figure 5.11. We observe that *VoIP* uniquely remains unaffected by the choice of algorithm. This phenomenon likely arises because *VoIP* services are constrained to terminate at ground gateways, making them susceptible only to traffic from other services with whom it shares links, rather than algorithmic variations.

Figure 5.11a shows that Airtime exhibits the lowest latency for *Games*, *Web* and *Streaming* compared to the other algorithms. While Figure 5.11c reveals an increase of latency over time, Figure 5.11b shows that all A-MECs servers are continuously available, whereas the Aircraft count increases with time. We derive that the algorithm itself is not able to cause any changes in latency over time and that the increase in latency is consequently due to the increasing aircraft count in the network. Comparing the different services in Figure 5.11d we observe a low percentage A-MEC servers being used for *Streaming*, this is due to the high bandwidth requirement and limited available aircraft link capacity (see Table 5.2, Table 5.1).

Airports demonstrates longer latency values compared to the other algorithms; this can be attributed to two primary factors. Firstly, the algorithm deploys a limited number of A-MEC servers, typically ranging from 1 to 3, throughout the simulation period. Secondly, this lower server count often coincides with periods of high aircraft density, as shown in Figure 5.11b. Consequently, there is a notable decrease in the percentage of A-MEC usage starting from 14:30, accompanied by a gradual increase in latency over time, as detailed in Figure 5.11b.

Random lies in between Airports and Airtime regarding latency. However, it shows an interesting behavior between 10:00 and 12:00, where we observe a low A-MEC usage for all services, a large latency for *Games* and *Web* compared to the other algorithms, followed by a steep increase in A-MEC usage when an additional A-MEC server becomes active. A detailed analysis of the flight plans revealed that this drop in latency was caused by the A-MEC server departing from Munich to San

Diego. The A-MEC that became active at 12:35 departed from Frankfurt to Helsinki and did not influence the latency due to the availability of the previous aircraft. The next drop in latency could be observed at 15:00 due to an A-MEC becoming available on the route Frankfurt to Shanghai. This one compensates the unavailability of the just landed Frankfurt-Helsinki aircraft and the further away Munich-San Diego flight.

The insights gathered from our previous observations lead to several recommendations for designing an effective A-MEC server selection algorithm. Firstly, careful consideration should be given to which specific aircraft are equipped with an A-MEC server, taking into account factors such as their availability and position. It is also advisable to deploy A-MEC servers near the sources of traffic to optimize efficiency. Ensuring high availability of these servers is crucial to maintain consistent network performance. Therefore, MEC server selection algorithm should be designed to be fail-safe; the inclusion of a random component in the algorithm should not compromise their availability. Furthermore, incorporating adaptive capacity scaling could enhance service during peak demand periods.

5.5.3 SOCKS

In our second use-case scenario, we concentrate on task offloading from satellites, analyzing how different optimization objectives affect latency in case MEC servers are required to process data. The first analysis is conducted for a network with four existing ground-based MEC systems complemented by four A-MEC servers.

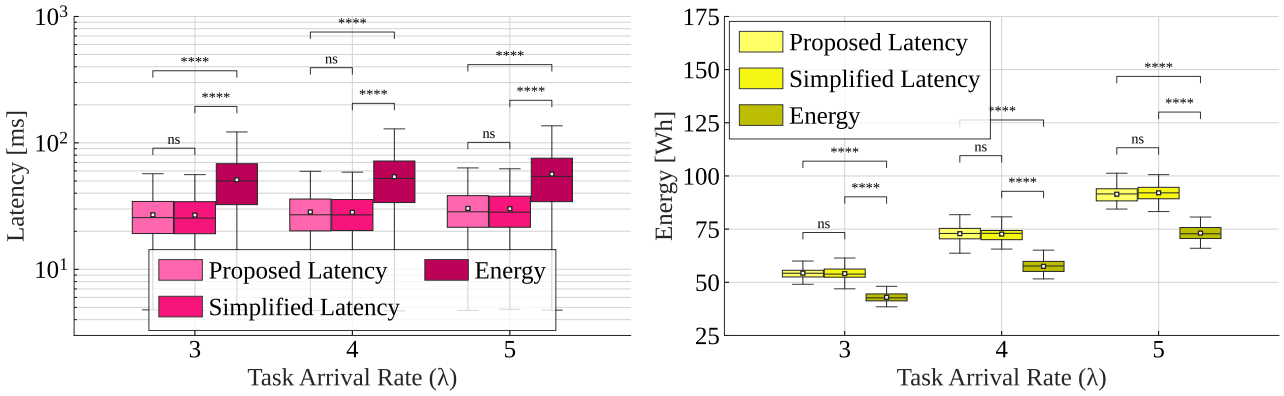

(a) Latency **(b)** Energy

Figure 5.12 Comparison of different optimization formulations on network properties for various task arrival rates

Figure 5.12 displays the latency per task service. No noticeable difference is observed between the proposed and the simplified latency formulation. This is due to both similarly routing the traffic to the MEC servers located at gateways. Hereby they utilize the high-bandwidth satellite links. In the energy-based formulation, more satellites offload tasks to the slower A-MEC, which, while being connected at a lower bandwidth, also exhibit a lower energy cost per instruction calculated. The gap in energy becomes evident in Figure 5.12b, where the energy-optimized approach results in lower energy consumption. As task arrival rates λ increase, we observe a greater rise in energy costs for Latency formulations compared to Energy formulations. This is attributed to the tendency of Latency formulations to offload primarily to gateways, which incur higher computational costs and rely more on high capacity, energy-intensive gateway-satellite links for transmission. Conversely, the Energy formulation achieves a reduction in energy costs by minimizing the energy required for both transmission and computation. Additionally, a more detailed MEC analysis indicates that with rising λ, task distribution becomes more evenly spread across the gateways. On average, approximately 72-83% of energy consumption is attributed to computing, depending on the goal and task arrival rates. This percentage tends to decrease with higher λ; in Latency formulations, this is due to data

being transmitted over more hops, while in Energy formulations, despite a reduction in hop count, the use of higher power satellite links increases.

Since all offloaded tasks are successfully executed within the specified time-frame, the strategy of optimizing for energy demonstrates greater effectiveness. Our forthcoming analysis will further explore how varying the count of MEC deployments influences the optimization of energy efficiency. The results are depicted in Figure 5.13.

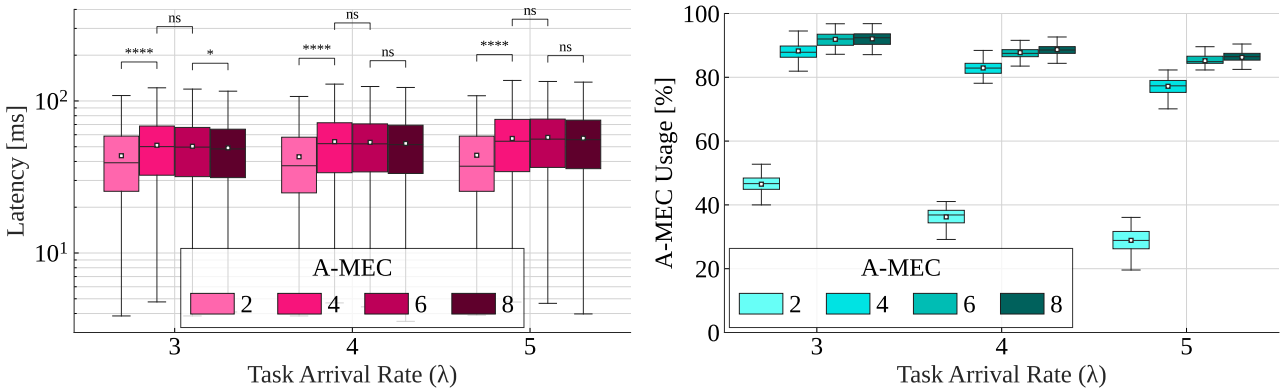

(a) Latency **(b)** A-MEC Usage

Figure 5.13 Comparison of additional A-MEC servers on network properties for the Energy formulation

Two distinct trends emerge from our observations. Firstly, as the task arrival rates increase, so does the latency, which can be attributed to the greater volume of tasks requiring transmission. It is important to note that the mere processing of an increased number of tasks does not influence latency; rather, it is the transmission that is the key factor. Secondly, a higher deployment of A-MEC servers correlates with increased latency, as seen when λ is 5. This rise in latency is a result of workload transfer from gateway MEC servers to A-MEC servers. However, when there is a substantial deployment of A-MEC servers coupled with a low λ, a reduction in latency is observed. This decrease is due to less congestion on aircraft links, enabling swifter data transmission. These dynamics are partially reflected in the utilization patterns of A-MEC servers. There is a decrease in usage with higher task volumes as the servers on the aircraft approach their capacity limits. Conversely, as tasks are redistributed from gateways to aircraft with the availability of more aerial capacity, we see an increased A-MEC usage. This indicates that strategic deployment of A-MECs can help balance the network load and improve latency also for task offloading with an energy minimization objective.

5.5.4 Deployment Vision

Airlines are the most suitable entities to deploy the envisioned offloading framework, primarily due to their access to detailed aircraft location data - a key factor in this network model. Airlines, are the primary beneficiaries and have the capability to integrate a centralized controller within their technical infrastructure. This controller would use real-time location data to optimize traffic routes. We demonstrated that the optimization can be executed for the 300 s intervals, as the optimization only takes a fraction of the next interval. The traffic routes could be further optimized by using an improved channel estimation based on weather information. Here, the aircraft weather radar data could be utilized for refining these estimates, particularly for inter-aircraft and aircraft to ground links.

Traffic properties for the network can be inferred from historical data and updated with real time current requests, as airlines have direct access to passenger IFECS usage on each aircraft. In consequence, ensuring a high quality of experience for passengers. Placing the central controller near the headquarters or major flight hubs could also serve as an additional gateway for aircraft, enhancing information accessibility and reducing control traffic.

Furthermore, the unused capacity of MEC servers presents an opportunity for airlines to generate additional revenue by offering computational resources to external customers, such as satellite providers. These providers could utilize these resources for offloading tasks that require processing power and that the satellites are not capable of. This approach fosters a symbiotic relationship between satellite operators and airlines, each benefiting from shared resources and enhanced network capabilities.

5.6 Summary and Conclusions

We have proposed the Aerial-Aided Multi-Access Edge Computing (AA-MEC) network architecture which positions MEC servers closer to the sources of service requests to enhance service quality through improved latency and reduce energy cost. Within this architecture we propose an optimization framework which optimizes MEC server destination selection and the route to it for the provision of airborne internet services through In-Flight Entertainment and Connectivity Services (IFECSs) and the computational offloading from satellites for Satellites Offloading Computational Taskss (SOCKSs). We have shown the practicality and effectiveness of the optimization framework for dynamic aerial-based MEC networks.

We have shown a reduction in average for IFECS of 25.5% in latency compared to state of art, a network without A-MEC servers, with a maximum of 42.4% for *Games*. We proposed a simplification for latency minimization formulation, which reduces the run time on average from 880 s to 95 s, while increasing the average latency for *Streaming* by 16 ms and the other by less than 1 ms. We further showed that our proposed energy minimization formulation reduces the energy cost per flight on average by a factor of 3.1 compared to the latency-based. We showed that the network is future proofed by projecting higher utilization ratios of IFECS. We showed that in the SOCKS use case, an energy-based formulation was able to reduce the required energy by a factor of 2.02 while increasing the latency only by a factor of 1.41 and adhering to optimization and simulation constraints.

Our findings suggest that deploying an energy-based optimization can effectively reduce operational costs, rendering it the default objective. However, as network load intensifies, transitioning to a latency-focused optimization strategy during operation of the network becomes beneficial for maintaining network performance. Our optimization framework allows to find the optimal A-MEC server deployment count, for our Lufthansa-based network we showed that the largest decrease in latency is gained with four A-MEC servers. The different A-MEC server selection algorithms demonstrated the importance of deploying A-MEC server on aircraft that exhibit a high availability and are near dense areas of service sources.

We outline following limitations of this work. The deployment of A-MEC servers involves navigating a complex landscape of airspace and telecommunication regulations, along with coordinating the operations among airlines, satellite operators, and ground stations. This introduces regulatory, operational and contractual limitations which are not discussed. The system complexity of such a multi-server network requires the management of control traffic, aircraft position and service request information, and additional data which require management strategies increasing the demands on the technological infrastructure and operational protocols. Within our optimization framework a trade-off between energy efficiency and performance, particularly latency, exists. We optimize for either one but not both, future work could combine these optimizations and assign them a cost factor to find a Pareto front, to exactly describe when to deploy the latency or a energy-based optimization. Looking ahead, two potential areas of future research emerge. First, the selection of aircraft as A-MEC should focus on optimizing their availability and physical position in the network. Developing an optimization formulation will be key to enhancing network resource utilization. This could integrate predictive analytics to preemptively allocate resources based on anticipated traffic patterns. The second area is cost and investment. Future studies should concentrate on the financial aspects of advanced network systems, including the initial setup costs, operational expenses, and potential

revenues. A thorough financial analysis will be crucial for evaluating the feasibility and sustainability of these systems.

Chapter 6

Summary and Conclusion

Navigating the complexities of communication within aircraft cabins introduces a spectrum of challenges, reflecting the intersection of evolving passenger expectations, technological advancements, and stringent regulatory frameworks. As we progress into an era where passengers demand an uninterrupted digital experience - including access to services they are used to on the ground - within the confines of an aircraft, the task of delivering seamless, high-speed internet and entertainment services becomes increasingly intricate. This expectation aligns with the operational goals of airlines to enhance safety protocols, operational efficiency, and overall passenger satisfaction, necessitating a reevaluation of established communication strategies.

Technically, the unique environment of the aircraft cabin, characterized by high device density and specific architectural features, presents substantial challenges in signal transmission and reception. The coexistence of multiple devices competing for limited bandwidth, combined with structural impediments, demands innovative approaches to wireless communication. Moreover, the integration of various technologies, including Wireless Fidelity (WiFi) and 5G, requires meticulous planning to mitigate interference, optimize spectrum usage, and ensure interoperability across different systems.

From an operational perspective, the challenge broadens to include the maintenance of system reliability and performance across diverse geographical locations and regulatory regimes. Airlines must navigate a complex web of international regulations governing wireless communications while adhering to rigorous safety standards.

To effectively address these challenges, a comprehensive strategy that considers the dynamic relationship between the physical layer of the cabin, the link layer of the cabin and the application layer is essential. Through the adoption of new channel modelling techniques, link scheduling for Multi-Radio Access Technology (Multi-RAT) and Multi-Radio Access Point (RAP) beamforming (BF) and an Aerial-Aided Multi-Access Edge Computing (AA-MEC) network architecture, it is feasible to surmount these obstacles.

6.1 Summary

This thesis addresses critical challenges in enhancing aircraft and aircraft cabin communication systems. It delves into the technical intricacies of physical layer channel modeling, beam pattern optimization in the link layer, and the application layer's integration within a Multi-Layer Network (MLN).

Physical Layer: We introduced an intricate 3D model of a Boeing 737-300 cabin, which serves as a critical tool for accurate wireless channel modeling. Our research involved deriving Path Loss (PL), Tapped Delay Line (TDL), and Clustered Delay Line (CDL) models for the 2.45 GHz and 5.16 GHz frequency bands, catering to various cabin scenarios. We advanced beyond existing channel models by employing a broader array of base functions and random distributions, not previously utilized in literature. This method and using multiple predictors allowed for a more nuanced model fitting, specifically for the small-scale effects and multipath components. Selecting the optimal fit based on the lowest Akaike information criterion (AIC) value further enhanced the accuracy and reliability of our channel models for aviation communication systems. These methods can extend

beyond the specific context of aircraft cabins, offering valuable insights applicable to a wide range of environments where precise wireless channel modeling is critical. The inclusion of human presence and propagation direction further enhanced the realism and applicability of these models for in-cabin communication systems. Furthermore, the insights gained from our analysis reveal that both PL and TDL models exhibit a pronounced dependency on signal propagation direction. By leveraging the directional sensitivity of the channel models, we can significantly enhance the efficacy of in-cabin wireless communication systems. This directional sensitivity is further pronounced for our CDL models, with which we are able to optimize the deployment of technologies employing BF. In addition to new communication technologies, the effect of different antennas is now easier to be determined. The openly accessible 3D model of an aircraft cabin facilitates in-depth exploration of channel characteristics across newly used frequencies, such as the emerging 6 GHz band, but also lays a robust foundation to test new parts and forms and their influence on the channel.

Link Layer: Moving beyond the physical layer, our focus shifted to the link layer, where we addressed the challenge of delivering data in a fully utilized spectrum in the aircraft cabin. We first determined the benefit of using BF over Multi User MIMO (MU-MIMO) in the aircraft cabin. We then introduced an antenna system selected for its beam width to optimize BF scheduling strategies. Here, the goal was to mitigate interference and enhance network throughput in a space crowded with multiple RAPs and two technologies operating on similar frequencies by finding the optimal beam angle, link direction and transmission power. For this we presented a mathematical optimization problem formulation of the network. This formulation was then simplified and solved by three different methods. First, we maximized the throughput for all users with an off-the-shelf Mixed Integer Nonlinear Program (MINLP) solver. These results were then compared with similar performing meta-heuristics. Finally, we provide a Deep Reinforcement Learning (DRL)-based solution which is also suggested to be deployed in a real world due to its shortest run time. In the exploration of BF, our findings challenge the conventional approach of deploying extensive RAP configurations. Through the strategic application of BF, we address the critical issue of interference and enhancing the overall network reliability. Our study further confirms the benefits of adaptive power allocation, which not only further mitigates interference but also contributes to operational energy savings. This approach would directly impact fuel efficiency, taking a small step towards eco-friendly aviation operations. Moreover, the capacity for utilizing wider channels opens the door to supporting advanced technologies such as virtual reality and ultra-high-definition video streaming (4K/8K), which have traditionally been constrained to wired connections.

Application Layer: Finally, we integrated the aircraft into a globally-spanning MLN transitioning us to the application layer. We, therefore, defined services that would be provided by airlines, described the satellite constellation that was used and explained how we elucidated the link properties between nodes in our MLN spanning over a terrestrial, aerial and satellite layer. In the next step, we mathematically modelled the network allowing us to find the optimal routing and service placement with the goal to minimize latency and energy consumption for all services. We then presented an alternative mathematical formulation, which led to a substantial reduction in the optimization algorithm's run time, facilitating latency and energy optimization for a practical implementation. To reveal the impact that the Multi-Access Edge Computing (MEC)-server placement has on our optimization goals, we compared different deployment algorithms, resulting in distinct recommendations on which aircrafts should carry MEC servers. This work presented us with the opportunity to conceptualize the aircraft not just as a passive node but as an active participant in a global network. By facilitating inter-aircraft communication, in addition to existing satellite link communications, the proposed MLN architecture significantly bolsters the network's robustness and reach. This enhancement is particularly evident in the substantial reduction in latency, which is not only critical for delivering a range of in-cabin services (VoIP, Web Surfing, Gaming, Streaming) but also future-proofs the network against evolving service requirements. The focus on energy optimization in the MLN framework increases the sustainability in aerial communication networks, laying the first steps in reducing the carbon footprint and operational costs while aligning with the industry's environmental

objectives on the network level. The dynamic nature of service positioning and routing ensures that the network remains resilient in the face of routine changes and unexpected disruptions, such as the loss of nodes or servers, thereby maintaining consistent service quality and network performance. Perhaps one of the most transformative aspects of our MLN-based approach is the opening of new revenue streams for airlines. By enabling the sale of processing capacities, airlines can diversify their business models, reducing reliance on traditional revenue sources subject to seasonal fluctuations. This diversification not only introduces a new dimension to airline operations but also stabilizes financial performance, positioning airlines to capitalize on the digital transformation of the aviation sector.

6.2 Future Work

The exploration undertaken in this thesis lays a solid groundwork for advancing communication technologies within and beyond the aircraft cabin. However, several promising avenues for future research have emerged, each with the potential to further bring in-cabin connectivity and MLN operation forward. Said avenues include the following:

A direct extension of this work involves conducting channel measurements within modern aircraft cabins to validate the channel models presented herein. This empirical approach will offer a closer examination of the actual communication channels within aircraft, providing additional insights. Independent of a measurement campaign, current channel models could be refined with data, e.g., channel state information, from in-cabin access points. Moreover, enhancing the CDL model to encompass other cabin scenarios, such as fully occupied flights and the integration of personal devices, will offer a more nuanced understanding of in-cabin wireless communication dynamics. Additionally, exploring alternative forms of channel representation, such as utilizing an H-matrix in MU-MIMO communications where matrix elements vary based on the spatial configuration of receivers and transmitters, could significantly enhance model accuracy and applicability.

Incorporating the previously refined channel models into our proposed BF-based cabin controller, with a particular emphasis on accounting for reflections, could significantly enhance our prediction and understanding of the throughput and thereby also allow a more accurate optimization. Additionally, the controller could leverage advancements in intelligent surfaces, which dynamically modify the electrical properties of materials. By doing so, the beam could be strategically reflected off surfaces to concentrate signal strength in targeted areas of the cabin, or absorb the signal to minimize interference.

A thorough analysis of the economic feasibility of MLNs is crucial for their future successful implementation. Therefore, we suggest as new areas of research, the development of a comprehensive cost model to evaluate the viability of MLNs and the monetization potential of computational services provided by MEC servers. Furthermore, optimizing the placement of MEC servers within the network raises critical questions, e.g., should the deployment be based on minimizing latency, minimizing energy, minimizing operational cost or even maximizing earnings from offered computational capacity. This task encompasses not only identifying the most suitable aircraft for server deployment but also the flight plan to achieve the desired goal.

Finally, integrating the insights from all three scopes of this work allows the development of a versatile framework to analyze different properties of the network and the interplay between channel models, resource allocation in BF, and the operation of MLNs. This comprehensive framework would facilitate a deeper exploration of different caching strategies, transmission protocols, medium access protocols, etc. to assess their impact on network efficiency, latency, and energy, further improving the passenger experience. Pursuing these avenues would establish the groundwork of aircraft and cabin communication systems beyond the immediate future generation.

Building on the foundation laid by this thesis, the next chapters in the evolution of aircraft cabin communication are poised to be written, promising a future where the skies offer not just a mode of travel but a pinnacle of digital connectivity and service excellence.

Appendix

Appendix A

Channels

A.1 CDL 3GPP

Table A.1 3GPP CDL Aisle 2.45 GHz

Cluster	Direction	Type	Gain [dB]	MToA [s]	Delay Spread [s]	$\overline{\phi^A}$ [rad]	$\sigma(\phi^A)$ [rad]	$\overline{\theta^A}$ [rad]	$\sigma(\theta^A)$ [rad]	$\overline{\phi^D}$ [rad]	$\sigma(\phi^D)$ [rad]	$\overline{\theta^D}$ [rad]	$\sigma(\theta^D)$ [rad]	MPC
0	Aft	LoS	-34.1	3.6×10^{-11}	2.29×10^{-11}	-3.14	0.012	1.48	0.012	-0.00	0.012	1.66	0.012	6
1	Aft	NLoS	-41	2.03×10^{-9}	1.63×10^{-9}	3.07	0.033	1.48	0.028	1.63	0.081	1.62	0.065	5
2	Aft	NLoS	-41.1	1.78×10^{-9}	5.79×10^{-10}	-3.07	0.023	1.48	0.027	-1.62	0.072	1.62	0.065	8
3	Aft	NLoS	-44.1	1.54×10^{-8}	3.26×10^{-9}	-3.14	0.031	1.52	0.047	-3.13	0.108	1.55	0.137	4
4	Aft	NLoS	-46.3	4.17×10^{-9}	1.43×10^{-9}	-3.08	0.009	1.50	0.009	-2.33	0.072	1.64	0.012	4
5	Aft	NLoS	-48.8	1.37×10^{-9}	2.37×10^{-10}	-3.14	0.010	1.45	0.010	-3.11	0.008	0.02	0.015	8
6	Aft	NLoS	-37.5	9.52×10^{-10}	1.91×10^{-9}	-3.14	0.102	1.53	0.199	0.00	0.124	1.62	0.209	6
7	Aft	NLoS	-55.1	3.78×10^{-8}	1×10^{-8}	0.03	0.066	1.61	0.107	0.01	0.021	1.64	0.042	3
8	Aft	NLoS	-60.7	4.18×10^{-9}	1.67×10^{-9}	-3.08	0.009	1.53	0.005	-0.80	0.042	1.73	0.016	3
9	Aft	NLoS	-45.7	6.93×10^{-9}	3.82×10^{-9}	3.08	0.015	1.50	0.014	2.35	0.088	1.63	0.028	3
10	Aft	NLoS	-60.6	3.97×10^{-9}	1.88×10^{-9}	3.07	0.007	1.54	0.004	0.79	0.056	1.73	0.018	3

Table A.2 3GPP CDL Screens 2.45 GHz with humans

Cluster	Direction	Type	Gain [dB]	MToA [s]	Delay Spread [s]	$\overline{\phi^A}$ [rad]	$\sigma(\phi^A)$ [rad]	$\overline{\theta^A}$ [rad]	$\sigma(\theta^A)$ [rad]	$\overline{\phi^D}$ [rad]	$\sigma(\phi^D)$ [rad]	$\overline{\theta^D}$ [rad]	$\sigma(\theta^D)$ [rad]	MPC
1	Aft	NLoS	-81	1.12×10^{-8}	1.48×10^{-9}	-0.60	0.048	1.01	0.043	-0.11	0.028	1.80	0.014	2
2	Aft	NLoS	-81.5	1.21×10^{-8}	5.29×10^{-10}	0.08	0.018	0.80	0.015	-0.09	0.012	1.79	0.006	1
3	Aft	NLoS	-77.9	6.89×10^{-9}	7.22×10^{-10}	1.01	0.046	0.90	0.066	0.21	0.031	1.87	0.014	2
4	Aft	NLoS	-75.7	4.79×10^{-9}	3.98×10^{-10}	-1.14	0.020	1.01	0.038	-0.25	0.019	1.88	0.011	2
5	Aft	NLoS	-87.4	1.17×10^{-8}	3.51×10^{-10}	0.11	0.008	1.25	0.008	-0.10	0.011	1.82	0.006	1
6	Aft	NLoS	-77.4	2.75×10^{-9}	4.9×10^{-10}	1.05	0.032	1.70	0.022	0.02	0.029	1.89	0.009	3
7	Aft	NLoS	-83.3	5.48×10^{-9}	2.42×10^{-10}	-0.77	0.011	0.59	0.010	-0.14	0.011	1.84	0.004	1
8	Aft	NLoS	-88.4	3.27×10^{-9}	4.35×10^{-10}	-0.83	0.026	1.51	0.017	0.15	0.015	1.86	0.008	1
9	Aft	NLoS	-87.2	9.05×10^{-9}	2.28×10^{-10}	-0.11	0.008	0.88	0.009	0.10	0.010	1.77	0.003	1
10	Aft	NLoS	-82.5	5.88×10^{-9}	2.85×10^{-10}	-0.19	0.016	0.48	0.011	0.20	0.015	1.86	0.007	1
11	Aft	NLoS	-94.3	1.57×10^{-8}	2×10^{-10}	0.36	0.005	1.15	0.004	0.04	0.004	1.71	0.002	1
12	Aft	NLoS	-88	1.66×10^{-8}	3.33×10^{-10}	-0.13	0.007	1.40	0.006	-0.16	0.007	1.71	0.006	2
13	Aft	NLoS	-87.4	1.67×10^{-8}	2.17×10^{-10}	0.14	0.007	1.39	0.006	0.16	0.007	1.72	0.006	2
14	Aft	NLoS	-81.8	9.54×10^{-9}	4.5×10^{-10}	-0.31	0.009	1.32	0.012	-0.31	0.013	1.82	0.016	1
15	Aft	NLoS	-83.1	9.84×10^{-9}	3.24×10^{-10}	0.30	0.009	1.34	0.009	0.30	0.013	1.82	0.013	1
0	Cockpit	LoS	-47.4	3.79×10^{-10}	1.96×10^{-10}	0.00	0.027	1.03	0.019	-3.14	0.027	2.11	0.019	1
1	Cockpit	NLoS	-67.4	1.72×10^{-9}	6.74×10^{-10}	0.18	0.067	1.29	0.041	2.81	0.038	1.84	0.041	3
2	Cockpit	NLoS	-67.4	1.62×10^{-9}	6.46×10^{-10}	-0.14	0.070	1.29	0.032	-2.82	0.036	1.83	0.038	3
3	Cockpit	NLoS	-69.5	1.02×10^{-8}	2.13×10^{-10}	0.36	0.015	1.23	0.016	0.66	0.029	2.33	0.022	1
4	Cockpit	NLoS	-65.9	2.49×10^{-9}	2.14×10^{-10}	0.14	0.012	1.03	0.011	2.69	0.013	1.88	0.012	2
5	Cockpit	NLoS	-81.7	1.34×10^{-8}	2.51×10^{-10}	-0.20	0.006	1.33	0.006	-0.43	0.017	2.18	0.014	1
6	Cockpit	NLoS	-71.7	1.02×10^{-8}	1.63×10^{-10}	-0.20	0.009	1.29	0.007	-0.75	0.021	2.30	0.015	1
7	Cockpit	NLoS	-76	2.99×10^{-9}	2.35×10^{-10}	0.25	0.010	1.19	0.010	3.08	0.011	2.04	0.008	2

Table A.3 3GPP CDL Seats 2.45 GHz with humans

Cluster	Direction	Type	Gain [dB]	MToA [s]	Delay Spread [s]	$\overline{\phi^A}$ [rad]	$\sigma(\phi^A)$ [rad]	$\overline{\theta^A}$ [rad]	$\sigma(\theta^A)$ [rad]	$\overline{\phi^D}$ [rad]	$\sigma(\phi^D)$ [rad]	$\overline{\theta^D}$ [rad]	$\sigma(\theta^D)$ [rad]	MPC
0	Aft	LoS	-30.8	3.69×10^{-10}	1.79×10^{-10}	3.14	0.037	0.82	0.026	-0.00	0.037	2.32	0.026	3
1	Aft	NLoS	-59.3	4.39×10^{-9}	6.36×10^{-10}	1.27	0.037	1.54	0.038	0.11	0.033	1.90	0.015	3
2	Aft	NLoS	-69.9	1.03×10^{-8}	1.68×10^{-9}	-0.26	0.071	0.86	0.040	-0.01	0.035	1.78	0.011	2
3	Aft	NLoS	-59.9	3.23×10^{-9}	7.11×10^{-10}	2.22	0.072	1.36	0.044	0.13	0.031	1.88	0.016	3
4	Aft	NLoS	-60.1	3.14×10^{-9}	1.14×10^{-9}	-1.84	0.214	1.40	0.069	-0.08	0.045	1.85	0.021	4
5	Aft	NLoS	-73.4	8.95×10^{-9}	4.34×10^{-10}	1.23	0.019	0.64	0.025	0.13	0.015	1.81	0.008	1
6	Aft	NLoS	-68.6	5.76×10^{-9}	6.32×10^{-10}	2.15	0.040	0.65	0.035	0.09	0.027	1.84	0.017	2
7	Aft	NLoS	-61.6	2.43×10^{-9}	2.38×10^{-10}	-2.85	0.026	1.20	0.011	0.15	0.013	1.87	0.005	2
8	Aft	NLoS	-75.5	5.9×10^{-9}	4.54×10^{-10}	-2.66	0.016	0.93	0.014	-0.06	0.011	1.75	0.006	1
9	Aft	NLoS	-78.1	6.6×10^{-9}	3.42×10^{-10}	-0.48	0.012	0.28	0.015	-0.04	0.008	1.74	0.003	1
10	Aft	NLoS	-63.2	3.01×10^{-9}	2.63×10^{-10}	2.45	0.019	1.22	0.013	-0.17	0.014	1.85	0.005	2
0	Cockpit	LoS	-31.2	3.56×10^{-10}	1.84×10^{-10}	-0.00	0.034	0.87	0.023	3.14	0.034	2.27	0.023	3
1	Cockpit	NLoS	-57.7	1.05×10^{-8}	3.52×10^{-10}	0.30	0.025	1.12	0.020	0.61	0.043	2.36	0.029	2
2	Cockpit	NLoS	-50.9	1.95×10^{-9}	5.4×10^{-10}	3.10	0.065	0.85	0.053	-3.13	0.041	1.86	0.029	3
3	Cockpit	NLoS	-55.2	1.91×10^{-9}	8.22×10^{-10}	0.06	0.101	1.12	0.068	3.14	0.065	1.89	0.053	3
4	Cockpit	NLoS	-57.2	1.25×10^{-8}	8.58×10^{-10}	-0.26	0.025	1.17	0.019	-0.42	0.040	2.27	0.043	2
5	Cockpit	NLoS	-68.5	4.27×10^{-9}	5.11×10^{-10}	-2.17	0.042	1.14	0.022	-3.07	0.018	1.76	0.006	2
6	Cockpit	NLoS	-68.2	3.23×10^{-9}	6.07×10^{-10}	-1.06	0.048	1.41	0.028	-3.07	0.024	1.79	0.010	2
7	Cockpit	NLoS	-75	5.16×10^{-9}	4.06×10^{-10}	1.28	0.018	1.55	0.016	3.09	0.010	1.76	0.004	3
8	Cockpit	NLoS	-76.8	4.93×10^{-9}	2.48×10^{-10}	-2.39	0.011	0.42	0.012	3.10	0.008	1.72	0.002	1

Table A.4 3GPP CDL Screens 5.16 GHz with humans

Cluster	Direction	Type	Gain [dB]	MToA [s]	Delay Spread [s]	$\overline{\phi^A}$ [rad]	$\sigma(\phi^A)$ [rad]	$\overline{\theta^A}$ [rad]	$\sigma(\theta^A)$ [rad]	$\overline{\phi^D}$ [rad]	$\sigma(\phi^D)$ [rad]	$\overline{\theta^D}$ [rad]	$\sigma(\theta^D)$ [rad]	MPC
1	Aft	NLoS	-85.1	8.57×10^{-9}	4.72×10^{-10}	-0.65	0.012	0.74	0.022	-0.15	0.011	1.89	0.007	1
2	Aft	NLoS	-82.4	4.34×10^{-9}	2.11×10^{-10}	-1.12	0.019	1.02	0.031	-0.29	0.012	1.90	0.010	2
3	Aft	NLoS	-85.4	6.08×10^{-9}	4.58×10^{-10}	1.02	0.029	0.89	0.049	0.25	0.021	1.89	0.013	2
4	Aft	NLoS	-86.7	1.43×10^{-8}	3.02×10^{-10}	0.09	0.012	0.71	0.009	-0.04	0.008	1.82	0.003	2
5	Aft	NLoS	-89	1.03×10^{-8}	3.32×10^{-10}	-0.80	0.010	1.15	0.013	-0.20	0.009	1.86	0.004	1
6	Aft	NLoS	-84.2	2.41×10^{-9}	1.09×10^{-10}	1.05	0.007	1.66	0.008	0.09	0.008	1.90	0.004	3
7	Aft	NLoS	-87.5	7.71×10^{-9}	2.98×10^{-10}	0.24	0.010	1.34	0.012	0.26	0.010	1.86	0.011	1
8	Aft	NLoS	-89.1	1.38×10^{-8}	3.62×10^{-10}	0.42	0.012	0.95	0.009	0.05	0.008	1.79	0.003	1
9	Aft	NLoS	-86.2	2.39×10^{-9}	1.03×10^{-10}	1.11	0.006	1.73	0.005	-0.11	0.008	1.95	0.003	3
10	Aft	NLoS	-88.5	1.13×10^{-8}	4.25×10^{-10}	-0.20	0.010	1.13	0.009	0.10	0.010	1.97	0.007	1
11	Aft	NLoS	-88.1	1.17×10^{-8}	4.16×10^{-10}	0.23	0.009	1.14	0.013	-0.07	0.011	1.98	0.013	1
12	Aft	NLoS	-84.1	1.67×10^{-9}	1.23×10^{-10}	-0.43	0.014	1.70	0.006	-0.18	0.007	1.86	0.003	1
13	Aft	NLoS	-87.6	1.37×10^{-8}	1.95×10^{-10}	-0.30	0.012	0.81	0.010	0.10	0.006	1.75	0.003	1
14	Aft	NLoS	-89.8	1.59×10^{-8}	1.76×10^{-10}	-0.41	0.006	0.99	0.008	-0.12	0.006	1.79	0.004	1
15	Aft	NLoS	-88.1	1.03×10^{-8}	1.13×10^{-10}	-0.32	0.006	1.41	0.011	-0.30	0.014	1.75	0.021	3
0	Cockpit	LoS	-53.8	1.86×10^{-10}	9.47×10^{-11}	0.00	0.013	1.03	0.009	-3.14	0.013	2.11	0.009	1
1	Cockpit	NLoS	-72.9	6.15×10^{-9}	1.94×10^{-10}	0.24	0.011	1.31	0.007	1.41	0.016	2.46	0.017	1
2	Cockpit	NLoS	-72.8	1.62×10^{-9}	6.57×10^{-10}	0.13	0.074	1.27	0.038	2.78	0.038	1.82	0.041	3
3	Cockpit	NLoS	-73.2	1.7×10^{-9}	6.82×10^{-10}	-0.11	0.071	1.28	0.032	-2.77	0.036	1.82	0.039	3
4	Cockpit	NLoS	-74.3	1.03×10^{-8}	1.85×10^{-10}	0.37	0.013	1.21	0.014	0.59	0.025	2.36	0.019	2
5	Cockpit	NLoS	-81.4	6.86×10^{-9}	6.05×10^{-10}	-0.75	0.014	1.31	0.020	-2.87	0.013	1.89	0.010	2
6	Cockpit	NLoS	-82.4	9.91×10^{-9}	1.38×10^{-10}	-0.19	0.010	1.25	0.007	-0.75	0.015	2.32	0.013	2
7	Cockpit	NLoS	-70.6	5.34×10^{-9}	5.95×10^{-11}	-0.23	0.007	1.29	0.008	-1.21	0.015	2.75	0.016	1

Table A.5 3GPP CDL Seats 5.16 GHz with humans

Cluster	Direction	Type	Gain [dB]	MToA [s]	Delay Spread [s]	$\overline{\phi^A}$ [rad]	$\sigma(\phi^A)$ [rad]	$\overline{\theta^A}$ [rad]	$\sigma(\theta^A)$ [rad]	$\overline{\phi^D}$ [rad]	$\sigma(\phi^D)$ [rad]	$\overline{\theta^D}$ [rad]	$\sigma(\theta^D)$ [rad]	MPC
0	Aft	LoS	-37.3	1.82×10^{-10}	8.51×10^{-11}	3.14	0.017	0.82	0.012	-0.00	0.017	2.32	0.012	3
1	Aft	NLoS	-69.6	3.84×10^{-9}	4.22×10^{-10}	1.25	0.027	1.55	0.029	0.08	0.022	1.86	0.010	3
2	Aft	NLoS	-62.8	3.84×10^{-9}	1.47×10^{-10}	2.70	0.010	1.21	0.011	-0.09	0.011	2.16	0.008	2
3	Aft	NLoS	-67.4	3.08×10^{-9}	6.82×10^{-10}	2.22	0.063	1.36	0.043	0.13	0.025	1.89	0.016	3
4	Aft	NLoS	-78.6	1.28×10^{-8}	8.72×10^{-10}	-0.52	0.026	0.87	0.024	-0.12	0.012	1.79	0.008	1
5	Aft	NLoS	-67	2.98×10^{-9}	9.45×10^{-10}	-2.38	0.080	1.24	0.066	-0.10	0.032	1.87	0.020	3
6	Aft	NLoS	-78.9	8.93×10^{-9}	1.99×10^{-10}	1.26	0.011	0.52	0.016	0.12	0.008	1.85	0.005	2
7	Aft	NLoS	-78.2	8.98×10^{-9}	5.1×10^{-10}	0.00	0.018	0.79	0.015	0.12	0.009	1.78	0.004	2
8	Aft	NLoS	-73.9	3.93×10^{-9}	6.62×10^{-10}	-1.15	0.056	1.52	0.033	-0.03	0.031	1.86	0.012	3
9	Aft	NLoS	-78.5	5.62×10^{-9}	3.45×10^{-10}	2.24	0.025	0.56	0.020	0.16	0.011	1.86	0.010	2
10	Aft	NLoS	-77.2	5.09×10^{-9}	3.3×10^{-10}	1.79	0.015	2.02	0.011	0.04	0.011	2.07	0.006	2
11	Aft	NLoS	-83.6	5.74×10^{-9}	2.74×10^{-10}	-0.22	0.019	0.32	0.014	-0.12	0.008	1.78	0.003	1
0	Cockpit	LoS	-37.6	1.75×10^{-10}	8.74×10^{-11}	-0.00	0.016	0.87	0.011	3.14	0.016	2.27	0.011	2
1	Cockpit	NLoS	-64.6	1.07×10^{-8}	2.94×10^{-10}	0.31	0.023	1.14	0.019	0.61	0.034	2.35	0.023	3
2	Cockpit	NLoS	-55.9	1.58×10^{-9}	5.21×10^{-10}	3.12	0.065	0.84	0.044	-3.14	0.045	1.87	0.029	4
3	Cockpit	NLoS	-61.8	2.06×10^{-9}	6.95×10^{-10}	0.02	0.062	1.12	0.053	-3.12	0.049	1.94	0.052	3
4	Cockpit	NLoS	-68.6	1.08×10^{-8}	2.11×10^{-10}	2.81	0.016	0.77	0.013	0.61	0.024	2.35	0.021	2
5	Cockpit	NLoS	-63.5	1.25×10^{-8}	6.35×10^{-10}	-0.24	0.020	1.18	0.015	-0.41	0.028	2.28	0.034	2
6	Cockpit	NLoS	-75.3	3.87×10^{-9}	3.43×10^{-10}	-2.20	0.031	1.15	0.015	-3.06	0.014	1.76	0.005	2
7	Cockpit	NLoS	-77	2.67×10^{-9}	3.49×10^{-10}	-1.18	0.019	1.41	0.019	-3.10	0.017	1.79	0.008	3
8	Cockpit	NLoS	-74.8	6.48×10^{-9}	1.38×10^{-10}	2.90	0.006	0.83	0.007	1.39	0.015	2.47	0.018	1

A.2 CDL Predictor-based Models

Table A.6 Aisle CDL-Model Property Equations for 2.45 GHz

Cluster	Direction	Type	Gain [dB]	MToA [s]	Delay Spread [s]	MPC
0	Aft	LoS	$-22.8 - 19.4\log_{10}(d)$	$1.29\times10^{-10} - 4.62\times10^{-11}\log(d)$	$8.93\times10^{-11} - 2.96\times10^{-11}\log(d)$	6.87
1	Aft	NLoS	$-30.6 - 15.4\log_{10}(d)$	$6.19\times10^{-12}d + 1.97\times10^{-9}$	$2.21\times10^{-9} - 1.93\times10^{-9}e^{-0.137d}$	$\lfloor 4.48 + 0.846\log_{10}(d)\rfloor$
2	Aft	NLoS	$-30.9 - 15.3\log_{10}(d)$	$1.9\times10^{-9} - 6.05\times10^{-11}\log(d)$	$6.07\times10^{-10} - 4.19\times10^{-10}\sin(0.372d + 6.09)$	$\lfloor 7.55 + 15.3e^{-0.687d}\rfloor$
3	Aft	NLoS	$-39.2 - 0.579d$	$1.56\times10^{-8} - 1.4\times10^{-11}d$	$3.3\times10^{-9} - 4.81\times10^{-8}e^{-4.17d}$	$\lfloor 4.92 - 0.739\sin(0.724d + 0.773)\rfloor$
4	Aft	NLoS	$-39.8 - 0.984d$	$4.26\times10^{-9} - 1.05\times10^{-12}e^{0.318d}$	$1.73\times10^{-9} - 6.77\times10^{-12}e^{0.264d}$	$\lfloor 3.66 + 4.48e^{-0.312d}\rfloor$
5	Aft	NLoS	$-44.4 - 0.479d$	$1.69\times10^{-9} - 1.37\times10^{-10}\log(d)$	2.37×10^{-10}	$\lfloor 9.26 - 1.89\sin(0.81d - 0.127)\rfloor$
6	Aft	NLoS	$-23.4 - 17.2\log_{10}(d)$	$1.39\times10^{-9} - 1.94\times10^{-10}\log(d)$	$2.54\times10^{-9} - 2.05\times10^{-9}\sin(0.204d - 6.28)$	$\lfloor 6.85 + 2.65\sin(0.443d + 2.98)\rfloor$
7	Aft	NLoS	$-46.8 - 12.9\sin(0.109d + 6.2832)$	$1.15\times10^{-8}\log(d) + 9.2\times10^{-9}$	1.01×10^{-8}	$\lfloor 1.68 + 1.6\log_{10}(d)\rfloor$
8	Aft	NLoS	$-62.9 - 5.49\sin(0.42d + 4.95)$	$8.58\times10^{-9} - 3.32\times10^{-10}d$	$2.16\times10^{-9} - 6.48\times10^{-9}e^{-0.262d}$	$\lfloor -1.41 + 4.26\log_{10}(d)\rfloor$
9	Aft	NLoS	$-35.9 - 13.6\log_{10}(d)$	$1.02\times10^{-8} - 7.47\times10^{-9}e^{-0.0857d}$	$4.64\times10^{-9} - 6.3\times10^{-9}e^{-0.303d}$	$\lfloor 3.3 + 2.7\times10^{6}e^{-13.9d}\rfloor$
10	Aft	NLoS	$-62.6 - 5.03\sin(0.412d + 5.17)$	$8.71\times10^{-9} - 3.42\times10^{-10}d$	$2.18\times10^{-9} - 7.17\times10^{-9}e^{-0.291d}$	$\lfloor -1.12 + 4.29\log_{10}(d)\rfloor$

Cluster	$\overline{\phi^A}$ [rad]	$\overline{\phi^D}$ [rad]	$\overline{\theta^A}$ [rad]	$\overline{\theta^D}$ [rad]
0	rot(−0.000547)	−0.000547	$\mathrm{rot}(-1.61 - 0.689e^{-0.493d})$	$1.61 + 0.689e^{-0.493d}$
1	$\mathrm{rot}(-0.0324 - 0.566e^{-0.496d})$	$1.62 + 0.123e^{-0.363d}$	$\mathrm{rot}(-1.61 - 0.34e^{-0.277d})$	$1.58 + 0.558e^{-0.559d}$
2	$\mathrm{rot}(0.0328 + 0.562e^{-0.48d})$	$-1.61 - 0.122e^{-0.336d}$	$\mathrm{rot}(-1.61 - 0.342e^{-0.284d})$	$1.58 + 0.52e^{-0.495d}$
3	$\mathrm{rot}(0.00964 - 0.000557d)$	$\mathrm{rot}(0.0151 - 0.00614\sin(0.705d + 0.161))$	$\mathrm{rot}(-1.6 - 0.183e^{-0.312d})$	$1.55 - 0.0197\sin(-0.302d + 6.2832)$
4	$\mathrm{rot}(0.0287 + 0.396e^{-0.421d})$	$-2.36 + 0.0371\log_{10}(d)$	$\mathrm{rot}(-1.6 - 0.277e^{-0.294d})$	$1.6 + 0.281e^{-0.296d}$
5	rot(0.000469)	rot(0.0244)	$\mathrm{rot}(-1.63 - 0.641e^{-0.311d})$	$\mathrm{rot}(-3.11 - 0.00711\log_{10}(d))$
6	$\mathrm{rot}(-0.0115 + 0.0132\log_{10}(d))$	$0.0119 - 0.0127\log_{10}(d)$	$\mathrm{rot}(-1.56 - 1.68e^{-0.626d})$	$\mathrm{rot}(-1.5 - 0.945e^{-0.66d})$
7	$0.12 - 0.00676d$	$0.0582 - 0.0466\log_{10}(d)$	$1.52 + 0.687e^{-0.257d}$	$1.6 + 0.607e^{-0.404d}$
8	$\mathrm{rot}(0.053 + 1.76e^{-0.804d})$	$\mathrm{rot}(2.32 + 0.58e^{-0.431d})$	$\mathrm{rot}(-1.73 + 0.109\log_{10}(d))$	$\mathrm{rot}(-1.41 - 0.357e^{-0.501d})$
9	$\mathrm{rot}(-0.0264 - 0.434e^{-0.469d})$	$\mathrm{rot}(-0.784 + 0.0104\sin(-0.149d + 6.2832))$	$\mathrm{rot}(-1.6 - 0.281e^{-0.294d})$	$1.6 + 0.291e^{-0.328d}$
10	$\mathrm{rot}(-0.0328 - 0.212e^{-0.16d})$	$\mathrm{rot}(-2.33 - 0.495e^{-0.398d})$	$\mathrm{rot}(-1.59 - 0.155e^{-0.231d})$	$\mathrm{rot}(-1.41 - 0.33e^{-0.451d})$

Cluster	$\sigma(\phi^A)$ [rad]	$\sigma(\phi^D)$ [rad]	$\sigma(\theta^A)$ [rad]	$\sigma(\theta^D)$ [rad]	Limits [m]
0	$0.00562 + 0.0965e^{-0.514d}$	$0.00562 + 0.0965e^{-0.514d}$	$0.00532 + 0.0797e^{-0.45d}$	$0.00532 + 0.0797e^{-0.45d}$	$d = [1, 21]$
1	$0.0872 - 0.0581\log_{10}(d)$	$0.0748 + 0.0286e^{-0.207d}$	$0.0508 - 0.00205d$	$0.106 - 0.00364d$	$d = [1, 21]$
2	$0.0314 - 0.000894d$	$0.0642 + 0.0391e^{-0.211d}$	$0.0465 - 0.00178d$	$0.0981 - 0.00301d$	$d = [1, 21]$
3	$-0.00561 + 0.0724e^{-0.072d}$	$0.107 - 0.01\sin(0.756d + 1.3)$	$0.0376 + 0.166e^{-0.637d}$	$0.136 + 0.0269\sin(0.75d + 1.28)$	$d = [1, 21]$
4	$0.01 + 0.00832\sin(0.528d + 1.17)$	$0.0756 - 0.000306d$	$0.0233 - 0.0149\log_{10}(d)$	$0.0267 - 0.0158\log_{10}(d)$	$d = [1, 21]$
5	$0.0154 - 0.00053d$	$0.012 - 0.000367d$	$0.00783 + 1.66\times10^{-14}e^{1.34d}$	$0.0155 + 0.00502\sin(0.412d + 4.16)$	$d = [2, 21]$
6	$0.047 + 0.598e^{-0.331d}$	$0.0487 + 0.774e^{-0.32d}$	$0.309 - 0.00946d$	$0.0987 + 0.397e^{-0.136d}$	$d = [2, 21]$
7	0.0677	$0.0222 - 0.01\sin(0.268d + 3.88)$	$0.114 - 0.0449\sin(0.948d - 0.847)$	$0.0455 - 0.0152\sin(0.965d - 0.654)$	$d = [2, 21]$
8	$0.0279 - 0.00125d$	$0.0454 + 0.0189\sin(0.503d + 1.91)$	$0.0138 - 0.000583d$	$0.0155 + 0.00509\sin(0.968d - 3.27)$	$d = [3, 21]$
9	$0.0244 - 0.000889d$	$0.0719 + 0.0169\log_{10}(d)$	$0.0259 - 0.00113d$	$0.0556 - 0.00266d$	$d = [1, 21]$
10	$0.00728 + 0.00553\sin(0.435d + 3.06)$	$0.0521 + 0.0214\sin(0.506d + 2.14)$	$0.00654 - 0.00018d$	0.0156	$d = [3, 21]$

Table A.7 Screens CDL-Model Property Equations for 2.45 GHz with humans

Cluster	Direction	Type	Gain [dB]	MToA [s]	Delay Spread [s]	MPC
1	Aft	NLoS	$-89.7 + 8.67\sin(0.271r + 1.31) - 4.28\sin(0.861s - 1.26)$	$2.39\times10^{-9}\sin(0.898s + 0.183) - 1.2\times10^{-9}r + 1.75\times10^{-8}$	$1.5\times10^{-5}\sin(0.00364s + 1.57) - 8.98\times10^{-10}\sin(0.369r + 3.01) - 1.5\times10^{-5}$	$\lfloor 1.47 - 0.858\sin(0.388r + 2.69) + 0.512\sin(4.18s + 10.4)\rfloor$
2	Aft	NLoS	$-76.1 - 8.3\log(r) - 3.38\sin(1.85s + 3.07)$	$1.21\times10^{-9}s - 1.32\times10^{-9}r + 1.9\times10^{-8}$	$3.71\times10^{-10}\sin(4.22s + 3.48) + 2.82\times10^{-10}\sin(0.964r - 0.634) + 3.89\times10^{-10}$	$\lfloor 2.33 - 1.02\sin(0.537r + 0.936) + 1.34\sin(1.35s + 0.897)\rfloor$
3	Aft	NLoS	$-89.1 + 9.06\sin(0.358r + 0.884) + 4.82\sin(0.844s + 0.653)$	$8.89\times10^{-9} - 4.28\times10^{-9}\sin(0.688s - 0.0765) - 2.97\times10^{-10}r$	7.5×10^{-10}	$\lfloor 1.54 + 1.41\sin(0.629r - 0.872) + 0.957\sin(0.737s + 0.223)\rfloor$
4	Aft	NLoS	$-78.8 - 1.92r - 8.03\sin(0.923s - 0.18)$	$3.0\times10^{-9}\sin(0.603s + 0.382) - 6.22\times10^{-10}r + 8.24\times10^{-9}$	$9.2\times10^{-12}r + 5.49\times10^{-11}s + 4.11\times10^{-10}$	$\lfloor 1.31 + 1.03\sin(0.875r - 1.64) - 1.24\sin(1.07s + 0.0589)\rfloor$
5	Aft	NLoS	$-84.6 - 1.2r - 5.4\sin(2.63s + 17.1)$	1.34×10^{-8}	4.4×10^{-10}	1.61
6	Aft	NLoS	$-92.7 + 9.57\sin(0.391r + 0.201) - 6.07\sin(0.894s - 0.408)$	$3.99\times10^{-10}\log(\lvert s\rvert) - 2.99\times10^{-9}\log(r) + 7.69\times10^{-9}$	$4.48\times10^{-10} - 9.57\times10^{-11}s - 2.68\times10^{-11}r$	$\lfloor 1.02 - 2.27\sin(0.505r + 2) - 1.65\sin(0.812s - 0.236)\rfloor$
7	Aft	NLoS	$-86.8 + 0.273r - 6.68\log(\lvert s\rvert)$	$3.38\times10^{-9}\sin(1.14s + 0.515) - 1.05\times10^{-9}r + 1.11\times10^{-8}$	$3.04\times10^{-10} - 2.09\times10^{-11}e^{0.567\lvert s\rvert} - 9.97\times10^{-9}e^{-1.81r}$	1.22
8	Aft	NLoS	$-84.6 - 0.943r - 245e^{-3.18\lvert s\rvert}$	$1.59\times10^{-8} - 3.27\times10^{-9}\lvert s\rvert - 8.87\times10^{-10}r$	5.17×10^{-10}	1.49
9	Aft	NLoS	$-92.9 + 5.73\sin(1.34r - 2.73) - 7.83\sin(4.9s + 14.8)$	$2.17\times10^{-8} - 1.84\times10^{-9}s - 1.92\times10^{-9}r$	$3.45\times10^{-11}\sin(4.62s + 5.52) - 1.1\times10^{-8}e^{-1.98r} + 2.11\times10^{-10}$	1
10	Aft	NLoS	-87.2	$7.05\times10^{-9} - 5.32\times10^{-9}\sin(0.994s - 0.936) - 8.34\times10^{-10}\sin(1.5r + 3.12)$	$3.99\times10^{-11}r - 4.36\times10^{-11}s + 1.38\times10^{-10}$	$\lfloor 0.398 + 1.1\log(r) - 0.882\log(\lvert s\rvert)\rfloor$
11	Aft	NLoS	$-73.4 + 5.6\sin(0.585r + 0.851) - 26.8\sin(0.541\lvert s\rvert + 0.608)$	$3.4\times10^{-8} - 1.13\times10^{-9}s - 2.52\times10^{-9}r$	$3.36\times10^{-12}r + 4.3\times10^{-11}\lvert s\rvert + 6.54\times10^{-11}$	1
12	Aft	NLoS	$-88.5 + 0.0603r - 6.83\log(\lvert s\rvert)$	$3.98\times10^{-9}s - 2.42\times10^{-9}r + 2.94\times10^{-8}$	$6.87\times10^{-10} - 8.74\times10^{-10}\sin(1.26s - 1.0) - 1.07\times10^{-11}r$	$\lfloor 2.44 + 2.34\times10^{-15}e^{1.9r} - 3.36\sin(1.22s - 0.975)\rfloor$
13	Aft	NLoS	$-81.9 - 3.6\log(r) + 9.69\sin(-1.37s - 4.32)$	$2.84\times10^{-8} - 2.45\times10^{-9}s - 2.1\times10^{-9}r$	2.29×10^{-10}	$\lfloor 3.97 + 1.53\times10^{-15}e^{1.92r} + 5.8\sin(1.24s + 1.06)\rfloor$
14	Aft	NLoS	$-90 - 9.8\sin(0.903r - 2.1) + 8.81\sin(1.01s - 1.38)$	$9.07\times10^{-9}\sin(0.742r - 1.27) + 8.27\times10^{-9}\sin(0.93s + 0.478) + 6.68\times10^{-9}$	3.73×10^{-10}	$\lfloor 85.2 - 1.32\sin(1.3r - 2.44) + 84.5\sin(0.0573s - 1.49)\rfloor$
15	Aft	NLoS	-89.5	$2.49\times10^{-8} - 5.15\times10^{-9}\sin(0.918s - 0.543) - 9.0\times10^{-9}\log(r)$	3.1×10^{-10}	1.76
0	Cockpit	LoS	$-68.6 + 30.2\sin(0.25r + 1.87) + 3.96\sin(11.4s + 17.3)$	$4.63\times10^{-10} - 2.55\times10^{-10}e^{-0.713\lvert s\rvert} - 2.61\times10^{-13}e^{0.652r}$	$-1.35\times10^{-6}\sin(0.00197r + 4.7) - 2.54\times10^{-11}\sin(2.44s - 33.0) - 1.35\times10^{-6}$	$\lfloor 2.43 - 0.332r + 0.012e^{1.71\lvert s\rvert}\rfloor$
1	Cockpit	NLoS	$-59 - 1.75r - 2.44\log(\lvert s\rvert)$	$2.87\times10^{-10}e^{-0.363s} - 1.14\times10^{-9}\log(r) + 3.8\times10^{-9}$	$1.59\times10^{-9} - 4.77\times10^{-10}e^{0.0508r} - 2.99\times10^{-13}e^{2.42s}$	$\lfloor 2.42\times10^{4} - 1.03\sin(1.1r - 1.69) - 2.42\times10^{4}\sin(0.00153s + 1.56)\rfloor$
2	Cockpit	NLoS	$-59.5 - 1.93r - 2.07\sin(0.78s - 0.885)$	$1.58\times10^{-10}s - 9.27\times10^{-11}r + 2.45\times10^{-9}$	$4.78\times10^{-7} - 4.77\times10^{-7}e^{8.94\times10^{-5}r} - 6.21\times10^{-6}\sin(3.14s - 3.14)$	$\lfloor 3.86 - 0.0878r + 1.43\times10^{-12}e^{9.17s}\rfloor$
3	Cockpit	NLoS	$-66.9 - 1.78r - 2.72\sin(1.67s - 0.504)$	$-1.56\times10^{-9}\sin(0.446r + 2.36) - 1.51\times10^{-6}\sin(0.0071s - 1.52) - 1.5\times10^{-6}$	$1.1\times10^{-10} - 1.05\times10^{-10}\sin(23.6\lvert s\rvert - 67.2) - 1.31\times10^{-10}\sin(0.378r + 2.67)$	$\lfloor 2.09 - 0.1r - 0.362s\rfloor$
4	Cockpit	NLoS	$-50.5 - 4.92r + 2.04s$	$2.57\times10^{-9}\log(\lvert s\rvert) - 2.46\times10^{-9}\log(r) + 4.65\times10^{-9}$	2.32×10^{-10}	2.06
5	Cockpit	NLoS	$-80.4 - 3.61\log(r) + 4.9\sin(0.81s + 0.98)$	$1.41\times10^{-9}s - 3.55\times10^{-10}r + 1.48\times10^{-8}$	$4.81\times10^{-11}r + 2.26\times10^{-10}\lvert s\rvert - 5.29\times10^{-10}$	$\lfloor 1.23 + 0.642\sin(0.436r + 2.73) + 0.739\sin(1.55s - 1.67)\rfloor$
6	Cockpit	NLoS	$2.43\times10^{3} - 10.3\log(r) - 2.49\times10^{3}e^{-0.000588s}$	$2.73\times10^{-9}\sin(0.709s + 0.16) - 3.02\times10^{-10}r + 1.18\times10^{-8}$	1.37×10^{-10}	1.24
7	Cockpit	NLoS	$-55.6 - 14.2\log(r) - 4.35\sin(1.23s - 0.066)$	2.77×10^{-9}	2.17×10^{-10}	$\lfloor -0.419 + 0.216r - 1.19\sin(2.14s + 2.39)\rfloor$

Cluster	$\overline{\phi^A}$ [rad]	$\overline{\phi^D}$ [rad]	$\overline{\theta^A}$ [rad]	$\overline{\theta^D}$ [rad]
1	$\mathrm{rot}(2.51 + 0.00543r - 0.0324s)$	$-0.159 + 0.0077r + 0.0427\log(\lvert s\rvert)$	$0.983 - 0.0472\sin(0.694r + 1.07) - 0.056\sin(-2.36s + 20.7)$	$1.62 + 0.349e^{-0.152r} - 0.0163\sin(4.88s + 8.6)$
2	$3.6\times10^{3} + 0.0582\sin(1.27r - 2.38) + 3.6\times10^{3}\sin(0.00349s - 1.57)$	$-0.0863 + 0.0102r - 0.132\sin(4.93s - 14.6)$	$\mathrm{rot}(-2.47 - 0.063\sin(-1.11r + 40.8) - 0.228\sin(0.498\lvert s\rvert + 2.87))$	$\mathrm{rot}(-1.17 - 0.114\log(r) - 6.29\times10^{-13}e^{8.49s})$
3	$\mathrm{rot}(-2.04 - 0.0249r - 0.0538\sin(4.91s - 5.46))$	$-0.124 + 0.617e^{-0.146r} + 0.0398\sin(0.897s + 0.159)$	$0.817 + 1.02e^{-0.775r} + 2.58\times10^{-13}e^{-8.84s}$	$1.67 + 0.645e^{-0.289r} + 0.0318\sin(0.625s - 0.259)$
4	$\mathrm{rot}(1.92 + 0.00633r + 0.00648e^{-1.09s})$	$\mathrm{rot}(2.62 + 0.196\log(r) + 0.0301\sin(-1.84s + 8.26))$	$-363 - 0.112\log(r) + 364\sin(0.0104s + 1.57)$	$\mathrm{rot}(88.7 + 90.1\sin(0.0119r + 4.6) - 0.0319\sin(17.7s + 33.7))$
5	$0.0629 + 0.00727r + 0.00836s$	$-0.0694 + 0.00724r - 0.103\log(\lvert s\rvert)$	$1.26 - 0.00226r - 0.0154s$	$1.84 - 0.00629r + 0.0816\sin(2.3s + 4.29)$
6	$\mathrm{rot}(-2.17 + 0.005r - 0.0307s)$	$-798 + 1.47e^{-0.995r} + 798e^{4.94\times10^{-5}s}$	$1.68 - 0.0662\sin(0.533r + 1.43) + 0.0516\sin(-4.98s - 5.79)$	$1.86 + 0.202\sin(0.285r + 2.12) - 3.29\sin(0.00235s - 0.0262)$
7	$\mathrm{rot}(2.28 + 0.0178r + 0.129\sin(0.995s + 0.848))$	$\mathrm{rot}(2.97 + 0.00755r + 0.0161s)$	$\mathrm{rot}(-2.54 - 0.00478r - 0.0386\sin(-1.58s + 0.887))$	$\mathrm{rot}(-1.11 - 0.0344r + 0.0328\sin(29.4s + 25.4))$
8	$-0.928 + 0.0681\sin(-28.6r + 105) - 0.112\sin(0.706\lvert s\rvert + 2.97)$	$0.249 - 0.0656\log(r) - 0.0564\sin(8.01s + 5)$	$\mathrm{rot}(-1.72 + 0.0809\log(r) - 0.0349\log(\lvert s\rvert))$	$1.57 + 0.618e^{-0.156r} + 4\times10^{-6}e^{-8.65s}$
9	$-0.089 - 0.0516\sin(-0.658r + 10.5) + 0.0458\sin(1.19s + 0.588)$	$0.126 - 0.0385\log(r) + 0.00417e^{1.13s}$	$0.873 + 0.0605\sin(0.905r - 1.27) - 0.0527\sin(-1.88s - 1.96)$	$\mathrm{rot}(-1.2 - 0.1\log(r) - 2.49\times10^{-12}e^{-8.27s})$
10	$-0.584 + 0.378\log(r) - 0.233\log(\lvert s\rvert)$	$\mathrm{rot}(-2.87 - 0.0322r + 0.102\log(\lvert s\rvert))$	$0.473 - 0.00129r + 1.25\times10^{-10}e^{-9.95s}$	$2.16 - 0.173\log(r) + 0.0785\sin(1.59s - 5.31)$
11	0.366	$0.122 - 0.0122r + 0.0107s$	rot(−1.98)	$\mathrm{rot}(-1.34 - 0.0123r + 0.00364s)$
12	$-0.0935 + 0.00368r - 0.0835\log(\lvert s\rvert)$	$-0.134 + 0.0451\sin(0.33r + 3.01) - 0.0306\sin(0.616s - 0.931)$	$1.36 + 0.00599r + 0.00477s$	$740 - 0.0308\sin(0.311r + 3.22) - 738\sin(-0.00482s + 1.57)$
13	$0.0943 - 0.00199r + 0.0968\sin(1.39s - 1.5)$	$0.244 - 0.0461\log(r) - 0.0296\sin(1.04s + 0.729)$	$-63.5 + 0.0481\log(r) + 64.8\sin(6.3s + 20.4)$	$1.29 - 0.0279\log(r) + 0.502\sin(0.433\lvert s\rvert + 0.656)$
14	$-0.361 + 0.0123r - 1.93\times10^{-13}e^{-8.9s}$	$-0.258 - 1.48e^{-1.07r} - 0.000393e^{1.61s}$	$1.23 + 0.0872\log(r) - 0.0257\log(\lvert s\rvert)$	$1.96 + 0.166\sin(0.548r + 1.96) - 0.0545\sin(0.794s + 0.125)$
15	$\mathrm{rot}(-2.01 - 0.394\sin(0.419r - 6.39) - 0.567\sin(0.5\lvert s\rvert + 0.591))$	$\mathrm{rot}(-2.87 - 0.00516r + 0.0601\log(\lvert s\rvert))$	$\mathrm{rot}(-1.87 + 0.0811\log(r) - 0.00153e^{-1.29s})$	$\mathrm{rot}(-1.24 + 0.0914\sin(0.366r + 2.91) + 0.0544\sin(0.788s + 0.051))$
0	$0.00207 - 0.00243r - 0.558\sin(0.665s - 0.0251)$	$\mathrm{rot}(0.00207 - 0.00243r - 0.558\sin(0.665s - 0.0251))$	$\mathrm{rot}(-1.64 - 1.19e^{-0.388r} - 0.268e^{-0.544\lvert s\rvert})$	$1.64 + 1.19e^{-0.388r} + 0.268e^{-0.544\lvert s\rvert}$
1	$-0.106 + 0.823e^{-0.199r} - 0.316\sin(0.462s - 0.552)$	$\mathrm{rot}(-0.199 - 0.85e^{-0.23r} + 0.0897\sin(0.587s + 0.897))$	$1.08 + 0.0965\log(r) + 0.0127\log(\lvert s\rvert)$	$2.09 - 0.119\log(r) + 0.000111\log(\lvert s\rvert)$
2	$-0.442 + 0.186\log(r) - 0.328\sin(0.514s + 0.467)$	$\mathrm{rot}(0.192 + 0.778e^{-0.22r} + 0.079\sin(0.582s - 0.819))$	$\mathrm{rot}(-1.79 - 0.503e^{-0.29r} - 5.93\times10^{3}e^{-13.3\lvert s\rvert})$	$1.76 + 0.795e^{-0.348r} - 0.0165\sin(0.989s + 1.05)$
3	$-0.165 + 0.785e^{-0.135r} + 0.0741e^{-0.441s}$	$\mathrm{rot}(2.15\times10^{3} + 2.15\times10^{3}\sin(0.00147r + 4.7) - 0.0992\sin(1.9s + 9.6))$	$1.3 + 0.141\sin(0.257r + 4.4) - 0.0692\sin(-0.904s - 0.392)$	$2.31 - 0.051\sin(0.347r + 14.5) - 0.032\sin(0.557s - 2.65)$
4	$-0.0652 + 0.0172r + 0.169\sin(1.01\lvert s\rvert - 0.283)$	2.68	1.04	$\mathrm{rot}(-1.29 - 0.0568\sin(0.929r - 2.25) + 0.101\sin(0.827s + 0.603))$
5	$-0.357 + 0.0188r - 0.106\sin(0.718s - 0.757)$	$\mathrm{rot}(2.72 - 0.00524r + 0.0747\sin(0.809s + 0.293))$	$1.24 + 0.0133r - 0.0576\sin(1.04s - 0.626)$	$2.15 + 0.00819r - 0.0304s$
6	$-0.259 + 0.0136r - 0.00608e^{1.13s}$	$\mathrm{rot}(2.43 - 0.00474r + 0.0487\sin(-1.11s - 3.6))$	$\mathrm{rot}(-1.81 + 0.12\sin(0.276r + 3.78) + 0.0785\sin(-206s + 160))$	2.31
7	$0.261 - 0.00382r - 0.0714\sin(0.873s + 0.113)$	$\mathrm{rot}(-0.0721 + 0.0562\sin(0.355r + 2.04) - 0.0141\sin(1.34s + 1.11))$	$1.09 + 0.00958r + 0.0477\sin(14.1s - 6.17)$	$\mathrm{rot}(-1.04 - 0.0186e^{0.127r} - 0.0937\sin(-7.46s - 9.9))$

Cluster	$\sigma(\phi^A)$ [rad]	$\sigma(\phi^D)$ [rad]	$\sigma(\theta^A)$ [rad]	$\sigma(\theta^D)$ [rad]	Limits [m]
1	$0.0248 - 0.033\sin(0.42r + 3) + 0.0311\sin(0.915s + 1.61)$	$0.0433 - 0.00303r + 6.08\sin(-9.42s + 34.6)$	$-0.00809 - 0.0322\sin(0.414r + 2.76) - 0.0539\sin(-0.497s + 11.1)$	$0.0299 - 0.00212r - 0.00883\log(\lvert s\rvert)$	$r = [1, 17]$, $s = [-3, 3]$
2	$0.0308 - 0.00232r + 0.00246s$	$-0.00228 + 0.0253e^{-0.154r} + 0.00721\sin(-1.88s - 2.59)$	$0.0208 - 0.00181r + 0.00964\sin(1.87s - 0.707)$	$0.0126 - 0.00558\log(r) + 0.00452\sin(-1.67s + 10.4)$	$r = [1, 15]$, $s = [-3, 3]$
3	$0.00289 - 0.0288\sin(0.581r + 2.12) + 0.0358\sin(1.01\lvert s\rvert - 0.2)$	$0.0161 - 0.0184\sin(0.451r + 2.8) + 0.00994\sin(0.738s + 0.14)$	$0.0866 - 0.00739r + 0.0267\sin(0.777s + 0.578)$	$0.022 - 0.00185r - 0.000271s$	$r = [1, 13]$, $s = [-3, 3]$
4	$0.00849 + 0.0123\sin(0.918r - 2.11) - 0.00891\sin(1.15s + 0.484)$	$0.0121 + 0.0104\sin(0.976r - 2.14) - 0.00691\sin(1.21s + 0.415)$	$0.0215 + 0.0205\sin(0.802r - 1.31) - 0.0233\sin(0.996s - 0.272)$	$0.0217 - 0.00213r - 0.00354\log(\lvert s\rvert)$	$r = [2, 9]$, $s = [-3, 3]$
5	$0.0114 - 0.000612r - 0.00154s$	$0.0206 - 0.00202r + 7.63\times10^{-5}e^{1.89s}$	0.0099	$0.0115 - 0.00128r + 0.000677e^{1.09s}$	$r = [3, 15]$, $s = [-3, 3]$
6	$0.0318 - 0.00328r - 0.00769s$	$0.0406 - 0.00428r - 0.0064s$	$0.00353 - 0.0147\sin(0.516r + 2.36) - 0.0142\sin(1.23s + 0.987)$	$0.0111 - 0.000929r - 0.00454\sin(0.928s - 0.305)$	$r = [2, 14]$, $s = [-3, 2]$
7	$0.00641 + 0.00441\log(r) + 0.0122\sin(1.24s + 0.964)$	0.0111	$0.0248 - 0.0018r - 0.0114\log(\lvert s\rvert)$	$0.00616 - 0.000392r + 8.32\times10^{-5}s$	$r = [2, 10]$, $s = [-3, 3]$
8	$0.00559 - 0.0193\sin(-0.836r + 33.5) + 0.0233\sin(1.18s - 1.69)$	$0.00687 + 0.00758\sin(0.886r - 2.12) + 0.00778\sin(1.17s - 1.66)$	$0.00861 - 0.000799r + 0.022\log(\lvert s\rvert)$	$0.00956 - 0.000918r + 0.0021s$	$r = [2, 12]$, $s = [-1, 3]$
9	$0.0076 - 0.00591\sin(1.53r - 7.7) - 0.00803\sin(0.949s + 1.19)$	$0.00593 - 0.00296\sin(0.63r + 2.03) - 0.00472\sin(1.4s + 7.47)$	$0.00515 - 0.000257r + 0.00585\log(\lvert s\rvert)$	$0.00285 - 0.000167r + 0.00111\log(\lvert s\rvert)$	$r = [2, 11]$, $s = [-3, 3]$
10	$-0.00139 + 0.0155\log(r) - 0.0202\sin(1.32s - 1.04)$	0.0173	0.0125	0.00777	$r = [2, 8]$, $s = [-2, 3]$
11	0.00404	$0.00172 + 2.79\times10^{-5}r + 1.14\times10^{-13}e^{8.19s}$	0.00296	0.00156	$r = [2, 15]$, $s = [-3, 3]$
12	$0.0129 - 0.000214r - 0.0185\sin(1.23s - 0.933)$	$0.0107 - 0.000347r - 0.00489\sin(1.39s - 1.16)$	$0.0117 - 0.000199r - 0.0133\sin(1.25s - 0.992)$	$0.0102 - 8.72\times10^{-5}r + 1.51\sin(-3.14s + 12.6)$	$r = [3, 19]$, $s = [-2, 3]$
13	0.00762	$4.82\times10^{-5} + 0.0124e^{-0.0487r} - 0.0052\sin(14s + 23.2)$	0.00592	0.00749	$r = [2, 19]$, $s = [-3, 3]$
14	$0.00498 - 0.000408r + 0.000119e^{1.44s}$	$0.00075 - 0.000677r + 0.00616\lvert s\rvert$	0.0115	$0.011 - 0.00115r + 0.000141e^{1.72s}$	$r = [2, 18]$, $s = [-3, 3]$
15	0.00831	0.012	0.00932	$0.012 - 0.000529r - 0.00411s$	$r = [2, 19]$, $s = [-3, 3]$
0	$0.0419 + 0.0337\sin(0.197r + 2.93) - 0.00144\sin(16.7s + 33)$	$0.0273 + 0.0337\sin(0.197r + 2.93) + 0.0155\sin(0.352\lvert s\rvert + 1.07)$	$-0.0678 + 0.0599e^{-0.476r} + 0.0757e^{-0.0285\lvert s\rvert}$	$-0.0678 + 0.0599e^{-0.476r} + 0.0757e^{-0.0285\lvert s\rvert}$	$r = [1, 11]$, $s = [-3, 3]$
1	$0.0744 - 0.0322\sin(1.57r - 3.18) + 0.042\sin(0.984s - 0.0832)$	$0.0626 - 0.00134r - 0.00519\lvert s\rvert$	$0.0693 - 0.00225r - 0.0134\log(\lvert s\rvert)$	$0.0594 - 0.00182r - 0.00426s$	$r = [3, 20]$, $s = [-3, 3]$
2	$0.0598 + 0.0437\sin(0.344r + 4.8) - 0.048\sin(0.866s + 0.164)$	$0.0104 - 0.0195\sin(-6.01r + 40.1) + 0.0211\sin(0.962\lvert s\rvert - 0.113)$	$0.0503 - 0.00207r - 0.0074\sin(1.04s + 0.326)$	$0.0582 - 0.00239r + 0.0016s$	$r = [3, 20]$, $s = [-3, 3]$
3	$0.00402 - 0.00978\sin(0.32r + 3.28) - 0.0105\sin(1.2s + 0.811)$	$0.00962 - 0.0199\sin(0.328r + 2.93) + 0.0157\sin(-1.37s - 7.81)$	$0.00712 - 0.0119\sin(0.424r + 2.75) - 0.0095\sin(70.4s + 32)$	$0.0177 - 0.00669\sin(0.984r + 0.246) - 0.0128\sin(1.34s + 1.19)$	$r = [1, 15]$, $s = [-3, 3]$
4	$0.0219 - 0.00223r + 0.00158\lvert s\rvert$	$0.0145 + 0.00836\sin(1.18r - 3.65) + 0.00372\sin(1.02s + 1.9)$	$0.0091 - 0.00811\sin(1.15r - 0.376) + 0.00383\sin(1.71s - 1.56)$	0.0128	$r = [3, 12]$, $s = [-3, 3]$
5	0.00451	$-0.00153 + 0.00696\log(r) + 0.00605\log(\lvert s\rvert)$	0.00538	$-0.000726 + 0.0016r - 0.000407s$	$r = [1, 18]$, $s = [-3, 3]$
6	$0.00516 + 0.00563\sin(0.654r + 0.756) + 0.00447\sin(1.58s - 1.36)$	$0.0201 + 0.00612\sin(0.679r - 0.51) + 0.00864\sin(2.55s - 4.12)$	$0.00867 - 0.00242\log(r) + 0.00198\log(\lvert s\rvert)$	$0.0128 + 0.00889\sin(0.739r - 0.657) + 0.005\sin(0.995s - 0.465)$	$r = [1, 18]$, $s = [-3, 3]$
7	0.00751	$0.0319 - 0.00922\log(r) + 3.02\times10^{-13}e^{8.01\lvert s\rvert}$	0.00923	$0.0151 - 0.00053r + 0.00146s$	$r = [3, 20]$, $s = [-3, 3]$

Table A.8 Seats CDL-Model Property Equations for 2.45 GHz with humans

Cluster	Direction	Type	Gain [dB]	MToA [s]	Delay Spread [s]	MPC
0	Aft	LoS	$470 + 523\sin(0.029r + 4.39) + 3.05\sin(5.61s - 55)$	$6.32\times10^{-10} - 3.43\times10^{-10}e^{-0.258\lvert s\rvert} - 5.97\times10^{-9}e^{-4.21r}$	$4.55\times10^{-10} - 2.85\times10^{-10}e^{-0.093\lvert s\rvert} - 2.59\times10^{-10}e^{-1.51r}$	$\lfloor 4.27 - 0.469r - 0.0359s\rfloor$
1	Aft	NLoS	$2.18\times10^{3} + 2.29\times10^{3}\sin(0.00896r + 4.52) - 15.8\sin(0.437s - 1.04)$	$1.79\times10^{-9}\sin(12.8r - 86.8) - 9.33\times10^{-10}\sin(2.39s + 42.6) + 3.37\times10^{-9}$	$4.68\times10^{-10} - 2.31\times10^{-10}\sin(0.703r + 1.33) - 3.16\times10^{-10}\sin(0.691s + 0.575)$	$\lfloor 1.82 + 0.728\log(r) - 1.72\sin(0.764s - 0.0189)\rfloor$
2	Aft	NLoS	$-2.29\times10^{5} + 14.5\sin(0.187r + 1.8) - 2.29\times10^{5}\sin(-0.00247s - 1.57)$	$2.6\times10^{-9}\sin(1.08s + 0.259) - 3.51\times10^{-11}r + 1.04\times10^{-8}$	$9.91\times10^{-10}\sin(0.862s + 0.517) - 1.13\times10^{-9}\sin(0.331r + 2.81) + 8.06\times10^{-10}$	$\lfloor 1.68 - 0.561\sin(0.397r + 1.94) + 0.54\sin(0.64s + 0.681)\rfloor$
3	Aft	NLoS	$-131 - 2.25r - 81.9\sin(0.213s - 7.78)$	$7.36\times10^{-9} - 2.12\times10^{-9}\sin(0.683s + 1.17) - 2.2\times10^{-9}\log(r)$	$3.46\times10^{-10} - 4.62\times10^{-10}\sin(0.36r + 2.62) - 3.4\times10^{-10}\sin(0.64s - 0.153)$	$\lfloor -3.56\times10^{4} + 0.741\log(r) - 3.56\times10^{4}\sin(0.00331s - 1.57)\rfloor$
4	Aft	NLoS	$-80.9 - 14.4\sin(0.254r + 3.8) + 9.26\sin(0.665s + 1.02)$	$8.71\times10^{-10}\log(\lvert s\rvert) - 1.46\times10^{-9}\log(r) + 5.28\times10^{-9}$	$5.68\times10^{-10}\sin(0.721s + 0.175) - 5.79\times10^{-10}\sin(0.351r + 2.52) + 6.55\times10^{-10}$	$\lfloor 1.33 - 1.1\sin(0.975r - 0.418) + 3.25\sin(0.337s + 1.01)\rfloor$
5	Aft	NLoS	$-88.3 - 10.7\sin(0.285r + 10.3) - 6.52\sin(0.645s - 1.16)$	$-5.7\times10^{-6}\sin(0.00294r + 11.0) - 2.92\times10^{-9}\sin(0.87s - 0.041) - 5.7\times10^{-6}$	$4.06\times10^{-10} - 9.39\times10^{-11}\sin(0.885r - 0.24) - 2.15\times10^{-10}\sin(0.682s + 0.875)$	$\lfloor 1.39 - 0.492\sin(1.01r - 0.744) - 0.404\sin(0.927s - 0.128)\rfloor$
6	Aft	NLoS	$-85.9 - 10.8\sin(0.292r + 3.42) + 9.24\sin(-3.89s - 247)$	$3.13\times10^{-8}e^{-0.696r} - 2.08\times10^{-9}\sin(0.852s - 0.135) + 4.78\times10^{-9}$	$6.16\times10^{-8} - 5.43\times10^{-9}e^{-0.802r} - 6.08\times10^{-8}e^{0.00142s}$	$\lfloor 2.22 - 0.404\sin(-1.28r + 37.6) - 1.27\sin(4.15s - 10)\rfloor$
7	Aft	NLoS	$-88.1 + 11.5\sin(0.295r + 0.819) + 9.25\sin(0.633s + 0.732)$	$3.18\times10^{-9} - 3.53\times10^{-10}\lvert s\rvert - 3.91\times10^{-11}r$	2.42×10^{-10}	$\lfloor 0.736 - 1.96\sin(0.544r + 0.865) + 1.62\sin(0.704s + 1.16)\rfloor$
8	Aft	NLoS	$-73.9 - 1.07r + 5.08\sin(0.941s + 7.53)$	$3.37\times10^{-8}e^{-0.302r} - 1.05\times10^{-8}\sin(0.899\lvert s\rvert - 0.293) + 1.05\times10^{-8}$	$2.86\times10^{-11}s - 3.42\times10^{-11}r + 7.66\times10^{-10}$	$\lfloor 1.81 + 0.664\sin(1.17r - 4.45) + 0.888\sin(1.27s + 0.737)\rfloor$
9	Aft	NLoS	$-61.2 - 13\log(r) + 5.29\sin(1.81s + 4.52)$	$4.64\times10^{-9}\sin(1.32s + 1.36) - 1.31\times10^{-9}\sin(1.34r - 3.72) + 7.57\times10^{-9}$	$2.21\times10^{-10}\sin(1.24s + 0.801) - 1.77\times10^{-11}r + 5.25\times10^{-10}$	1.19
10	Aft	NLoS	$-68.3 - 1.97r - 12.2\sin(1.42s + 1.76)$	$6.25\times10^{-9} - 5.61\times10^{-9}\sin(1.42s - 1.15) - 4.69\times10^{-11}r$	2.74×10^{-10}	2.52
0	Cockpit	LoS	$-39.9 + 15.1\sin(0.261r + 2.05) - 2.67\sin(-0.645s - 33)$	$5.34\times10^{-10} - 2.68\times10^{-10}e^{-0.589\lvert s\rvert} - 6.15\times10^{-10}e^{-1.03r}$	$3.04\times10^{-10} - 1.08\times10^{-10}e^{-0.356\lvert s\rvert} - 1.91\times10^{-10}e^{-0.487r}$	$\lfloor 1.92 + 1.43\sin(0.424r + 1.15) - 0.749\sin(1.49s - 4.71)\rfloor$
1	Cockpit	NLoS	$-57.9 - 2.12r - 8.2\sin(0.58s - 1.05)$	$1.35\times10^{-9}\log(r) - 1.42\times10^{-9}\sin(0.663s - 0.322) + 7.69\times10^{-9}$	$2.96\times10^{-10} - 1.15\times10^{-10}\sin(0.959r - 0.6) - 1.28\times10^{-10}\sin(0.862s - 0.533)$	$\lfloor 2.04 - 1.41\sin(0.46r + 1.47) - 0.715\sin(0.752s - 0.687)\rfloor$
2	Cockpit	NLoS	$-40.8 - 3.01r - 3.62\sin(2.22s - 17)$	$2.82\times10^{-9} - 1.12\times10^{-9}\sin(0.857\lvert s\rvert - 0.0509) - 5.49\times10^{-10}\sin(0.978r - 2.56)$	$3.52\times10^{-7}\sin(12.6s + 203.0) - 1.89\times10^{-10}\sin(0.451r + 0.346) - 3.5\times10^{-7}$	$\lfloor 6.68 - 0.225r - 0.543\lvert s\rvert\rfloor$
3	Cockpit	NLoS	$-38.9 - 2.15r - 5.63\lvert s\rvert$	$1.06\times10^{-10}\sin(1.28s + 1.16) + 4.5\times10^{-10}\sin(0.424r + 2.96) + 2.03\times10^{-9}$	$1.41\times10^{-7} - 1.39\times10^{-7}e^{0.00131\lvert s\rvert} - 7.14\times10^{-9}e^{-0.744r}$	$\lfloor 4.46 + 0.246\log(r) - 2.43\log(\lvert s\rvert)\rfloor$
4	Cockpit	NLoS	$-59.4 - 1.45r + 4.96\sin(0.777s + 0.887)$	$2.09\times10^{-9}\log(r) + 2.03\times10^{-5}e^{3.77\times10^{-5}s} - 2.03\times10^{-5}$	$4.42\times10^{-10}\sin(0.832s + 0.449) - 6.11\times10^{-10}\sin(0.317r + 2.36) + 3.3\times10^{-10}$	$\lfloor 1.87 - 0.368\sin(0.877r + 0.134) + 0.529\sin(1.1s + 0.137)\rfloor$
5	Cockpit	NLoS	$-61.6 - 1.74r - 3.52\sin(3.94s + 1.82)$	$1.42\times10^{-9}\sin(1.78s + 0.709) - 1.54\times10^{-9}\sin(0.419r + 1.74) + 4.34\times10^{-9}$	$2.79\times10^{-10}\sin(0.911s + 0.236) - 2.8\times10^{-11}r + 6.92\times10^{-10}$	$\lfloor 2.15 - 0.989\sin(1.08r - 3.32) + 0.905\sin(1.21s - 0.945)\rfloor$
6	Cockpit	NLoS	$-67.9 - 1.57r + 10\sin(0.5s + 1.06)$	$7.75\times10^{-9} - 1.23\times10^{-9}\sin(0.882s + 1.0) - 1.97\times10^{-9}\log(r)$	$6.29\times10^{-7}\sin(0.00562s - 1.54) - 2.94\times10^{-10}\sin(1.26r - 3.63) + 6.3\times10^{-7}$	$\lfloor -2.26 + 2.17\log(r) + 1.03\sin(0.676s + 0.126)\rfloor$
7	Cockpit	NLoS	$-1.46\times10^{5} - 8.24\sin(0.776r + 0.0392) - 1.46\times10^{5}\sin(-0.00189s - 1.57)$	$1.19\times10^{-9}\sin(1.35s + 1.7) + 3.2\times10^{-9}\sin(0.659r + 1.99) + 6.23\times10^{-9}$	3.8×10^{-10}	$\lfloor 7.38\times10^{3} + 2.85\sin(0.554r + 0.574) - 7.38\times10^{3}\sin(0.00419s + 1.57)\rfloor$
8	Cockpit	NLoS	$-52.8 - 17.7e^{0.0481r} - 0.0255e^{-2.26s}$	$9.25\times10^{-10}\log(r) + 3.91\times10^{-9}\sin(4.77s + 40.0) + 4.49\times10^{-9}$	2.77×10^{-10}	$\lfloor 0.718 + 0.0298r + 0.377\sin(1.54s - 1.59)\rfloor$

Cluster	$\overline{\phi^A}$ [rad]	$\overline{\phi^D}$ [rad]	$\overline{\theta^A}$ [rad]	$\overline{\theta^D}$ [rad]
0	$\mathrm{rot}(-0.011 + 0.00762r + 0.819\sin(0.623s - 0.00239))$	$-0.011 + 0.00762r + 0.819\sin(0.623s - 0.00239)$	$\mathrm{rot}(280 - 0.995e^{-0.755r} - 282e^{-0.000417\lvert s\rvert})$	$-280 + 0.995e^{-0.755r} + 282e^{-0.000417\lvert s\rvert}$
1	$\mathrm{rot}(-1.88 + 0.0473\sin(0.553r + 1.31) - 0.116\sin(0.791s + 1.18))$	$0.0647 + 0.589e^{-0.419r} + 0.0765\sin(0.967s + 0.57)$	$1.53 + 3.49\times10^{-7}e^{0.703r} - 0.019\sin(1.34s + 0.635)$	$1.75 + 0.917e^{-0.403r} + 3.66\times10^{-12}e^{7.76s}$
2	$-0.0744 + 0.27\sin(0.136r + 3.22) - 0.133\sin(-1.67s + 0.438)$	$2.05\times10^{3} + 2.05\times10^{3}\sin(0.00106r + 4.7) + 0.106\sin(0.703s - 0.331)$	$\mathrm{rot}(-2.24 - 0.0253\log(r) - 0.0254\sin(1.72s - 0.321))$	$1.64 + 0.468e^{-0.224r} + 0.000617e^{-1.2s}$
3	$\mathrm{rot}(-0.851 + 0.0481\sin(0.4r + 2.1) + 0.225\sin(0.764s + 0.407))$	$0.0479 + 0.406e^{-0.252r} + 0.0872\sin(0.765s + 0.161)$	$1.32 - 0.0674\sin(0.398r + 1.29) - 0.0916\sin(0.831s - 0.48)$	$1.71 + 0.676e^{-0.252r} - 0.02\sin(102s - 133)$
4	$-1.69 - 0.0708\log(r) + 0.393\sin(0.532s - 0.662)$	$-0.0282 - 0.393e^{-0.342r} + 0.095\sin(0.676s - 0.594)$	$\mathrm{rot}(-1.86 + 0.0393\log(r) + 0.0882\sin(0.661s + 0.571))$	$\mathrm{rot}(982 + 983\sin(0.00269r + 4.68) - 0.0155\sin(1.58s - 2.47))$
5	$\mathrm{rot}(-1.91 - 0.0328\sin(0.796r + 0.539) + 0.0574\sin(-1.89s + 1.04))$	$9.71\times10^{-6} + 0.3e^{-0.144r} + 0.0348\sin(1.3s - 0.44)$	$0.608 + 1.35e^{-1.05r} + 0.118\sin(1.13s - 1.21)$	$1.68 + 0.644e^{-0.27r} + 0.026\sin(92.7s + 240)$
6	$1.76 + 0.218\log(r) + 0.0827\sin(1.13s + 0.531)$	$0.141 - 0.0142r + 0.0871\sin(1.16\lvert s\rvert - 0.109)$	$0.708 + 0.0959\sin(0.253r + 3.37) + 0.0737\sin(17.8s + 5.17)$	$2.01 - 0.301\sin(0.139r + 5.94) - 0.0301\sin(1.33s - 0.495)$
7	$-2.93 + 0.0311\log(r) + 0.059\log(\lvert s\rvert)$	$0.148 + 0.0498\sin(0.673r - 0.263) + 0.118\sin(0.854s - 1.39)$	$-527 + 0.131\log(r) + 528e^{4.59\times10^{-5}s}$	$1.71 + 0.93e^{-0.42r} + 0.0731e^{-0.262s}$
8	$-2.64 - 0.000661e^{0.283r} + 0.0555\sin(2.19s - 10.6)$	$-0.0605 + 0.0285\sin(0.687r - 0.154) + 0.0534\sin(0.844s - 1.04)$	$\mathrm{rot}(-1.91 - 0.0429\sin(-0.39r + 4.67) - 1.71\sin(0.00151\lvert s\rvert + 0.161))$	$\mathrm{rot}(-1.4 - 0.0454\sin(0.288r + 3.14) - 0.0189\sin(-2.63s + 4.2))$
9	$-0.439 - 0.142\sin(0.853r - 1.87) - 0.157\sin(1.09s + 0.0821)$	$800 + 0.0597\log(r) + 800\sin(0.00372s - 1.56)$	$0.309 + 0.0367\sin(0.753r + 0.742) + 0.0716\sin(-3.93s + 1.39)$	$1.65 + 0.579e^{-0.237r} - 0.0243\sin(-4.04s - 7.75)$
10	$\mathrm{rot}(-0.669 + 0.0421\sin(0.512r + 2.3) + 0.0369\sin(1.31s + 3.32))$	$-0.286 + 0.0126r - 0.0702\sin(1.06s + 0.125)$	$-2.06\times10^{3} - 0.0452\sin(1.14r - 3.13) - 2.06\times10^{3}\sin(-0.00233s - 1.57)$	$1.69 + 0.649e^{-0.288r} + 0.0663e^{-0.699\lvert s\rvert}$
0	$0.000631 + 0.000932r - 0.87\sin(0.603s - 0.01)$	$\mathrm{rot}(0.000631 + 0.000932r - 0.87\sin(0.603s - 0.01))$	$\mathrm{rot}(-461 - 460\sin(0.00839r + 4.64) - 0.135\sin(7.17s - 92.7))$	$461 + 460\sin(0.00839r + 4.64) + 0.135\sin(7.17s - 92.7)$
1	$-0.0784 + 0.582e^{-0.0834r} - 0.2\sin(0.507s + 0.696)$	$0.539 + 3.19\times10^{3}e^{-10.1r} + 0.168\sin(-70.5s + 281)$	$1.24 - 0.167\sin(0.246r + 1.15) - 0.0802\sin(-1.5s - 1.08)$	$\mathrm{rot}(-0.806 + 0.0121\log(r) - 0.0461\sin(2.32s - 11.6))$
2	$\mathrm{rot}(-0.0223 - 0.0264\sin(0.607r + 1.45) + 0.339\sin(0.428s - 0.0904))$	$\mathrm{rot}(0.0885 - 0.035\log(r) - 0.223\sin(0.348s + 0.096))$	$0.86 - 0.0641\sin(0.529r + 0.0166) - 0.0107\sin(0.876s + 0.933)$	$1.76 + 0.919e^{-0.351r} - 0.0186\sin(0.825s - 0.863)$
3	$0.194 - 0.059\log(r) - 0.151\sin(0.628s + 0.158)$	$\mathrm{rot}(0.024 + 0.000146r - 0.0954\sin(0.473s + 0.523))$	$\mathrm{rot}(-2.05 + 0.00447r - 0.0178\log(\lvert s\rvert))$	$1.78 + 0.608e^{-0.206r} + 0.0141\sin(1.43s + 1.8)$
4	$-0.0451 + 0.124\log(r) - 0.331e^{0.172s}$	$-0.462 + 0.044\sin(0.667r - 0.394) + 0.0927\sin(0.913s + 0.426)$	$1.27 - 0.143\sin(0.3r + 0.572) + 0.0397\sin(-1.34s - 0.241)$	$2.29 - 0.00619r - 0.0771\sin(1.89s - 2.9)$
5	$\mathrm{rot}(0.961 + 6.5e^{-0.961r} + 0.141\sin(0.791s - 1.38))$	$\mathrm{rot}(-1.61\times10^{3} + 0.291e^{-0.192r} + 1.61\times10^{3}e^{-9.96\times10^{-6}s})$	$1.1 - 0.0649\sin(1r - 2.04) + 0.0893\sin(0.897s - 0.914)$	$1.66 + 0.81e^{-0.248r} + 0.0124\sin(-8.6s + 13.8)$
6	$-1.03 - 0.121\sin(5.56r - 102) - 0.211\sin(0.897s - 1.29)$	$\mathrm{rot}(-473 - 0.0966\log(r) - 473\sin(0.00531s - 1.56))$	$1.1 - 0.0407\sin(2.39r - 6.58) + 0.321\sin(0.369\lvert s\rvert + 0.797)$	$1.68 + 1.12e^{-0.302r} - 0.0166\sin(4.94s + 0.534)$
7	$\mathrm{rot}(-1.85 + 0.0484\sin(0.602r + 0.393) + 0.0701\sin(-2.22s - 23))$	$\mathrm{rot}(-0.0307 - 2.38e^{-0.505r} - 0.0603\sin(0.74s + 0.613))$	$1.22 - 0.0664\sin(1.59r - 7.23) + 0.357\sin(0.431\lvert s\rvert + 0.717)$	$1.48 + 0.686e^{-0.225r} + 0.191e^{0.0244s}$
8	$-2.42 - 0.00145r - 0.194\sin(1.48s - 0.169)$	$\mathrm{rot}(-0.222 + 0.0938\log(r) - 0.108\sin(0.968s - 1.02))$	$\mathrm{rot}(-2.67 - 0.00176r - 0.061\sin(1.5s - 1.51))$	$1.63 + 0.703e^{-0.235r} + 0.000995e^{-1.27s}$

Cluster	$\sigma(\phi^A)$ [rad]	$\sigma(\phi^D)$ [rad]	$\sigma(\theta^A)$ [rad]	$\sigma(\theta^D)$ [rad]	Limits [m]
0	$0.0176 - 0.0129\log(r) + 0.0346e^{-0.188\lvert s\rvert}$	$0.0175 - 0.0129\log(r) + 0.0346e^{-0.187\lvert s\rvert}$	$-0.0494 + 0.0531e^{-0.897r} + 0.074e^{-0.108\lvert s\rvert}$	$-0.0494 + 0.0531e^{-0.897r} + 0.074e^{-0.108\lvert s\rvert}$	$r = [1, 6]$, $s = [-3, 3]$
1	$0.0419 - 0.00154r - 0.0108\sin(0.945s - 0.166)$	$-0.0219 + 0.0878e^{-0.11r} - 0.0144\sin(0.718s + 0.246)$	$0.0263 - 0.017\sin(0.767r + 0.603) - 0.0172\sin(0.54s + 0.113)$	$0.0182 - 0.00126r - 0.00679\sin(0.663s + 0.12)$	$r = [1, 19]$, $s = [-3, 3]$
2	$0.0324 - 0.0524\sin(0.337r + 2.85) + 0.0383\sin(0.792s + 0.551)$	$0.0187 - 0.024\sin(-0.312r + 12.3) + 0.0144\sin(0.734s + 0.0711)$	$0.0144 - 0.0285\sin(0.34r + 2.47) + 0.0246\sin(0.66s + 0.936)$	$0.00572 - 0.00782\sin(-0.266r + 11.9) + 0.00595\sin(0.811s + 0.807)$	$r = [1, 19]$, $s = [-3, 3]$
3	$0.0354 - 0.0513\sin(0.332r + 2.53) - 0.0371\sin(0.76s - 1.22)$	$0.0145 - 0.0221\sin(0.329r + 3.04) - 0.0154\sin(0.818s - 0.224)$	$0.0207 - 0.0346\sin(0.322r + 2.62) - 0.0267\sin(0.92s - 0.654)$	$0.0241 - 0.00143r - 0.0103\sin(0.943s - 0.426)$	$r = [1, 19]$, $s = [-3, 3]$
4	$0.219 - 0.0101r + 0.128\sin(0.608s + 0.739)$	$0.0258 - 0.0296\sin(0.336r + 3) + 0.0261\sin(0.684s - 0.479)$	$0.0831 - 0.00386r + 0.034\sin(0.691s + 0.35)$	$0.015 - 0.00702\sin(0.615r + 1.94) + 0.0119\sin(0.825s + 0.25)$	$r = [2, 19]$, $s = [-3, 3]$
5	$0.0267 - 0.00141r - 0.00322s$	$0.0086 - 0.00735\sin(0.367r + 3.05) - 0.00667\sin(-1.34s + 1.43)$	$0.0144 - 0.0114\sin(0.71r + 0.866) - 0.0162\sin(1.57s + 1.41)$	$0.00528 - 0.00579\sin(0.267r + 4.3) - 0.00324\sin(0.994s + 0.598)$	$r = [2, 19]$, $s = [-3, 3]$
6	$0.0262 - 0.0294\sin(0.414r + 1.48) - 0.0164\sin(0.861s - 0.704)$	$0.0149 - 0.0153\sin(0.362r + 2.51) + 0.0103\sin(4.95s + 4.47)$	$-152 - 0.024\sin(0.374r + 1.84) - 152\sin(0.00552s - 1.57)$	$0.0108 - 0.0116\sin(0.399r + 2.08) - 0.00795\sin(1.06s - 0.691)$	$r = [2, 19]$, $s = [-3, 3]$
7	$0.00571 - 0.0126\sin(0.859r - 0.14) + 0.0232\sin(1.08s - 0.1)$	$0.0205 - 0.000985r - 0.00276\log(\lvert s\rvert)$	$0.00364 - 0.00112r + 0.0185\sin(0.892\lvert s\rvert - 0.168)$	$0.00152 + 0.0145e^{-0.283r} + 0.000271e^{-0.849s}$	$r = [3, 18]$, $s = [-3, 3]$
8	0.0188	$0.0173 - 0.000702r + 0.000783s$	$0.0143 + 0.0126\sin(0.513r + 2.46) + 0.011\sin(0.919s + 1.04)$	$0.00818 - 0.000203r + 0.00349\sin(0.969s + 0.641)$	$r = [3, 19]$, $s = [-3, 3]$
9	$0.014 - 0.000328r + 0.00772\sin(1.93s - 0.0757)$	$0.0137 - 0.000661r + 0.000459s$	$0.047 - 0.0143\log(r) + 0.0117\sin(1.37s + 0.737)$	$0.0102 - 0.00363\log(r) + 0.417\sin(9.42s - 31.4)$	$r = [4, 19]$, $s = [-3, 3]$
10	$0.0208 - 0.00183r + 0.0165\log(\lvert s\rvert)$	$0.0336 - 0.0129\log(r) + 0.00412\log(\lvert s\rvert)$	$0.0107 - 0.000944r + 0.0115\log(\lvert s\rvert)$	$0.0106 - 0.00333\log(r) + 0.00154\sin(4.6s + 66.4)$	$r = [3, 19]$, $s = [-3, 3]$
0	$0.056 + 0.0443\sin(0.173r + 3.21) - 0.00496\sin(-14.9s + 95.8)$	$0.0558 + 0.0444\sin(0.172r + 3.22) + 0.00512\sin(0.76s - 17.2)$	$28.3 + 28.3\sin(0.00785r + 4.65) - 0.00716\sin(-2.36s - 61.2)$	$28.4 + 28.4\sin(0.00784r + 4.65) - 0.00716\sin(-2.36s - 61.2)$	$r = [1, 11]$, $s = [-3, 3]$
1	$0.0204 - 0.0116\sin(0.804r + 0.542) - 0.0116\sin(10.6s - 22.7)$	$0.025 - 0.0166\sin(0.338r + 2.58) - 0.0137\sin(0.6s - 0.915)$	$0.0118 - 0.0114\sin(0.356r + 3.4) - 0.0117\sin(1.2s - 0.586)$	$0.0254 - 0.00836\sin(0.838r - 0.322) - 0.00944\sin(0.911s - 0.815)$	$r = [1, 19]$, $s = [-3, 3]$
2	$0.0413 - 0.0104\sin(0.814r - 0.895) + 0.0335\sin(0.949\lvert s\rvert + 0.0637)$	$-93 - 0.0115\sin(0.908r - 1.88) - 93\sin(0.00283s - 1.57)$	$0.103 - 0.00282r - 0.0138\lvert s\rvert$	$0.00571 + 0.0113\log(r) - 0.00603\sin(0.78s - 0.888)$	$r = [1, 20]$, $s = [-3, 3]$
3	$0.11 - 0.0343\sin(0.831r - 1.27) + 0.0448\sin(1.04s + 1.42)$	$0.118 - 0.00379r - 0.0092\lvert s\rvert$	$0.0638 - 0.0226\sin(0.852r - 1.51) + 0.0307\sin(2.31s + 29.8)$	$0.0727 - 0.0276\sin(0.438r + 0.553) - 0.0362\sin(0.703\lvert s\rvert - 0.615)$	$r = [2, 20]$, $s = [-3, 3]$
4	$0.0254 - 0.00858\sin(0.991r - 6.12) + 0.016\sin(1.27s + 0.939)$	$0.0295 - 0.0183\sin(0.367r + 1.93) + 0.011\sin(0.921s + 0.125)$	$0.00967 - 0.0113\sin(0.383r + 2.64) + 0.0139\sin(1.1s + 0.661)$	$0.0211 - 0.0284\sin(0.346r + 2.26) + 0.0175\sin(0.895s + 0.455)$	$r = [1, 19]$, $s = [-3, 3]$
5	$0.0327 - 0.0202\sin(12.1r - 148) + 0.00684\sin(0.972\lvert s\rvert + 0.867)$	$0.0117 - 0.012\sin(0.395r + 1.45) + 0.0075\sin(0.822s - 0.123)$	$0.0162 + 0.0159\sin(0.414r + 3.88) + 0.00859\sin(0.986s + 0.0196)$	$0.0105 - 0.000606r + 0.00127s$	$r = [3, 20]$, $s = [-3, 3]$
6	$0.0375 - 0.0226\sin(1.07r - 2.71) + 0.027\sin(0.948s + 0.704)$	$0.00863 - 0.0163\sin(0.335r + 2.29) + 0.0147\sin(0.699s + 0.331)$	$-480 - 0.00223r + 480\sin(0.00245s + 1.57)$	$0.00588 - 0.00575\sin(0.944r - 1.46) + 0.00573\sin(0.739s + 0.25)$	$r = [3, 20]$, $s = [-3, 3]$
7	$-30.9 - 0.00899\sin(0.671r + 2.1) - 31\sin(0.0102s - 1.57)$	$0.0196 - 0.000968r - 0.000218s$	$-0.586 - 0.0139\sin(0.569r + 3.31) - 0.611\sin(0.0693s - 1.55)$	0.00367	$r = [5, 20]$, $s = [-3, 3]$
8	$0.0109 - 0.00303\sin(0.753r - 0.454) + 0.00528\sin(-1.94s + 0.527)$	$0.0125 - 0.000497r + 0.0022\log(\lvert s\rvert)$	$0.00877 + 0.000104r + 0.00518\log(\lvert s\rvert)$	$0.0127 - 0.00445\log(r) + 0.000579\log(\lvert s\rvert)$	$r = [4, 19]$, $s = [-3, 3]$

Table A.9 Screens CDL-Model Property Equations for 5.16 GHz with humans

Cluster	Direction	Type	Gain [dB]	MToA [s]	Delay Spread [s]	MPC
1	Aft	NLoS	$-83.1 - 4.53\log(r) - 5.24\log(\lvert s\rvert)$	$4.9\times10^{-9}\sin(1.11s+0.654) - 1.53\times10^{-9}r + 1.47\times10^{-8}$	$8.01\times10^{-10} - 6.03\times10^{-10}\log(\lvert s\rvert) - 2.58\times10^{-11}r$	$\lfloor 2.86 - 0.531\log(r) - 0.934\log(\lvert s\rvert)\rfloor$
2	Aft	NLoS	$-93.5 + 5.75\sin(1.09r - 1.41) - 6.6\sin(0.965s + 0.0224)$	$1.39\times10^{-9}s - 5.52\times10^{-10}r + 8.44\times10^{-9}$	$4.73\times10^{-11}\sin(1.19r - 2.4) - 7.35\times10^{-11}\sin(1.25s + 0.67) + 1.28\times10^{-10}$	2.28
3	Aft	NLoS	$-98 + 6.85\sin(0.645r - 0.593) + 6.84\sin(0.37s + 1.15)$	$1.19\times10^{-8} - 4.27\times10^{-9}\sin(0.647s + 0.138) - 1.23\times10^{-9}r$	$2.46\times10^{-10}\lvert s\rvert - 8.82\times10^{-11}r + 4.33\times10^{-10}$	$\lfloor 2.58 - 0.087r + 0.26s\rfloor$
4	Aft	NLoS	$-86.8 - 0.761r - 1.02e^{-0.994s}$	$2.12\times10^{-8} - 6.09\times10^{-9}\sin(1.52s - 1.65) - 1.49\times10^{-9}r$	$4.59\times10^{-10}\sin(1.33s + 0.914) - 9.12\times10^{-11}r + 7.42\times10^{-10}$	$\lfloor 1.79 + 0.0895r + 0.48s\rfloor$
5	Aft	NLoS	$-94.2 + 0.132r - 3.5\sin(1.03s - 0.364)$	$1.94\times10^{-4}\sin(0.0203s + 1.57) + 2.65\times10^{-8}e^{-0.866r} - 1.94\times10^{-4}$	3.64×10^{-10}	1.29
6	Aft	NLoS	$-103 + 13.2\sin(0.45r + 18.4) + 7.33\sin(-1.6s + 0.378)$	$1.41\times10^{-9}\sin(0.463r + 0.168) - 6.63\times10^{-9}\sin(10.5s - 7.7) + 5.07\times10^{-9}$	$2.6\times10^{-11}\sin(0.912r + 3.17) - 7.64\times10^{-10}\sin(3.13s - 0.00193) + 9.82\times10^{-11}$	$\lfloor 0.921 - 2.71\sin(0.55r + 1.82) - 2.16\sin(1.65s - 0.0144)\rfloor$
7	Aft	NLoS	$-95.2 - 3.1\sin(1.32r - 3.54) + 6.13\sin(0.838s - 0.87)$	$1.66\times10^{-8} - 1.4\times10^{-9}s - 1.97\times10^{-9}r$	$1.71\times10^{-10}\log(\lvert s\rvert) - 2.97\times10^{-11}r + 1.77\times10^{-10}$	1.62
8	Aft	NLoS	$-94.5 - 0.118r + 5.41\log(\lvert s\rvert)$	$1.89\times10^{-8} - 5.99\times10^{-9}\sin(1.15s - 0.304) - 1.4\times10^{-9}r$	2.08×10^{-10}	$\lfloor 1.03 + 1.88\times10^{-14}e^{3.77r} + 0.000146e^{3.08s}\rfloor$
9	Aft	NLoS	$-127 + 20.7\log(r) - 14.4\sin(1.49s + 1.78)$	$4.67\times10^{-9}\sin(1.37s + 1.55) - 6.82\times10^{-9}\log(r) + 1.47\times10^{-8}$	$1.05\times10^{-11}\sin(1.46s - 1.1) - 5.22\times10^{-7}e^{-3.1r} + 1.04\times10^{-10}$	2.64
10	Aft	NLoS	-95	1.17×10^{-8}	3.8×10^{-10}	1.53
11	Aft	NLoS	$-93.6 + 5.78\sin(20.4r - 108) - 2.23\sin(1.02s + 0.123)$	$1.82\times10^{-8} - 5.31\times10^{-9}\log(\lvert s\rvert) - 9.15\times10^{-10}r$	3.8×10^{-10}	$\lfloor 0.611 - 0.0147r + 0.458\lvert s\rvert\rfloor$
12	Aft	NLoS	-90.8	$1.92\times10^{-9}\sin(1.22s - 0.188) - 4.17\times10^{-9}\log(r) + 9.4\times10^{-9}$	$2.5\times10^{-12}r - 2.93\times10^{-12}s + 8.64\times10^{-11}$	$\lfloor 0.398 + 0.0964r + 0.0899e^{0.921s}\rfloor$
13	Aft	NLoS	$-116 + 8.81\log(r) + 10.3\log(\lvert s\rvert)$	1.22×10^{-8}	2.1×10^{-10}	1.17
14	Aft	NLoS	$-94.7 - 3.9\sin(1.55r - 4.58) + 3.47\sin(1.12s + 0.638)$	$1.14\times10^{-9}s - 2.78\times10^{-9}r + 2.73\times10^{-8}$	1.57×10^{-10}	1.37
15	Aft	NLoS	$-97 - 9.45\sin(1.31r - 4.47) - 8.48\sin(1.16s + 1.9)$	$2.11\times10^{-8}\sin(1.16s + 1.9) + 5.18\times10^{-9}\sin(0.87r - 0.958) + 2.72\times10^{-8}$	$1.29\times10^{-10}\sin(0.858s - 0.846) - 1.57\times10^{-11}r + 1.1\times10^{-10}$	3.2
0	Cockpit	LoS	$-71.4 + 24.2\sin(0.326r + 1.55) - 3.13\sin(46.4s + 118)$	$1.69\times10^{-10} - 3.35\times10^{-11}\sin(0.461r + 3.04) - 3.02\times10^{-11}\sin(8.67s + 23.5)$	$4.64\times10^{-11} - 6.01\times10^{-11}\sin(0.218r + 3.52) - 6.82\times10^{-12}\sin(2.31s + 4.57)$	$\lfloor 2.61 - 0.278r + 6.21\times10^{-11}e^{7.8\lvert s\rvert}\rfloor$
1	Cockpit	NLoS	$-70.7 - 9.75\log(r) + 4.21\sin(3.57s - 29.1)$	$6.02\times10^{-9} - 1.49\times10^{-9}\sin(0.68r + 0.721) - 1.24\times10^{-9}\sin(0.741s - 0.555)$	$2.4\times10^{-10}\log(r) - 2.98\times10^{-5}e^{-3.77\times10^{-6}s} + 2.98\times10^{-5}$	$\lfloor 1.25 + 0.00924r + 0.369\sin(-2.76s - 4.2)\rfloor$
2	Cockpit	NLoS	$-50.6 - 15.1\log(r) + 1.94\sin(0.864s + 0.82)$	$2.62\times10^{-10}\log(\lvert s\rvert) - 1.26\times10^{-9}\log(r) + 4.05\times10^{-9}$	$2.8\times10^{-10}\sin(1.3s + 0.626) - 4.77\times10^{-11}r + 1.17\times10^{-9}$	$\lfloor 3.67 - 0.0346r + 2.35\times10^{-10}e^{-7.55s}\rfloor$
3	Cockpit	NLoS	$-84.6 - 10.8\sin(0.208r + 4.35) - 1.93\sin(0.437s - 0.524)$	$4.53\times10^{-10}\sin(8.02s - 2.52) - 1.44\times10^{-9}\log(r) + 4.57\times10^{-9}$	$1.11\times10^{-9} - 3.45\times10^{-10}\sin(1.09s - 0.313) - 4.97\times10^{-11}r$	$\lfloor 2.9 + 0.0643r - 0.863\sin(1.23s + 0.053)\rfloor$
4	Cockpit	NLoS	$-71.1 - 4.43e^{0.162r} + 3.78\sin(-1.82s + 0.489)$	$1.06\times10^{-8} - 6.72\times10^{-10}s - 1.14\times10^{-10}r$	$-9.3\times10^{-11}\sin(0.894r - 1.01) - 4.34\times10^{-7}\sin(0.0102s - 1.57) - 4.33\times10^{-7}$	$\lfloor 2.53 - 1.23\sin(0.828r - 0.546) - 0.423\sin(0.865s + 0.7)\rfloor$
5	Cockpit	NLoS	$-2.28\times10^{4} - 1.04e^{0.28r} + 2.27\times10^{4}\sin(-0.0113s + 20.4)$	$3.27\times10^{-9}\sin(1.03s + 0.117) - 5.5\times10^{-9}\log(r) + 1.51\times10^{-8}$	$4.39\times10^{-10}\sin(1.43s + 0.371) - 7.37\times10^{-10}\sin(0.964r - 1.71) + 6.25\times10^{-11}$	3.15
6	Cockpit	NLoS	$-83.4 - 4.2\log(r) + 3.21\log(\lvert s\rvert)$	$1.35\times10^{-9}s - 3.52\times10^{-10}r + 1.2\times10^{-8}$	$1.24\times10^{-9} - 2.07\times10^{-10}e^{-0.515s} - 4.45\times10^{-10}\log(r)$	$\lfloor 2.28 - 0.114r + 0.332s\rfloor$
7	Cockpit	NLoS	$-66.7 - 8.83\log(r) - 10.4\log(\lvert s\rvert)$	$8.22\times10^{-10}\sin(0.896s - 0.153) - 1.25\times10^{-9}\sin(0.36r + 1.96) + 4.6\times10^{-9}$	5.71×10^{-11}	$\lfloor 2.64 - 0.00857r - 1.82\log(\lvert s\rvert)\rfloor$

Cluster	$\overline{\phi^A}$ [rad]	$\overline{\phi^D}$ [rad]	$\overline{\theta^A}$ [rad]	$\overline{\theta^D}$ [rad]
1	$-0.573 - 0.027r + 0.0737\log(\lvert s\rvert)$	$\mathrm{rot}(2.94 + 0.0109r + 0.066\sin(0.754s + 0.284))$	$0.831 - 0.0286r + 0.0213s$	$1.98 - 0.0251r + 9.19\times10^{-8}e^{4.5s}$
2	$-1.29 + 0.00825r + 0.0772\lvert s\rvert$	$\mathrm{rot}(2.81 - 0.192\sin(0.386r + 2.09) + 0.0399\sin(0.641s - 0.613))$	$-38.6 + 0.0485\sin(1.09r - 1.74) + 39.6\sin(0.0242s + 1.56)$	$\mathrm{rot}(-1.28 + 0.123\sin(0.667r + 0.398) - 0.0417\sin(0.913s + 0.445))$
3	$\mathrm{rot}(-2.04 - 0.0734\log(r) - 0.0856\sin(-2.08s + 3.01))$	$0.365 - 0.0323r + 0.0438\sin(0.684s + 0.483)$	$\mathrm{rot}(-2.23 - 0.0193r + 0.0731\log(\lvert s\rvert))$	$1.85 + 0.129\sin(0.462r + 1.12) + 0.0231\sin(0.721s - 0.0641)$
4	0.0734	$-0.0558 + 0.00783r - 0.0952\sin(1.12s - 0.559)$	$0.78 - 0.0486\log(r) + 0.036\sin(2.53s + 0.285)$	$\mathrm{rot}(-1.2 - 0.0902\log(r) - 0.00413e^{1.79s})$
5	$-0.799 - 0.0715\sin(1.88r - 2.98) - 0.0893\sin(1.2s - 0.622)$	$\mathrm{rot}(2.9 + 0.0117r - 0.00576s)$	$\mathrm{rot}(-1.93 - 0.0134r - 2.31\times10^{-13}e^{8.81s})$	$\mathrm{rot}(-1.27 + 0.0574\sin(1.02r - 0.503) + 0.015\sin(4.1s - 4.18))$
6	$\mathrm{rot}(-2.13 - 0.000887r + 0.165\log(\lvert s\rvert))$	$384 + 226\sin(0.00592r + 4.67) + 157\sin(0.0124s - 1.55)$	$1.64 - 0.124\sin(0.366r + 1.95) + 0.0427\sin(0.772s + 0.31)$	$\mathrm{rot}(-1.15 + 0.209\sin(0.325r + 2.04) - 0.0388\sin(3.91s + 4.28))$
7	$\mathrm{rot}(-2.86 - 0.00682r - 0.0199s)$	$\mathrm{rot}(-2.85 - 0.0495\log(r) + 0.0631\log(\lvert s\rvert))$	$-650 - 0.0675\sin(0.765r + 1.07) - 651\sin(-0.00287s - 1.57)$	1.86
8	$\mathrm{rot}(-2.73 + 0.0394\log(r) - 0.118\sin(60.2s - 71.6))$	$0.00449 + 0.0653\log(r) - 7.96\times10^{-13}e^{8.62s}$	$\mathrm{rot}(-2.2 + 0.000971r - 0.0433\sin(-2.32s + 29.2))$	$\mathrm{rot}(-1.22 - 0.0822\log(r) - 3.14\times10^{-11}e^{7.17s})$
9	$\mathrm{rot}(-2.11 + 0.0105r + 0.0864\sin(3.73s - 0.543))$	$-0.178 - 0.0659\sin(1.32r - 2.03) - 0.077\sin(1.36s + 1.57)$	$1.71 - 0.00438r - 0.0248s$	$2.02 + 0.0794\sin(1.08r - 1.59) - 0.0974\sin(20.3s + 74.2)$
10	$-0.192 + 0.0739\sin(0.821r - 0.461) + 0.0309\sin(1.66\lvert s\rvert - 1.66)$	$0.0833 - 0.00962r + 0.121\log(\lvert s\rvert)$	$\mathrm{rot}(-2.06 + 0.0152r - 0.0397\log(\lvert s\rvert))$	$\mathrm{rot}(-1.16 - 0.069\sin(1.07r - 1.88) + 0.076\sin(-7.42s - 11.1))$
11	0.205	$-0.0925 - 0.0719\sin(1.08r - 1.75) - 0.0839\sin(0.771s - 1.01)$	$1.08 + 0.00999r - 0.0834\sin(4.96s + 2.47)$	$2.03 + 0.0014r - 0.0358\lvert s\rvert$
12	$\mathrm{rot}(2.71 + 0.00183r + 0.0296s)$	$-0.127 - 0.137\sin(-0.545r - 3.07) + 0.12\sin(1.3s + 0.871)$	1.7	$-2.49\times10^{3} - 0.163\log(r) + 2.49\times10^{3}e^{4.42\times10^{-6}s}$
13	-0.266	0.106	$0.795 + 0.0969\sin(2.11r - 6.6) - 0.0459\sin(-2.61\lvert s\rvert + 7.73)$	$\mathrm{rot}(-1.24 - 0.0229r - 0.0669\sin(4.96s - 2.66))$
14	$\mathrm{rot}(2.69 + 0.0123r - 0.0215s)$	$\mathrm{rot}(-4.53\times10^{3} + 0.0329\sin(1.25r - 2.6) + 4.54\times10^{3}\sin(-0.00163s + 1.57))$	$-85 + 0.0675\sin(0.94r - 1.2) + 86\sin(0.00405s + 1.55)$	$1.83 - 0.0115r + 0.000318e^{1.83s}$
15	$-0.137 - 0.146\log(r) + 0.105\sin(0.868s + 0.162)$	$\mathrm{rot}(2.38 + 0.0499\sin(1.41r - 3.01) - 0.572\sin(-0.193s - 1.68))$	$\mathrm{rot}(-1.62 - 0.221e^{-0.173r} - 0.0726\sin(1.87s + 3.08))$	$\mathrm{rot}(-1.31 - 0.0129r - 0.0118s)$
0	$0.00334 - 0.00199r - 0.561\sin(0.632s - 0.0171)$	$\mathrm{rot}(0.00334 - 0.00199r - 0.561\sin(0.632s - 0.0171))$	$\mathrm{rot}(-1.63 - 1.17e^{-0.365r} - 0.262e^{-0.534\lvert s\rvert})$	$1.63 + 1.17e^{-0.365r} + 0.262e^{-0.534\lvert s\rvert}$
1	$-78.3 - 158\sin(0.00455r + 4.67) - 79\sin(0.0449\lvert s\rvert + 1.49)$	1.4	$1.4 + 0.0887\sin(0.269r + 2.91) - 0.089\sin(1.48s + 4.87)$	$\mathrm{rot}(-0.695)$
2	$-0.0676 + 0.705e^{-0.184r} - 0.266\sin(0.606s - 0.279)$	$2.36 + 0.203\log(r) + 0.0676\sin(0.766s + 0.616)$	$\mathrm{rot}(639 - 1.08e^{-0.427r} - 641e^{1.15\times10^{-5}\lvert s\rvert})$	$2.02 - 0.104\log(r) + 0.0182\log(\lvert s\rvert)$
3	$0.0487 - 0.985e^{-0.299r} - 0.299\sin(0.626s + 0.352)$	$-2.38 - 0.187\log(r) + 0.0528\sin(0.601s - 0.596)$	$\mathrm{rot}(-1.77 - 0.403e^{-0.218r} - 1.34\times10^{-12}e^{7.93s})$	$1.74 + 0.623e^{-0.326r} - 0.0217\sin(0.965s + 0.582)$
4	$0.505 - 0.0389r + 0.0258e^{-0.676s}$	$\mathrm{rot}(-2.8 + 0.0937\sin(2.94r - 1.74) - 0.277\sin(0.646\lvert s\rvert + 3.13))$	$\mathrm{rot}(-1.83 + 0.139\sin(0.235r + 3.83) - 0.029\sin(-15.3s - 15.8))$	$-850 + 0.0534\log(r) + 853e^{1.29\times10^{-5}s}$
5	$\mathrm{rot}(2.33 + 1.49\times10^{-14}e^{2.53r} + 17.2e^{-5.3\lvert s\rvert})$	$-2.75 - 0.0236e^{0.207r} - 0.00563e^{0.94s}$	$\mathrm{rot}(1.41\times10^{3} + 0.0511\sin(1.25r - 2.77) - 1.41\times10^{3}\sin(0.00176s + 1.56))$	$\mathrm{rot}(326 + 339\sin(0.00665r + 10.9) + 11.4\sin(0.0199s + 1.56))$
6	$-0.264 + 0.017r - 0.0135e^{0.911s}$	$\mathrm{rot}(2.36 - 0.0335\sin(0.877r - 0.303) + 0.065\sin(1.47s - 0.765))$	$1.14 + 0.153r - 0.0552\sin(1.45s - 0.204)$	2.32
7	$-0.369 + 0.0855\sin(0.344r + 3.08) + 0.193\sin(0.253s + 1.86)$	$\mathrm{rot}(1.93 - 0.0594\sin(0.876r - 1.44) - 0.0734\sin(1.05s - 0.706))$	$\mathrm{rot}(-1.81 + 0.0791\sin(0.375r + 2.19) - 0.0183\sin(1.4s + 0.504))$	$2.68 + 0.0339\log(r) - 0.0215\log(\lvert s\rvert)$

Cluster	$\sigma(\phi^A)$ [rad]	$\sigma(\phi^D)$ [rad]	$\sigma(\theta^A)$ [rad]	$\sigma(\theta^D)$ [rad]	Limits [m]
1	$0.0192 - 0.00131r - 0.00972\log(\lvert s\rvert)$	0.012	0.0187	$0.0132 - 0.000903r - 0.00675\log(\lvert s\rvert)$	$r = [1,8]$, $s = [-3,3]$
2	$0.00781 + 0.0101\sin(1.11r - 2.11) - 0.0123\sin(0.95s + 0.807)$	$0.00664 + 0.00658\sin(1.09r - 1.7) - 0.00541\sin(0.933s + 0.572)$	$0.0159 + 0.0192\sin(1.23r - 2.56) - 0.0255\sin(1.09s + 0.653)$	$0.00485 + 0.00511\sin(0.964r - 1.2) - 0.00546\sin(1.11s + 0.585)$	$r = [1,7]$, $s = [-3,3]$
3	$0.0119 + 0.0302\sin(0.798r - 1.12) + 0.0245\sin(0.619s + 1.19)$	$17.9 + 0.0172\sin(0.861r - 1.52) + 17.9\sin(0.00476s - 1.53)$	$0.0216 + 0.046\sin(0.784r - 1.1) + 0.0335\sin(0.804s + 0.369)$	$0.0188 - 0.00312r + 0.00352\lvert s\rvert$	$r = [1,10]$, $s = [-3,3]$
4	$0.0223 - 0.0028r + 0.00381s$	0.0087	$0.0199 - 0.00266r + 0.00228s$	$0.00889 - 0.001r - 0.00352\log(\lvert s\rvert)$	$r = [1,9]$, $s = [-3,3]$
5	0.0111	0.0101	0.0137	0.00487	$r = [1,6]$, $s = [-3,3]$
6	$0.00136 - 0.00503\sin(0.495r + 2.3) - 0.00385\sin(1.63s - 0.0934)$	$0.0131 - 0.00108r - 0.00209\log(\lvert s\rvert)$	0.00727	0.00371	$r = [3,12]$, $s = [-3,1]$
7	0.00992	$74.8 - 0.0051\sin(1.62r - 5.09) + 74.8\sin(0.00563s - 1.57)$	0.0125	$-0.00846 + 0.00303r + 0.0122\log(\lvert s\rvert)$	$r = [1,8]$, $s = [-3,3]$
8	0.00913	0.00869	0.00815	0.00243	$r = [2,9]$, $s = [-3,3]$
9	$-5.48 + 5.49\sin(0.017r + 1.49) - 0.00789\sin(1.48s + 1.61)$	$0.0126 - 0.000297r - 0.00406\log(\lvert s\rvert)$	0.00554	$-3.4 - 0.00266\sin(2.92r - 8.24) + 3.4\sin(0.00732s + 1.57)$	$r = [3,6]$, $s = [-3,1]$
10	0.00854	0.00915	0.00709	$0.0084 - 0.0077\sin(1.01r - 1.33) + 0.0067\sin(2.39s - 4.09)$	$r = [1,10]$, $s = [-3,3]$
11	0.00803	0.0109	0.0104	0.0126	$r = [1,11]$, $s = [-3,3]$
12	$0.00292 + 0.00143r - 0.00329s$	$0.00911 - 0.000481r - 0.000154s$	0.0054	$0.00823 - 0.00273\log(r) - 0.00245\sin(3.86s + 4.27)$	$r = [2,10]$, $s = [-2,3]$
13	0.00674	0.00637	0.00949	0.00418	$r = [3,12]$, $s = [-3,2]$
14	$0.00472 - 8.42\times10^{-5}r - 0.00276\log(\lvert s\rvert)$	0.004	0.00667	0.00251	$r = [1,8]$, $s = [-3,3]$
15	$0.00481 + 0.0122\sin(0.954r - 0.538) + 0.0119\sin(0.804s - 0.577)$	$0.0126 - 0.00695\sin(-8.23r - 1.17) + 0.014\sin(0.449s - 1.14)$	$-0.0142 + 0.00141r + 0.00651\lvert s\rvert$	$-0.022 + 0.00896r - 0.0223\sin(-5.14s - 0.267)$	$r = [1,6]$, $s = [-3,3]$
0	$0.0642 + 0.0586\sin(0.0957r + 3.86) - 0.00135\sin(13.6s - 7.75)$	$0.0719 + 0.0669\sin(0.0889r + 3.91) + 0.00154\sin(-29s + 48.6)$	$0.00011 + 0.0282e^{-0.478r} + 0.00568e^{-0.595\lvert s\rvert}$	$0.00011 + 0.0282e^{-0.478r} + 0.00568e^{-0.595\lvert s\rvert}$	$r = [1,10]$, $s = [-3,3]$
1	$-0.00139 + 0.00298\log(r) + 0.00125e^{1.14s}$	0.0164	$0.00431 + 7.45\times10^{3}e^{-13.5r} + 0.000307e^{1.27s}$	$0.01 + 0.00607\sin(0.958r - 2.69) - 0.0112\sin(-36.4s - 80.4)$	$r = [1,20]$, $s = [-3,3]$
2	$0.105 - 0.00317r + 0.0481\sin(1.09s - 0.105)$	$0.0704 - 0.00166r - 0.00806\lvert s\rvert$	$0.0636 - 0.00287r + 0.00109s$	$0.0645 - 0.00239r - 0.00442s$	$r = [3,20]$, $s = [-3,3]$
3	$0.0555 - 0.0552\sin(0.388r + 1.56) - 0.0489\sin(0.953s + 0.081)$	$0.0486 - 0.00138r - 0.0147\sin(0.749s - 0.784)$	$0.0493 - 0.00215r - 0.000238s$	$0.0664 - 0.0019r - 0.00645\lvert s\rvert$	$r = [2,20]$, $s = [-3,3]$
4	$0.0215 - 0.000459r - 0.0113\log(\lvert s\rvert)$	$0.0102 - 0.00849\sin(0.607r + 0.945) + 0.0186\sin(1.01\lvert s\rvert - 0.131)$	$0.0206 - 0.00162r - 0.00897\sin(1.1s - 0.0834)$	$0.0214 - 0.00816\sin(0.797r - 0.877) - 0.0102\sin(0.978s - 1.27)$	$r = [1,13]$, $s = [-3,3]$
5	0.0138	$0.00564 - 0.0121\sin(0.906r - 1.34) + 0.00453\sin(1.57s + 0.657)$	$0.0112 - 0.0254\sin(1.01r - 2.08) + 0.021\sin(1.73s + 1.04)$	$0.0153 - 0.00142r + 0.00378s$	$r = [4,12]$, $s = [-3,3]$
6	$-2.07\times10^{3} + 0.13e^{-0.565r} - 2.07\times10^{3}\sin(6.28s - 7.86)$	$0.0124 + 1.78\times10^{4}e^{-13.3r} + 8.75\times10^{-5}e^{1.57s}$	$0.00169 + 0.221e^{-1.69r} + 0.00692\sin(4.61s - 13.2)$	$-1.35\times10^{3} + 0.227e^{-1.21r} + 1.35\times10^{3}\sin(0.00162s + 1.57)$	$r = [1,18]$, $s = [-3,3]$
7	$0.0187 - 0.00491\log(r) - 0.00695\log(\lvert s\rvert)$	$0.0146 + 0.0122\sin(0.55r + 2.76) - 0.0118\sin(0.434s - 0.193)$	$-15.5 + 0.098e^{-1.45r} + 15.5e^{-0.000124\lvert s\rvert}$	0.0159	$r = [1,18]$, $s = [-3,3]$

Table A.10 Seats CDL-Model Property Equations for 5.16 GHz with humans

Cluster	Direction	Type	Gain [dB]	MToA [s]	Delay Spread [s]	MPC
0	Aft	LoS	$253 + 317\sin(0.0313r + 4.26) + 2.62\sin(-2.36s - 134)$	$2.46 \times 10^{-10} - 1.32 \times 10^{-10} e^{-0.672\lvert s\rvert} - 5.03 \times 10^{-10} e^{-2.56r}$	$1.27 \times 10^{-10} - 8.79 \times 10^{-11} e^{-1.18r} - 5.33 \times 10^{-11} e^{-0.443\lvert s\rvert}$	$\lfloor 3.82 - 0.399r - 0.127s \rfloor$
1	Aft	NLoS	$-149 - 2.19r - 87.6\sin(0.167s - 1.41)$	$2.18 \times 10^{-9} \sin(6.48r - 55.0) - 5.22 \times 10^{-10} \sin(2.58s + 5.33) + 2.99 \times 10^{-9}$	$2.34 \times 10^{-10} - 2.69 \times 10^{-10} \sin(0.414s + 0.117) - 2.24 \times 10^{-10} \sin(0.689r + 1.08)$	$\lfloor -2.05 \times 10^{3} - 2.05 \times 10^{3} \sin(0.00764r + 4.63) - 1.66\sin(0.942s + 0.0705) \rfloor$
2	Aft	NLoS	$-84.9 + 11.9\sin(0.766r - 0.157) - 3.74\sin(-33.9s + 7.69)$	$1.73 \times 10^{-9} \sin(0.892s + 0.62) - 1.71 \times 10^{-9} \sin(0.46r + 1.13) + 4.97 \times 10^{-9}$	$1.04 \times 10^{-11} r - 1.41 \times 10^{-10} \log(\lvert s\rvert) + 1.4 \times 10^{-10}$	$\lfloor 1.53 + 0.28r - 1.41 \log(\lvert s\rvert) \rfloor$
3	Aft	NLoS	$-68.1 - 1.94r - 9.73\sin(0.673s - 7.59)$	$7.7 \times 10^{-9} - 2.38 \times 10^{-9} \log(r) - 2.28 \times 10^{-9} \sin(0.635s + 1.11)$	$4.68 \times 10^{-10} - 4.15 \times 10^{-10} \sin(0.727r + 0.85) - 3.84 \times 10^{-10} \sin(0.646s - 0.0897)$	$\lfloor 3.8 - 1.78\sin(0.356r + 1.53) + 0.979\sin(0.938s + 1.22) \rfloor$
4	Aft	NLoS	$2.29 \times 10^{4} + 2.3 \times 10^{4} \sin(0.003r + 4.66) - 3.48\sin(416s + 420)$	$6.04 \times 10^{-9} \sin(1.05s + 0.331) - 6.23 \times 10^{-10} r + 1.68 \times 10^{-8}$	$5.44 \times 10^{-10} \sin(0.694s + 0.298) - 6.02 \times 10^{-10} \sin(0.398r + 2.54) + 3.66 \times 10^{-10}$	$\lfloor -29.4 - 0.4\sin(0.479r + 1.67) + 31.4\sin(0.0585s + 1.47) \rfloor$
5	Aft	NLoS	$-66.3 - 1.86r + 8.83\sin(0.866s + 7.59)$	$5.46 \times 10^{-9} \sin(0.262s - 1.38) - 2.4 \times 10^{-9} \log(r) + 1.17 \times 10^{-8}$	$2.26 \times 10^{-10} \sin(0.824s + 0.153) - 5.35 \times 10^{-10} \sin(0.742r + 0.739) + 7.93 \times 10^{-10}$	$\lfloor 1.18 - 0.533\sin(0.792r - 0.286) + 2.63\sin(0.373s + 1.29) \rfloor$
6	Aft	NLoS	$-90.4 + 7.8\sin(0.259r + 1.32) - 6.68\sin(0.805s - 0.993)$	$8.19 \times 10^{-9} - 3.57 \times 10^{-9} \sin(1.03s - 0.146) - 1.74 \times 10^{-10} r$	$1.88 \times 10^{-10} - 3.01 \times 10^{-9} e^{-1.08r} - 9.06 \times 10^{-11} \sin(1.21s - 0.323)$	$\lfloor 0.926 + 0.521 \log(r) - 1.05\sin(1.51s + 0.696) \rfloor$
7	Aft	NLoS	$-64.6 - 13.7\log(r) + 4.83\sin(0.822s + 0.66)$	$1.93 \times 10^{-9} \sin(0.483r + 1.92) - 3.87 \times 10^{-9} \sin(1.07s - 0.586) + 1.19 \times 10^{-8}$	$3.09 \times 10^{-10} \sin(0.863s + 0.176) - 3.45 \times 10^{-10} \sin(0.452r + 1.91) + 1.19 \times 10^{-10}$	$\lfloor 1.46 + 0.128r - 0.576 \log(\lvert s\rvert) \rfloor$
8	Aft	NLoS	$-8.68 \times 10^{4} - 1.56r + 8.67 \times 10^{4} \sin(0.00376s + 1.57)$	$1.83 \times 10^{-13} e^{-3.36s} - 2.77 \times 10^{-10} r + 5.7 \times 10^{-9}$	$3.79 \times 10^{-10} \sin(0.884s - 0.23) - 4.36 \times 10^{-10} \sin(0.644r + 0.885) + 2.88 \times 10^{-10}$	$\lfloor 1.34 + 0.785\sin(0.967r - 3.21) + 1.77\sin(0.731\lvert s\rvert - 0.0166) \rfloor$
9	Aft	NLoS	$-87.9 - 6.49\sin(0.366r + 3.17) - 6.06\sin(5.15s - 13.9)$	$2.32 \times 10^{-8} e^{-0.48r} - 2.6 \times 10^{-9} \sin(0.857s - 0.0309) + 3.78 \times 10^{-9}$	$5.01 \times 10^{-10} - 1.77 \times 10^{-10} \sin(0.858s - 0.923) - 3.18 \times 10^{-11} r$	$\lfloor 1.42 + 0.304 \log(r) + 0.848\sin(-2.28s + 5.36) \rfloor$
10	Aft	NLoS	$-71.1 - 1.52r - 7.41\log(\lvert s\rvert)$	$6.96 \times 10^{-9} \sin(0.602s - 0.651) - 1.73 \times 10^{-9} \sin(0.554r + 1.72) + 9.37 \times 10^{-9}$	3.25×10^{-10}	$\lfloor -0.559 + 2.09 \log(r) - 0.841 \log(\lvert s\rvert) \rfloor$
11	Aft	NLoS	$-67.8 - 11.5\log(r) - 0.0204 e^{1.98s}$	$3.94 \times 10^{-9} \sin(1.08s + 1.04) - 1.8 \times 10^{-10} r + 7.68 \times 10^{-9}$	$1.53 \times 10^{-10} \sin(1.19s + 0.859) - 1.39 \times 10^{-10} \sin(0.8r + 0.284) + 2.21 \times 10^{-10}$	$\lfloor 1.9 - 0.0412r + 0.541\sin(1.8s + 0.0739) \rfloor$
0	Cockpit	LoS	$-46.1 + 15\sin(0.264r + 2.04) + 2.38\sin(-5.57s - 369)$	$2.6 \times 10^{-10} - 1.27 \times 10^{-10} e^{-0.569\lvert s\rvert} - 2.98 \times 10^{-10} e^{-1.06r}$	$1.4 \times 10^{-10} - 8.9 \times 10^{-11} e^{-0.476r} - 4.95 \times 10^{-11} e^{-0.439\lvert s\rvert}$	$\lfloor 1.72 + 1.25\sin(0.477r + 0.729) - 0.574\sin(-1.34s - 11) \rfloor$
1	Cockpit	NLoS	$-122 + 17.3\sin(0.168r + 1.42) - 43.4\sin(0.243s - 1.39)$	$9.86 \times 10^{-9} - 9.06 \times 10^{-10} \sin(0.859r + 0.246) - 9.83 \times 10^{-10} \sin(0.821s + 0.231)$	$1.87 \times 10^{-10} \log(r) - 1.7 \times 10^{-10} \log(\lvert s\rvert) + 6.89 \times 10^{-11}$	$\lfloor 0.98 - 1.73\sin(0.368r + 2.21) - 1.71\sin(0.429s - 0.853) \rfloor$
2	Cockpit	NLoS	$-64.4 + 40\sin(6.39r - 91.4) - 13.3\sin(0.51\lvert s\rvert - 2.27)$	$4.31 \times 10^{-10} \sin(1.51s + 1.71) - 6.08 \times 10^{-10} \sin(0.972r - 2.48) + 1.83 \times 10^{-9}$	$2.92 \times 10^{-10} \sin(1.21s - 4.83) - 2.78 \times 10^{-10} \sin(0.784r - 1.55) + 6.78 \times 10^{-10}$	$\lfloor 6.06 - 0.226r - 0.393\sin(0.997s - 0.735) \rfloor$
3	Cockpit	NLoS	$-41.8 - 17.1\log(r) - 8.2\sin(0.854s - 1.48)$	$2.85 \times 10^{-10} \sin(1.08s - 0.351) + 6.85 \times 10^{-10} \sin(0.374r + 3.89) + 2.02 \times 10^{-9}$	$3.6 \times 10^{-10} \sin(1.17s + 1.25) - 4.04 \times 10^{-10} \sin(0.395r + 0.991) + 6.8 \times 10^{-10}$	$\lfloor 3.43 + 0.554 \log(r) - 2.26 \log(\lvert s\rvert) \rfloor$
4	Cockpit	NLoS	$-92 - 19.8\sin(0.149r + 4.49) - 6.62\sin(13.4s - 101)$	$9.1 \times 10^{-9} - 1.61 \times 10^{-9} \sin(0.251r + 3.36) - 1.13 \times 10^{-9} \sin(1.12s + 0.605)$	$1.31 \times 10^{-10} - 1.78 \times 10^{-10} \sin(1.25s + 0.852) - 9.4 \times 10^{-11} \sin(1.39r - 4.82)$	$\lfloor 1.41 - 1.51\sin(0.377r + 1.86) - 1.01\sin(0.917s - 0.338) \rfloor$
5	Cockpit	NLoS	$-7.09 \times 10^{4} - 1.26r + 7.09 \times 10^{4} \sin(0.00656s + 1.57)$	$5.72 \times 10^{-10} \log(r) + 1.85 \times 10^{-9} \sin(0.763s - 0.744) + 1.1 \times 10^{-8}$	$6.08 \times 10^{-10} \sin(1.29\lvert s\rvert - 0.815) - 6.17 \times 10^{-10} \sin(0.405r + 1.56) + 3.49 \times 10^{-11}$	$\lfloor 2.36 - 0.0695r + 1.03\sin(0.866s + 0.419) \rfloor$
6	Cockpit	NLoS	$-1.67 \times 10^{5} - 9.16\sin(0.254r + 3.51) + 1.67 \times 10^{5} \sin(-0.00392s - 4.71)$	$2.01 \times 10^{-9} \sin(0.747s + 0.632) - 2.5 \times 10^{-9} \log(r) + 8.21 \times 10^{-9}$	$2.09 \times 10^{-10} \sin(0.785s + 0.405) - 1.82 \times 10^{-10} \sin(0.451r + 1.08) + 1.6 \times 10^{-10}$	$\lfloor 2.29 + 1.23\sin(0.325r + 10.5) + 0.734\sin(1.52s - 0.261) \rfloor$
7	Cockpit	NLoS	$-56.4 - 14.5\log(r) + 5.65\sin(0.65s + 0.405)$	$6.54 \times 10^{-9} - 4.51 \times 10^{-9} \sin(0.349s + 0.977) - 9.59 \times 10^{-10} \sin(0.522r + 0.923)$	$3.25 \times 10^{-6} \sin(0.00427s - 1.57) - 1.79 \times 10^{-10} \sin(0.76r - 0.883) + 3.25 \times 10^{-6}$	$\lfloor 1.72 + 1.79\sin(-0.435r + 13.7) + 2.04\sin(0.437\lvert s\rvert + 0.315) \rfloor$
8	Cockpit	NLoS	$-71.8 - 7.69\log(r) + 5.76\sin(-1.41s + 16.9)$	$3.55 \times 10^{-9} - 1.48 \times 10^{-9} \sin(0.354r + 2.43) - 3.32 \times 10^{-9} \sin(0.347s - 1.06)$	$8.13 \times 10^{-11} \sin(0.857r - 1.46) - 1.12 \times 10^{-10} \sin(2.42s + 4.16) + 1.26 \times 10^{-10}$	$\lfloor -0.929 + 0.566 \log(r) + 1.99\sin(0.943\lvert s\rvert - 0.342) \rfloor$

Cluster	$\overline{\phi^A}$ [rad]	$\overline{\phi^D}$ [rad]	$\overline{\theta^A}$ [rad]	$\overline{\theta^D}$ [rad]
0	$\mathrm{rot}(-0.0127 + 0.00863r + 0.811\sin(0.602s + 0.0162))$	$-0.0127 + 0.00863r + 0.811\sin(0.602s + 0.0162)$	$\mathrm{rot}(-2.55 + 0.293\log(r) + 0.201\log(\lvert s\rvert))$	$2.55 - 0.293\log(r) - 0.201\log(\lvert s\rvert)$
1	$1.19 - 0.000556r - 0.135\sin(0.983s + 1.14)$	$0.0502 + 0.52e^{-0.438r} + 0.0604\sin(0.875s + 0.604)$	$\mathrm{rot}(-1.6 - 1.45e^{-1.22r} - 0.0343\sin(0.907s + 0.0363))$	$349 + 694\sin(0.00344r + 4.67) - 347\sin(0.00142s - 1.57)$
2	$2.7 + 0.00531r - 0.0772\log(\lvert s\rvert)$	$-0.0481 - 0.0581\sin(0.337r + 1.21) + 0.0447\sin(1.14s + 0.471)$	$\mathrm{rot}(-1.91 - 1.9e^{-1.79r} + 0.0809\sin(1.82s - 0.354))$	$\mathrm{rot}(-0.932 - 0.0425\log(r) + 0.0511\log(\lvert s\rvert))$
3	$\mathrm{rot}(-0.914 + 0.00763r + 0.205\sin(0.924s + 0.561))$	$-0.0129 + 0.365e^{-0.143r} + 0.0729\sin(0.702s + 0.195)$	$-243 - 245\sin(0.00328r + 4.67) - 0.0708\sin(0.924s - 0.202)$	$1.72 + 0.738e^{-0.287r} + 0.0165\sin(5s - 5.57)$
4	$-1.42 \times 10^{3} + 0.0558\sin(0.539r - 28.6) - 1.42 \times 10^{3} \sin(0.00493s - 1.56)$	$-0.00355 - 0.269e^{-0.158r} + 0.0601\sin(0.867s - 0.403)$	$\mathrm{rot}(-2.27 + 0.0217\sin(0.61r + 0.318) - 0.0334\sin(0.923s + 0.415))$	$1.65 + 0.391e^{-0.21r} + 2.04 \times 10^{-12} e^{7.77s}$
5	$\mathrm{rot}(0.582 + 0.44e^{-0.21r} + 0.226\sin(0.761s - 0.167))$	$-0.0557 - 0.477e^{-0.388r} + 0.0995\sin(0.625s - 0.38)$	$1.18 + 0.0546\sin(5.44r - 45) + 0.156\sin(0.823s + 0.642)$	$1.72 + 0.702e^{-0.275r} + 0.024\sin(4.9s + 2.65)$
6	$\mathrm{rot}(-2 + 0.012r - 0.151\sin(1.01s + 0.517))$	$0.308 - 0.0988\log(r) + 0.0467\sin(0.856s - 0.152)$	$\mathrm{rot}(-2.78 + 0.0294\sin(10.4r - 73.6) - 0.203\sin(0.696\lvert s\rvert + 3.06))$	$1.74 + 0.721e^{-0.394r} - 0.0204\sin(1.84s - 0.544)$
7	$-21.5 + 21.7\sin(0.00405r + 1.44) + 0.138\sin(-22.6s - 52.5)$	$0.305 - 0.104\log(r) + 0.0684\sin(0.553s - 0.929)$	$0.735 - 0.055\sin(0.452r + 2.33) + 0.0666\sin(0.966s - 0.85)$	$1.64 + 0.441e^{-0.212r} - 0.0195\sin(0.555s + 5.31)$
8	$\mathrm{rot}(2.01 - 0.0739\sin(0.656r - 0.395) + 0.0836\sin(-4.11s - 1.18))$	$-0.0242 - 0.736e^{-0.677r} + 0.0599\sin(0.867s - 0.744)$	$\mathrm{rot}(-1.61 + 0.0405\sin(0.728r + 1.3) + 0.0207\sin(0.867s - 0.532))$	$1.74 + 1.06e^{-0.438r} + 0.000713e^{-0.209s}$
9	$2.25 + 40.6\sin(3.14r - 12.6) + 0.148\sin(0.673s - 0.383)$	$-0.0932 + 0.463e^{-0.105r} + 0.06\sin(0.626s + 0.118)$	$0.565 + 0.927e^{-1.19r} - 0.0573\sin(0.83s + 0.646)$	$1.84 - 0.105\sin(-0.328r + 11.5) - 0.0383\sin(0.706s - 0.381)$
10	1.8	$-0.0964 + 0.0968\log(r) - 0.0493\log(\lvert s\rvert)$	$\mathrm{rot}(-0.999 + 0.152\sin(0.273r + 1.99) + 0.0927\sin(0.857s + 0.235))$	$2 + 0.13\sin(-0.399r + 8.92) - 0.0575\sin(1.05s + 0.0781)$
11	$-0.159 - 0.109\sin(0.896r + 0.671) - 0.486\sin(0.752s + 1.27)$	$-0.233 + 0.142\log(r) - 0.109e^{-0.232s}$	$\mathrm{rot}(-2.86 + 0.00744r - 0.0506\sin(3.9s + 10.5))$	$1.87 - 0.188\sin(0.191r + 5.63) + 0.0172\sin(2.38s + 1.21)$
0	$0.00439 - 0.000734r - 0.875\sin(0.608s - 0.0127)$	$\mathrm{rot}(0.00439 - 0.000734r - 0.875\sin(0.608s - 0.0127))$	$-309 - 311\sin(0.0101r + 4.63) - 0.135\sin(-26s + 228)$	$\mathrm{rot}(309 + 311\sin(0.0101r + 4.63) + 0.135\sin(-26s + 228))$
1	$-0.059 + 0.649e^{-0.117r} - 0.174\sin(0.649s + 0.78)$	$0.559 + 0.00311r - 0.164\sin(1.54s + 2.05)$	$\mathrm{rot}(-1.87 + 0.179\sin(0.286r + 3.9) + 0.0589\sin(1.18s + 0.411))$	$\mathrm{rot}(-0.811 + 0.0483\sin(-0.288r + 9.7) + 0.0599\sin(1.47s + 1.79))$
2	$\mathrm{rot}(0.0049 - 0.0241\sin(0.746r + 0.979) + 0.327\sin(0.462s - 0.142))$	$\mathrm{rot}(0.0171 - 0.00198r - 0.0675s)$	$\mathrm{rot}(-2.26 - 0.544e^{-0.449r} + 0.0246\sin(-2.16s + 20.4))$	$1.79 + 0.995e^{-0.417r} - 0.0125\sin(0.802s - 0.689)$
3	$0.107 - 0.0412\log(r) - 0.124\sin(0.793s + 0.359)$	$\mathrm{rot}(0.0105 - 0.00115r + 0.011e^{-0.599s})$	$\mathrm{rot}(-669 + 0.00745r + 667\sin(-0.00461s + 1.57))$	$2.22 - 0.133\log(r) + 1.55\sin(9.42s + 3.15)$
4	$\mathrm{rot}(0.0943 - 0.892e^{-0.144r} + 0.28\sin(0.53s + 0.459))$	$\mathrm{rot}(-2.58 - 1.48e^{-1.53r} + 0.195\sin(1.43s - 1.23))$	$0.816 + 0.147\sin(0.194r + 4.65) - 0.0598\sin(-1.1s + 0.253)$	$2.32 - 0.0425\sin(0.324r + 2.73) - 0.0534\sin(-2.55s - 4.15)$
5	$-0.354 + 0.0156r - 0.15\sin(0.567s - 0.928)$	$\mathrm{rot}(2.7 + 0.0331\sin(1.21r - 3.33) + 0.0526\sin(0.933s + 0.0274))$	$\mathrm{rot}(-1.59 - 0.653e^{-0.0997r} - 0.0638\sin(-4.92s + 0.0746))$	$2.3 - 0.00493r - 0.0985\sin(-1.94s - 6.14)$
6	$-2.2 - 0.0622\sin(0.48r + 2.9) - 0.0693\sin(1.17s + 1.07)$	$\mathrm{rot}(-0.0314 + 0.572e^{-0.273r} + 0.0672e^{-0.339s})$	$1.1 + 2.25 \times 10^{-13} e^{1.4r} + 0.106\sin(0.674s - 0.261)$	$-283 + 0.817e^{-0.259r} + 285e^{1.06 \times 10^{-5} s}$
7	$-0.805 - 0.056\sin(-0.638r - 2.84) - 0.443\sin(0.529\lvert s\rvert + 0.243)$	$\mathrm{rot}(-0.0781 + 0.544e^{-0.327r} + 0.0995\sin(-7.01\lvert s\rvert - 3.74))$	$1.4 + 0.0499\sin(0.635r + 0.0878) - 0.0646\sin(-4.8s + 32.9)$	$1.69 + 1.26e^{-0.326r} + 0.0196\sin(1.23s - 0.495)$
8	$\mathrm{rot}(144 + 0.145\sin(0.268r + 3.87) + 145\sin(0.00977s - 1.51))$	$1.3 + 0.00883r + 0.000154e^{2.43s}$	$0.884 + 0.106\sin(0.339r + 2.84) + 0.0803\sin(0.836s + 0.0493)$	$\mathrm{rot}(-0.636 + 0.0389\sin(0.774r + 0.808) - 0.0872\sin(-7.7s + 10.3))$

Cluster	$\sigma(\phi^A)$ [rad]	$\sigma(\phi^D)$ [rad]	$\sigma(\theta^A)$ [rad]	$\sigma(\theta^D)$ [rad]	Limits [m]
0	$0.00389 - 0.00597\log(r) + 0.0206e^{-0.135\lvert s\rvert}$	$0.00389 - 0.00596\log(r) + 0.0206e^{-0.135\lvert s\rvert}$	$-0.00622 + 0.0226e^{-0.791r} + 0.0186e^{-0.278\lvert s\rvert}$	$-0.00622 + 0.0226e^{-0.791r} + 0.0186e^{-0.278\lvert s\rvert}$	$r = [1, 6]$, $s = [-3, 3]$
1	$0.0262 - 0.00799\sin(0.686r + 1.26) - 0.00622\sin(1.47s - 0.666)$	$0.0322 - 0.00271r - 0.00414s$	$0.0207 - 0.0102\sin(0.783r + 0.106) - 0.0157\sin(0.459s + 0.269)$	$0.00627 - 0.00425\sin(0.734r + 1.24) - 0.00413\sin(0.903s + 0.485)$	$r = [2, 19]$, $s = [-3, 3]$
2	$0.021 - 0.00384\log(r) - 0.011\log(\lvert s\rvert)$	0.0108	$0.0106 + 0.0128\sin(0.538r + 1.27) - 0.0108\sin(1.55s - 1.08)$	0.00873	$r = [1, 19]$, $s = [-3, 3]$
3	$0.0409 - 0.0506\sin(0.34r + 2.52) - 0.0323\sin(1.2s - 1.13)$	$0.0173 - 0.0132\sin(0.644r + 1.43) - 0.012\sin(0.863s + 0.0676)$	$0.0184 - 0.0333\sin(0.331r + 2.63) - 0.0275\sin(0.974s - 0.685)$	$0.0218 - 0.00142r - 0.0104\sin(0.845s - 0.323)$	$r = [1, 19]$, $s = [-3, 3]$
4	$-1.18 \times 10^{3} - 0.0176\sin(0.357r + 3.09) + 1.18 \times 10^{3} \sin(-0.0017s + 1.57)$	$-1.32 - 0.00851\sin(0.412r + 2.71) + 1.34\sin(0.0204s + 1.5)$	$-122 - 0.0158\sin(0.364r + 2.46) + 122\sin(0.00524s + 1.57)$	$0.0125 - 0.000963r + 0.00111s$	$r = [1, 18]$, $s = [-3, 3]$
5	$0.0371 - 0.0612\sin(0.346r + 2.44) + 0.0419\sin(0.879s + 0.604)$	$0.0148 - 0.0247\sin(0.358r + 2.61) + 0.0155\sin(0.82s - 0.241)$	$0.0409 - 0.0553\sin(0.33r + 2.23) + 0.0386\sin(1.06s + 0.709)$	$0.0193 - 0.00504\sin(0.765r + 0.573) + 0.0104\sin(1.06s + 0.436)$	$r = [1, 19]$, $s = [-3, 3]$
6	$0.0155 - 0.000586r - 0.00623\log(\lvert s\rvert)$	$0.0108 - 0.000639r + 0.000111e^{1.56s}$	$0.0067 - 0.00774\sin(0.597r + 1.67) - 0.00776\sin(1.69s + 1.04)$	$0.00458 - 7.25 \times 10^{-5} r - 0.00255\sin(1.49s - 0.192)$	$r = [2, 18]$, $s = [-3, 3]$
7	$0.00518 - 0.0134\sin(0.512r + 1.77) + 0.0132\sin(0.783s - 0.0314)$	$0.0126 - 0.000772r + 0.00144s$	$0.00376 - 0.0107\sin(0.444r + 2.41) + 0.00998\sin(0.798s - 0.0214)$	$0.00741 - 0.000614r + 0.000853s$	$r = [2, 16]$, $s = [-3, 3]$
8	$0.0246 - 0.0308\sin(0.532r + 1.49) + 0.0345\sin(0.877s - 0.204)$	$0.0153 - 0.02\sin(0.581r + 1.82) + 0.0174\sin(0.845s - 0.594)$	$0.0179 - 0.0173\sin(0.768r + 0.5) + 0.0194\sin(0.92s - 0.0247)$	$0.00555 - 0.0067\sin(0.673r + 1.6) + 0.00782\sin(1.09s - 0.699)$	$r = [2, 19]$, $s = [-3, 3]$
9	$0.0175 - 0.0148\sin(0.394r + 2.04) - 0.0164\sin(1.35s - 0.773)$	$0.00735 - 0.000817r + 0.0109\sin(0.967\lvert s\rvert - 0.158)$	$0.0108 - 0.0107\sin(0.538r + 1.16) - 0.0114\sin(2.1s + 0.944)$	$0.00723 - 0.00602\sin(0.501r + 1.67) - 0.00739\sin(1.13s - 0.736)$	$r = [2, 15]$, $s = [-3, 3]$
10	0.0142	0.0103	0.0118	0.00579	$r = [2, 14]$, $s = [-3, 3]$
11	$0.0245 - 0.00147r - 0.0118\sin(-1.88s - 0.197)$	$0.0109 - 0.000686r - 0.000375s$	$0.0173 - 0.00111r + 0.00786\sin(1.84s - 0.083)$	$0.008 - 0.00332\log(r) + 9.43 \times 10^{-6} e^{-1.97s}$	$r = [3, 13]$, $s = [-3, 3]$
0	$0.0238 + 0.0183\sin(0.19r + 3.08) + 0.00236\sin(-2.36s - 26.7)$	$0.0238 + 0.0183\sin(0.189r + 3.08) + 0.00236\sin(3.92s - 26.7)$	$12.7 + 12.7\sin(0.00807r + 4.65) - 0.00321\sin(24.3s - 165)$	$12.7 + 12.7\sin(0.00807r + 4.65) - 0.00321\sin(26s - 165)$	$r = [1, 11]$, $s = [-3, 3]$
1	$0.0136 - 0.0142\sin(0.485r + 1.85) - 0.016\sin(1.12s - 0.995)$	$0.02 + 0.00513\log(r) - 0.0144\sin(0.914s - 0.679)$	$0.0125 - 0.012\sin(0.535r + 1.75) - 0.0141\sin(1.15s - 1.04)$	$0.0142 - 0.0118\sin(0.409r + 1.52) - 0.0106\sin(0.731s - 1.25)$	$r = [1, 19]$, $s = [-3, 3]$
2	$0.0769 - 0.00134r + 0.0229\sin(27.4s + 137)$	$0.0422 - 0.0144\sin(0.877r - 1.84) + 0.00957\sin(0.519s + 1.16)$	$0.0203 + 0.027\sin(-0.187r + 9.21) + 0.0154\sin(1.19\lvert s\rvert + 0.201)$	$0.0382 - 0.0176\sin(0.331r + 19.7) - 0.0138\sin(0.954\lvert s\rvert - 0.82)$	$r = [1, 20]$, $s = [-3, 3]$
3	$0.0616 - 0.0478\sin(0.368r + 1.54) - 0.0464\sin(0.486\lvert s\rvert - 0.592)$	$0.0323 - 0.0368\sin(0.371r + 1.63) + 0.0131\sin(1.25\lvert s\rvert - 0.00449)$	$0.0467 - 0.0175\sin(0.863r - 1.64) - 0.0338\sin(2.36s + 7.77)$	$0.0395 - 0.0359\sin(18.5r - 293) + 0.0336\sin(2.47s + 17.2)$	$r = [3, 20]$, $s = [-3, 3]$
4	$0.00642 - 0.00991\sin(0.325r + 2.71) - 0.0123\sin(1.09s - 0.759)$	$0.0132 - 0.011\sin(0.402r + 2.02) - 0.0106\sin(0.951s - 0.0366)$	$0.00342 - 0.00935\sin(0.291r + 3.26) - 0.0106\sin(1.03s - 0.46)$	$0.00899 - 0.0122\sin(0.373r + 2.02) - 0.0115\sin(1.12s + 0.39)$	$r = [1, 19]$, $s = [-3, 3]$
5	$0.0139 - 0.011\sin(0.614r + 1.06) + 0.0114\sin(1.19s + 0.941)$	$0.0197 - 0.011\sin(0.829r - 1.41) + 0.013\sin(0.741s + 0.216)$	$0.00893 - 0.00827\sin(0.64r + 0.619) + 0.0107\sin(1.04s + 0.799)$	$0.0163 - 0.0283\sin(0.417r + 1.42) + 0.0122\sin(1.33\lvert s\rvert - 0.41)$	$r = [1, 19]$, $s = [-3, 3]$
6	$0.0486 - 0.00168r + 0.0115\sin(1.19s + 0.551)$	$0.0194 - 0.00102r + 0.00348s$	$0.00946 + 0.0126\sin(0.402r + 3.88) + 0.00816\sin(0.979s + 0.525)$	$0.0014 + 0.00392\sin(0.393r + 4.51) + 0.00291\sin(0.777s + 0.591)$	$r = [4, 20]$, $s = [-3, 3]$
7	$0.0142 - 0.000119r + 1.59 \times 10^{-12} e^{7.68s}$	$0.0183 - 0.0101\sin(-0.346r + 1.53) - 0.0128\sin(1.17\lvert s\rvert - 0.373)$	$0.018 + 0.0146\sin(2.08r - 12.8) - 0.00989\sin(4.13\lvert s\rvert - 1.35)$	$0.00151 + 0.000386r + 0.00204s$	$r = [3, 20]$, $s = [-3, 3]$
8	$0.00313 + 0.0021\sin(0.542r + 2.33) - 0.00356\sin(1.54s + 1.7)$	$0.0135 - 0.00014r - 0.00624\sin(1.07s + 0.822)$	$-77.4 + 77.4\sin(0.00138r + 7.84) - 0.00731\sin(1.46s + 1.37)$	$0.0126 + 0.00681\sin(0.836r - 1.46) - 0.0109\sin(1.03s + 0.955)$	$r = [1, 19]$, $s = [-3, 3]$

List of Figures

List of Tables

List of Publications

Journal Articles

[Man+22a] Jörg von Mankowski, Emre Durmaz, Arled Papa, Hansini Vijayaraghavan, and Wolfgang Kellerer. "Aerial-Aided Multi-Access Edge Computing: Dynamic and Joint Optimization of Task and Service Placement and Routing in Multi-Layer Networks". In: *IEEE Transactions on Aerospace and Electronic Systems* (2022).

[Man+23b] Jörg von Mankowski, Hansini Vijayaraghavan, Yannik Hilla, and Wolfgang Kellerer. "Characterization of the 2.4 GHz and 5 GHz Channels in a Single-Aisle Commercial Aircraft Cabin Using Ray-Tracing". In: *IEEE Transactions on Aerospace and Electronic Systems* (2023), pp. 1–16.

[MVK24] Jörg von Mankowski, Hansini Vijayaraghavan, and Wolfgang Kellerer. "RAT-mania: Advancing Multi-RAT Networks with Optimal Beamforming, Slot and Power Allocation, through Optimization, Heuristics, and Learning". In: *IEEE Access* (2024).

[Pap+23] Arled Papa, Jorg von Mankowski, Hansini Vijayaraghavan, Babak Mafakheriy, Leonardo Gorattiy, and Wolfgang Kellerer. "Enabling 6g applications in the sky: Aeronautical federation framework". In: *IEEE Network* (2023).

[Vij+23] Hansini Vijayaraghavan, Jörg Von Mankowski, Carmen Mas-Machuca, and Wolfgang Kellerer. "PlaciFi: Orchestrating Optimal 3D Access Point Placement for LiFi-WiFi Heterogeneous Networks". In: *IEEE Access* (2023).

Conference Proceedings

[Man+22b] Jörg von Mankowski, Hansini Vijayaraghavan, Alberto Martinez Alba, Leonardo Goratti, and Wolfgang Kellerer. "Towards the Optimal Pattern of Joint Beamforming, User Scheduling and Power Allocation in a multi-RAT Network". In: *2022 IEEE 19th Annual Consumer Communications & Networking Conference (CCNC)*. IEEE. 2022, pp. 338–345.

[Vij+22] Hansini Vijayaraghavan, Jörg von Mankowski, Stephan Pellegrino, and Carmen Mas-Machuca. "Optimized 3D Placement of LiFi Access Points towards maximizing Wireless Network Performance". In: *GLOBECOM 2022-2022 IEEE Global Communications Conference*. IEEE. 2022, pp. 1278–1283.

Bibliography

[Hei+22] Iryna Heiets, Jiezhuoma La, Wenhui Zhou, Shaoxin Xu, Xingyue Wang, and Yuchen Xu. "Digital transformation of airline industry". In: *Research in Transportation Economics* 92 (2022), p. 101186.

[Aira] Airbus. *Airspace Link*. Accessed: 2024-03-06. URL: https://www.airbus.com/en/newsroom/stories/2022-06-airspace-link-bringing-the-connected-vision-to-reality.

[Sch+21] Jorge F Schmidt, Daniel Neuhold, Christian Bettstetter, Jirka Klaue, and Dominic Schupke. "Wireless connectivity in airplanes: Challenges and the case for UWB". In: *IEEE Access* 9 (2021), pp. 52913–52925.

[Unz+20] Luis Unzueta et al. "Building a Camera-based Smart Sensing System for Digitalized On-demand Aircraft Cabin Readiness Verification." In: *ROBOVIS*. 2020, pp. 98–105.

[Sch17] Michael Schmidt. "A review of aircraft turnaround operations and simulations". In: *Progress in Aerospace Sciences* 92 (2017), pp. 25–38.

[CC18] Mark Anthony Camilleri and Mark Anthony Camilleri. *Aircraft operating costs and profitability*. Springer, 2018.

[MC+23] Alison de Oliveira Moraes, Flávia Renata Dantas Alves Silva Ciaccia, et al. "Smart cabin design concept for regional aircraft: Technologies, Applications & architecture". In: *Journal of Aerospace technology and Management* 15 (2023), e2023.

[Gür+16] Murat Gürsu, Mikhail Vilgelm, Samuele Zoppi, and Wolfgang Kellerer. "Reliable coexistence of 802.15. 4e TSCH-based WSN and Wi-Fi in an aircraft cabin". In: *2016 IEEE International Conference on Communications Workshops (ICC)*. IEEE. 2016, pp. 663–668.

[Dia+04] NR Diaz, JEJ Esquitino, T Eisenberg, P Veith, et al. *In-Cabin Channel Measurement Performance and Result Report*. Tech. rep. IST-2001-37466 WirelessCabin D-11. Deutsches Zentrum für Luft- und Raumfahrt, 2004.

[HVB05] Genevieve Hankins, Linda Vahala, and John H Beggs. "Propagation prediction inside a B767 in the 2.4 GHz and 5 GHz radio bands". In: *2005 IEEE Antennas and Propagation Society International Symposium*. Vol. 1. IEEE. 2005, pp. 791–794.

[MC08] Nektarios Moraitis and Philip Constantinou. "Radio channel measurements and characterization inside aircrafts for in-cabin wireless networks". In: *2008 IEEE 68th Vehicular Technology Conference*. IEEE. 2008, pp. 1–5.

[FKP08] Robert Felbecker, Wilhelm Keusgen, and Michael Peter. "Incabin millimeter wave propagation simulation in a wide-bodied aircraft using ray-tracing". In: *2008 IEEE 68th Vehicular Technology Conference*. IEEE. 2008, pp. 1–5.

[Mor+09] Nektarios Moraitis, Philip Constantinou, Fernando Perez Fontan, and Pavel Valtr. "Propagation measurements and comparison with EM techniques for in-cabin wireless networks". In: *EURASIP Journal on Wireless Communications and Networking* 2009 (2009), pp. 1–13.

[Top+22] Ozan Alp Topal, Mustafa Ozger, Dominic Schupke, Emil Björnson, and Cicek Cavdar. "mmWave Communications for Indoor Dense Spaces: Ray-Tracing Based Channel Characterization and Performance Comparison". In: *arXiv preprint arXiv:2202.08774* (2022).

[Cav+18] Cicek Cavdar, Damini Gera, Sandra Hofmann, Dominic Schupke, Ayan Ghosh, and Anders Nordlöw. "Demonstration of an integrated 5G network in an aircraft cabin environment". In: *2018 IEEE/AIAA 37th Digital Avionics Systems Conference (DASC)*. IEEE. 2018, pp. 1–10.

[Man+23a] Jörg von Mankowski, Hansini Vijayaraghavan, Yannik Hilla, and Wolfgang Kellerer. *Single Aisle Aircraft 3D-Model*. https://doi.org/10.14459/2023mp1707095. Dataset. 2023.

[YT20] Ranjeet Yadav and Ashutosh Tripathi. "A survey on hybrid, 3D, interference mitigation and secure data beamforming techniques for 5G system". In: *Wireless Personal Communications* 114 (2020), pp. 883–900.

[Che+17] Mingzhe Chen, Mohammad Mozaffari, Walid Saad, Changchuan Yin, Mérouane Debbah, and Choong Seon Hong. "Caching in the sky: Proactive deployment of cache-enabled unmanned aerial vehicles for optimized quality-of-experience". In: *IEEE Journal on Selected Areas in Communications* 35.5 (2017), pp. 1046–1061.

[Pac+21] Lucas Pacheco et al. "Towards the Future of Edge Computing in the Sky: Outlook and Future Directions". In: *2021 17th International Conference on Distributed Computing in Sensor Systems (DCOSS)*. IEEE. 2021, pp. 220–227.

[Wei+23] Peng Wei, Wei Feng, Yunfei Chen, Ning Ge, Wei Xiang, and Shiwen Mao. "Task-Oriented Satellite-UAV Networks With Mobile Edge Computing". In: *IEEE Open Journal of the Communications Society* (2023).

[ICA22] International Civil Aviation Organization (ICAO). *Handbook on Radio Frequency Spectrum Requirements for Civil Aviation*. ICAO, 2022.

[Airb] Airbus. *Cabin and Comfort*. Accessed: 2024-03-24. URL: https://www.airbus.com/en/products-services/commercial-aircraft/cabin-and-comfort.

[ETS20] The European Telecommunications Standards Institute (ETSI). *Study on channel model for frequencies from 0.5 to 100 GHz*. Technical Report 138 901. Version 16.1.0. Nov. 2020.

[Bal12] C A Balanis. *Balanis' Advanced Engineering Electromagnetics*. John Wiley and Sons, 2012, pp. 423–433. ISBN: 9780470589489.

[Rem20] Remcom, Inc. *Wireless InSite Reference Manual*. Sept. 2020. URL: https://www.remcom.com/wireless-insite-em-propagation-software.

[Tar+21] Sulaiman Tariq, Hussain Al-Rizzo, Md Nazmul Hasan, Nijas Kunju, and Said Abushamleh. *Stochastic versus Ray Tracing Wireless Channel Modeling for 5G and V2X Applications: Opportunities and Challenges*. Ed. by Hussain Al-Rizzo and Said Abushamleh. Rijeka: IntechOpen, 2021. Chap. 1.

[Dia+02] NR Diaz, J Müller, O Franzrahe, and P Veith. *In-Cabin Channel Measurement Planning Document*. Tech. rep. IST-2001-37466 WirelessCabin D-10. Deutsches Zentrum für Luft- und Raumfahrt, 2002.

[Ges+07] David Gesbert, Marios Kountouris, Robert W Heath, Chan-Byoung Chae, and Thomas Salzer. "Shifting the MIMO paradigm". In: *IEEE signal processing magazine* 24.5 (2007), pp. 36–46.

[Ahm+18] Irfan Ahmed et al. "A Survey on Hybrid Beamforming Techniques in 5G: Architecture and System Model Perspectives". In: *IEEE Communications Surveys Tutorials* 20.4 (2018), pp. 3060–3097.

[Fut] Future Travel Experience. *How airlines and suppliers must reinvent their inflight content strategies to create new digital experiences*. Accessed: 2024-01-18. URL: https://www.futuretravelexperience.com/2020/11/how-airlines-and-suppliers-must-reinvent-their-inflight-content-strategies-to-create-new-digital-experiences/.

[WRA19] Ramadhan Cakra Wibawa, Siti Rochimah, and Radityo Anggoro. "A development of quality model for online games based on ISO/IEC 25010". In: *2019 12th International Conference on Information & Communication Technology and System (ICTS)*. IEEE. 2019, pp. 215–218.

[CMP19] Tamal Chakraborty, Iti Saha Misra, and Ramjee Prasad. *Voip technology: Applications and challenges*. Springer, 2019.

[Cui+20] Gaofeng Cui, Xiaoyao Li, Lexi Xu, and Weidong Wang. "Latency and energy optimization for MEC enhanced SAT-IoT networks". In: *IEEE Access* 8 (2020), pp. 55915–55926.

[Wan+21] Dengke Wang, Marco Giordani, Mohamed-Slim Alouini, and Michele Zorzi. "The Potential of Multilayered Hierarchical Nonterrestrial Networks for 6G: A Comparative Analysis Among Networking Architectures". In: *IEEE Vehicular Technology Magazine* 16.3 (2021), pp. 99–107.

[Var+19] Amir Varasteh et al. "Mobility-Aware Joint Service Placement and Routing in Space-Air-Ground Integrated Networks". In: *ICC 2019 - 2019 IEEE International Conference on Communications (ICC)*. 2019, pp. 1–7.

[Qin+21] Zhen Qin, Hai Wang, Yuben Qu, Haipeng Dai, and Zhenhua Wei. "Air-Ground Collaborative Mobile Edge Computing: Architecture, Challenges, and Opportunities". In: *arXiv preprint arXiv:2101.07930* (2021).

[Iri] Iridium. *Iridium Network*. Accessed: 2022-04-14. URL: https://www.iridium.com/.

[GZ21] Marco Giordani and Michele Zorzi. "Non-Terrestrial Networks in the 6G Era: Challenges and Opportunities". In: *IEEE Network* 35.2 (2021), pp. 244–251.

[Sae+21] Nasir Saeed, Heba Almorad, Hayssam Dahrouj, Tareq Y Al-Naffouri, Jeff S Shamma, and Mohamed-Slim Alouini. "Point-to-point communication in integrated satellite-aerial 6G networks: State-of-the-art and future challenges". In: *IEEE Open Journal of the Communications Society* (2021).

[Che+21a] Quan Chen, Lei Yang, Xianfeng Liu, Jianming Guo, Shuai Wu, and Xiaoqian Chen. "Multiple gateway placement in large-scale constellation networks with inter-satellite links". In: *International Journal of Satellite Communications and Networking* 39.1 (2021), pp. 47–64.

[Inc16] IRIDIUM Communications Inc. *2016 Annual Report*. Tech. rep. IRIDIUM Communications Inc., 2016.

[Pan+21a] Xiaowei Pang, Nan Zhao, Jie Tang, Celimuge Wu, Dusit Niyato, and Kai-Kit Wong. "IRS-assisted secure UAV transmission via joint trajectory and beamforming design". In: *IEEE Transactions on Communications* 70.2 (2021), pp. 1140–1152.

[Pan+21b] Xiaowei Pang, Min Sheng, Nan Zhao, Jie Tang, Dusit Niyato, and Kai-Kit Wong. "When UAV meets IRS: Expanding air-ground networks via passive reflection". In: *IEEE Wireless Communications* 28.5 (2021), pp. 164–170.

[God+22] Ralf God, Lothar Kerschgens, Leonardo Goratti, and Steven Lemaire. "Smart and Connected Aircraft Cabin: A Balancing Act between Operational Cabin Management, Airline Business and Passenger Expectations". In: *International Journal of Aerospace and Mechanical Engineering* 16.12 (2022), pp. 360–365.

[Wen+19] Jinxiao Wen, Yan Zhang, Guanshu Yang, Zunwen He, and Wancheng Zhang. "Path loss prediction based on machine learning methods for aircraft cabin environments". In: *IEEE Access* 7 (2019), pp. 159251–159261.

[PSG12] Caleb Phillips, Douglas Sicker, and Dirk Grunwald. "A survey of wireless path loss prediction and coverage mapping methods". In: *IEEE Communications Surveys & Tutorials* 15.1 (2012), pp. 255–270.

[Sch+20] Paul Schwarzbach, Julia Engelbrecht, Albrecht Michler, Michael Schultz, and Oliver Michler. "Evaluation of technology-supported distance measuring to ensure safe aircraft boarding during COVID-19 pandemic". In: *Sustainability* 12.20 (2020), p. 8724.

[Jac+09] Martin Jacob et al. "Influence of passengers on the UWB propagation channel within a large wide-bodied aircraft". In: *2009 3rd European Conference on Antennas and Propagation*. IEEE. 2009, pp. 882–886.

[AWL08] Mohamad Khattar Awad, Kainam Thomas Wong, and Zheng-bin Li. "An integrated overview of the open literature's empirical data on the indoor radiowave channel's delay properties". In: *IEEE Transactions on Antennas and Propagation* 56.5 (2008), pp. 1451–1468.

[Jem+08] J Jemai et al. "UWB channel modeling within an aircraft cabin". In: *2008 IEEE International Conference on Ultra-Wideband*. Vol. 2. IEEE. 2008, pp. 5–8.

[SV87] Adel AM Saleh and Reinaldo Valenzuela. "A statistical model for indoor multipath propagation". In: *IEEE Journal on selected areas in communications* 5.2 (1987), pp. 128–137.

[CCM09] Simon Chiu, James Chuang, and David G Michelson. "Characterization of UWB channel impulse responses within the passenger cabin of a boeing 737-200 aircraft". In: *IEEE Transactions on Antennas and Propagation* 58.3 (2009), pp. 935–945.

[Cha+19] Aniruddha Chandra et al. "60-GHz millimeter-wave propagation inside bus: Measurement, modeling, simulation, and performance analysis". In: *IEEE Access* 7 (2019), pp. 97815–97826.

[BHV07] Ramya Bhagavatula, Robert W Heath Jr, and Sriram Vishwanath. "Optimizing MIMO antenna placement and array configurations for multimedia delivery in aircraft". In: *2007 IEEE 65th Vehicular Technology Conference-VTC2007-Spring*. IEEE. 2007, pp. 425–429.

[Wu+16] Shangbin Wu, Sooyoung Hur, Kuyeon Whang, and Maziar Nekovee. "Intra-cluster characteristics of 28 GHz wireless channel in urban micro street canyon". In: *2016 IEEE Global Communications Conference (GLOBECOM)*. IEEE. 2016, pp. 1–6.

[Che+21b] Yi Chen, Yuanbo Li, Chong Han, Ziming Yu, and Guangjian Wang. "Channel measurement and ray-tracing-statistical hybrid modeling for low-terahertz indoor communications". In: *IEEE Transactions on Wireless Communications* 20.12 (2021), pp. 8163–8176.

[AN00] Georgia E Athanasiadou and Andrew R Nix. "Investigation into the sensitivity of the power predictions of a microcellular ray tracing propagation model". In: *IEEE transactions on Vehicular Technology* 49.4 (2000), pp. 1140–1151.

[Lag+98] AN Lagarkov, SM Matytsin, KN Rozanov, and AK Sarychev. "Dielectric properties of fiber-filled composites". In: *Journal of Applied Physics* 84.7 (1998), pp. 3806–3814.

[Sok+05] VI Sokolov, SI Shalgunov, IG Gurtovnik, LG Mikheeva, and ID Simonov-Emel'yanov. "Dielectric characteristics of glass fibre reinforced plastics and their components". In: *International Polymer Science and Technology* 32.7 (2005), pp. 62–67.

[GRO] EURO-COMPOSITES ® GROUP. *Defence Technology Naval Application*. Accessed: 2022-11-04. URL: https://www.euro-composites.com/wp-content/uploads/EC562-126e.pdf.

[Sei19] Patrick Sascha Seiler. "Dielektrische Materialcharakterisierung Bis Zu Terahertz Frequenzen Unter Verwendung Planarer Leitungen: Dielectric Material Characterization Up to Terahertz Frequencies Using Planar Transmission Lines". PhD thesis. Technische Universität Dresden, 2019.

[Raj+09] KV Rajani, S Rajesh, KP Murali, P Mohanan, and R Ratheesh. "Preparation and microwave characterization of PTFE/PEEK blends". In: *Polymer composites* 30.3 (2009), pp. 296–300.

[Gor+20] Aleksandr Gorst, Kseniya Zavyalova, Sergey Shipilov, Vladimir Yakubov, and Aleksandr Mironchev. "Microwave Method for Measuring Electrical Properties of the Materials". In: *Applied Sciences* 10.24 (2020), p. 8936.

[WY+19] Liang Wang, Hongyu Yu, et al. "A Method to Determine Broadband Complex Permittivity of Thin Film Dielectric Materials up to 60 GHz". In: *arXiv preprint arXiv:1908.00128* (2019).

[AAS17] MI Ahmed, MF Ahmed, and AA Shaalan. "Investigation and comparison of 2.4 GHz wearable antennas on three textile substrates and its performance characteristics". In: *Open Journal of Antennas and Propagation* 5.3 (2017), pp. 110–120.

[Mey15] G Joel Meyer. "Polyurethane foam: Dielectric materials for use in radomes and other applications". In: *General plastics manufacturing company* (2015).

[Ada+15] Salah-Eddine Adami, Dibin Zhu, Yi Li, Evangelos Mellios, Bernard H Stark, and Steve Beeby. "A 2.45 GHz rectenna screen-printed on polycotton for on-body RF power transfer and harvesting". In: *2015 IEEE Wireless Power Transfer Conference (WPTC)*. IEEE. 2015, pp. 1–4.

[Kom12] Vyacheslav V Komarov. *Handbook of dielectric and thermal properties of materials at microwave frequencies*. Artech house, 2012.

[ETS19] The European Telecommunications Standards Institute (ETSI). *Wideband transmission systems; Data transmission equipment operating in the 2,4 GHz band; Harmonised Standard for access to radio spectrum*. Harmonised European Standard 300 328. Version 2.2.2. July 2019.

[ETS17] The European Telecommunications Standards Institute (ETSI). *5 GHz RLAN; Harmonised Standard covering the essential requirements of article 3.2 of Directive 2014/53/EU*. Harmonised European Standard 301 893. Version 2.1.1. May 2017.

[MCF21] Allan Wainaina Mbugua, Yun Chen, and Wei Fan. "On simplification of ray tracing channels in radio channel emulators for device testing". In: *2021 15th European Conference on Antennas and Propagation (EuCAP)*. IEEE. 2021, pp. 1–5.

[Est+96] Martin Ester, Hans-Peter Kriegel, Jörg Sander, and Xiaowei Xu. "A density-based algorithm for discovering clusters in large spatial databases with noise". In: *Proceedings of the 2nd ACM SIGKDD International Conference on Knowledge Discovery and Data Mining*. Vol. 96. 34. 1996, pp. 226–231.

[Czi+05] Nicolai Czink, Pierluigi Cera, Jari Salo, Ernst Bonek, Jukka-Pekka Nuutinen, and Juha Ylitalo. "Automatic clustering of MIMO channel parameters using the multi-path component distance measure". In: *International Symposium on Wireless Personal Multimedia Communications, Aalborg, Denmark, September 18-22, 2005*. 2005, pp. 537–541.

[Wan+22] Lei Wang, Bo Ai, Yong Niu, Meilin Gao, and Zhangdui Zhong. "Adaptive Beam Alignment Based on Deep Reinforcement Learning for High Speed Railways". In: *2022 IEEE 95th Vehicular Technology Conference:(VTC2022-Spring)*. IEEE. 2022, pp. 1–6.

[CXJ19] Qimei Chen, Xiaoxia Xu, and Hao Jiang. "Spatial multiplexing based nr-u and wifi coexistence in unlicensed spectrum". In: *2019 IEEE 90th Vehicular Technology Conference (VTC2019-Fall)*. IEEE. 2019, pp. 1–5.

[CF20] Francisco Costa Neto and Tarcisio Ferreira Maciel. "SDMA Grouping Based on Unsupervised Learning for Multi-User MIMO Systems". In: *Journal of Communication and Information Systems* 35.1 (May 2020), pp. 124–132.

[KWL14] Meng-Lin Ku, Li-Chun Wang, and Yu-Lung Liu. "Joint antenna beamforming, multiuser scheduling, and power allocation for hierarchical cellular systems". In: *IEEE Journal on Selected Areas in Communications* 33.5 (2014), pp. 896–909.

[ASS19] Yousef Ali Abohamra, M Reza Soleymani, and Yousef R Shayan. "Using beamforming for dense frequency reuse in 5g". In: *IEEE Access* 7 (2019), pp. 9181–9190.

[FSC18] Leila Aissaoui Ferhi, Kaouthar Sethom, and Fethi Choubani. "Multi-carrier 3D beamforming for 5G ultra-dense cellular networks". In: *2018 International Conference on Advanced Systems and Electric Technologies (IC_ASET)*. IEEE. 2018, pp. 221–226.

[SF20] Li-Hsiang Shen and Kai-Ten Feng. "Mobility-aware subband and beam resource allocation schemes for millimeter wave wireless networks". In: *IEEE Transactions on Vehicular Technology* 69.10 (2020), pp. 11893–11908.

[Ahn+22] Suyoung Ahn, Joonpyo Hong, Yunhee Cho, Jehyeon Na, and Jeongho Kwak. "Sequential Beam, User, and Power Allocation for Interference Management in 5G mmWave Networks". In: *2022 International Conference on Information Networking (ICOIN)*. IEEE. 2022, pp. 429–434.

[Wu+21] Di Wu, Yong Zeng, Shi Jin, and Rui Zhang. *Environment-Aware and Training-Free Beam Alignment for mmWave Massive MIMO via Channel Knowledge Map*. IEEE, 2021.

[RNK22] Vishnu Raj, Nancy Nayak, and Sheetal Kalyani. "Deep reinforcement learning based blind mmwave MIMO beam alignment". In: *IEEE Transactions on Wireless Communications* 21.10 (2022), pp. 8772–8785.

[Gao+20] Jiabao Gao, Caijun Zhong, Xiaoming Chen, Hai Lin, and Zhaoyang Zhang. "Deep reinforcement learning for joint beamwidth and power optimization in mmWave systems". In: *IEEE Communications Letters* 24.10 (2020), pp. 2201–2205.

[Ben+23] Rima Benelmir, Salim Bitam, Scott Fowler, and Abdelhamid Mellouk. "A novel MmWave Beam Alignment Approach for Beyond 5G Autonomous Vehicle Networks". In: *IEEE Transactions on Vehicular Technology* (2023).

[WLF20] Yue Wang, Wei Liu, and Linquan Fang. "Adaptive Modulation and Coding Technology in 5G System". In: *2020 International Wireless Communications and Mobile Computing (IWCMC)*. IEEE. 2020, pp. 159–164.

[Urb19] DJ Urban. "The Importance Of Wi-Fi 6 Technology For Delivery Of gbps Internet Service". In: *SCTE ISBE Cable-Tec Expo* (2019).

[Alh+19] Mariam Alhammadi, Mouza Almansoori, Isaias Tesfu, Daniel Habte, and Irfan Ahmed. "Large-scale empirical model for a 2.4 GHz wireless network in an outdoor environment". In: *2019 Advances in Science and Engineering Technology International Conferences (ASET)*. IEEE. 2019, pp. 1–4.

[TV05] David Tse and Pramod Viswanath. "The wireless channel". In: *Fundamentals of Wireless Communication*. Cambridge University Press, 2005, pp. 10–48.

[3GP18] 3GPP. *TR 28.801 V15.1.0 (2018-01); Technical Report; Study on management and orchestration of network slicing for next generation network (Release 15)*. Tech. rep. 3rd Generation Partnership Project (3GPP), 2018.

[YH01] Hiroyuki Yomo and Sliinsuke Hara. "An uplink/downlink asymmetric slot allocation algorithm in CDMA/TDD-based wireless multimedia communications systems". In: *IEEE 54th Vehicular Technology Conference. VTC Fall 2001. Proceedings (Cat. No. 01CH37211)*. Vol. 2. IEEE. 2001, pp. 797–801.

[And04] M. Andrews. "Instability of the proportional fair scheduling algorithm for HDR". In: *IEEE Transactions on Wireless Communications* 3.5 (2004), pp. 1422–1426.

[Gur23] Gurobi Optimization, LLC. *Gurobi Optimizer Reference Manual*. 2023. URL: https://www.gurobi.com.

[SY18] Kaiming Shen and Wei Yu. "Fractional programming for communication systems—Part I: Power control and beamforming". In: *IEEE Transactions on Signal Processing* 66.10 (2018), pp. 2616–2630.

[Gol89] David E. Goldberg. *Genetic Algorithms in Search, Optimization and Machine Learning*. 1st. Addison-Wesley Longman Publishing, 1989.

[XS20] Jiankai Xue and Bo Shen. "A novel swarm intelligence optimization approach: sparrow search algorithm". In: *Systems science & control engineering* 8.1 (2020), pp. 22–34.

[Sch+17] John Schulman, Filip Wolski, Prafulla Dhariwal, Alec Radford, and Oleg Klimov. "Proximal policy optimization algorithms". In: *arXiv preprint arXiv:1707.06347* (2017).

[Raf+21] Antonin Raffin, Ashley Hill, Adam Gleave, Anssi Kanervisto, Maximilian Ernestus, and Noah Dormann. "Stable-Baselines3: Reliable Reinforcement Learning Implementations". In: *Journal of Machine Learning Research* 22.268 (2021), pp. 1–8. URL: http://jmlr.org/papers/v22/20-1364.html.

[JCH+84] Rajendra K Jain, Dah-Ming W Chiu, William R Hawe, et al. "A quantitative measure of fairness and discrimination". In: *Eastern Research Laboratory, Digital Equipment Corporation, Hudson, MA* (1984).

[Stu08] Student. "The probable error of a mean". In: *Biometrika* 6.1 (1908), pp. 1–25.

[Dun61] Olive Jean Dunn. "Multiple comparisons among means". In: *Journal of the American statistical association* 56.293 (1961), pp. 52–64.

[Liu+18] Jiajia Liu, Yongpeng Shi, Zubair Md Fadlullah, and Nei Kato. "Space-air-ground integrated network: A survey". In: *IEEE Communications Surveys & Tutorials* 20.4 (2018), pp. 2714–2741.

[Med+10] Daniel Medina, Felix Hoffmann, Francesco Rossetto, and C-H Rokitansky. "A crosslayer geographic routing algorithm for the airborne internet". In: *2010 IEEE International Conference on Communications*. IEEE. 2010, pp. 1–6.

[Che+21c] Qian Chen, Weixiao Meng, Shuai Han, Cheng Li, and Hsiao-Hwa Chen. "Reinforcement learning-based energy-efficient data access for airborne users in civil aircrafts-enabled SAGIN". In: *IEEE Transactions on Green Communications and Networking* 5.2 (2021), pp. 934–949.

[Pha+20] Quoc-Viet Pham et al. "A survey of multi-access edge computing in 5G and beyond: Fundamentals, technology integration, and state-of-the-art". In: *IEEE access* 8 (2020), pp. 116974–117017.

[Wan+18] Yuanjun Wang, Jiaxin Zhang, Xing Zhang, Peng Wang, and Liangjingrong Liu. "A Computation Offloading Strategy in Satellite Terrestrial Networks with Double Edge Computing". In: *2018 IEEE International Conference on Communication Systems (ICCS)*. 2018, pp. 450–455.

[ZZT19] Zhenjiang Zhang, Wenyu Zhang, and Fan-Hsun Tseng. "Satellite Mobile Edge Computing: Improving QoS of High-Speed Satellite-Terrestrial Networks Using Edge Computing Techniques". In: *IEEE Network* 33.1 (2019), pp. 70–76.

[Che+19] Nan Cheng et al. "Space/aerial-assisted computing offloading for IoT applications: A learning-based approach". In: *IEEE Journal on Selected Areas in Communications* 37.5 (2019), pp. 1117–1129.

[Yu+21] Shuai Yu, Xiaowen Gong, Qian Shi, Xiaofei Wang, and Xu Chen. "EC-SAGINs: Edge-Computing-Enhanced Space–Air–Ground-Integrated Networks for Internet of Vehicles". In: *IEEE Internet of Things Journal* 9.8 (2021), pp. 5742–5754.

[Sat] Inmar Sat. *Inmarsat Orchestra*. Accessed: 2021-10-15. URL: https://www.inmarsat.com/en/about/technology/orchestra.html.

[Kel] Kelso, T.S. *CelesTrak*. Accessed: 2023-11-01. URL: https://celestrak.org/.

[DCC19] Inigo Del Portillo, Bruce G Cameron, and Edward F Crawley. "A technical comparison of three low earth orbit satellite constellation systems to provide global broadband". In: *Acta astronautica* 159 (2019), pp. 123–135.

[Kal+19] I Kallfass et al. "High system gain E-band link in a wideband aircraft-to-ground data transmission". In: *2019 IEEE International Conference on Microwaves, Antennas, Communications and Electronic Systems (COMCAS)*. IEEE. 2019, pp. 1–5.

[Num+22] Abdullah Numani, Sardar Muhammad Gulfam, Muhammad Awais Javed, Bilal Muhammad, Ramjee Prasad, and Syed Junaid Nawaz. "Network Architecture and Wireless Ad Hoc Routing for Airborne Internet Services". In: *Wireless Personal Communications* (2022), pp. 1–15.

[BS15] KD Büchter and A Sizmann. *High-bandwidth Aeronautical Telecommunication Options*. Deutsche Gesellschaft für Luft-und Raumfahrt-Lilienthal-Oberth eV, 2015.

[ETS12] The European Telecommunications Standards Institute (ETSI). *Electromagnetic compatibility and Radio spectrum Matters (ERM); System Reference document (SRdoc); Broadband Direct-Air-to-Ground Communications System employing beamforming antennas, operating in the 2,4 GHz and 5,8 GHz bands*. Technical Report 101 599. Version 1.1.3. Sept. 2012.

[ETS16] The European Telecommunications Standards Institute (ETSI). *Digital cellular telecommunications system (Phase 2+) (GSM); Universal Mobile Telecommunications System (UMTS); LTE; Policy and charging control architecture*. Technical Specification 123 203. Mar. 2016.

[STV15] Marco Savi, Massimo Tornatore, and Giacomo Verticale. "Impact of processing costs on service chain placement in network functions virtualization". In: *2015 IEEE conference on network function virtualization and software defined network (NFV-SDN)*. IEEE. 2015, pp. 191–197.

[GB18] Johan Garcia and Anna Brunstrom. "Clustering-based separation of media transfers in DPI-classified cellular video and VoIP traffic". In: *2018 IEEE Wireless Communications and Networking Conference (WCNC)*. IEEE. 2018, pp. 1–6.

[Sth+21] Saurav Sthapit, Subhash Lakshminarayana, Ligang He, Gregory Epiphaniou, and Carsten Maple. "Reinforcement learning for security-aware computation offloading in satellite networks". In: *IEEE Internet of Things Journal* 9.14 (2021), pp. 12351–12363.

[Pap+20] Arled Papa, Tomaso De Cola, Petra Vizarreta, Mu He, Carmen Mas-Machuca, and Wolfgang Kellerer. "Design and evaluation of reconfigurable SDN LEO constellations". In: *IEEE Transactions on Network and Service Management* 17.3 (2020), pp. 1432–1445.